Numerical Study of Hydrodynamic and Sediment Transport Within the Brisbane River Estuary and Moreton Bay, Australia

Author

Yu, Yingying

Published

2017

Thesis Type

Thesis (PhD Doctorate)

School

Griffith School of Engineering

DOI

Downloaded from

Griffith Research Online

Numerical study of hydrodynamic and sediment transport within the Brisbane River estuary and Moreton Bay, Australia

Yingying Yu

MPhil

Griffith School of Engineering

Griffith Sciences

Griffith University

Submitted in fulfilment of the requirements of the degree of

Doctor of Philosophy

December 2016

Abstract

The coastal region influences many aspects of our lives, including our economy, our quality of life and our safety and security. Many large cities in Australia are located along estuaries and coasts. As a consequence of the growing human population, most coastal areas throughout Australia are now facing threats of over urbanisation, and industrialisation, resulting in significant impacts on the coastal aquatic environments. Additional challenges may also come from more frequent severe flooding resulting to climate changes, which could degrade the environment even further and more rapidly.

Sediment accumulation and transport in estuaries and coastal bays is one of major issues, not only impacting on the maintenance of navigation channel but also resulting in ecological problems. For several decades, a large number of investigations of sediment transport have been conducted in Australia, which them mostly addressing conditions of the sediment delivered to the estuary within the dry season. However, a limited number of researches have been done in great detail, focusing on the hydrodynamic and sediment transport in the wet season.

In recent years, with the development of computing and satellite technologies, the study on the hydrodynamic and sediment transport has allowed studies to be conducted on large spatial and temporal scales. Additionally, this has meant it is now easier to investigate the event-driven behaviour severe flooding events.

In this context, the primary aim of this research is to examine the features of hydrodynamic and sediment transport in a shallow coastal area in both the dry and wet seasons, to develop a thorough understanding of sediment transport characteristics which would assist in the management of coastal and estuarine water quality.

A preliminary investigation into the designs and effects of the flexible grids conducted through the various mesh resolution led to an efficient and higher-performance bathymetry for the numerical model. Using this model and measurement data, a comprehensive study, both in the short- and long-term, into the salinity and sediment distributions in the estuary was carried out and the dispersion coefficient in the estuary was calibrated. Furthermore, the horizontal dispersion in the shallow bay was evaluated, applying both experimental

Lagrangian drifter data and numerical simulation. Based on the calibrated model and dispersion information, the behaviour of sediment transport in the shallow coastal system following severe flood events was investigated.

The investigation revealed the dominant tidal effects on the salinity and turbidity distribution in the estuary under normal weather conditions. Results showed that the longitudinal salinity varied at approximately 0.45 and 0.61 psu/hour during neap and spring tides, respectively. The salinity dilution changes as the upstream distance in the estuary, following a fourth-order polynomial function. The turbidity stayed at a higher level and was less impacted by tide in the upper estuary, however, the water cleared up while the tide changed from flood to ebb in the mid and lower estuary. The typical lengths of turbidity maximum zone were estimated during the wet and dry seasons. It was found that the turbidity maximum zone was about 10 km longer during the wet season than the dry season. In the dispersion study, based on the Lagrangian drifter data, a power function of the squared separation distance over the apparent dispersion coefficient produced an R^2 exceeding 0.7, indicating a significant relationship between them. The study results also demonstrated that the tidal effects on dispersion were dependent on the effect of tidal excursion and residual current. In addition, results of sediment transport under severe weather conditions showed that the characteristics of sediment transport were determined by the combined effects of flood runoff and tidal currents. Four distinct characteristics of sediment transport in the shallow coastal area were identified during the severe flood event. It was found that the simulated sediment horizontal flux increased in magnitude with distance toward the river mouth, approaching 5 $kg/m^2/s$. However, the flux changed to decrease by approximately 15.4 % at the river mouth, significantly drop by 48.3% in a short distance from the river mouth, further decrease by about one order of magnitude within the bay. The study also gave an insight into the application of remote Satellite observation in the estimation of water turbidity which in turn monitored the sediment movement in the coastal system.

This research firstly increases the fundamental understanding of hydrodynamic and sediment transport behaviours in a shallow coastal system, during a short- (tidal cycles) and long- (wet and dry seasons) terms and severe flood events. Secondly, the calibrated model with dispersion information can serve as an effective tool to investigate effects of management scenarios on sediment transport. Last but not least, the application of satellite-observed water reflectance provides a practical solution for estimating water turbidity and sediment concentration levels in a shallow coastal water not only under normal weather conditions but

also during flood events, which is particularly prominent for immediate assessment of flood impacts.

Statement of Originality

This work has not previously been submitted for a degree or diploma in any university. To the best of my knowledge and belief, the thesis contains no material previously published or written by another person except where due reference is made in the thesis itself.

Yingying Yu

December

2016

Acknowledgement of Published Papers

Section 9.1 of the Griffith University Code for the Responsible Conduct of Research ("Criteria for Authorship"), in accordance with Section 5 of the Australian Code for the Responsible Conduct of Research, states:

To be named as an author, a researcher must have made a substantial scholarly contribution to the creative or scholarly work that constitutes the research output, and be able to take public responsibility for at least that part of the work they contributed. Attribution of authorship depends to some extent on the discipline and publisher policies, but in all cases, authorship must be based on substantial contributions in a combination of one or more of:

- *Conception and design of the research project.*

- *Analysis and interpretation of research data.*

- *Drafting or making significant parts of the creative or scholarly work or critically revising it so as to contribute significantly to the final output.*

Section 9.3 of the Griffith University Code ("Responsibilities of Researchers"), in accordance with Section 5 of the Australian Code, states:

Researchers are expected to:

- *Offer authorship to all people, including research trainees, who meet the criteria for authorship listed above, but only those people.*

- *Accept or decline offers of authorship promptly in writing.*

- *Include in the list of authors only those who have accepted authorship.*

- *Appoint one author to be the executive author to record authorship and manage correspondence about the work with the publisher and other interested parties.*

- *Acknowledge all those who have contributed to the research, facilities or materials but who do not qualify as authors, such as research assistants, technical staff, and advisors on cultural or community knowledge.*

- *Obtain written consent to name individuals.*

Included in this thesis are three peer- reviewed published conference papers in Chapter 3, two peer-reviewed published papers in Chapter 4 and 5, and one paper submitted for publication in Chapter 6, which are co-authored with other researchers (principal supervisors). My contribution to each co-authored paper is outlined at the front of the relevant chapter.

The bibliographic details for these papers are:

Chapter 3:

Yu, Y., Zhang, H., Lemckert, C.J., 2012. Effects of mesh resolution for hydrodynamic and transport modelling in coastal area, Proceedings of the 4th International Conference on Computational Methods. Crowne Plaza, Gold Coast, Australia, 21-27.

Yu, Y., Zhang, H., Lemckert, C.J., 2013. The tidal influence on the turbidity maximum in a tide-dominated estuary: The Brisbane River estuary, Australia, Proceedings of the 35th IAHR World Congress. Chengdu, China, 7998-8007.

Yu, Y., Zhang, H., Lemckert, C.J. 2015. Turbidity distribution in the Brisbane River estuary during the 2010-2011 Queensland floods. the 36th International Association for Hydro-Environment Engineering and Research (IAHR) World Congresses. The Hague, the Netherlands.

Chapter 4:

Yu, Y., Zhang, H., Lemckert, C.J., 2014. Salinity and turbidity distributions in the Brisbane River estuary, Australia, Journal of Hydrology 519, 3338-3352.

Chapter 5:

Yu, Y., Zhang, H., Spencer, D., Dunn, R.J.K., Lemckert, C.J., 2016. An investigation of dispersion characteristics in shallow coastal waters, Estuarine, Coastal and Shelf Science, 180, 21-32.

Yingying Yu

Prof Hong Zhang (principal supervisor and co-author)

Prof Charles Lemckert (principal supervisor and co-author)

Acknowledgements

I would like to express my sincere gratitude and thanks to my supervisor, Professor Hong Zhang, for her insight guidance and continuous encouragement throughout the course of this study and for the opportunity to undertake this research. Without her, the work described in this thesis would not have been possible.

My heartfelt thanks to Professor Charles Lemckert for his inspiration, support encouragement during my entire period of candidature.

Thanks also to Mr David Spencer and Mr Johan Gustafson with all field trips and data collection.

The assistance from the kind staff from the Griffith English Language Institute, Gold Coast campus, Griffith University is acknowledged. Mr. Terry Mitchell and Mrs. Petrina Maizey are noted with appreciation for their professional editing of this thesis.

I would like to thank my husband, Chuen, for his unconditional love, support, encouragement, and invaluable assistance. Last but not least, I must thank my parents for their emotional support, understanding, patience and sacrifice throughout my education.

Publications

The following peer reviewed publications were produced to disseminate the concept and results of the research presented in this thesis:

Journal papers:

Yu, Y., Zhang, H. and Lemckert, C.J., 2013b. Seasonal variations of the salinity and turbidity in the Brisbane River estuary, Queensland, Australia., Journal of Coastal Research, Special Issue No. 65.

Yu, Y., Zhang, H., Lemckert, C.J., 2014. Salinity and turbidity distributions in the Brisbane River estuary, Australia, Journal of Hydrology 519, PartD, 3338-3352.

Yu, Y., Zhang, H., Spencer, D., Dunn, R.J.K., Lemckert, C.J., 2016. An investigation of dispersion characteristics in shallow coastal waters, Estuarine, Coastal and Shelf Science 180, 21-32.

Yu, Y., Zhang, H., Lemckert, C.J. Sediment transport in a tidal estuary following severe flood events (submitted to *Environmental Fluid Mechanics* in December 2016)

Referred Conference papers:

Yu, Y., Zhang, H., Lemckert, C.J., 2012. Effects of mesh resolution for hydrodynamic and transport modelling in coastal area, Proceedings of the 4th International Conference on Computational Methods. Crowne Plaza, Gold Coast, Australia, 21-27.

Yu, Y., Zhang, H., Lemckert, C.J., 2013c. The tidal influence on the turbidity maximum in a tide-dominated estuary: The Brisbane River estuary, Australia, Proceedings of the 35th IAHR World Congress. Chengdu, China, 7998-8007.

Yu, Y., Spencer, D., Zhang, H., Lemckert, C.J., 2014. Numerical and experimental study of dispersion in a shallow coastal area, the 11th Pacific Asia Offshore Mechanics Symposium. Shanghai, China.

Yu, Y., Zhang, H., Lemckert, C.J. 2015. Turbidity distribution in the Brisbane River estuary during the 2010-2011 Queensland floods. the 36th International Association

for Hydro-Environment Engineering and Research (IAHR) World Congresses. The Hague, the Netherlands.

Table of Contents

List of Figures

XVI

XVIII

List of Tables

List of Symbols

A	area of cross section
A_{max}	maximum size of mesh element area
a	regression coefficients of dispersion
a_1	dispersion factor
a_2	discharge factor
b	regression coefficients of dispersion
b_1	dispersion exponent
b_2	discharge exponent
$\bar{C}$	depth-averaged mass concentration
C	suspended sediment concentration
C_b	near bed concentration
C_D	drag coefficient
C_v	volumetric concentration of flocs
CFL_HD	the hydrodynamic Courant-Friedrich-Levy
C_t	constant coefficient of Turbulence Two-equation model
c^*, d^*	coefficients in tidal excursion function
c_a, c_b	empirical factors of wind stress on water surface
D^2	squared separation distance
D_c	dispersion coefficient
D_h, D_v	horizontal/vertical diffusion coefficient
De	deposition rate
d_p	particle diameter
E	erosion rate
E_0	empirical erosion coefficient
E_m	power of erosion
F	suspended sediment flux
F_d	fluid drag force
F_g	gravity force
F_q	river discharge flux

F_s	salinity flux
$F_{u\text{-}avg}$, $F_{v\text{-}avg}$	depth-averaged sediment flux in u- and v- components
Fh_{avg}	depth-averaged horizontal flux
f	momentum forcing
f_c	current friction factor
f_{cw}	combined wave-current friction factor
f_w	wave friction factor
h	local water depth
I_f	flow resistance term
K	apparent dispersion coefficient
K_d	linear decay coefficient
K_{tc}	tide-cycle-averaged apparent dispersion coefficient
k_l	coefficient related to sediment compositions
k_s	bed roughness
k_t	turbulent kinetic energy
L	tidal excursion
l	length of mesh element
l_t	length scale of turbulence
m	coefficient related to flocs non-linear effects
m_d	drift term
n_d	dispersion term
n_1	coefficient related to Re
n_2	coefficient related to turbulence properties
n_3	coefficient related to particle settling velocity
P_D	probability ramp function of deposition
P_e	the Peclet number
p_i	coefficient of salinity dilution function
p_t, m_t, n_t	parameters taking the form of different turbulent closures
Q	river discharge rate
Q_{cum}	cumulative sediment loading
q	lateral inflow
R_e	the Reynolds number
RC	relative height of centroid

S	salinity in psu
S_c	source/sink term
S_p	salinity dilution rate in percentage
SL	sediment loading
T_{ur}	water turbidity
U	donates instantaneous flow velocity
$\bar{u}_0$	velocity above the bottom
$u*$	residual current
u_b	wave orbital velocity
$U_{current}$	tide-driven current
U_r, V_r	tidal residual current
U_{shear}	wind-driven current
U_{slip}	wind drag on particles that are exposed to wind
V_h, V_v	horizontal / vertical eddy viscosity
v_m	velocity at the river mouth
W_0	settling velocity of a single sediment particle
W_d	wind direction in degrees
W_r	water reflectance
W_S	settling rate
W_W	calibration factor for wind drag on particle
α	empirical constant of erosion formula
β	momentum distribution coefficient
$\varDelta t$	time step interval
η_{obs}	observation data
η_{sim}	simulation results
θ_F	angle between Fh_{avg} and the true north
θ_w	wind drift angle
κ	von Karman's constant
μ_c	efficiency factor of current
μ_w	efficiency factor of wave
ξ	a random number in tracking module in MIKE DHI
ρ	density of water
ρ_s	density of sediment

ρ_w	density of homogeneous water
σ	geometrically-averaged centroid of cluster
σ_T	the Prandtl number
τ_b	bed shear stress
τ_{cd}	critical bed shear stress for deposition
τ_{ce}	critical bed shear stress for erosion
υ	kinematic viscosity of the fluid
ψ	genetic parameter of the GLS model

Chapter 1 Introduction

1.1   Background

Coastal regions are an important as they influence many aspects of our lives, including our economy, quality of life, safety and security. The coasts are also the most productive and resource-rich areas on the planet. In recent years, coastal regions have faced many environmental challenges, such as enhanced sediment load resulting from channel erosion, intensive land use and severe weather conditions (Nezlin et al., 2008, Wolanski et al., 2008, Yu et al., 2013b, Gibbes et al., 2014, Wolanski, 2014).   This poses both economic and environmental problems. For instance, elevated turbidity levels that limits the availability of light penetration through water columns for primary producers. Additionally, resuspended sediment from a river bed can carry excessive nutrients and harmful organic contaminants into the water columns, resulting in economic and environmental problems (Lemckert et al., 2011, O'Brien et al., 2012). Further, increased sediment inflow into the coastal zone will result in the infilling of channels, which subsequently impact of navigability and shipping. Therefore, developing a thorough understanding of sediment transport characteristics is important to assist in the management of coastal and estuarine water quality and the maintenance of navigable port areas.

Turbidity is the most visible indicator of sediment concentration level and water quality (Ecosystem Health Monitoring Program, 2007). Turbidity regions usually coincide with transition zones between rivers and oceans, where sediment accumulates over time (Wolanski, 2014). The formation of Estuarine Turbidity Maxima (ETM) zones is usually observed in macro − tidal estuaries, where strong flow currents can suspend large amounts of find sediment from the bottom and thus suspended sediment concentration (SSC) increases to high level (Uncles et al., 2002). SSC levels within the ETM are typically one or two orders of magnitude higher than upstream river and downstream coastal regions downstream (Wolanski, 2014). The existence and variation of turbidity not only affect the water quality, but also result in strong spatial and temporal gradients in physical processes, which further influences flow dynamics (Hughes et al., 1998, Massei et al., 2003).

Generally, the movement of sediment in coastal rivers primarily depends on turbulence, which raises sediment to the surface and supports it to move downcurrent before the

turbulence subsides (Zhang and Chan, 2003, Cambell, 2009, Amoudry and Souza, 2011). Apart from the effects of turbulence, sediment transport in a tide dominated estuary is also significantly controlled by tides. Although sediment particles have a chance to settle to the bottom during slack water (when turbulence is at a minimum), they are lifted into the water column and transported downcurrent as the tidal current increases. A large amount of sediment will therefore accumulate in an estuary (Dyer, 1989). Resuspension of accumulated sediment in estuaries usually leads to high turbidity in waterways, which limits light penetration and prevents the occurrence of algal blooms (Eyre et al., 1998, Hollywood et al., 2001, Hossain et al., 2004). Due to the dependence of sediment movement on tidal conditions and river inflow, sediment transport characteristics and turbidity distributions in coastal regions can be periodically and seasonally different. In addition, the sediment transport is an event-driven process, particularly during a period of severe flood events, in which large flood-runoff accelerates channel erosion and discharges massive inputs of fresh water and sediments into coastal areas result in an increase in large sediment and nutrient loads and forms of flood-driven sediment plumes.

A flood-driven sediment plume consisting of freshwater and high concentrations of sediment spreads and disperses in adjacent coastal and marine areas. This has hydrographical implications, such as large amount of sediment deposition in navigable channels (Eyre et al., 1998). Yangtze Estuary, for example, where over $1 \times 10^6 \, \text{m}^3$ of sediment has been dredged pre year from 2006 to 2008 (Liu et al., 2010). The significant increase of suspended sediments, especially the muds, is also an issue that can negatively impact many marine organisms (Wolanski, 2014). For instance, Chesapeake Bay experienced a flood with the maximum daily discharge of around $3.2 \times 10^3 \, \text{m}^3$/s in 1972, resulting in about 3.1×10^6 tonnes of suspended sediment deposition in the bay (Page and Shaw, 1973, Loftus and Seliger, 1976). As a consequence, nutrients and organic matters were raised and experienced elevated plankton production for many years (Schubel, 1977).

Understanding sediment transport process is therefore of great significance. Knowledge of the physical progresses of sediment delivery, dilution, deposition, erosion and settling helps to predict how long the dumped contaminant can last before it erodes; how often a channel and harbour need to be dredged; and how beaches change (which is particularly important to those living near a beach. Hence, environmental assessment and estuary management will also benefit from the accurate understanding of sediment transport.

The study of turbidity behaviour and sediment transport in coastal water systems is usually complex as many boundary forcing mechanisms such as tides, wind, wave and river discharge (Wolanski, 2014). Previous sedimentation studies have been conducted through theoretical, experimental, field-based and numerical approaches. Numerical models have been extensively applied in recent years. The distinct advantage of the numerical methods is that it can be employed over a wide range of spatial and temporal scales, and can take relevant forcing mechanisms into account. It also allows for numerical experiments to be undertaken, whereby different parameters can be varied in order to evaluate their relative impact. It is known that hydrodynamic flow patterns associated with suspended sediment make estuaries a complex environment, which is difficult to model (Schacht, 2005). Therefore, a number of aspects can be explored to improve the modelling of sediment transport, such as accurate representation of flow dispersion and physical processes of sediment.

1.2   The study area

As Australia is a country surrounded by oceans, its estuary resources are rich and diverse. However, an ongoing increase in intensive land use has been linked to the degradation of coastal water and sediment quality within Australian estuaries. It is thought that the growth of sediment loading may significantly affect surrounding vulnerable ecosystems. This is particularly evident in Moreton Bay (Ecosystem Health Monitoring Program, 2007).

The Brisbane River estuary (BRE) and Moreton Bay are located in Southeast Queensland, Australia. The sediment from a number of adjacent estuaries is discharged into the Bay, with the Brisbane River estuary being the largest contributor (Dennison and Abal, 1999). The high sediment loading from the BRE, has not only been a major health problem for the Moreton Bay ecosystem, but also has affected the navigable entrances to the Port of Brisbane. So far, several studies have produced estimations of the water quality and sediment quantity within the BRE and Moreton Bay (Eyre et al., 1998, Howes et al., 2002, Schacht and Lemckert, 2003, Hossain et al., 2004, Olley and Croke, 2011, O'Brien et al., 2012). However, insufficient detailed studies of sediment transport dynamics have been undertaken thus far. Another concern is that the BRE and Moreton Bay have experienced increasingly severe flood events (both in terms of frequency and magnitude), implying that a large volume of sediment has been discharged and has settled in the bay (Babister and Retallick, 2011). Due to the knowledge gap of the lack of suspended sediment forcing mechanisms in a shallow bay

system, the BRE and Moreton Bay are therefore used to elucidate on these mechanisms, focusing on the:

- Proper consideration of driving mechanisms, such as tides, winds and river discharge;
- Adequate representations of dispersion –advection features in a numerical model; and
- Particularly, comprehensive studies of variation of turbidity distribution and sediment transport following severe flood events.

1.3   **Research objectives and scopes**

The research work presented in this study was motivated by the existence of the above gaps. Therefore, the specific objectives of this thesis, which will use the BRE and Moreton Bay as test sites, are:

- To consider of relevant driving mechanisms, including river discharge, winds and tides in the simulation and examining the impacts of these environmental forces on the sediment transport;
- To investigate the characteristics of salinity and turbidity distribution during tidal cycle and dry and wet seasons;
- To estimate and implement dispersion module in model by using field measurement data; and
- To study the physical processes of sediment transport in response to severe flood events.

Based upon these, this study will enhance our knowledge of sediment transport which could benefit environmental assessment and management.

1.4   **Structure of the thesis**

The remainder of this thesis has been organised into six chapters. Chapter 2 reviews previous studies of turbidity behaviour and sediment transport in coastal systems, including the features of turbidity distributions and properties of sediment particles, important factors of sediment transport and study methods.

In Chapter 3, three preliminary studies on numerical model and turbidity conditions in the BRE have been conducted. In the first section of this chapter, the effects of mesh resolution of bathymetry on the numerical modelling were investigated. This study proposed an efficient and high-performance bathymetry, and so has significant implications for the model set-up.

The outcome of this study has been published in *the 4th International Conference on Computational Methods (2011)*, under the title 'Effects of mesh resolution for hydrodynamic and transport modelling in coastal area'. In the second section of this chapter, the tidal influences on the turbidity maximum under non-significant flood conditions were examined. This study has been published in *the 35th International Association for Hydro-Environment Engineering and Research (IAHR) World Congresses*, entitled 'The tidal influence on the turbidity maximum in a tide-dominated estuary: The Brisbane River estuary, Australia'. The study presented in the third section of this chapter focused on the turbidity distribution during flood events. The results have been published in *the 36th International Association for Hydro-Environment Engineering and Research (IAHR) World Congresses,* under the title 'Turbidity distribution in the Brisbane River estuary during the 2010-2011 Queensland floods'.

Based on the validated model and preliminary results presented in Chapter 3, comprehensive investigations (both in the short- and long-term) into the salinity and turbidity distributions in the BRE were conducted in Chapter 4. Findings of periodical and seasonal variation of distributions of salinity and turbidity would be essential to investigate sediment transport in coastal regions. This study has been published in the *Journal of Hydrology*, volume 519, 2014, entitled 'Salinity and turbidity distributions in the Brisbane River estuary, Australia'.

In Chapter 5, as one of the most important factors influencing sediment transport in coastal regions, hydrodynamic dispersion was examined experimentally and numerically. A cluster of four Lagrangian drifters were released into two shallow coastal regions and the movement of drifters were recorded. The study has been published in the *Estuarine, Coastal and Shelf Science*, volume 180, 2016, under the title 'An investigation of dispersion characteristics in shallow coastal waters, Estuarine'.

Chapter 6 focuses on the investigation of sediment spread, suspension and settling in the BRE and Moreton Bay during severe flood events. The flood-driven plume evolution was simulated, sediment flux was estimated, and effects of flooding discharge and tides on sediment transport were examined. This chapter entitled 'Sediment transport in a tidal estuary following severe flood events', will be submitted to Environmental Fluid Mechanics.

The overall conclusions of the present research are summarised in Chapter 7, which also offers recommendations and improvements for further study. All references are listed after Chapter 7. At the end of the thesis, two attachments of publications carried out as part of the learning process associated with this PhD research.

Chapter 2 Literature review

2.1 Turbidity behaviour in coastal regions

The input and suspension of fine sediment can cause water to be turbid. The turbidity, therefore, is a most visible indicator of sediment concentration level (Ecosystem Health Monitoring Program, 2007). Based on the correlation between turbidity and fine sediment, the turbidity level is usually used as a surrogate measurement of suspended sediment concentration (Henley et al., 2000). When there is a lack of sediment data, for example it is difficult to obtain sediment concentration data in real time during flood events, the knowledge of turbidity behaviour provides a way to understand sediment transport.

The tidal influences on turbidity distribution in estuaries were usually classified into three categories according to different tidal ranges, from micro-tidal, in which the tidal range is less than 2 m, to meso-tidal, with a tidal range from 2 to 4 m, and macro-tidal, in which the tidal range exceeds 4 m (Hughes et al., 1998). Compared to the ETM zone within the micro-tidal estuary, which is always triggered by flood events, the ETM zone in meso- and macro-tidal estuaries heavily relies on tidal conditions to resuspend and transport suspended sediments (Hunt et al., 2006). Two mechanisms were proposed for the development and maintenance of the ETM zone in higher tidal ranges (Hughes et al., 1998). The first mechanism is caused by fine sediment accumulation and tidal resuspension, as a result of the combined effects of tidal-induced residual currents and gravitational circulation. The second mechanism is attributed to the distortion of tidal waves, associated with non-linear interactions between the tide and channel morphology (Dyer, 1986).

Under non-significant flood event conditions, the distribution of turbidity in estuaries varies between wet and dry seasons; the distribution generally experiences regular variations during a tidal cycle. Uncles et al. (2006) measured the turbidity over one year throughout the length of the Humber estuary, UK. They found that a strong ETM formed and settled in the lower estuary during the wet season but moved to the upper estuary during the dry season. Following severe flood events, saltwater is usually washed out of estuaries; however, flood inflow carries a large amount of sediment and particles, which would be transported, and then settled in estuaries, resulting in extreme high turbidity levels (Hunt et al., 2006).

2.2   **Sediment properties and flow conditions**

Although the turbidity behaviour indirectly reflects the sediment transport, sediment movement is naturally dependent on particles' properties and ambient flow conditions. Sediment is fragmented material generated primarily by the physical and chemical break-up of rocks from the earth's crust. These particles range in size, shape, specific gravity and composition. According to the fundamental difference in mineral compositions, sediment can be classified into two types: non- cohesive (e.g. sand) or cohesive (e.g. mud) sediment. The sediment discussed herein is cohesive. A number of sediment properties have impacts on sediment movements; for instance, sediment size influences settling velocity (Van Rijin, 1984). Fine- grained particles (<0.006 mm) are found in low-energy conditions near river banks and in tidal regions, while coarse grains are dominant in high-energy conditions in deep channels, where finer grains cannot easily exist under stronger flow currents.

Flow conditions (such as river discharge, tidal forces, turbulence and wave) are also factors that influence sediment movement. High rainfall and associated run-off events would bring a large amount of sediment downstream resulting in high turbidity in river estuaries (Dennison and Abal, 1999). The tide asymmetry between the flood and ebb tides generally determines the direction of sediment transport under normal weather conditions. Particles are eroded from beds and transported landward during the flood tide, until the velocity of current is not sufficient to carry particles; these particles then sink to river/bay bottom. As the ebb tide starts, the particles are re-suspended and carried seaward when the current achieves sufficient speed, the particles would then resettle with decreasing current velocity (Neumann, 2004).

Eddies in turbulence move randomly and therefore complicate flow conditions (Dyer, 1986). Sumer and Oguz (1978) observed particle trajectories over a smooth bed and interpreted sediment resuspension in terms of the turbulent bursting process. They proposed that sediment particles lift up from the bottom as a result of the temporary local adverse pressure gradient created by the burst passing over the particle. The lifted particles are then carried into the body of the flow and gradually rise. As eddies break into smaller eddies, until the smallest eddies disappear due to the viscous forces, particles start to settle down, only to be caught up in the next burst.

Waves motion does not produce net sediment transport itself, except for the second order mass transport known as Stokes drift (Dyer, 1986). When wavers propagate into shallow waters near coasts, they may encounter relatively strong currents that affect the current

velocities and bed-shear stress, thus becoming a very effective stirring mechanism (Van Rijin, 1984). Dyer (1986) proposed that the most significant occurrences of sediment transport in shallow water are likely to occur when the tidal movement is enhanced by wave motion. Although the sediment movement is produced by the wave-current interaction on the bottom stress is critical to the modelling of sediment transport processes, particularly in shallow coastal areas where the wave effects are felt at the sea bottom (Zhang et al., 2004, Liang et al., 2007, Warner et al., 2008).

Within a natural environment there exists a continuous transport cycle of cohesive sediment that experiences settling, deposition, erosion, and resuspension. Due to these complex characteristics of sediment particles, descriptions of sediment transport processes are largely empirical at this early stage. In recent years, numerous laboratory experiments and *in-situ* research have been carried out to investigate sediment behaviour. The most important properties and processes of sediment transport from previous studies are summarised below:

2.2.1 Settling

Estuarine field investigations have found that suspended sediment exists mainly in the form of flocs, which can vary in size from 1 μm up to several millimetres (Neumann, 2004). Different mechanisms are responsible for formation of flocs; these include collision mechanisms, the influence of velocity gradients, and biological activities (Neumann, 2004). The formation of flocs can be enhanced or hindered primarily in water columns by physical hydrodynamic effects (Fugate and Friedrichs, 2002), while flocs are transported along estuaries under river flows and tide conditions in tidal estuaries (Liu et al., 2010).

The most fundamental characteristics of floc settlement is the sediment settling velocity, W_s, which determines the suspended sediment concentration (SSC) profile (Hill et al., 1998) In the simplest condition (in which a non-cohesive spherical particle is settling in a still semi-infinite fluid domain), the settling velocity is the fall rate when the fluid drag force acting on the particle (Eq. (2.2-1)) is in equilibrium with the gravity force (Eq. (2.2-2)), yielding Eq. (2.2-3)

$$F_{\mathrm{d}} = \frac{1}{8} C_D \rho W_s \pi d_p{}^2 \qquad\qquad (2.2\text{-}1)$$

$$F_g = \frac{1}{6}(\rho_s - \rho)g{d_p}^3 \tag{2.2-2}$$

$$W_s = \sqrt{\frac{4gd_p}{3C_D}\frac{\rho_s - \rho}{\rho}} \tag{2.2-3}$$

Where W_s is the settling rate of a smooth, spherical sediment particle, ρ_s and ρ represent the densities of the sediment particle and water, respectively, g is the gravitational acceleration and d_p is the particle diameter. The drag coefficient, C_D, is a function of the settling particle Reynolds number, $R_e = W_s d_p / \upsilon$, where υ denotes the kinematic viscosity of the fluid.

In the Stokes region with R_e smaller than 1, the viscous forces are more significant than the fluid inertial force. Under this condition, the drag coefficient is given by $C_D = 24/R_e$ (Rhodes, 1998). Therefore, Stokes' law defines the settling rate of single, fine-grained non-cohesive spherical particles in still water, as in Eq. (2.2-4):

$$W_s = \frac{1}{18}\frac{\rho_s - \rho}{\rho}\frac{g{d_p}^2}{\upsilon} \tag{2.2-4}$$

Although Eq. (2.2-4) derives for a spherical particle, it is also valid for a non-spherical particles which the sieve diameter, d, is less than 100 μm, according to Stokes' law (Hill et al., 1998). However, Stokes' law begins to break down with an increasing Reynolds number (Rhodes, 1998). Thus these assumptions do not represent typical suspended particle behavior within a coastal system where sediment settles through turbulence. Additionally, Kranck (1980) stated that another main factors in the variation of settling velocity is the existence of the flocculation process, which leads to a relative change in flocs size, d.

Considering the settling velocity of a single particle in water columns is modified by the presence of other particles, sediment settling velocity has been therefore related to suspended sediment concentration (SSC), C. For non-cohesive sediments, such relevance is commonly taken to follow the experimental results of Richardson and Zaki (1954), giving:

$$\frac{W_s}{W_0} = (1 - C)^{n1} \tag{2.2-5}$$

where W_0 is the settling velocity of a single sediment particle, and $n1$ relates to R_e:

$$\begin{cases} n1 = 4.35 R_e^{-0.03} & 0.2 < R_e \leq 1 \\ n1 = 4.45 R_e^{-0.10} & 1 < R_e \leq 500 \\ n1 = 2.39 & 500 < R_e \end{cases}$$

For cohesive sediments, Mehta (1986) stated that the settling velocity is almost constant and does not depend on the concentration at very low-level concentrations ($C \leq 0.3 \, \text{kg/m}^3$). At moderate concentration ($0.1 < C < 10$ kg/m^3), the settling velocity increases with concentration, according to Mehta (1986):

$$W_s = k_1 C^{n2} \tag{2.2-6}$$

where k_1 relates to sediment compositions; and $n2$ varies from 1 to 2 depending on turbulence properties. For higher-level concentrations ($C \geq 10 \, \text{kg/m}^3$), the flocs do not fall freely, resulting in a decreasing settling velocity with concentration, which is found to follow:

$$\frac{W_s}{W_0} = (1 - k_2 C)^{n3} \tag{2.2-7}$$

where k_2 is a coefficient that depends on the particle; and $n3$ ranges from 3 to 5 (Richardson and Zaki, 1954). More recently, another formula was introduced for hindered settling of suspended cohesive sediment by Winterwerp (2002):

$$\frac{W_s}{W_0} = \frac{(1 - C_v)^m (1 - C)}{1 + 2.5 C_v} \tag{2.2-8}$$

where C_v represents the volumetric concentration of flocs; and m is responsible for possible non-linear effects.

Overall, cohesive sediment settling in water columns through turbulence may experience three different regimes – namely constant falling, flocculation, and hindered. Therefore, the analysis of settling velocity for cohesive sediment in suspension can be divided into these three categories. In numerical simulations (for example, the numerical model called MIKE3 DHI), all three regimes are considered, (i) if concentrations are assumed not to influence the settling velocity, the constant settling velocity will be applied; (ii) if flocculation concentrations occur when hindered settling is ignored, Eq. (2.2-6) will be selected; (iii) if

flocculation take place with hindered settling, the calculation of settling velocity will be offered as Eq. (2.2-7) and (2.2-8).

2.2.2 Deposition and erosion

In general, the suspended matter is trapped in estuaries and moves with tides, being deposited or re-suspended a number of times before eventually settling at the bottom (Liu et al., 2010). Deposition is predominant when the bed shear stress, τ_b, is smaller than a critical value for deposition, τ_{cd}.

When the concentration was above 10 kg/m^3, a fluid mud of sediment flocs was found to exist (Krone, 1962). Under this condition, the settling velocity reduces for increasing concentration towards the bed due to hindered settling effect, resulting in a smaller falling rate near the bed, but a relatively larger one in the upper layers. The difference in velocities produces the formulation of a near-bed fluid mud layer, particularly over a neap tide period. The thickness of the fluid mud layer will increase, resulting in the deposition rate at the upper side of the layer being greater than the consolidate rate at the bottom side. The depth of the fluid mud layer up to several meters, for example, was observed in the Severn Estuary in England (Kirby and Parker, 1980, Kirby and Parker, 1983). The deposition process in the concentration ranging from 0.3 to 10 kg/m^3 is dominated by flocculation effects. Eisma (1986) conducted a number of experiments in both a straight flume and a circular flume. His experimental results showed an equilibrium concentration was attained after a short period of rapid deposition. Flocs with a high shear resistance (strong flocs) could be deposited, while flocs with a low shear resistance were broken down in the near-bed layer and smaller flocs re-suspended. However, the flocculation effect appeared to be of minor significance to deposition at concentrations below 0.3 kg/m^3 (Krone, 1962). Furthermore, deposition of fine particles is usually parameterized following Krone (1962):

$$D_e = W_s C_b P_D \text{, for } \tau_b < \tau_{cd} \tag{2.2-9}$$

$$P_D = \max(0, \min(1, 1 - \frac{\tau_b}{\tau_{cd}})) \tag{2.2-10}$$

where D_e is the deposition rate; P_D is a probability ramp function of deposition which is defined in Eq. (2.2-10); and C_b is the near bed concentration.

Generally, there are two common expressions – Teeter Profile and Rouse Profile – to describe the near-bed concentration in terms of depth-averaged concentration. Teeter (1986) profile, based on an approximate solution to the vertical sediment fluxes during deposition, defines the near-bed concentration to be proportional to the depth-averaged mass concentration, $\overline{C}$, following Eq. (2.2-11)

$$C_b = \overline{C}\left(1 + \frac{P_e}{1.25 + 4.75 P_D^{2.5}}\right)$$
(2.2-11)

where P_e is the Peclet number defining as $P_e = 6W_s / (\kappa \sqrt{\tau_b \rho})$, in which κ is von Karman's constant, taken as 0.4. In addition to the Teeter profile, the Rouse (1937) profile was developed assuming an equilibrium suspension and balance between upward sediment transfer due to turbulent mixing and downward settling, and defined as:

$$C_b = \frac{\overline{C}}{RC}$$
(2.2-12)

in which RC is relative height of centroid, which is determined as the distance from the sea bed to the mass centre of the concentration profile divided by the local water depth. It is time-independent based on the equilibrium assumptions, and therefore the concentration profile is treated as stationary, resulting in the P_D in Eq. (2.2-9) being a constant number of 1.

In addition to the deposition, erosion is an important process for sediment transport. The erosion of a bed layer is the transfer of sediment from the bed to the water column when the applied the current-induced or wave-induced bed shear stress, τ_b, is larger than the critical shear stress for erosion τ_{ce}. The bottom shear stresses are the dominant forces causing erosion which takes place from the bed layer. For a dense consolidated bed with density of more than 600 kg/m³, the erosion rate, E, is related to a power of the available excess shear stress (Partheniades, 1965):

$$E = E_0(\tau_b - \tau_{cd})^{E_m} \qquad\qquad (2.2\text{-}13)$$

where E_0 is the empirical erosion coefficient and E_m is the power of erosion. In particular, a linear formula ($E_m = 1$) has been widely applied in research studies (Ariathurai and Krone, 1976, Mehta et al., 1989, Sanford and Halka, 1993). For a soft, partly – consolidated bed, the exponential form in Eq. (2.2-12) is usually used to estimate the erosion rate:

$$E = E_0 e^{\alpha(\tau_b - \tau_{ce})} \qquad\qquad (2.2\text{-}14)$$

where α is an empirical constant that usually ranges from 4 to 26 (Parchure and Mehta, 1985).

From the criteria for deposition and erosion occurrence as summarised above, it can be seen that the physical process taking place at the bed layer largely depends on the value of the bottom shear stress. Li and Amos (2001) concluded three status for the bed layer: (i) depositional state with only deposition when $\tau_b < \tau_{cd}$; (ii) stable state without erosion or deposition when $\tau_{cd} < \tau_b < \tau_{ce}$; (iii) erosion state with only erosion when $\tau_{ce} < \tau_b$. Winterwerp and Van Kesteren (2004) added the fourth statement – that the deposition and erosion of the bed layer are continuous, thus allowing simultaneous erosion and deposition if $\tau_{ce} < \tau_b < \tau_{cd}$ which is the reality of physical process under most conditions.

2.2.3   Recent studies on sediment transport

The Yellow River in China has an average sediment load of 1.6×10^9 tonnes, which is one of the largest contributors of global riverine sediment flux from land to sea (Shi et al., 2002). Therefore, extensive researches have been conducted on this site over the last few decades, including studies on the transport paths of suspended sediment from the Yellow River mouth to nearby Bohai Sea. These studies used the limited data collected before 1990s. Some studies suggested the suspended sediment spreading away from the river mouth moved to the south or southeast before changing to the northeast through the central part of Laizhou Bay (Shi et al., 1985, Hu et al., 1998). Another study, Jiang et al. (2000) proposed the suspended sediments dispersed and arrived just south of Laizhou Bay coast, and were then driven offshore along the southern bay coast to the Bohai Strait.

Considering the discharge of Yellow River sediment has markedly decreased during the past years (Wang et al., 2006b), Qiao et al. (2010) applied updated hydrological and sedimentological data of salinity, turbidity, SSC and grain size to re-examine the sediment transport off the Yellow River mouth. They found the suspended sediments from the river moved mainly to the south and southeast over both the short-and long- term. During the flood tide (short-term), tide- induced residual currents were the main factor driving sediments southward, while the existing anti-clockwise and clockwise circulations near the river mouth became the major hydrodynamics responsible for long-term sediment transport. In contrast to the effects of tide and currents, Qiao et al. (2010) emphasized the direct effect of river inflow lessened due to the reduction in river water discharge. Yang et al. (2011) used hydrographic data collected at twenty-four grid survey stations during 200t6 to investigate seasonal variation of sediment transport off the Yellow River. Although the river water and sediment discharges to the sea were much greater during summers, it was found the intensity of sediment transport during winters was much stronger than in summers due to the powerful effect of winter storm waves. The massive sediment off the Yellow River to the sea accumulated in a narrow coastal area during summer, then strongly re-suspended by storm waves during winter and transported to the offshore area. Thus it was concluded that the coastal area off the Yellow River acted as a sediment sink during summers, changing to a sediment source in winters.

In addition, to the seasonal variation in sediment transport, the shear front (as an important dynamics factor in controlling sediment rapid deposition at the Yellow River mouth), has been investigated. A shear front is defined as a velocity front existing along the current shearing interface between two flow bodies. It is classified as homogeneous and reversed shear fronts according to the direction of two flow bodies (Nielsen, 1992). Li et al. (2001) investigated spatial-temporal changes in the shear front based on *in-situ* measurements and Landsat scanning images. Their results revealed the reversed shear front appeared and disappeared periodically off the Yellow River mouth during a tidal cycle. Both a zero-velocity frontline and a low-velocity zone existed inside the shear front due to shearing, which resulted in the suspended sediment converging within the upper layer inside the shear front. Thus the combination of low velocities and high sediment concentration caused a large volume of sediment to accumulate in the shear front. This is similar to the findings of Wang et al. (2006a) that demonstrated the shear front acted as a barrier to the seaward transport of the suspended sediment.

Based on the field measurement data of the Yellow River sediment, numerical modelling has been applied in recent years to maintain continuous observations of sediment transport with high spatial resolution. Jiang et al. (2004) set up a numerical three-dimensional transport model to study suspended sediment distribution within the Bohai Sea, which took into account the influences of currents, wind waves, erosion and deposition processes. The model was verified by *in-situ* and remote satellite data, and the simulated outcomes showed that seasonal variation indicating suspended sediment concentration was higher during spring than in summer following the seasonal winds. Further, Lu et al. (2011) coupled a sediment numerical model with a wave-tide-circulation model to simulate the transport processes of the Yellow River, which included the surface wave-induced vertical mixing (Qiao et al., 2004); the wave-current coupled bottom shear stress (ECOMSED, 2002); and wave-induced pore pressure (Lambrechts et al., 2010). Their studies demonstrated the wave was responsible for the westward transport of sediments; the wind weakened the southward transport of sediments; and the tide accounted for the majority of sediment depositions on the Yellow Sea floor.

Like the Yellow River in the Northern Hemisphere, the Great Barrier Reef (GBR) on the Southern Hemisphere, as the world's largest reef system, receives an average annual sediment load of 14 million tonnes (Furnas, 2003). Previous studies demonstrated that most of the suspended sediment settled within 5 km of the coastline, where it may be later re-suspended and driven offshore by waves and currents (Lambeck and Woolfe, 2000, Lambrechts et al., 2010). Due to more frequent flooding events in Australia recently, sediment and nutrient runoff has posed a major threat to coast coral reefs and therefore, the fate of sediment during a river flood in the GBR has been discussed. Wolanski et al. (2008) recorded a series of fine sediment data in the GBR, during a moderate flood with a peak of more than 160 m^3/s that occurred in 2007. Their observations showed SSC peaked at 0.2 kg/m^3 near the surface and 0.4 kg/m^3 at a depth of 10 m during calm weather; while it increased to 0.5 kg/m^3 near the surface and 2 kg/m^3 at a depth of 10 m. They also found the riverine mud originating from eroded soils extended to 10 km wide in coastal waters during the river flood. A more severe flood event with a peak discharge of 10286 m^3/s occurred during 2010-2011 wet season. MODIS true colour satellite images were used by Bainbridge et al. (2012) to identify and map sediment distribution during this flood event. This observed the sediment plume significantly extended more than 50 km offshore in the GBR, and at least as far north as the Palm Island Group. The water samples collected by Bainbridge et al. (2012)

three days after the flood peak showed rapid deposition of suspended sediment < 10 km from the coastline. In the water column, they found smaller mud flocs (<100 μm) at the surface; large flocs (>100 μm) at depths >2 m; and large floc aggregates (> 200 μm) near the bottom; proving the smaller flocs had aggregated as they sank through the water column.

One of the earliest research on the suspended sediment in Moreton Bay was conducted by Eyre et al. (1998), and proposed an annual suspended sediment budget for both an average flow year and a wet year. The research confirmed Moreton Bay was the dominant source that delivered suspended sediment to the Brisbane River estuary under normal weather conditions. However, the Brisbane River estuary was the largest contributor of sediment to Moreton Bay during the wet season (Yu et al., 2014b). Based on a series of field investigations, Hollywood et al. (2001) and Howes et al. (2002) revealed the turbidity maxima existed in the 60 km upstream of the Brisbane River estuary. The turbidity levels were closely correlated to the re-suspended sediment conditions near bed. Schacht and Lemckert (2003) added that the significant sediment flux activity also occurred in the upper regions of the water column as a result of the salinity structure variation from turbulent mixing, as well as the turbidity maximum zones within the upper estuary. Hossain et al. (2004) pointed out the existence of a second turbidity maximum zone at the Brisbane River mouth, which is due to the extensive dredging generating a large tidal ingress.

In contrast to some researches focusing on the turbidity maximum zone within the upper Brisbane River estuary, relatively few studies have been conducted into sediment dynamics near the river mouth or in Moreton Bay, particularly during flood seasons. The only research regarding sediment transport in Moreton Bay was conducted by You and Yin (2007). Field data from off the Brisbane River mouth was collected for about three weeks, and it was found that the wind-waves were the main driving force for fine sediment re-suspension.

2.3   Satellite remote sensing and numerical modelling

In recent years, satellite remote sensing technology have been widely applied for detection of coastal and oceanic conditions. In comparison with time-consuming, expensive and weather dependent *in-situ* measurement, the main advantages of satellite remote sensing are the capability of covering large areas with spatially continuous records, and the ability to obtain instant information about water colour (Yates et al., 1993). Various visible and near infrared bands were proposed as water turbidity level indicators in previous studies (Tang et al., 2003, Wang and Lu, 2010). For instance, Shi and Wang (2009) used the satellite images to observe

the flood-driven Mississippi River sediment plume development. Wang et al. (2009) retrieved water reflectance at Band 4 (with a wavelength range of 770 to 860 nm) from The Enhanced Thematic Mapper Plus (ETM+) images to estimate the suspended sediment concentration in the large, turbid Yangtze River. A similar investigation was conducted by Wang and Lu (2010), which retrieved water reflectance at Band 2 (with wavelength range of 841 to 876 nm) from the Moderate Resolution Imaging Spectroadiometer (MODIS) aboard NASA'S Terra satellite to estimate the suspended sediment concentration in the Lower Yangtze River. It can be seen in previous studies (Wang et al., 2009, Wang and Lu, 2010) that the band selection for turbidity estimation generally depends on the wavelengths of bands and other geographically correlated factors, such as the particle properties.

Besides satellite remote sensing technology, numerical model is also a powerful tool used in sediment research. Numerical models of natural coastal processes are both an exploratory scientific tool and an essential environmental management facility in the form of predictive simulations. The development and set-up of reliable numerical models rely upon the degree to which the relevant natural physical processes and mechanisms involved are understood and can be represented by simulations. Coastal and estuarine sediment transport is a complex dynamic, and models must describe both sediment and ambient fluid motions and their interactions. Therefore, successful simulation of hydrodynamics and sediment transport requires both the natural laws that govern varying physical behaviours such as settling, consolidation, deposition and erosion, and appropriate descriptions of hydrodynamic properties (Parker, 1994).

A number of existing three-dimensional models have been applied to investigate sediment transport. Suspended sediment concentration ($C(x, y, z, t)$ in Cartesian co-ordinates) as a scalar quantity in sediment numerical modelling is generally given by solving an advection-diffusion governing equation, which results from sediment mass conservation:

$$\frac{\partial C}{\partial t} + \frac{\partial uC}{\partial x} + \frac{\partial vC}{\partial y} + \frac{\partial W_S C}{\partial z} = \frac{\partial}{\partial x}(D_h \frac{\partial C}{\partial x}) + \frac{\partial}{\partial y}(D_h \frac{\partial C}{\partial y}) + \frac{\partial}{\partial z}(D_v \frac{\partial C}{\partial z}) + S_C \qquad (2.3\text{-}1)$$

where D_h and D_v respectively donate the horizontal and vertical diffusion coefficients; and S_C is source/sink term that accounts for erosion or deposition and depends, for erosion, on the bed profile.

Moreover, the determination of key process of settling, deposition and erosion as described in Section 2.2, plays a vital role in transport models. Additionally, sediment transport models are generally coupled with a hydrodynamic model, in order to derive information on flow conditions. Therefore, specifications of turbulence and bottom shear stress under combined wave and current are also particularly crucial for sediment modelling.

2.3.1 Turbulence closures

Turbulence is three-dimensional and time-dependent, and requires a great deal of information to describe all mechanics of the flow (Celik, 1999). To analyse the turbulent flow, time-averaging of variables separates the mean quantities from fluctuations, which results in new unknown variables appearing in the governing equations. Therefore, additional equations, known as turbulence models, are introduced to close the system. Turbulence models were developed through either the turbulence viscosity/diffusivity concept or the differential transport equations for the turbulent momentum and heat/mass fluxes (Rodi, 1984).

Zero-equation models: The purpose of these models was to close the system without creating an extra differential equation. These relatively simple models can be achieved by specifying a constant eddy viscosity/diffusivity or the classical method of Prandtl mixing length (Done, 1982). However, the use of constant eddy viscosity/diffusivity only suited the problem that had little to do with turbulence; the disadvantage for Prandtl length method was the great difficulties in specifying mixing length within complex flow (Rodi, 1984).

One-equation models: To overcome the limitations of zero-equation models, a transport equation for the turbulent kinetic energy k_t was added to the system and solved with the Navier-Stokes equations. Unfortunately, the application of one-equation models was restricted to shear layers, and in flows that were more complex than shear layers little empirical information was available on the length scale turbulence l_t.

Two-equation models: To better represent the physics of turbulence in complex flows, two-equation models were developed. These models for turbulence closure have been widely applied to coastal simulation in present studies, including the Mellor and Yamada (MY25), modelling turbulent kinetic energy k_t and the length l_t (Mellor, 1982); the k-ε model, considering the turbulent kinetic energy k and its dissipation rate ε (Rodi, 1984); and the k-ω model that ω can be defined as either the rate at which turbulent kinetic energy is dissipated or as the inverse of the time scale of the dissipation following $\omega = c_t \sqrt{k_t} / l_t$, where c_t is

constant (Wilcox, 1988). The *k-ε* and the *k-ω* are physically based on the same cascading relation for the turbulence dissipation and should be equivalent, but this equivalence is not assured in mathematical terms (Amoudry and Souza, 2011).

In recent years, Umlauf and Burchard (2003) proposed a generic length scale (GLS) equation that can represent the transport of turbulence length l_t, k_t, ω by a single equation that added flexibility to the model by providing three turbulence closure options in a single coastal models, and allowed comparison and evaluation of the effect of different turbulence models in an identical numerical system. These three turbulence closures consisted of *k-kl*, which refers to MY25 with the specification of the buoyancy parameter, *k-ε* and the *k-ω*. The GLS model solved a transport equation for turbulent kinetic energy (k_t) and a transport equation for a genetic parameter (ψ), which was defined by:

$$\psi = (c_\mu^0)^{pt} k_t^{mt} l_t^{nt} \tag{2.3-2}$$

Depending on the value of *pt*, *mt* and *nt*, the parameter takes the form of different turbulent closures parameters.

Second-order closure models: In contrast to the two-equation turbulent models that related the individual Reynolds stresses to one velocity scale, the second-order closure models were developed to solve individual Reynolds stresses and turbulent dissipation. The major computational requirement for these advanced models was that six additional transport equations for the Reynolds stresses must be solved in addition to the typical Navier-Stokes and continuity equations (Rodi, 1984). Thus the second-order closure models were computationally expensive. On the other hand, the Reynolds stress in the model was only determined locally within the numerical cell, but disregarded long-range effects caused by walls and other objects within the flow (Celik, 1999).

2.3.2 Bed shear stress

The appropriate determination of the bottom boundary layer is essential for sediment transport, which strongly depends on the bottom shear stress (Celik, 1999).

In the case of a pure current, the bottom shear stress, τ_b, is commonly calculated using simple drag coefficient expressions. For example, quadratic bottom drag (Eq. (2.3-3)) and a

logarithmic velocity profile (Eq. (2.3-4)), where $\overline{u_0}$ is the velocity above the bottom, and k_s represents the bed roughness.

$$\tau_b = \rho C_D \overline{u_0} \, | \, \overline{u_0} \, | \tag{2.3-3}$$

$$\tau_b = \rho \left[\frac{\kappa}{\ln\left(z/k_s\right)} \right]^2 u(z)^2 \tag{2.3-4}$$

The logarithmic approach assumes the flow velocity follows the classic rough wall log-law vertical profile close to the bed. As shown in Eq. (2.3-4), a marked advantage of the log-law expression lies in the elevation dependence. The elevation of the bottom numerical grid will differ due to morphological changes, resulting in different bed shear stresses. This is not accounted for by the quadratic approach (Amoudry and Souza, 2011).

The majority of the wave bottom boundary layer models apply the concept of a wave friction factor, f_w, to describe the bottom shear, as defined in Eq. (2.3-5) where u_b is the wave orbital velocity. If the wave-current interaction is considered, the bed shear stress is similarly defined using the combined wave-current friction factor, f_{cw}, in Eq. (2.3-6) where u and v are the components of the horizontal velocity. Therefore, the calculations of bottom shear stress will then differ mainly through determination of the friction factors.

$$\tau_b = \frac{1}{2} \rho f_w u_b^2 \tag{2.3-5}$$

$$\tau_{b,x} = \frac{1}{2} \rho f_{cw} u \sqrt{(u^2 + v^2)} \, , \ \tau_{b,y} = \frac{1}{2} \rho f_{cw} v \sqrt{(u^2 + v^2)} \tag{2.3-6}$$

2.3.3 Intercomparison of existing popular models

Specification of parameters, turbulence and bottom shear stress are different from those of model-to-model. Four popular three-dimensional models are briefly described, then summarised and compared below.

ECOMSED

ECOMSED commercialized by ECOMSED (2002), is advanced sediment transport model based on the Princeton Ocean Model (POM) developed by Blumberg and Mellor (1987). The

transport of both cohesive and non-cohesive sediment can simulated with ECOMSED, but only two classed of grain size fractions (one of each) are allowed. The suspend sediment concentration is calculated by solving the advection-diffusion equation (2.3-1). The horizontal component D_h is constant and the vertical component D_v is determined in a Mellor-Yamada turbulence closure. The diffusive sediment flux is specified as zero at the surface boundary, while at the bottom the diffusive sediment depends upon the erosion and deposition. For cohesive sediment, the deposition is modelled by Eq. (2.2-9), and the erosion calculated by Eq. (2.2-13). The bottom shear stress is calculated using a logarithmic profile approach for pure currents and otherwise using the wave-current model, in which f_{cw} is determined in (Grant and Madsen, 1979).

The settling velocity is taken to be a function of sediment concentration. However, the featured processes, flocculation and hindered settling for cohesive sediment are not considered in ECOMSED.

DFLFT3D

Delft3D is a flexible integrated modelling suite that simulated three-dimensional flow and sediment transport (Martin et al., 1998). The sediment module in Delft3D allows up to five different classes for grain size fractions, which must be specified as either 'mud' or 'sand' (representing cohesive and non-cohesive sediment respectively). Concentration for both types of sediment is attained by solving Eq. (2.3-1). The boundary conditions in this model state the flux of sediment diffusivity is zero at both the surface and bottom layer. The sediment diffusivity is related to the eddy viscosity with the β factor introduced by Van Rijin (1984). The sediment settling velocity is a function of the fluid and sediment properties calculated using Eq. (2.2-6), without the consideration of flocculation or consolidation. The bed shear stress in Delft3D is given in Eq. (2.3-7), in which μ_c and μ_w are efficiency factors for the current and waves determined from water depth, roughness and wave parameters; f_c and f_w represent the current and wave friction factors respectively from the Zann (1995) formula. Additionally, turbulence closure consists of *k-l* and *k-ε* models in Delft3D.

$$\tau_{b,y} = \frac{1}{2}\mu_c \rho f_c u^2 + \frac{1}{2}\mu_w \rho f_w u_b{}^2 \tag{2.3-7}$$

EFDC

The Environmental Fluid Dynamics Code (EFDC) developed by Neil et al. (2002) is a three-dimensional surface water modelling system that includes hydrodynamic and sediment components. The EFDC is capable of modelling the transport and fate of multiple classes of cohesive and non-cohesive suspended sediment. The suspended sediment concentration is governed by Eq. (2.3-1). Regarding boundary conditions, there is no diffusive flux occurring at the bed and water surface. For cohesive sediment, erosion and deposition are calculated using Eq. (2.2-9) and (2.2-13) respectively. Apart from Eq. (2.2-6), a number of options are included for the specification of settling velocities in EFDC. The first formula was proposed by Hwant and Mehta (1989) based on an observation of settling at six sites in Lake Okeechobee. The second formulation was proposed by Ziegler and Nesbitt (1994) to express the settling rate as a function of the floc diameter, sediment concentration and turbulent shear stresses at a given position in the water column. Shrestha and Orlob (1996) provided the third option in EFDC, which is the formulation considering sediment concentration and magnitude of the vertical shear of the horizontal velocity. The Mellor-Yamada level 2.5 turbulence closure scheme is applied in EFDC to determine vertical eddy viscosity. The specification of the bed shear stress in wave-current interaction layer in EFDC is defined in Eq. (2.3-4).

MIKE3 DHI

MIKE FM developed by DHI is a general modelling package for simulating three-dimensional flow and transport processes in water systems including rivers, estuaries and coastal regions. In addition to hydrodynamic, salinity and temperature transport simulation, MIKE3 FM by DHI is also capable of simulating cohesive and non-cohesive sediment transport (DHI Water and Environment, 2014b). MIKE3 FM allows up to eight classes of grain size fractions for cohesive sediment. Sediment transport in the MIKE FM cohesive (mud) model is simulated through the application of the advection-diffusion equation (2.3-1). The surface boundary condition for sediment flux is set zero. At the bottom boundary, the condition is specified as the concentration at a reference level in the near-bed region using either the Teeter Profile or Rouse Profile in MIKE3 FM. For cohesive sediment, the deposition is modelled by Eq. (2.2-10) and the erosion calculated by Eq. (2.2-14). The bottom shear stress is calculated using a logarithmic profile approach for pure currents.

2.4 Summary

The features of turbidity distribution and main characteristics of sediment transport were reviewed above. It can be seen that a majority of previous studies focused on the

investigation of behaviour of sediment transport under non-flood conditions. The motivation for this research is therefore not only driven by the lack of comprehensive knowledge of salinity and turbidity distribution of the BRE in the short- (under tides) and long- term (during the wet and dry seasons), but also by the increasing demand for the understanding of sediment transport behaviour following severe flood events. From the review of numerical model comparison above, MIKE3 DHI shows outstanding capacity of modelling cohesive sediment in high resolutions. Hence, this research applies this numerical model to investigate the hydrodynamic and sediment transport in the BRE and Moreton Bay, particularly under flooding.

Chapter 3 Preliminary study on numerical model and turbidity conditions in the BRE

Statement of contribution to co-authored published paper

This chapter includes three co-authored peer- reviewed published papers.

The bibliographic details of articles, including all authors, are:

Section 3.1:

> **Yu, Y.**, Zhang, H., Lemckert, C.J., 2012. Effects of mesh resolution for hydrodynamic and transport modelling in coastal area, Proceedings of the 4th International Conference on Computational Methods. Crowne Plaza, Gold Coast, Australia, 21-27.

Section 3.2:
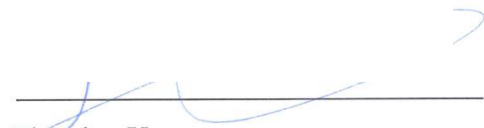
> **Yu, Y.**, Zhang, H., Lemckert, C.J., 2013. The tidal influence on the turbidity maximum in a tide-dominated estuary: The Brisbane River estuary, Australia, Proceedings of the 35th International Association for Hydro-Environment Engineering and Research (IAHR) World Congress. Chengdu, China, 7998-8007.

Section 3.3:
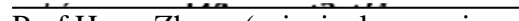
> **Yu, Y.**, Zhang, H., Lemckert, C.J. 2015. Turbidity distribution in the Brisbane River estuary during the 2010-2011 Queensland floods. the 36th International Association for Hydro-Environment Engineering and Research (IAHR) World Congresses. The Hague, the Netherlands.

Articles have been reformatted to meet the thesis style guidelines.

My contribution to these published papers involved: literature review, model set-up, calibration and validation of the model, simulations, data processing, figures and tables, analysis of results, writing and editing.

_____

Yingying Yu

_____

Prof Hong Zhang (principal supervisor and co-author)

_____

Prof Charles Lemckert (principal supervisor and co-author)

3.1 Effects of mesh resolution for hydrodynamic and transport modelling in coastal area

Abstract

This paper investigates the effects of mesh resolution on the numerical modelling in coastal studies. Flexible meshes with different resolutions are generated by DHI software packages and then applied to simulate flood events. The performance of the meshes is summarised and compared, which shows the model with higher-resolution meshes produces more accurate hydrodynamic results. The performance of the mesh structure in the simulation depends on the flow magnitude, and therefore, a higher-resolution mesh is required when a higher-magnitude flood event is investigated. A case study of a high-resolution unstructured mesh was proposed for Moreton Bay in Australia, which was expected to lead to useful suggestions for further studies for this area.

Keywords: Mesh design, Bathymetry, Numerical simulation, Flood events, Moreton Bay

3.1.1 Introduction

Numerical models are becoming increasingly valuable tools for investigating a variety of coastal issues. The simulation accuracy of various physical processes depends upon an appropriate domain and space-time discretisation method. Bathymetry has been one of the most important aspects of defining the domain in coastal modelling (McCave, 1979), and it has been proved that poor representation of bathymetry causes a number of numerical problems, such as internal waves and the separation of boundary currents (Van Leussen, 1988, Gorman et al., 2006). Therefore, the generation of a high quality mesh to accurately represent the bathymetry is vital to coastal modelling.

In coastal and oceanographic systems, physical processes occur over a wide spatial and temporal scale, ranging from meters to hundreds of kilometres, and from seconds to years. Hence, a variable resolution mesh has been most commonly applied in terms of nested structured grids or unstructured meshes (Legrand et al., 2006). Although the former was able to produce the variable resolution of grids, it was difficult to generate an efficient nested-grid model that worked well with complex topography. The advantage of unstructured meshes is they are able to represent the complex geometries to a high degree of accuracy (Lee and Valle-Levinson, 2012), so a relatively accurate numerical simulation of the study domain can be achieved by using flexible meshes.

Legrand et al. (2006) employed a hydrodynamic model to investigate the tidal jets and recirculation in the Great Barrier Reef with an unstructured mesh consisting of the smallest element length of 0.1 km in shallow regions and the largest of 5 km in very deep areas. The formula, $l(x)/l_{\max} = \sqrt{h(x)/h_{\max}}$, was applied to estimate the size of the element in the mesh (Legrand et al., 2006), where l_{max} represents the maximum expected element size and h_{max} is the maximum water depth in the study area. The effects of different mesh-resolutions on the shallow water flow simulation were investigated by Stern (1998), who found model prediction results were greatly improved by decreasing element sizes.

The finer mesh structure allows a high-resolution model to attain more accurate prediction results than coarser mesh (Legrand et al., 2006, Lee and Valle-Levinson, 2012). However, the effects of the mesh resolution on the hydrodynamic and transport modelling are uncertain. Therefore, these were investigated through the 3D modelling of a shallow coastal area using a

wide range of mesh resolutions. This paper consists of a description of the numerical model and test study area, followed by the design and generation of the mesh structures. The effects of mesh resolution on the numerical simulation are then presented in detail.

3.1.2 Hydrodynamic model

The model used in the present study is DHI Mike3 FM, which is based on the numerical solution of the 3D incompressible Reynolds averaged Navier-Stokes Equations, with the assumptions of Boussinesq and of hydrostatic pressure (DHI Water and Environment, 2011). The spatial discretisation of the primitive equations is solved using a cell-centered finite volume method. The time integration of the shallow water equations is performed using a semi-implicit scheme, where the horizontal terms are treated explicitly and the vertical terms implicitly (DHI Water and Environment, 2011). Due to the stability restriction of the explicit scheme in the shallow water hydrodynamic equations, the Courant-Friedrich-Levy (CFL) condition needs to be satisfied, which can be calculated in Eq. (3.1-1). To completely secure the stability of the numerical scheme in practice, it is recommended to set the value of the critical CFL_{HD} to 0.8 (DHI Water and Environment, 2011).

$$CFL_{HD} = (\sqrt{gh} + |u|)\frac{\Delta t}{\Delta x} + (\sqrt{gh} + |v|)\frac{\Delta t}{\Delta y} \qquad (3.1\text{-}1)$$

where h is the local water depth; Δt is the time step interval; u and v are the velocity components; Δx and Δy are characteristic length scales of meshes in the x- and y- direction respectively.

3.1.3 Study site

Moreton Bay, located in sub-tropical Southeast Queensland, Australia, extending from 153.1$^{\text{o}}$ E to 153.5$^{\text{o}}$ E and from 27.05$^{\text{o}}$ S to 27.5$^{\text{o}}$ S, was selected as the test site, as shown in Figure 3.1-1 (a). It is a shallow embayment with a number of islands and an average depth of 6.8 m. It is approximately 100 km long and 1 km wide in the south, extending to 31 km wide in the north (Dennison and Abal, 1999). Therefore, considering its complex topography and shallow depth it seems a better strategy to use a flexible high-resolution mesh to represent the bathymetry. Additionally, an increasing number of floods have occurred in the Brisbane catchment, and as a consequence a large volume of flood water-carried sediment has been driven into Moreton Bay (National Climate Centre, 2011). For example, during the severe flood event of January 2011, a total runoff of 1,600,000 ML in 18 days was discharged through the Brisbane estuary in the west of Moreton Bay (National Climate Centre, 2011),

compared with the mean annual runoff of 1,650,000 ML from the years 1889 to 2006 (Queensland Department of Natural Resources Mines and Water, 2006). To model a larger magnitude event, Stern (1998) suggested the high-resolution mesh might ensure fewer errors in the simulation results. Based on the considerations mentioned above, Moreton Bay is an ideal site for estimating the importance of mesh in the modeling.
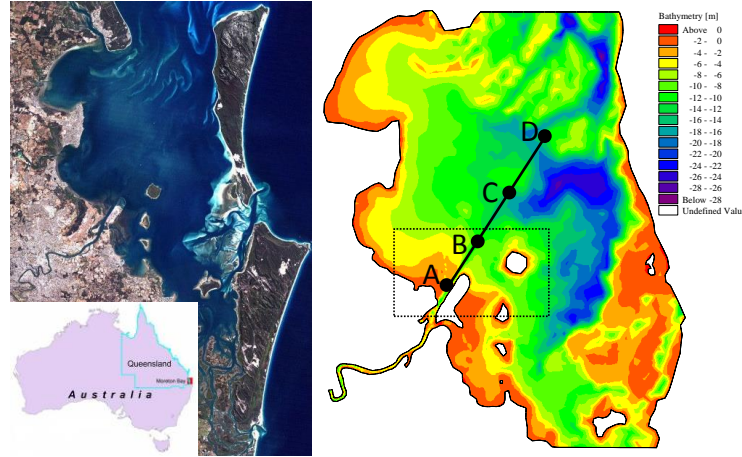
Figure 3.1-1 (a) Map of Moreton Bay on the left and its bathymetry on the right. (b) A small region was outlined by rectangular dashes and four points marked by black circles - these will be discussed later.

3.1.4 Mesh design and generation

It can be seen in Eq. (3.1-1) that the CFL_{HD} number is a function of the local water depth, flow velocity, mesh element size and the user-defined time step. Although the local flow velocity is a very important factor, it is likely to be far less than the local water depth ($\sqrt{gh} \gg |u|$ and $\sqrt{gh} \gg |v|$) under most circumstances. Therefore, it is reasonable to ignore the velocity terms, and the CFL_{HD} can be rewritten as Eq. (3.1-2).

$$CFL_{HD} = \sqrt{gh}\frac{\Delta t}{\Delta x} + \sqrt{gh}\frac{\Delta t}{\Delta y} \tag{3.1-2}$$

Based on the Delaunay triangulation methods, the mesh generation tool in DHI MIKE allows the user to design the element resolution by defining the maximum element area, A_{max} (DHI Water and Environment, 2011). It has been found that approximate-equilateral triangles for the majority of elements in mesh structure can be obtained in DHI MIKE (Dix et al., 2008). Therefore, the length of Δx is approximately estimated using Eq. (3.1-3) where $\theta \approx 60°$; and further, the CFL_{HD} is rearranged to Eq. (3.1-4) with the reasonable assumption of $\Delta x \approx \Delta y$.

$$\Delta x_{max} = 2\sqrt{A_{max} \cdot \tan(\theta/2)} \tag{3.1-3}$$

$$CFL_{HD} = \sqrt{gh} \frac{\Delta t}{\sqrt{A_{\max} \cdot \tan(\theta/2)}} \leq 0.8 \qquad (3.1\text{-}4)$$

Five meshes were created by DHI Mesh Generation package, and progressively adjusted until all elements satisfied the limitation in Eq. (3.1-4). Mesh quality was improved further through the smoothing tool of Dix et al. (2008) to increase spatial uniformity.

The statistics of the elements and nodes, element areas and side lengths for each case are given in Table 3.1-1. The mesh structure in Case 1, where the value of the A_{max} was 10 km^2, was applied in Yu et al. (2011) to investigate the moderate flood that occurred in Moreton Bay in May 2009, demonstrating the proper function of the mesh file. Based on the mesh file in Case 1, the A_{max} was decreased by a factor of 2 in the following cases. With the reduction of the A_{max}, the mesh structure attained a higher resolution of 94 m at element length near the river mouth in the last case, producing 11,617 elements covering the entire Moreton Bay. The results of the meshes in different element sizes for a small region near the Brisbane River mouth in Moreton Bay are shown in Figure 3.1-2. The element size was smaller near the coast (shallower areas), but became larger towards the far-field (deep areas) in each individual case. The time step, Δt, was set as 15 seconds in all cases to satisfy the critical CFL_{HD} of 0.8. A greater number of elements were expected to require much longer time to complete the simulations. The running times of each one-month-simulation of the flood event that occurred in Moreton Bay in 2011 were approximately 1.25, 1.5, 3, 8 and 19 hours for each case, respectively.

Table 3.1-1. Statistics of 5 unstructured meshes

		Case 1	Case 2	Case 3	Case 4	Case 5
Number of elements		1,577	1,944	3,355	5,990	11,617
Number of nodes		888	1,172	1,941	3,291	6,224
Maximum CFL_{HD}		0.52	0.58	0.63	0.75	0.78
Area (m^2)	Min.	39,150	39,150	13,585	6,950	5,595
	Max ($\times 10^5$).	100	50	25	12.5	6.25
	Mean	959,000	679,800	393,900	220,620	113,760
	SD	1,228,000	811,700	448,400	271,180	138,120
Element Length (m)	Min.	245	245	125	95	94
	Max.	4,800	3,400	2,400	1,700	1,200
	Mean	1,321	1,108	843	610	438
	SD	829	686	525	411	292
Running time (Hours)		1.25	1.5	3	8	19
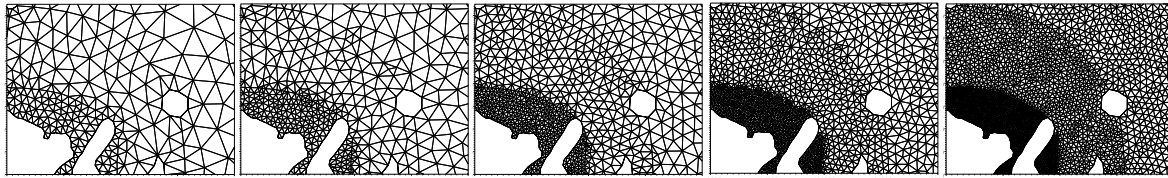
Figure 3.1-2 Unstructured mesh in Cases 1 to 5 (from left to right) at different element sizes, for a small section (outlined in Figure 3.1-1) near the river mouth in Moreton Bay.

3.1.5 Mesh resolution effects

To investigate how the model performance varied between different mesh resolutions, the model using different meshes was applied to simulate the severe flood that occurred in Moreton Bay in January 2011. Figure 3.1-3 shows the simulated results of the water level from the hydrodynamic model. It shows a larger difference between Case 1 and the observation data compared with other cases, suggesting the simulated water levels were accurately represented by the higher resolution mesh constructions. The root-mean-square (RMS) error of surface elevation was 12%, 9.16%, 9%, 8.71%, and 8.71% in each case, respectively. The decreasing RMS illustrated that the quality of simulation results was progressively improved by refining the mesh resolution; however, further reductions in element size produced relatively less improvement from Cases 3 to 5.
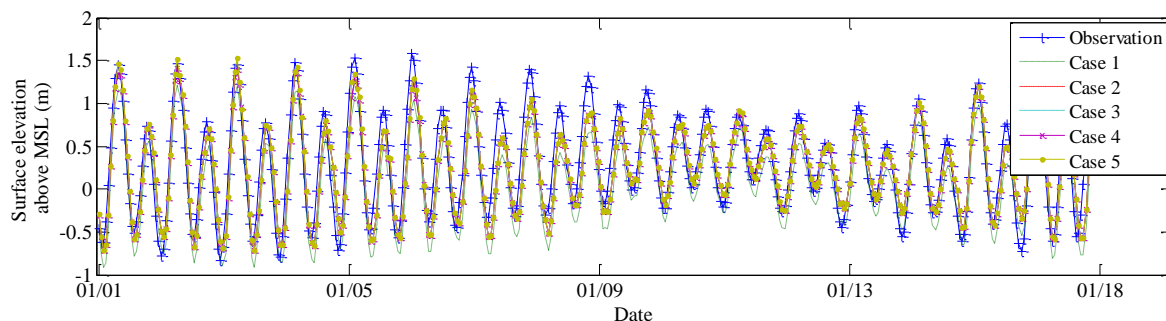
Figure 3.1-3 Effect of mesh resolution on surface elevation with the observed level at the Brisbane Bar in January 2011.

Further, it was found that the hydrodynamic characteristics might not be reproduced in the simulation when the coarse mesh resolution was applied. Figure 3.1-4 clearly shows the recirculation region next to the Port of Brisbane was almost lost in the first two cases, but clearly appeared in the last three cases with higher mesh resolution. This graphic comparison implies the higher mesh case exhibited the hydrodynamic details better than the lower case, which agreed with the findings of Stern (1998).
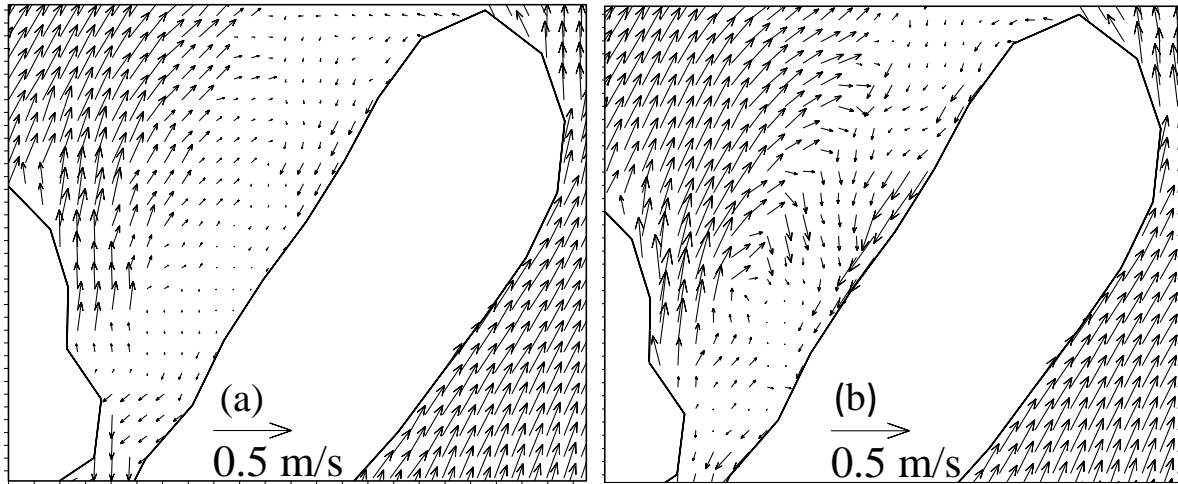
Figure 3.1-4 Recirculation region outlined by the dash rectangular near Port of Brisbane in (a) Case 1 and (b) Case 4. Vectors represent the current velocity.

In addition to the hydrodynamic features, the performance of the transport model was improved through decreasing element sizes. Four points, as marked in Figure 3.1-1, were selected to evaluate the simulated sea surface temperatures. The first three diagrams in Figure 3.1-5 show the convergence tendency of the model in terms of the temperature (a) before flood; (b) on the day of peak discharge; and (c) after flood. This clearly indicates the sea surface temperature results experienced significant improvement from Cases 1 to 3, and almost steadied in the last two cases. The average temperature differences between the satellite remote observations and simulated outcomes among the four marked points, decreased from (a) 1.8 to 0.7 ^{0}C; (b) 1.7 to 0.7 ^{0}C; and (c) 1.6 to 0.6 ^{0}C on 7, 12 and 17 January 2011 respectively as a result of increasing mesh resolution. For the entire simulation period, the RMSE of the sea surface temperature was 9.2%, 8.9%, 8.7%, 8.7% and 8.7% in each case, respectively. Figure 3.1-5 (d) further shows the comparison in temperatures between satellite observation and simulation results of Case 5. It can be seen that the simulated results in Case 5 closely represented the real temperature condition of the study site, particularly in the vicinity of the near- field region (with higher mesh resolution) such as Points A and B.
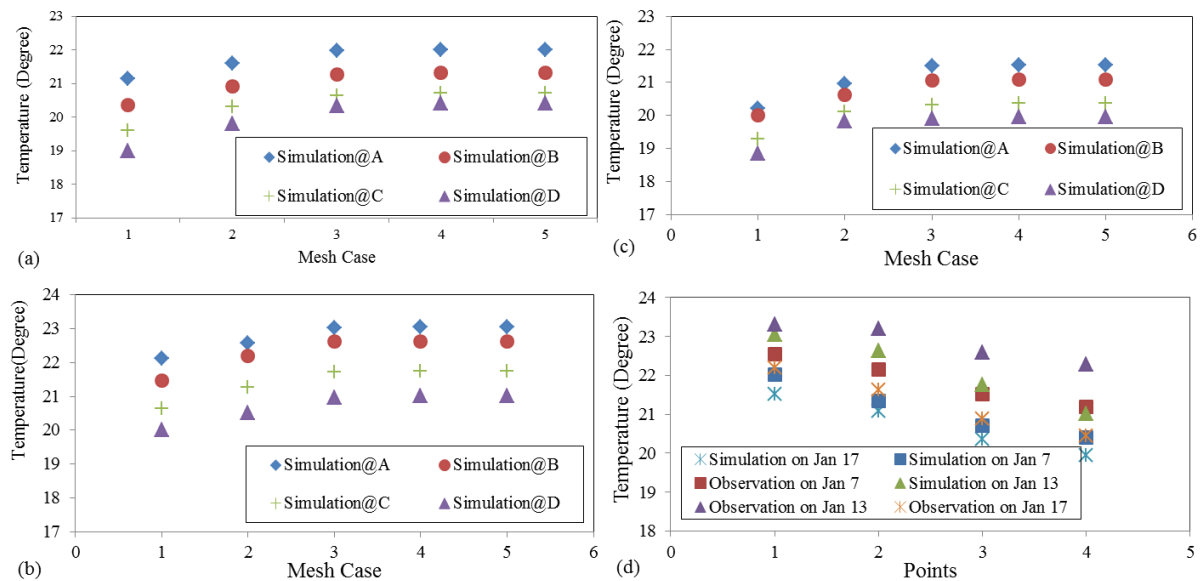
Figure 3.1-5 Modelled sea surface temperature at different points on (a) 7, (b) 12, (c) 17 January 2011 in all cases. (d) The comparison between simulation in Case 5 and observation results.

Table 3.1-2 Statistical comparison between different simulations

Events	Peak discharge (m^3/s)	Results	Root Mean Square Error				
			Case 1	Case 2	Case 3	Case 4	Case 5
Moderate flood in May 2009	900	Elevation	2.27%	1.92%	1.89%	1.89%	1.89%
		Temperature	2.35%	2.33%	2.33%	2.33%	2.33%
Severe flood in January 2011	10000	Elevation	12.01%	9.16%	9.02%	8.71%	8.71%
		Temperature	9.2%	8.9%	8.7%	8.7%	8.7%

The results discussed above applied to the simulation for the 2011 flood event. The effects of the mesh resolution would be more obvious if the investigation and comparison were conducted on two flood events which occurred in May 2009 and January 2011, with peak discharge of 900 and 8000 m^3/s respectively. The model performances in different flood simulations have been summarised, with Table 3.1-2 revealing both simulations showed similar sensitivity to the mesh resolutions. However, taking Case 1 as an example, the error in the simulated results of the flood event in 2011 was approximately five times as large as those for 2009. This implies a large magnitude event simulation may increase errors in results and therefore, the higher-resolution mesh is required when investigating a large magnitude event.

3.1.6 Conclusions

The designs and effects of the flexible mesh were investigated through the various mesh resolutions. The suitable and efficient high-resolution mesh was generated taking advantage of the knowledge of the bathymetry of the study area and physical factors of the problem. It has been confirmed that higher-resolution mesh produces more accurate results and performs better with small-scale hydrodynamic features. For large magnitude events, a suitable higher-resolution mesh leads to fewer errors in simulated results. Additionally, evaluation of the model performance suggested the mesh structure in Case 4 was more suitable than the others, considering the convergence tendency of the simulation results and running time. Further research may be required to investigate the generation and effects of the vertical distribution on the numerical simulations to attain a high-resolution and efficient 3D model.

3.1.7 Acknowledgement

3.2 The tidal influence on the turbidity maximum in a tide-dominated estuary: The Brisbane River estuary, Australia

Abstract

Studies have shown that the tides play an important role on the turbidity distribution in an estuary, particularly in the turbidity maximum zone in the tide-dominated estuary. In this project, a one dimensional hydrodynamic numerical model, which was calibrated and verified in terms of water levels, salinity and turbidity, was applied to investigate the tidal influence on the turbidity maximum in the Brisbane River estuary, Queensland, Australia. The simulated results show that the turbidity maximum zone always occurred in the upstream reach of the Brisbane River estuary, with a maximum value of approximately 160 NTU, during the wet season under non-significant flood conditions. It was also found that the upstream turbidity distribution was relatively less impacted by the tide and the turbidity remained at a high level during the tidal cycle. In contrast, the turbidity in the middle reach of the estuary was significantly influenced by the tidal condition. At downstream reach during the tidal cycle, the combined effects of relatively clean coastal water and asymmetry of tidal currents during the flood and ebb tides resulted in small changes in turbidity. Significantly, the outcomes of this work revealed that the tidal influences mainly impact the turbidity distribution in the middle reach of the river estuary. In contrast, the turbidity distributions are relatively stable at upstream and downstream reach during the tide cycle. This fundamental study will be helpful to estimate the estuary's turbidity distribution and ecosystem status and also useful for the further sediment transport study.

Keywords: Suspended sediment concentration, Estuarine turbidity, Estuarine dynamics, Tidal currents, Numerical modelling

3.2.1 Introduction

Estuaries are the interaction and transition areas between the rivers and oceans, and their health status of estuaries directly affects both river and marine conditions. A large number of studies have reported that the suspended particulate matter (SPM), often containing major compounds of suspended sediment, plays a vital role in estuarine ecology (Hollywood et al., 2001). One of the characteristic features of SPM distributions in the estuaries is the existence of a zone toward its head. Turbidity of the water in this zone is significantly higher than that observed further landward or seaward; therefore, this zone is termed the estuarine turbidity maximum (ETM) zone in the estuary (Dyer, 1986, Eisma, 1986). The ETM zone usually occurs in the vicinity of the fresh and salt water interface, resulting in strong spatial and temporal gradients in physical processes and then consequently affecting the flow dynamics (Hughes et al., 1998).

Within hourly time scales, the sediment resuspension, deposition, erosion and horizontal gradient in SPM are primarily governed by tide in a tide-dominated estuary (Uncles et al., 2002). Tidal currents that occur during the fortnightly neap-spring cycle lead to an increased mixing within the water column and produce higher level SPM. Previous studies that have investigated the ETM zone under tidal effects are usually classified into three categories, according to different tidal ranges, from micro-tidal in which the tidal range is less than 2 m, through to meso-tidal with a tidal range from 2 to 4 m, and macro-tidal in which the tidal range is greater than 4 m (Hayes, 1975, Hughes et al., 1998, Uncles et al., 2002). The ETM zone within the micro-tidal estuary generally occurred following sporadic river flood events (Uncles et al., 2002). In comparison with the micro-tidal estuary, the ETM zone in meso- and macro-tidal estuaries is greatly impacted by the tide. Two mechanisms have been proposed for the development of an ETM zone in higher tidal ranges. The first mechanism proposed that fine sediment accumulation and tidal resuspension produced a ETM zone, as a result of tidal-induced residual currents associated with gravitational circulation; in the second mechanism, the propagation and maintenance of a ETM zone from fine sediment accumulation are attributed to the distortion of tide wave associated with non-linear interactions between the tide and channel morphology (Dyer, 1986).

Considering that the tidal current is one of the determining factors of the development of the ETM zone, it is necessary to conduct a detailed investigation to understand how the turbidity

distributions change in response to the tidal condition. The motivation for this study is therefore not only driven by the lack of knowledge of sediment transport during a tidal cycle in the ETM zone in the Brisbane River estuary (BRE), but also the need for the further study on the assessment of the ecosystem health of South East Queensland in both the short- and long-term.

3.2.2 Study methods

3.2.2.1 Study Area

The Brisbane River is located in sub-tropical southeast Queensland, Australia. It has a catchment of 13,506 km^2 (Eyre et al., 1998). The Brisbane River estuary is a meso-tidal estuary, with a tidal range of 2.8 m (Richardson and Zaki, 1954)., As shown in Figure 3.2-1, the tidal section of the estuary is more than 80 km in length (Ecosystem Health Monitoring Program, 2007), with salt water intruding 60 km upstream from the river mouth during the most of the year (Richardson and Zaki, 1954). The Brisbane River estuary is distinctly brown in colour, particularly after heavy rainfall events. In addition to the main channel of the BRE, the Bremer River and Oxley Creek join the Brisbane River at 72 and 35 km respectively upstream from the river mouth.

Studies (Hollywood et al., 2001, Jimenez and Madsen, 2003) on suspended sediment dynamics within the Brisbane River estuary indicated that the ETM zone usually extended from approximate 20 to 60 km upstream from the river mouth, with peak turbidity levels occurring at around 45 km. An investigation into the seasonal turbidity distributions along the BRE, by Yu et al. (2013a), found that the location and magnitude of the ETM significantly differ in relation to wet and dry seasons. The length of ETM was approximately 35 km during wet seasons, which was three times as long as during dry seasons, and the peak turbidity levels occurred 55 and 70 km upstream from the river mouth during wet and dry seasons, respectively. The only research that discussed the relationship between the tide and turbidity conditions in the BRE was conducted by Howes et al. (2002), who measured the turbidity at a single site in the BRE over a period of thirteen months and proposed a non-linear best-fit curve to describe the relationship between the average turbidity in the estuary and the tidal range.
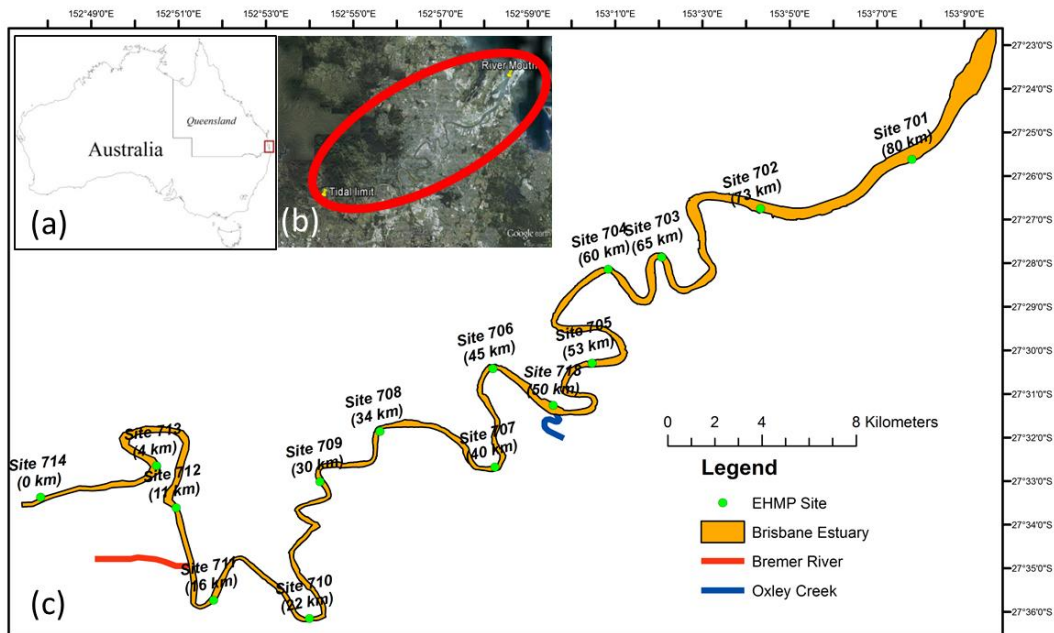
Figure 3.2-1 The Brisbane River estuary (BRE), Queensland, Australia. The green dots and their numbers indicate observation sites with their IDs along the BRE. The chainage (km) from the tidal limit are marked for each site. Source: (a) is from Geoscience Australia; (b) is from Google Map; and (c) is from Geoscience Australia and the EHMP Organisation.

3.2.3 Water Sample Collection and Hydrodynamic Data

The Ecosystem Healthy Monitoring Program (EHMP) Queensland has implemented continuous water sampling and monitoring at monthly intervals during the last 10 years. Note that all measurements are conducted during the ebb tides. Currently, there are 16 monitoring sites along the axis of the estuary from the river mouth up to the tidal limit, as marked in Figure 3.2-1. Water temperature is measured with TPS WP-82Y Dissolved Oxygen-Temperature meters fitted with a YSI 5739 DO probe with inbuilt thermistor (Ecosystem Health Monitoring Program, 2007). Turbidity is directly measured at 90^0 from the light source using a YSI 6920 turbidity sensor with the wavelength of light between 830 and 890 nm; and salinity is indirectly measured using a YSI 6920 conductivity sensor (Ecosystem Health Monitoring Program, 2007).

The Department of Environment and Resource Management (DERM) Queensland regularly measures the volume of water at their stream monitoring site in the Brisbane River Catchment. One site, on the Brisbane River named Savages Crossing (ID:143001C) located at 152.67 ^{0}E and 27.44 ^{0}S, has the closest proximity to the tidal limit of the BRE. The river inflow throughout the Savages Crossing site is therefore applied in this paper to represent the

freshwater runoff at the tidal limit of the BRE. In addition to the runoff data, tidal height data at the Brisbane Bar (near the river mouth) have been provided by Maritime Safety Queensland.

3.2.4   Model Description

In this study, MIKE 11, a one-dimensional hydrodynamic model coupled with the advection-dispersion module has been applied to simulate the cohesive sediment in the Brisbane River estuary and investigate the development of the ETM zone during the tidal cycle (DHI Water and Environment, 2014a).

Generally, to guarantee the stability of the numerical simulation, the Courant's number (C_r) must be calculated so that the Courant Friedrichs and Lewy (*CFL*) stability constraint can be applied to select the proper spatial and temporal resolutions (Mu and Zhang, 2007); hence, the spatial space and time step were determined to be 500 m and 15 seconds for the model in this study.

Figure 3.2-2 shows a Digit Elevation Model (DEM) in the Brisbane Catchment, Australia. The main course of the Brisbane River has been outlined by the dot- solid blue line from its tidal limit (Chainage 0 km) to the river mouth (Chainage 80 km). Along the water surface of the river, a number of cross sections have been added, at every 1000 m, representing the transverse section of the river. The orientation of the cross sections has been individually adjusted to be perpendicular to the flow direction.

The hourly observed river discharges were used as the upstream open boundary conditions at the entrances of the Brisbane River, the Bremer River and Oxley Creek, respectively (as shown in Figure 3.2-1). The water levels at the river mouth were used as the downstream open boundary condition. Due to the lack of wind data, the effects of wind were not taken into account in this study. The salinity and temperature data at 16 sites along the Brisbane River observed by the EHMP were added to the model as the initial conditions. The simulation in this study started from January 1, 2005 AEST. The model first ran for a 1-year spin-up period to allow the model to reach a relative steady dynamic state and to ensure that this spin-up would not impact final model outputs.
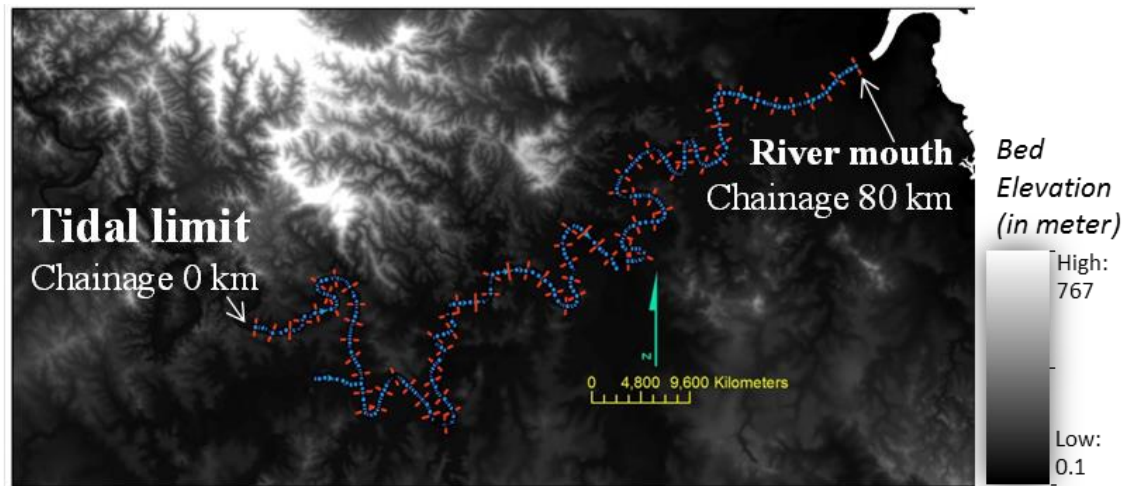
Figure 3.2-2 The Brisbane River Estuary (as marked by blue dots) and the cross sections (as marked by orange lines).

In addition to the hydrodynamic module, a number of parameters in the advection-dispersion module, such as the sediment settling velocity, critical shear stress for sediment deposition, and bed erosion, also significantly influence simulated results (Lumborg and Pejrup, 2005). Table 3.2-1 lists three character parameters for the simulation of sediment development in the Brisbane River, along with their typical values which have been proven to produce appropriate simulated results in previous studies (Margvelashvili et al., 2003, Bell, 2010).

Table 3.2-1 Parameters in the model

Parameters	Values	References
Critical shear stress for erosion	0.05 N/m^2	Margvelashvili et al. (2003)
Critical shear stress for deposition	0.03 N/m^2	Bell (2010)
Sediment setting velocity	$6.5 \times 10^{-4} \text{ m/s}$	Margvelashvili et al. (2003)

3.2.5 Model Calibrations and Verifications

In the hydrodynamic module, bed resistance is a vital and critical factor in the behaviour of the river flow and the development of other components such as sediment. In this study, Manning's n was used to represent the bed resistance. Due to the insufficient bathymetry data, uniform selection of Manning's n was adopted, with the assumption of uniform roughness along the river in the model. According to the report from the Brisbane City Council (Brisbane City Council, 2003), the values of Manning's n ranging from 0.02 to 0.05 were found to be appropriate for open channel and all floodplains in the Brisbane Catchment, respectively. Therefore, the values of Manning's n ranging from 0.01 to 0.06 were individually applied, to evaluate the performance of the hydrodynamic module.

It was found that the value of 0.03 for Manning's n within the model produced the most comparable simulated results. A comparison of simulated water levels and measured water levels from the site upstream over a 1-year period is displayed in Figure 3.2-3. As can be seen in the figure, the simulated water level generally matches the observed water level, not only reflecting the similar variation tendency but also indicating the peaks of the water level. The root mean square error (RMSE) is 0.05 m.
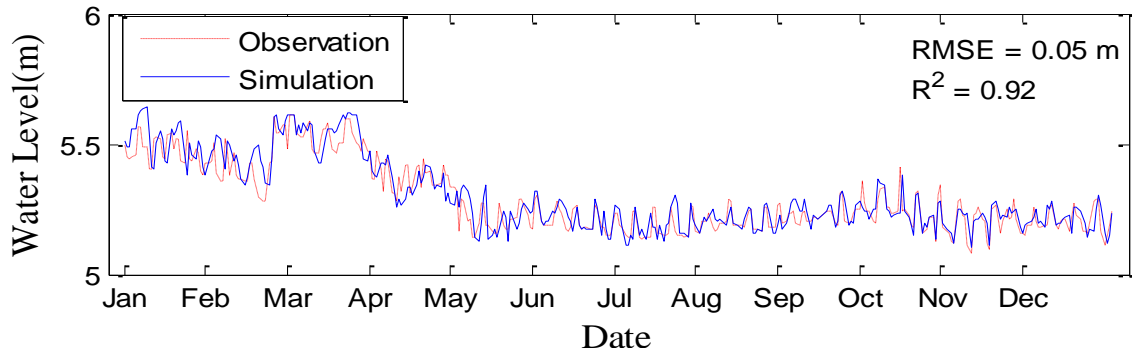
Figure 3.2-3 Comparison of the simulated and observed water levels in 2007.

The advection-dispersion module within the one-dimensional model is based on the advection-dispersion equation which is solved numerically using an implicit finite scheme (DHI Water and Environment, 2014a). The dispersion coefficient in the equation, which greatly influences the dispersive transport term due to concentration gradients, is defined as the following form:

$$D_c = a_1 U^{b_1} \qquad\qquad (3.2\text{-}1)$$

in which a_1 and b_1 are the dispersion factor and exponent, respectively, and U represents the magnitude of the mean flow velocity (DHI Water and Environment, 2014a). Bell (2010) estimated that the value of dimensional dispersion factor, a_1, ranged from 160 to 450 m in the Brisbane River, coupled with the constant dimensionless dispersion exponent, b_1, with a value of 1. Based on Bell (2010)'s estimations, the value of dispersion factor, a_1, ranging from 80 to 500 m, was tested in this study.

The salinity distributions were used to calibrate and verify the dispersion coefficient in the Brisbane River estuary. Yu et al. (2013a) proposed the equation describing the surface salinity distribution in the Brisbane River as a function of the river chainage. Based on their equation, the salinity was estimated to be 31.7 psu at the river mouth, and then decreased at rates of 0.13 psu/km from Chainage 0 to 10 km, 0.016 psu/km from Chainage 10 to 20 km,

0.23 psu/km from Chainage 20 to 60 km, and 0.28 psu/km from Chainage 60 to 80 km, respectively. In order to represent the dispersion condition more accurately, the river was broken into 4 regions as described in Table 3.2-2, corresponding to the different salinity changing rates at different river reaches. The calibration using the model results in 2006 shows that the non-dimensional dispersion factor reduced in magnitude from 500 at the river mouth to 350 at Chainage 10. In the vicinity of the tidal limit, the dispersion factor was set back to 400, which would produce comparable simulated salinity results. This set of values of the dispersion factor (Run 5) was verified using the model output in 2007, in terms of temperature and salinity, as shown in Figure 3.2-4. The RMSE of the simulated temperature and salinity is 9.4% and 5.7%, respectively, indicating the accuracy of performance of the model applied in this study.

Table 3.2-2 RMSE of salinity for varying dispersion factors in the BRE in 2006

RMSE (psu)	Run(#)					
	#1 $a_1 = 350$m	#2 $a_1 = 400$m	#3 $a_1 = 450$m	#4 $a_1 = 500$m	#5	
					RMSE (psu)	a_1 (m)
Chainage (km)						
0-10	0.30	0.24	0.28	0.32	0.24	400
10-20	0.82	0.82	1.32	1.85	0.75	350
20-60	2.58	2.35	2.73	2.81	2.34	400
60-80	2.47	1.88	1.49	1.32	1.26	500
0-80	2.19	1.91	2.12	2.27	1.78	-
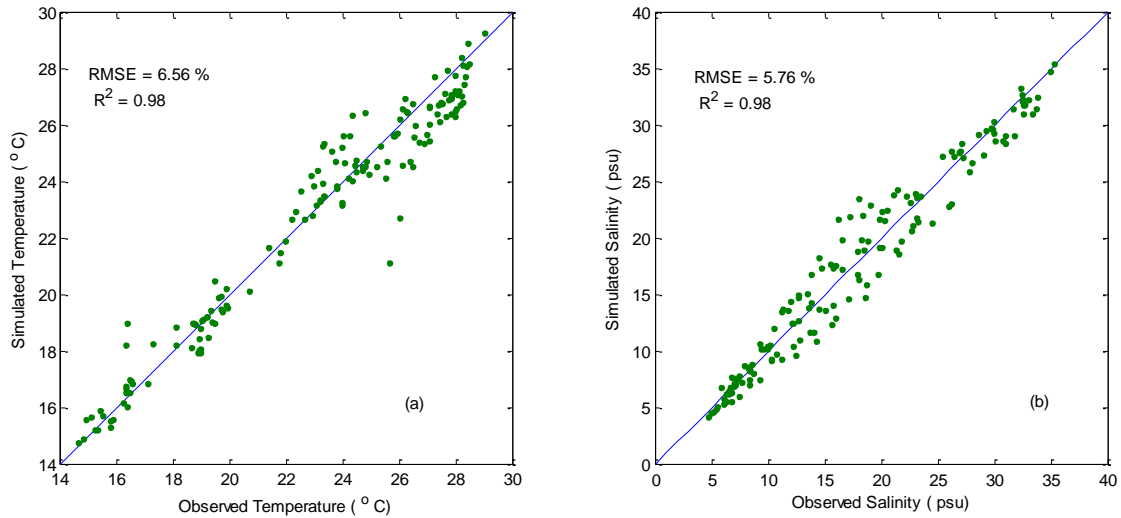
Figure 3.2-4 Comparison of the simulated and observed (a) temperature and (b) salinity in 2007

The available measured turbidity data were recorded in units of NTU; however, the model only works with the concentration of suspended sediment (SSC) in each cross section along the river. In order to use the SSC as the boundary condition and compare the model output with the observed turbidity, the simple correlation proposed by Hossain et al. (2004), as yielded in the equation (3.2-2), was applied to the entire Brisbane River estuary.

$$T_{ur} = 1.25 \times C + 9.85 \tag{3.2-2}$$

Using the estimated SSC boundary condition and parameters with the typical values listed in Table 3.2-1, the sediment transport in the Brisbane River was simulated and compared with the measured data. Figure 3.2-5 shows the simulated SSC with the RMSE of 10.36%. It can be seen that the model produced a fairly comparable output, although a fraction of the simulated result was underestimated when compared with the observed data. The possible reasons for the slight underestimation might be the usage of simple correlation between the turbidity and SSC, the exclusion of wind effects in the model and the difficulty in determining the values of characteristic parameters such as the critical shear stress for bed erosion.

Overall, the model performance has been verified in terms of the water level, temperature, salinity and sediment concentrations. It can be seen from Figure 3.2-3 to Figure 3.2-5 that the model can accurately reflect the flow characteristics and sediment development in the Brisbane River.
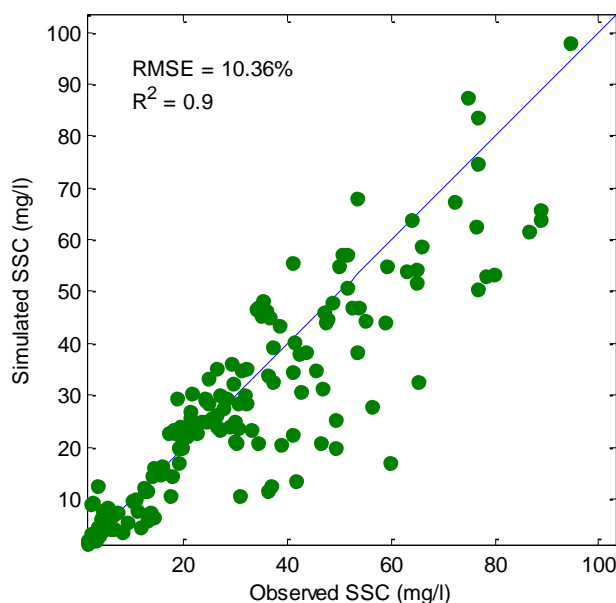
Figure 3.2-5 Comparison of the simulated and observed SSC in 2007

3.2.6 Results

3.2.6.1 Longitudinal Turbidity Profile

The depth-averaged longitudinal turbidity was simulated by using the verified MIKE 11 model. The depth-averaged longitudinal profile of the Brisbane River estuary, during spring (dot-solid blue line) and neap (dash-solid red line) tides in December 2007, is shown in Figure 3.2-6. The black squares are the estimated depth-averaged turbidity based on the observation data that were collected in the Brisbane River from 9 a.m. to 1 p.m. on 5 December 2007. Compared with the observed turbidity, the simulated turbidity results during the spring tide (11am, 5 December 2007), were in accord with the observation data, with R^2 of 0.98 and RMSE of 1.88%.

During the spring tide, the ETM zone occurred near Chainage 20 km (at a distance of 60 km from the estuary mouth), with a maximum value of approximately 160 NTU. During the neap tide, the maximum value of turbidity reduced to 130 NTU. The turbidity reduction in the ETM might be attributed to the lower sediment resuspension occurrence during the neap tide due to the smaller shear velocity. Figure 3.2-6 also shows that the ETM zone moved seaward and settled near Chainage 30 km during the neap tide. The seaward movement of the EMT zone might be driven by the smaller tidal current. The freshwater entering the river system at a higher rate might be another possible reason which caused the EMT zone to move further downstream. The turbidity from Chainage 40 to 80 km, however, was slightly higher during

the neap tide in comparison to the spring tide, as shown in Figure 3.2-6. The main possible reason was that the saline water flowing into the estuary at a lower rate during the neap tide compared with the spring tide, the velocity of the current is not sufficient to carry the sediment and deposit it upstream; therefore, a fraction of sediment was settled downstream instead of transported further upstream.
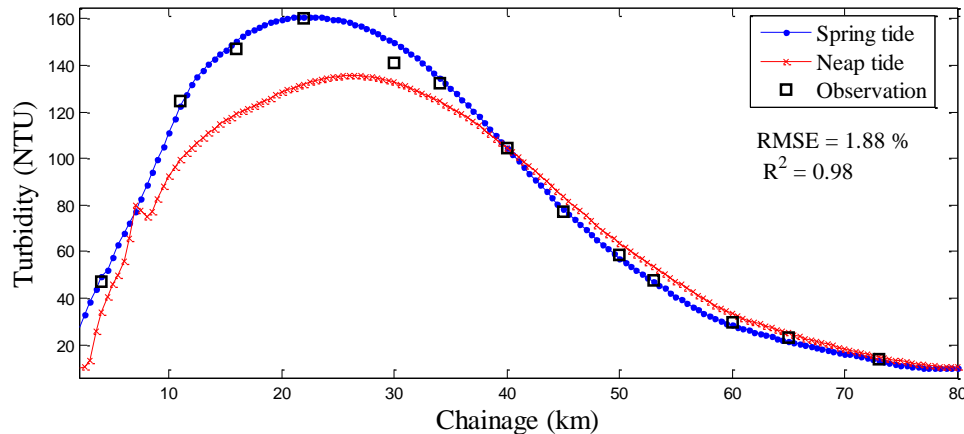
Figure 3.2-6 Simulated depth – averaged longitudinal turbidity profile during the spring (dot-solid blue line) and neap (dash-solid red line) tides in the Brisbane River in December 2007. The black squares represent the turbidity at specific sites that were observed by the EHMP during the neap tide in December 2007.

3.2.6.2 Turbidity-velocity Patterns

In order to examine the turbidity variations in response to the fluctuation of flow velocity, the simulated turbidity and velocity in the upstream, middle and downstream reaches of the estuary during the spring tides are shown in Figure 3.2-7, individually.

Figure 3.2-7 (a) indicates the turbidity and flow velocity conditions at Chainage 20 km from 5 to 10 December 2007. The turbidity at this site stayed at a high level of approximately 160 NTU, as a result of the high turbidity inflow entering from the tidal limit. The turbidity level at this site was stable during the tidal cycle, as this site is close to the tidal limit in the sense that the effect of tide was relatively weak on the turbidity variation.

In contrast, the turbidity at Chainage 30 km relied more on the tidal current condition, as shown in Figure 3.2-7 (b). The turbidity at this site increased from 120 NTU to reach a maximum of approximately 160 NTU. The peak turbidity occurred when the velocity reached its maximum (0.5 m/s). The elevated turbidity was sustained for almost the next 2 hours, and then started to decrease through the remainder of the flood tide. During the ebb tide, the turbidity continuously decreased, but only to 130 NTU, and then started to increase when the

velocity reached its maximum (in magnitude). The turbidity, at Chainage 30 km where the ETM zone occurred, generally stayed at a high level, although it fluctuated during the flood and ebb tides. For the middle reach, the general turbidity-velocity pattern, of strong flood currents along with high and sustained turbidity status but ebb currents associated with low turbidity condition was recorded.
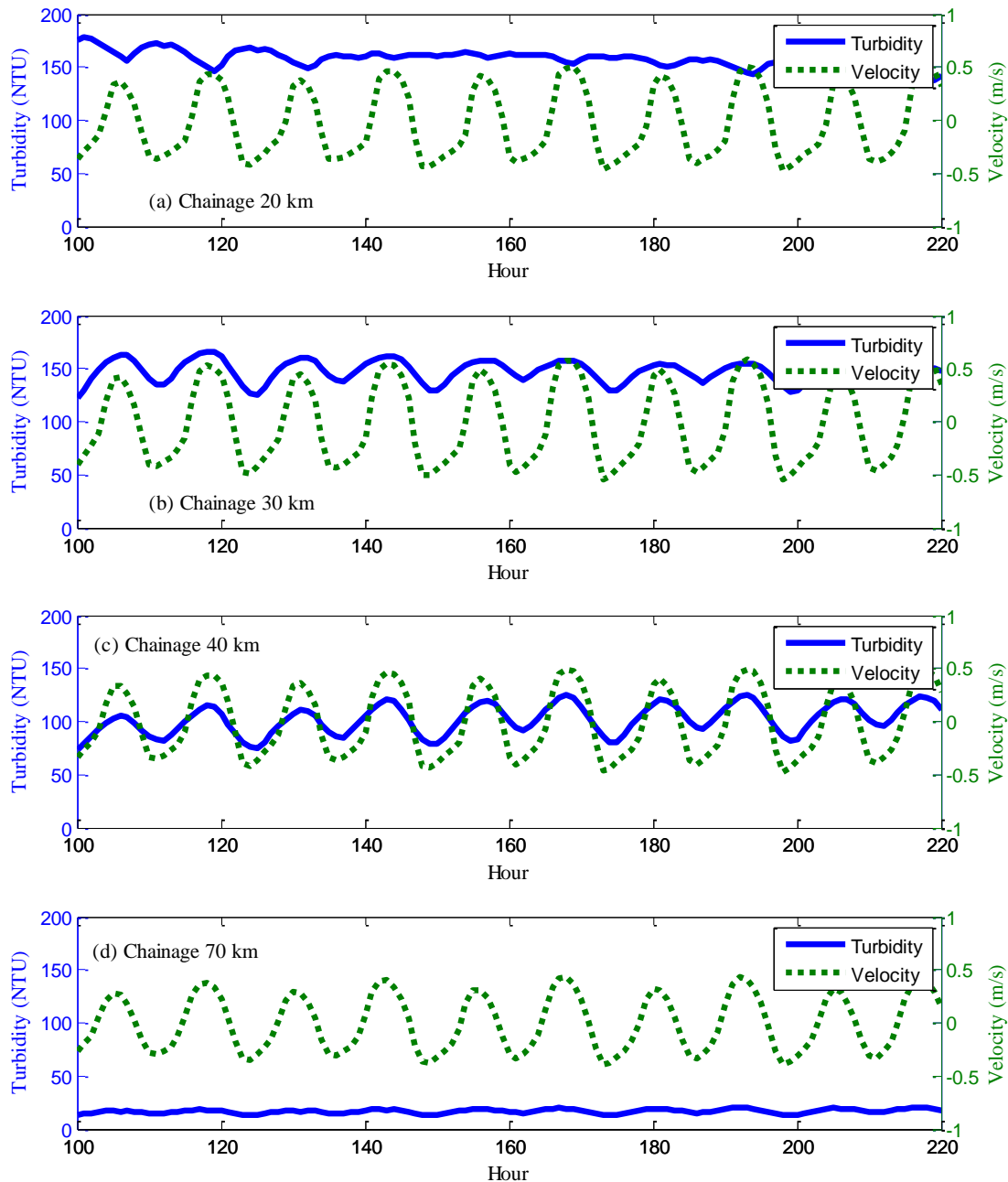
Figure 3.2-7 Simulated time series of velocity (dash green line) and turbidity (dot blue line) during the spring and neap tides at sites (a) Chainage 20 km, (b) Chainage 30 km, (c) Chainage 40 km, and (d) Chainage 70 km. Positive velocities are in the flood (water coming in) direction and negative velocities are in the ebb (water going out) direction. The 100th hour represents 4 a.m., on 5 December 2007.

The turbidity level at Chainage 40 km significantly varied as the tidal condition during the tidal cycle, as shown in Figure 3.2-7 (c). The turbidity level increased from 70 NTU to reach a maximum of approximately 130 NTU. The peak turbidity occurred when the velocity reached its maximum (0.5 m/s) during the flood tide. The turbidity then turned to decrease and reached a minimum of 74 NTU when the velocity was at 0.55 m/s during the ebb tide. The turbidity difference at Chainage 40 km in the middle reach of the estuary was approximately 60 NTU during one tidal cycle. The difference might be caused by the larger amount of the fine sediment accumulated in this section of the estuary which was available for suspension.

The slight modification for turbidity level occurred at Chainage 70 km, although this site was near the estuary mouth. As can be seen in Figure 3.2-7 (d), the turbidity level stayed as low as 20 NTU through the tidal cycle. It might be attributed to three aspects: the first is that the sediment carried by the freshwater from the tidal limit, might have settled and been deposited before arriving at the lower reaches, under non-significant condition. The saline water entering into the estuary during the flood tide was relative clean which was the second reason. Furthermore, as shown in Figure 3.2-7 (d), the flood current velocity was larger than the ebb current velocity; that is to say, the amount of sediment transported landward in this section during the flood tide was possibly equal to or greater than that being transported seaward during the ebb tide (Postma, 1967). Therefore, the asymmetry of tidal current might be the third reason that caused the turbidity to stay at a low level in this section.

3.2.7 Conclusions

The tidal influences on the turbidity maximum zone in the tidal-dominated Brisbane River estuary, Australia, were studies using a one dimensional verified numerical model. It was found that the ETM zone occurred near Chainage 20 km with a maximum value of approximately 160 NTU, during the spring tide under normal weather condition. During the neap tide, the ETM zone not only moved seaward and settled near Chainage 30 km, the peak value also decreased to 130 NTU. However, the turbidity, from Chainage 40 to 80 km, was slightly higher during the neap tide in comparison to the spring tide.

Furthermore, in the investigation of the tidal effects at different chainage of the river, the results indicated that the tidal currents impact the turbidity distribution at different degrees at different sites. The upstream turbidity distribution, where it was far away from the estuary mouth such as at Chainage 20 km, was less affected by the tide and the turbidity maintained

48

at a level as high as 160 NTU during the tidal cycle. In contrast, the turbidity, in the vicinity of the middle reach of the Brisbane River estuary, was significantly influenced by the tidal condition. For the middle reach, the general turbidity-velocity pattern, of strong flood currents along with high and sustained turbidity status but ebb currents associated with low turbidity condition was recorded. The turbidity difference between at the flood and ebb tides, reached a maximum of approximately 60 NTU during one tidal cycle. The significant difference might be caused by the larger amount of fine sediment accumulated in this section of the estuary which was available for suspension. Compared to the significant variations in turbidity in response to the tidal current in the middle reach of the estuary, it was found that the slight modification of turbidity levels occurred at the downstream reach, due to the combined effects of relatively clean coastal water and asymmetry of tidal currents during the flood and ebb tides in the Brisbane River estuary.

The results obtained from this study were valued for understanding the role of the tide on the turbidity variations and distributions in the estuary in detail; however, there remain several important issues that require further investigation. The effects of the wind need to be considered, due to the sediment resuspension is also highly related to the wind condition. Furthermore, the stratifications of salinity and turbidity in the water column need to be taken into account, in order to obtain more accurate simulation results.

3.2.8 Acknowledgement

3.3   **Turbidity distribution in the Brisbane River estuary during the 2010-2011 Queensland floods**

Abstract

The turbidity distribution within the Brisbane River estuary during the January 2011 flood event was investigated using a validated numerical model. The Brisbane River estuary turbidity maximum (ETM) zone generally extended throughout the mid- estuary under normal weather conditions. However, the turbidity distribution was significantly changed during the January 2011 flood events, from a high-low-high pattern of turbidity distribution to a gradual increasing pattern from upstream to downstream within the estuary. The ETM zone disappeared but the turbidity approached approximately 2000 NTU. In addition, it was found that the flood impact on sediment transport in the estuary was more significant than the tidal effects. An estimated 1,000,452 tonnes of sediment were delivered into Moreton Bay through the Brisbane River mouth during the January 2011 floods. These outcomes will be further applied to develop Moreton Bay models, thereby investigating the sediment settling in the coastal area following a flood and will also be used to assist the implementation of catchment management strategies.

Keywords: Numerical modelling, DHI MIKE11, River discharge, Turbidity distribution, Sediment loads

3.3.1 Introduction

Coastal rivers are generally the main means of sediment delivery to coastal oceans. Severe storm runoff carrying a large volume of sediments and contaminants not only results in significant morphological change to the bank shape of the river, but also is recognised as an important source of coastal pollution. The January 2011 event with the recorded flood level of 4.27 mAHD (elevation in meters with respect to the Australian Height Datum) was the largest experienced on the Brisbane River since the 1974 flood (Babister and Retallick, 2011). It was observed that the January 2011 flood delivered a massive load of sediment into Moreton Bay, Queensland, Australia, leading to an extensive turbidity plume.

A number of studies have been conducted on the Brisbane River floods, mainly looking at heavy rainfall, flood levels and the impacts of floods on structures and buildings. The peak precipitation from the 1974 event were substantially larger than those in 2011, with Brisbane's peak one-day total of 314 mm in 1974 compared with 1662 mm in 2011. However, the heavy precipitation was close to the coast in 1974, whereas in 2011, heavy rainfall spread further inland (National Climate Centre Bureau of Meteorology, 2011). Following heavy rainfall in the catchment during this event, the Brisbane River water level rapidly rose resulting in substantial loss of life, and destruction of thousands of properties were destroyed as reported by official correspondence and newspapers. The flood flow also constituted a hazard in coastal areas. It was reported that the January 2011 flood plume largely spread in Moreton Bay, depositing a major load of sediment into the bay, reducing water clarity and consequently decreasing the benthic light available for seagrass growth (Dennison et al., 2011).

Several studies have investigated issue of the sediment induced by the January 2011 flood event. The sediment samples collected in the Brisbane River estuary (BRE) during the event were cohesive mud sludge with a median particle size of approximately 25 μm (Brown et al., 2011). The flood waters from the river poured sediment into Moreton Bay producing an approximately 500 km^2 sediment plume which would take about a month to be diluted (Yu et al., 2013b). O'Brien et al. (2012)'s sediment sample collected in Moreton Bay after the flood shows that the sediment size distribution was bimodal, made up of mud (diameter less than 62.5 μm) and sand (diameter larger than 62.5 μm).

The Brisbane River flows through the large city of Brisbane, Queensland, Australia and is one of the largest rivers entering into Moreton Bay. The turbidity condition in the BRE not only reflects the quality of surrounding water resources, but also shows the potential impacts in Moreton Bay. Visual assessment suggests that the erosion of the river bank was severe and sediment was significantly widespread. However, the turbidity level and distribution during flood events have not yet been discussed in any existing studies. Therefore, the purpose of this study is to quantify turbidity levels and distributions in the BRE during the January 2011 flood event. These outcomes will be further applied to develop Moreton Bay models, thereby investigating the sediment settling in the coastal area following the flood and will also be used to inform the implementation of catchment management strategies.

3.3.2 Study area

The Brisbane River is located in south-east Queensland, Australia, as shown in Figure 3.2-1. It has a catchment area of about 13560 km^2 (Eyre et al., 1998). It is distinctly brown in colour, especially after heavy rainfall. Due to the existence of high turbidity and saline water, the biological diversity is generally low (Dennison and Abal, 1999). It is a micro-tidal estuary, with a mean neap and spring tidal range of 1 and 1.8 m, respectively (Wolanski, 2014). The tidal section within the estuary is about 80 km in length. The Bremer River and Oxley Creek join the estuary at 72 and 34 km respectively, upstream from the river mouth. In study, conducted in Ecosystem Health Monitoring Program (2007), it was found that the depth along the estuary varied from 15 m at the river mouth to approximately 4 m at the Bremer river junction.

Under a normal flow year (with an average flow rate of approximately 5.5 m^3/s), sediment delivered from the catchment and urban areas to the BRE were 178,000 and 112,000 tonnes, respectively(Eyre et al., 1998). An upstream dam construction has increased the trapping capacity of the estuary by the retention of flood water and also cut off sediment supply from a large proportion of the catchment. However, it is unknown whether the river has approached a new sediment equilibrium or its accretion is continuing to occur (Babister and Retallick, 2011). In January 2011, the Brisbane River catchment, which including the Bremer River and Oxley Creek experienced the largest flood event since 1974 and the river discharge approached over 10,000 m^3/s.

3.3.3 Study methods

3.3.3.1 Field measurement and remote satellite data

The Ecosystem Health Monitoring Program (EHMP), Queensland, Australia, has conducted consistent water sampling and monitoring at monthly intervals along the estuary over the last decade. Generally, the water samples are collected at ebb tides at 16 monitoring sites from the river mouth up to the tidal limit, as indicated in Figure 3.2-1. The turbidity at 90° from the light source is directly recorded using a YSI 6920 turbidity sensor consisting of a near-infrared LED with wavelengths between 830 and 890 nm; The water temperature and conductivity are respectively measured by a YSI 6920 temperature sensor and conductivity, and the profile of salinity is derived from the conductivity data (Ecosystem Health Monitoring Program, 2007). The Department of Environment and Heritage Protection, Queensland, Australia, regularly measures the volume of water at their stream monitoring sites. The observed flow rates of the Brisbane River at Savages Crossing, the Bremer River and Oxley Creek are used in this study to represent the freshwater runoff entering the BRE.

In addition to field measurement data, this study also used the MODIS Terra Surface Reflectance Daily L2G Global data to validate the model. These geometrically corrected data, with a spatial resolution of 250 m at Bands 1-7, were downloaded from the EOSDIS, NASA. Yu et al. (2014b) proposed a relationship (Eq. (3.3-1)) between the estuary's surface turbidity (T_{ur}) and the water reflectance (W_r) at Band 2 with a R^2 of 0.9 for the January 2011 flood event.

$$\ln(T_{ur}) = 0.1624 W_r + 2.8784 \qquad (3.3\text{-}1)$$

3.3.3.2 Model set-up and validation

To conduct investigation into the variation in turbidity levels and distribution in the BRE during the flood event, MIKE11 DHI, a one-dimensional hydrodynamic model coupled with advection-dispersion and sediment transport modules has been used in this study. Precipitation was ignored in the simulation. The hourly-observed river flows were used as the upstream open boundary conditions. The available measured turbidity (C_T) data were recorded in NTU; however, the MIKE11 DHI model only works with suspended sediment concentration (C_s). The simplified correlation in Eq.(3.3-2), proposed by Hossain et al. (2004) which described the relationship between sediment concentration and water turbidity level in rivers, was therefore applied in this study. The particle grain size was set at 25 μm, being consistent with Brown et al. (2011)'s findings. Based on Stokes law, the settling velocity of

particles is roughly estimated to be 5.4×10^{-5} m/s. The available salinity and temperature data along the estuary were added to the model as the initial simulation conditions.

$$T_{ur} = 1.25 \times C + 9.85 \tag{3.3-2}$$

The model was carefully calibrated in our previous work (Yu et al., 2014b). Validation of the model to ensure that the model was suited to simulate the January 2011 event can be seen below. The measured water level at the Brisbane Port Office Gauge (in the vicinity of site 703) during the flood peak was compared with the simulated results in Figure 3.3-1. It can be seen that the simulated water levels generally matched the observed levels and successfully captured fluctuations, with an R^2 of 0.9 and an RMSE of 0.52 m. Moreover, the turbidity levels estimated based on satellite remote sensing surface reflections was compared with the simulated results in Figure 3.3-2(a). With an RMSE of 55 NTU, the model produced a fairly comparable sediment output, although the difference slightly increased as the turbidity level rose. The simulated turbidity level was also compared with the measured turbidity data provided by EHMP. Figure 3.3-2(b) shows that, although a larger difference occurred at medium level, the simulated turbidity agreed reasonably with the measurement, not only at low turbidity, but also at high turbidity. Overall, the model performance has been validated in terms of flood water level and river turbidity. As evident in Figure 3.3-1 and Figure 3.3-2, the model is able to effectively reflect the varying flow conditions and sediment development in the BRE during the January 2011 flood event. The resulting differences might be attributed to several factors, including simplified development of the model without consideration of structures on the river, as well as data estimation among turbidity levels, suspended sediment concentration and water surface reflection.
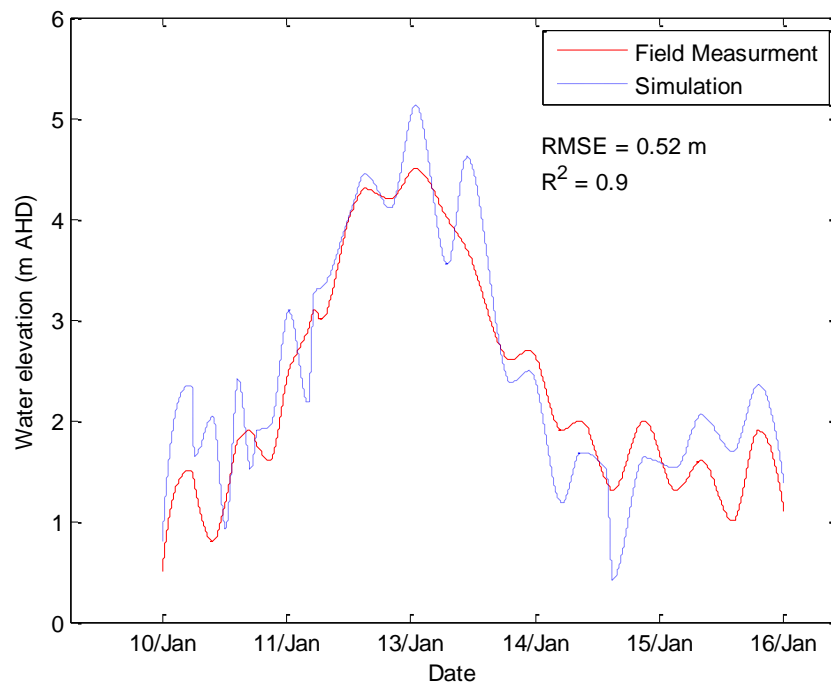
Figure 3.3-1 Comparison of the simulated and observed water levels at the Port Office in January 2011 Flood event.
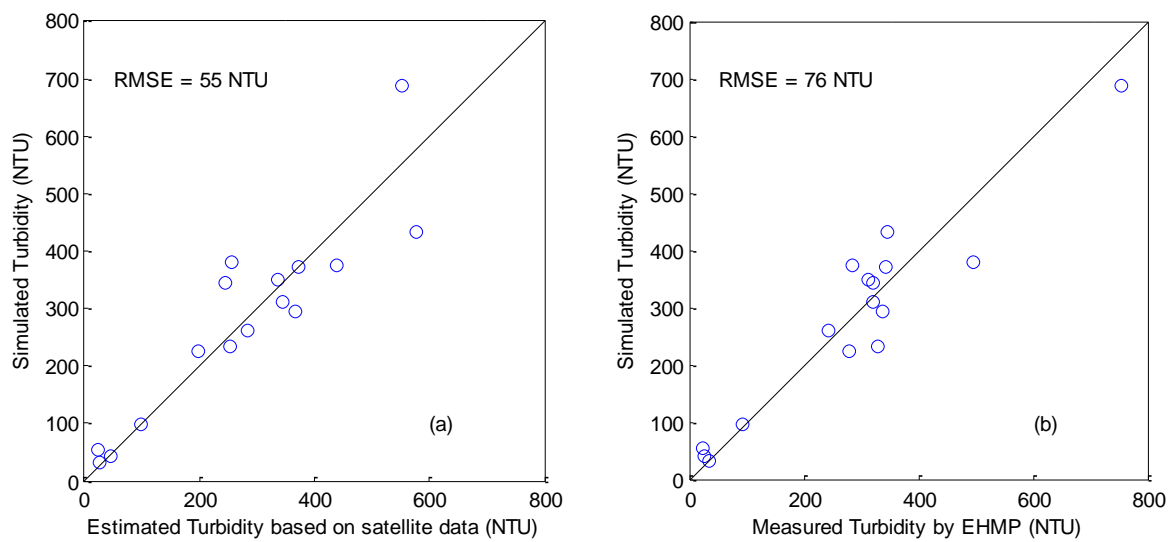
Figure 3.3-2 Comparison of the simulated and observed turbidity levels in the BRE on 24 January 2011.

3.3.4 Results and discussion

An analysis of the 10-year EHMP measurement data indicates that the Brisbane River estuary turbidity maximum zone (ETM) generally extended throughout the mid- estuary under normal weather conditions (with an average flow rate lower than 100 m³/s). The surface turbidity of river water within the ETM zone typically ranged from 50 to 150 NTU, as shown in Figure 3.3-3 (a). The turbidity distribution within the BRE was, however, significantly changed during the January 2011 flood events.

Before the occurrence of flood peaks, for example on 6 January with a flow rate less than 3000 m³/s, the turbidity in the entire BRE had reached a high level of around 1000 NTU, due to the sediment accumulation during the moderate flood in December 2010. Relatively higher turbidity was found in Chainage 0 km (tidal limits) and 80 km (the river mouth); on the contrary, the turbidity in the mid-estuary was comparably lower (approximately 200 NTU), producing a high-low-high distribution of turbidity as shown in Figure 3.3-3 (b). The decreasing tendency in turbidity levels in the upper-estuary might be attributed to the inflow from the Bremer River which joins the Brisbane River in the vicinity of Chainage 12 km. The sediment in the adjacent bay which would be delivered into the estuary during flood tides, was probably one of reasons causing the increase of turbidity level in between Chainage 70 and 80 km.
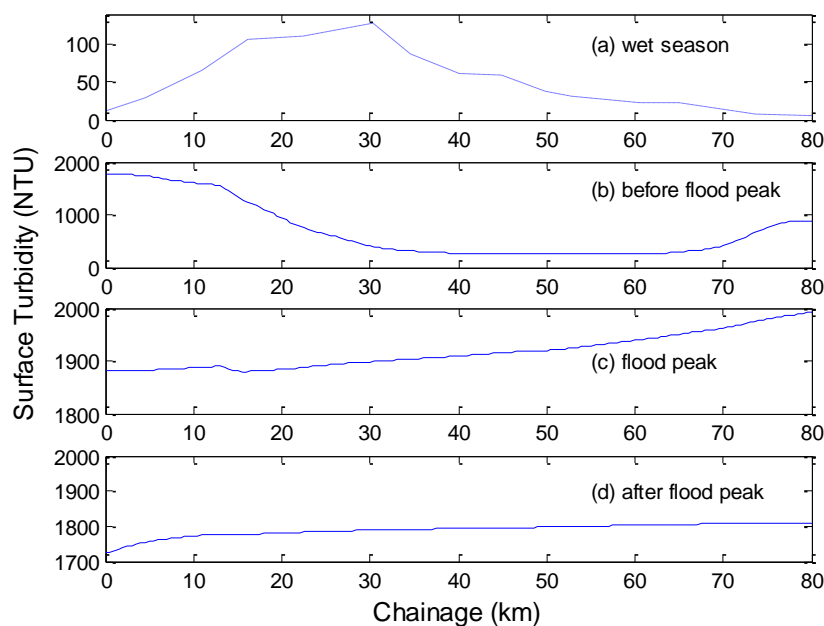
Figure 3.3-3 Typical turbidity distributions in the BRE in wet season (excluding flood events) during 2002-2011. High turbidity distributions in the BRE on (b) 6 January, (c) 14 January, and (d) 18 January 2011.

Flood peaks occurred on 11 and 12 January, with a highest flow rate of 10,000 m^3/s. As a result, the turbidity level generally increased from 1900 NTU at Chainage 0 km to 2000 NTU at the river mouth, as shown in Figure 3.3-3 (c). The main reason, causing the variation in surface turbidity distribution in the BRE, from a high-low-high pattern to a gradual growth turbidity distribution, was the massive and intense flood which not only delivered a large amount of fresh sediment from upstream to downstream but also resulted in the significant erosion of river bank. The gradually increasing turbidity distribution had remained for several days and then changed to a relatively even condition since the flow rate decreased to less than 3000 m^3/s on 18 January as shown in Figure 3.3-3 (d). The differences of surface turbidity along the BRE were less apparent compared with its previous distribution status, although turbidity levels still remained high (approximately 1800 NTU).
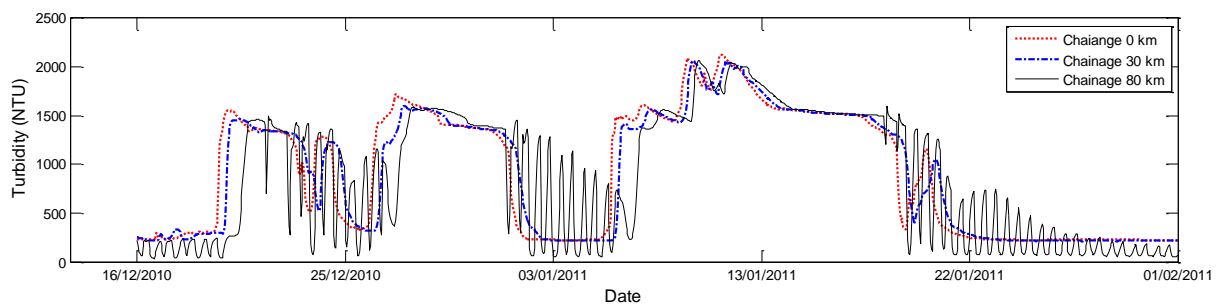
Figure 3.3-4 Turbidity variations at Chainage 0 km, 30 km and 80 km in the BRE during the January 2011 flood event.

Moreover, the variations in turbidity levels at the tidal limit (Chainage 0 km), within a typical ETM zone (Chainage 30 km) and at the river mouth (Chainage 80 km) during the flood event are exhibited in Figure 3.3-4. A striking feature is that the turbidity levels significantly increased immediately after the three flood peaks at all sites; however, variations in turbidity levels after the flood peaks were different. The turbidity at Chainage 0 km decreased at the fastest rate of 9.3 NTU/hour compared with the other two sites, implying that the turbidity level at this site highly depended on the sediment concentration of the flood inflow. The turbidity level at Chainage 30 km had a relatively smaller decreasing rate (8.5 NTU/hour), probably because the occurrence of sediment re-suspend within this typical ETM zone slowed down the rate of turbidity reduction, due to a smaller volume of flood water. Compared with other two sites, the turbidity levels experienced significant fluctuations at the river mouth after the flood peaks, which was due to tidal effects. It can be seen in Figure

3.3-4 that the turbidity level ranged from 100 to 1000 NTU at the river mouth, while the turbidity levels significantly decreased to 200 NTU at the other two sites. This remarkable fluctuation range suggested that i) the sediment re-suspension was induced during tidal cycles and, ii) a large amount of trapping sediment in the vicinity of the river mouth was delivered into/out of the estuary during flood/ebb tides.

To estimate the sediment loading (*SL*) at the river mouth during the January 2011 flood events, the Eq. (3.3-3) was applied in this study, in which *t* is the duration of one tidal cycle, *C*, *A* and v_m represent the sediment concentration, the area of cross-section, and the velocity at the river mouth, respectively. Figure 3.3-5 shows the simulated variations of river discharge upstream of the estuary, the flow velocity and water level downstream, and the sediment loading at the river mouth within each tidal cycle during the January 2011 flood. The similar shapes of the curves in Figure 3.3-5 indicate that the inflow at upstream of the estuary determined the changes of flow velocity, water level and tide-cycle sediment loading; although the effects of tidal fluctuation on the water flow at the river mouth became evident as the inflow upstream decreased. The net sediment loadings within each tidal cycle were all positive during the event, as shown in Figure 3.3-5 (c), implying that the flood-driven sediment transport in the estuary was dominant. Based on the sediment loading within each tidal cycle, an estimated 1,000,452 tonnes of sediment in total were delivered into Moreton Bay through the Brisbane River mouth during the January 2011 floods. This value was similar to the Olley and Croke (2011)'s evaluation which estimated the sediment load to be 1,040,000 tonnes.

$$SL = \int_{t1}^{t2} v_m A C dt \qquad (3.3\text{-}3)$$
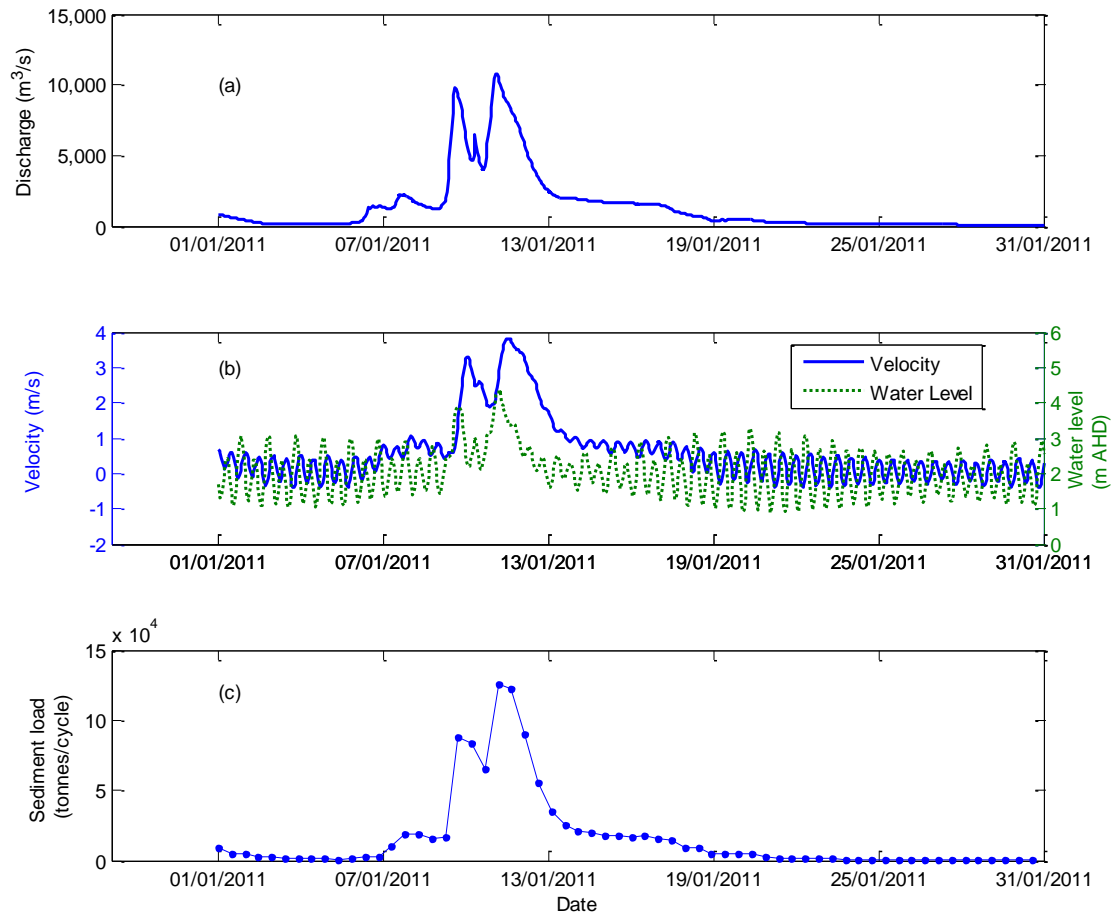
Figure 3.3-5 (a) River discharge at Chainage 0 km (upstream) during January 2011; (b) the variations of inflow velocity and water level at the river mouth (downstream); (c) the sediment load at the river mouth over a period of one tidal cycle.

3.3.5 Conclusions

In this study, the turbidity distribution within the Brisbane River estuary during the January 2011 flood event was investigated using a validated numerical model. The Brisbane River estuary turbidity maximum zone (ETM) generally extended throughout the mid- estuary under normal weather conditions (with an average flow rate lower than 100 m^3/s). However, the turbidity distribution was significantly changed during the January 2011 flood events. After a moderate flood event in December 2011 (an average flow rate < 3000 m^3/s), a high-low-high pattern of turbidity distribution was found in the estuary, with a higher turbidity of 1800 NTU upstream and downstream of the estuary, but comparably lower turbidity of 200 NTU in the middle estuary. After the experience of severe flood (10,000 m^3/s), the turbidity level generally increased from upstream to downstream within the estuary, and approached

approximately 2000 NTU. The gradually increasing turbidity distribution had remained for several days and then changed to a relatively even condition. In addition, it was found that the flood impact on sediment transport in the estuary was more significant than the tidal effects. An estimated 1,000,452 tonnes of sediment were delivered into Moreton Bay through the Brisbane River mouth during the January 2011 floods.

3.3.6 Acknowledgement

Chapter 4 Salinity and turbidity distributions in the Brisbane River estuary, Australia

---

Statement of contribution to co-authored published paper

This chapter includes a co-authored peer- reviewed published paper.

The bibliographic details of article, including all authors, is:

> **Yu, Y.**, Zhang, H., Lemckert, C.J., 2014. Salinity and turbidity distributions in the Brisbane River estuary, Australia, Journal of Hydrology 519, 3338-3352.

The article has been reformatted to meet the thesis style guidelines.

My contribution to these published papers involved: literature review, model set-up, calibration and validation of the model, simulations, data processing, figures and tables, analysis of results, writing and editing.

_____

Yingying Yu

_____

Prof Hong Zhang (principal supervisor and co-author)

_____

Prof Charles Lemckert (principal supervisor and co-author)

Salinity and turbidity distributions in the Brisbane River estuary, Australia

Abstract

The Brisbane River estuary (BRE) in Australia not only plays a vital role in ecosystem health, but is also of importance for people who live nearby. Comprehensive investigations, both in the short- and long-term, into the salinity and turbidity distributions in the BRE were conducted. Firstly, the analysis of numerical results revealed that the longitudinal salinity varied at approximately 0.45 and 0.61 psu/hour during neap and spring tides, respectively. The turbidity stayed at a higher level and was less impacted by tide in the upper estuary, however, the water cleared up while the tide changed from flood to ebb in the mid and lower estuary. The second investigation into the seasonal variations of salinity and turbidity in the BRE was conducted, using ten-year field measurement data. A fourth-order polynomial equation was proposed, describing the longitudinal variation in salinity dilution changes as the upstream distance in the BRE during the wet and dry seasons. From the observation, the mid and upper estuaries were vertically well-mixed during both seasons, but the lower BRE was stratified, particularly during the wet season. The estuary turbidity maximum (ETM) zone was about 10 km longer during the wet season than the dry season. Particular emphasis was given to the third investigation into the use of satellite remote sensing techniques for estimation of the turbidity level in the BRE. A linear relationship between satellite observed water reflectance and surface turbidity level in the BRE was validated with an R^2 of 0.75. The application of satellite-observed water reflectance therefore provided a practical solution for estimating surface turbidity levels of estuarine rivers not only under normal weather conditions, but also during flood events. The results acquired from this study are valuable for further hydrological research in the BRE and particularly prominent for immediate assessment of flood impacts.

4.1 Introduction

An estuary is an interaction and transition area between rivers and oceans, and the health status of an estuary significantly affects both the river and ocean environments. Two important characteristics, salinity and turbidity, directly determine the health condition of an estuary. An estuary, in general, brings coastal conditions into the waterway as far as the tidal limit, which raises two particular issues, namely salinity intrusion, and the existence of the turbidity maximum zone (ETM) in the estuary (Peck and Hatton, 2003). The salinity intrusion from the river mouth to the upstream estuary may change the hydrological structure of the estuary and probably lead to contamination of other water resources along the estuary (Uncles and Stephens, 1996). The existence and variation of turbidity not only affects the water quality, but also results in strong spatial and temporal gradients in physical processes, which further influences the flow dynamics (Hughes et al., 1998, Massei et al., 2003). Therefore, a more comprehensive knowledge of salinity and turbidity distribution under a variety of river flow and tidal conditions in an estuary is vital for further hydrological research and also provides coastal zone management options, particularly in relation to increasing demand for flood damage assessment (Yu et al., 2013b).

In recent years, a large number of studies have examined the characteristics of salinity intrusion and turbidity maximum development in estuaries during different seasons. Shetye and Murty (1987) measured the salinity distribution in the Zuari estuary, India, at monthly intervals from 1977 to 1978. Their results revealed that the Zuari estuary was vertically well-mixed during the dry season but partially stratified during the wet season. They demonstrated two processes determining the behaviour of salinity intrusion in the Zuari estuary: i) runoff drove advective transport out of the estuary during the wet season; and ii) tides induced diffusive transport into the estuary during the dry season. Uncles et al. (2006) measured the turbidity over one year throughout the length of the Humber estuary, UK. They found that a strong ETM formed and settled in the lower estuary during the wet season but moved to the upper estuary during the dry season.

Within hourly time scales, for a tide-dominated estuary, the saltwater intrusion and sediment transport including resuspension, deposition, and bed erosion, are essentially determined by tide (Lentz and Limeburner, 1995, Ataie-Ashtiani et al., 1999, Zhang and Chan, 2003, Zhang et al., 2004, Werner and Lockington, 2006). Uncles and Stephens (1996) found that salinity

intrusion in the Tweed estuary, UK, was a strong function of spring-neap tidal currents and a weaker function of freshwater inflow. The saltwater intruded up to 7.6 km into the estuary at flood tides and receded to 4.7 km from the river mouth at ebb tides (Uncles and Stephens, 1996). Ataie-Ashtiani et al. (1999) further illustrated that the tidal fluctuation did not have a large effect on how far the saltwater intruded into the estuary; however, it caused remarkable variations in the configuration of salinity concentration contours, particularly at the water surface. Additionally, the tidal influences on turbidity distribution in estuaries were usually classified into three categories according to different tidal ranges, from micro-tidal, in which the tidal range is not more than 2 m, through to meso-tidal, with a tidal range from 2 to 4 m, and macro-tidal, in which the tidal range is greater than 4 m (Hughes et al., 1998). Compared to the ETM zone within the micro-tidal estuary, which is always triggered by flood events and tide, the ETM zone in meso- and macro-tidal estuaries heavily relies on tidal conditions (Hunt et al., 2006). Two mechanisms were proposed for the development and maintenance of the ETM zone in higher tidal ranges (Hughes et al., 1998). In the first mechanism, the ETM zone is caused by fine sediment accumulation and tidal resuspension, as a result of combined effects of tidal-induced residual currents and gravitational circulation (Hughes et al., 1998); in the second mechanism, the propagation and maintenance of the ETM zone are attributed to the distortion of tidal waves, associated with non-linear interactions between the tide and channel morphology (Dyer, 1986).

Under non-significant flood event conditions, the distribution of salinity and turbidity in estuaries varies between wet and dry seasons; the distribution generally experiences regular variations during a tidal cycle. Following severe flood events, saltwater is usually washed out of estuaries; however, flood inflow carries a large amount of sediment and particles, which would be transported, and then settled in estuaries, resulting in extreme high turbidity levels. To conduct an investigation into the high level turbidity after floods, field measurement is one of the main approaches. In recent years, satellite remote sensing technology also has been widely applied for detection of coastal and oceanic conditions. In comparison with time-consuming, expensive and weather dependent *in-situ* measurement, the main advantages of satellite remote sensing are the capability of covering large areas with spatially continuous records, and the ability to obtain instant information about water colour (Yates et al., 1993). Various visible and near infrared bands were proposed as water turbidity level indicators in previous studies (Tang et al., 2003, Wang and Lu, 2010). For instance, Shi and Wang (2009) used the satellite images to observe the flood-driven Mississippi River sediment plume

development. Wang et al. (2009) retrieved water reflectance at Band 4 (with a wavelength range of 770 to 860 nm) from The Enhanced Thematic Mapper Plus (ETM+) images to estimate the suspended sediment concentration in the large, turbid Yangtze River. A similar investigation was conducted by Wang and Lu (2010), which retrieved water reflectance at Band 2 (with wavelength range of 841 to 876 nm) from the Moderate Resolution Imaging Spectroadiometer (MODIS) aboard NASA'S Terra satellite to estimate the suspended sediment concentration in the Lower Yangtze River. It can be seen in previous studies (Wang et al., 2009, Wang and Lu, 2010) that the band selection for turbidity estimation generally depends on the wavelengths of bands and other geographically correlated factors, such as the particle properties.

Studies (Eyre et al., 1998, Dennison and Abal, 1999, Howes et al., 2002, Schacht and Lemckert, 2003, Yu et al., 2013a) on the salinity intrusion and suspended sediment condition within the Brisbane River estuary (BRE) indicated that the saltwater intruded approximately 80 km upstream from the river mouth, and the ETM zone usually extended from about 20 to 60 km upstream from the river mouth under non-significant flood conditions. Additionally, Howes et al. (2002) observed the salinity and turbidity at a single site in the BRE over a period of thirteen months. They proposed a non-linear best-fit curve to describe the relationship between the average turbidity level in the BRE and the tidal range. Yu et al. (2011) conducted the investigation into the flood-driven plume in the BRE. They reported the extension of the sediment plume in Moreton Bay after the flood event in May 2009; A more significant flood event which occurred in the Brisbane River catchment in 2011 was also investigated by Yu et al. (2013b). It was observed that the severe flood event generated approximately 500 km^2 sediment plume in Moreton Bay and it was estimated that this plume would take about 20 days to become completely diluted. However, due to the lack of field measurement turbidity data, the turbidity level, distribution and variation have not yet been discussed in any subsequent study.

The Brisbane River flows through the large city of Brisbane, Queensland, Australia, and enters into Moreton Bay (see Figure 4.2-1); as such, the condition of the river significantly affects the quality of surrounding water resources, public perceptions of river water quality, and the health of the entire region's ecosystem. The motivation for this study is therefore not only driven by the lack of comprehensive knowledge of the salinity and turbidity distribution of the BRE in the short- (under tides) and long-term (during the wet and dry seasons), but also by the increasing demand for the efficient and immediate estimation of turbidity state

after flood events. This study will further incorporate numerical investigations of sediment transport in coastal areas under non-flood and flood conditions.

4.2 **Study area**

The present study domain, the Brisbane River, is located in sub-tropical southeast Queensland, Australia (Figure 4.2-1). It has a catchment area of approximately 13,506 km^2 (Eyre et al., 1998). The river flows through the city of Brisbane and enters into Moreton Bay. The BRE is distinctly brown in colour, particularly after heavy rainfall in the catchment (Dennison and Abal, 1999). In addition to the main channel of the BRE, the Bremer River and Oxley Creek join the Brisbane River at 72 and 34 km respectively, upstream from the river mouth, as shown in Figure 4.2-1. The Brisbane River estuary is micro-tidal, with a mean neap tidal range of 1 m and a mean spring tidal range of 1.8 m (Wolanski, 2014). The length of the tidal section within the BRE is approximately 80 km up to the junction of the Bremer River, and the depth along the estuary ranges from 15 m at the river mouth to about 4 m at the Bremer River junction (Hossain et al., 2004, Ecosystem Health Monitoring Program, 2007).

Figure 4.2-2 shows the typical river discharge in the Brisbane River over a period of 10 years from 2002 to 2011. During the dry season (June to November), the average flow in the BRE was 3.2 m^3/s. In contrast, during the wet season (December to May), the average flow increased to 7.7 m^3/s without considering the occurrence of flood events. In recent decades, a number of significant flood events have occurred in the Brisbane Catchment. For instance, the peak runoff of the flood event in May 2009 was 874 m^3/s, and the peak runoff of the severe flood event from December 2010 to January 2011 was over 10000 m^3/s (Babister and Retallick, 2011).
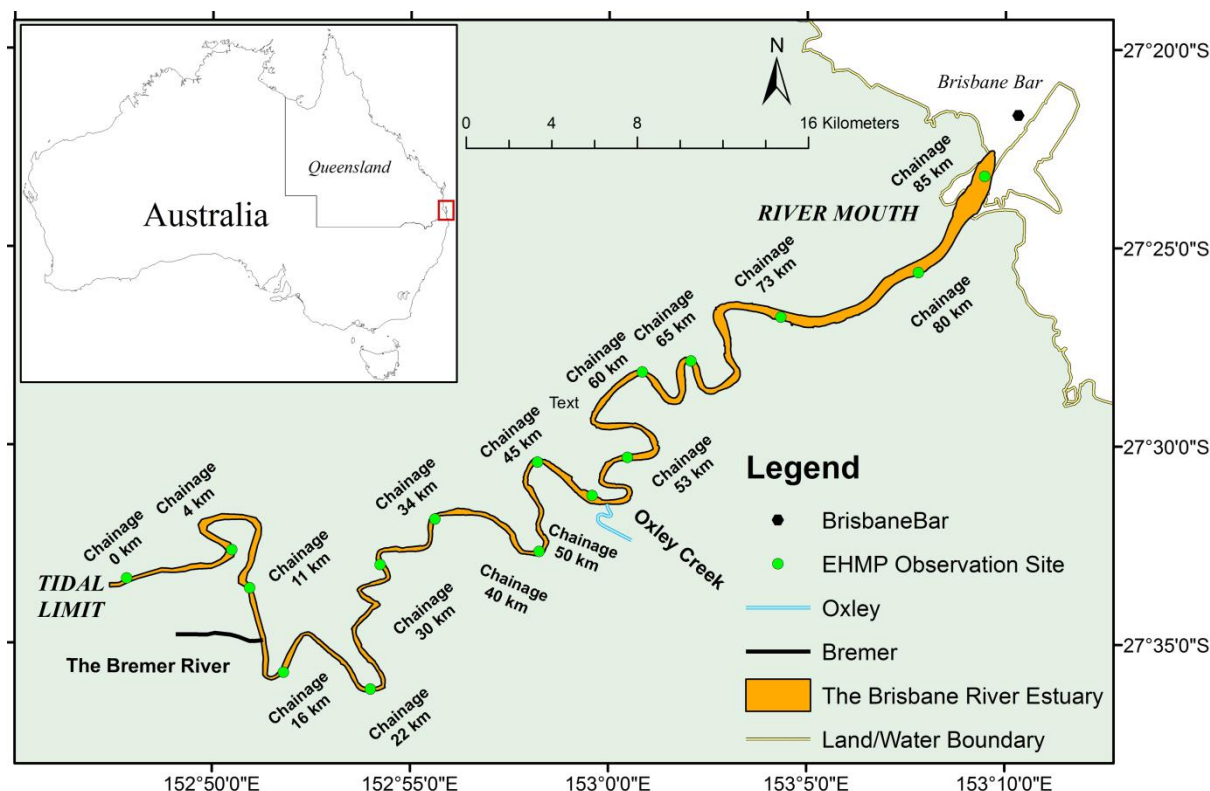
Figure 4.2-1 The Brisbane River estuary (BRE), Queensland, Australia, and locations of observation sites along the estuary. The chainages (km), distance from the tidal limit to certain observation site, are marked for each site. Source: Geoscience Australia; and the Ecosystem Health Monitoring Program (EHMP) Organisation.
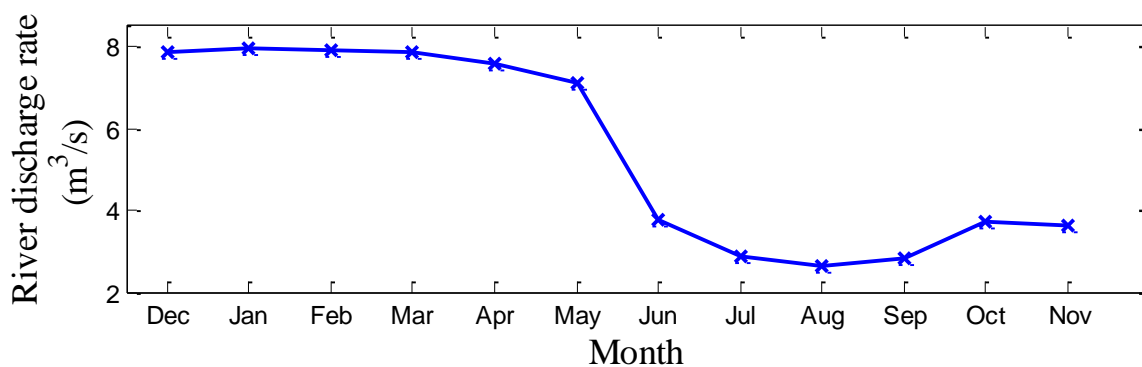
Figure 4.2-2 Monthly-averaged river discharge rate during a period of the last decade (excluded the flood events which occurred from 2002 to 2011).

4.3 **Study methods**

4.3.1 **Water samples collection and hydrodynamic data**

The Ecosystem Health Monitoring Program (EHMP) is one of the most comprehensive freshwater, estuarine and marine monitoring programs in Australia (Ecosystem Health Monitoring Program, 2007). The EHMP has been conducted with continuous water sampling and monitoring at monthly intervals over the last decade. The water samples have generally been collected at the ebb tides at 16 monitoring sites along the BRE from the river mouth up to the tidal limit, as marked in Figure 4.2-1. The profile of temperature, at depth intervals of 2 m, is measured with a YSI 6920 temperature sensor (Ecosystem Health Monitoring Program, 2007). The profile of salinity is derived from water conductivity which is measured using a YSI 6920 conductivity sensor (Ecosystem Health Monitoring Program, 2007). The turbidity at 90° from the light source is directly recorded using a YSI 6920 turbidity sensor consisting of a near-infrared LED with the wavelengths between 830 and 890 nm (Ecosystem Health Monitoring Program, 2007).

The Department of Environment and Heritage Protection (formerly, the Department of Environment and Resource Management), Queensland, Australia, regularly measures the river discharge at their stream monitoring sites. One site (ID: 143001C, which is located at 152.57^o E and 27.44^o S) has the closest proximity to the tidal limit of the BRE, as marked in Figure 4.2-1. The river inflow recorded at this site is therefore applied in this study to represent the freshwater runoff entering the BRE. Additionally, tidal height data at the Brisbane bar (in the vicinity of the river mouth, as marked in Figure 4.2-1) have been provided by Maritime Safety Queensland.

4.3.2 **Numerical model**

4.3.2.1 Model description and set-up

To conduct investigation into the variations in salinity and turbidity distribution during the tidal cycle, MIKE 11 DHI, a one-dimensional hydrodynamic model coupled with advection-dispersion modules has been applied in this study. The model, based on the dynamic wave description, solves the vertically integrated equations of conservation of continuity and momentum, as defined in Eq. (4.3-1) and (4.3-2)

$$\frac{\partial Q}{\partial x} + \frac{\partial A}{\partial t} = q \tag{4.3-1}$$

$$\frac{\partial Q}{\partial t} + \frac{\partial \left(\beta \frac{Q^2}{A} \right)}{\partial x} + gA\frac{\partial h}{\partial x} + gAI_f = \frac{f}{\rho_w} \tag{4.3-2}$$

where Q is the river discharge rate, A is the cross-sectional area, q is lateral inflow, h denotes water level, I_f represents the flow resistance term, f is the momentum forcing, ρ_w is the density of homogeneous water and β is the momentum distribution coefficient (DHI Water and Environment, 2014a). The advection-dispersion module applies the vertically and laterally integrated equation of mass conservation of a dissolved or suspended material, such as salinity and settling/suspended material concentration. The equation is defined as follows

$$\frac{\partial AC}{\partial t} + \frac{\partial QC}{\partial x} - \frac{\partial}{\partial x}\left(AD\frac{\partial C}{\partial x} \right) = -AK_dC + S_cq \tag{4.3-3}$$

in which C is the salinity/suspended material concentration, D is the dispersion coefficient, K_d is the linear decay coefficient, S_c represents source/sink concentration of the substance. Eq. (4.3-3) assumes that the considered substance is completely mixed over the cross-sections and reflects two transport mechanisms: 1) advective transport is with the mean flow; and 2) dispersive transport is due to concentration gradients (DHI Water and Environment, 2014a). The sediment in the BRE is river-borne silt, with a grain size of typically 0.004 mm (Wolanski, 2014). Based on Stokes law, the settling velocity of sediment particle is roughly estimated to be 1.4×10^{-6} m/s which is so slow that the settling can be ignored.

The main channel of the BRE from its tidal limit (Chainage 0 km, which is located at 152.99^o E and 27.52^o S) to the river mouth (Chainage 80 km, which is located at 153.13^o E and 27.43^o S), is shown in Figure 4.3-1a by a blue-dotted solid line. Along the channel in this figure, a number of cross-sections were added, at an interval of 1 km, representing the transverse section of the flow area. The orientations of these cross-sections were individually adjusted to be perpendicular to the flow direction. Some typical cross-sections within the BRE are displayed in Figure 4.3-1b to d. Within the upstream estuary, the cross-sections are usually shallow and narrow, for example the cross-section at Chainage 0 km (Figure 4.3-1b). The cross-sections in the mid-estuary, such as the estuary at Chainage 40 km (Figure 4.3-1c), remain narrow but become deep. Compared to the natural channel within the upper and mid

estuary, the lower estuary is generally dominated by a deep 9 m dredged channel, associated with a 13 m-deep dredged channel at the river mouth (Eyre et al., 1998, Hossain et al., 2004). The cross-sections of dredged channel within the lower estuary are much wider and flatter than the natural channel in the upper estuary, for instance the cross-section at Chainage 80 km, as shown in Figure 4.3-1d.
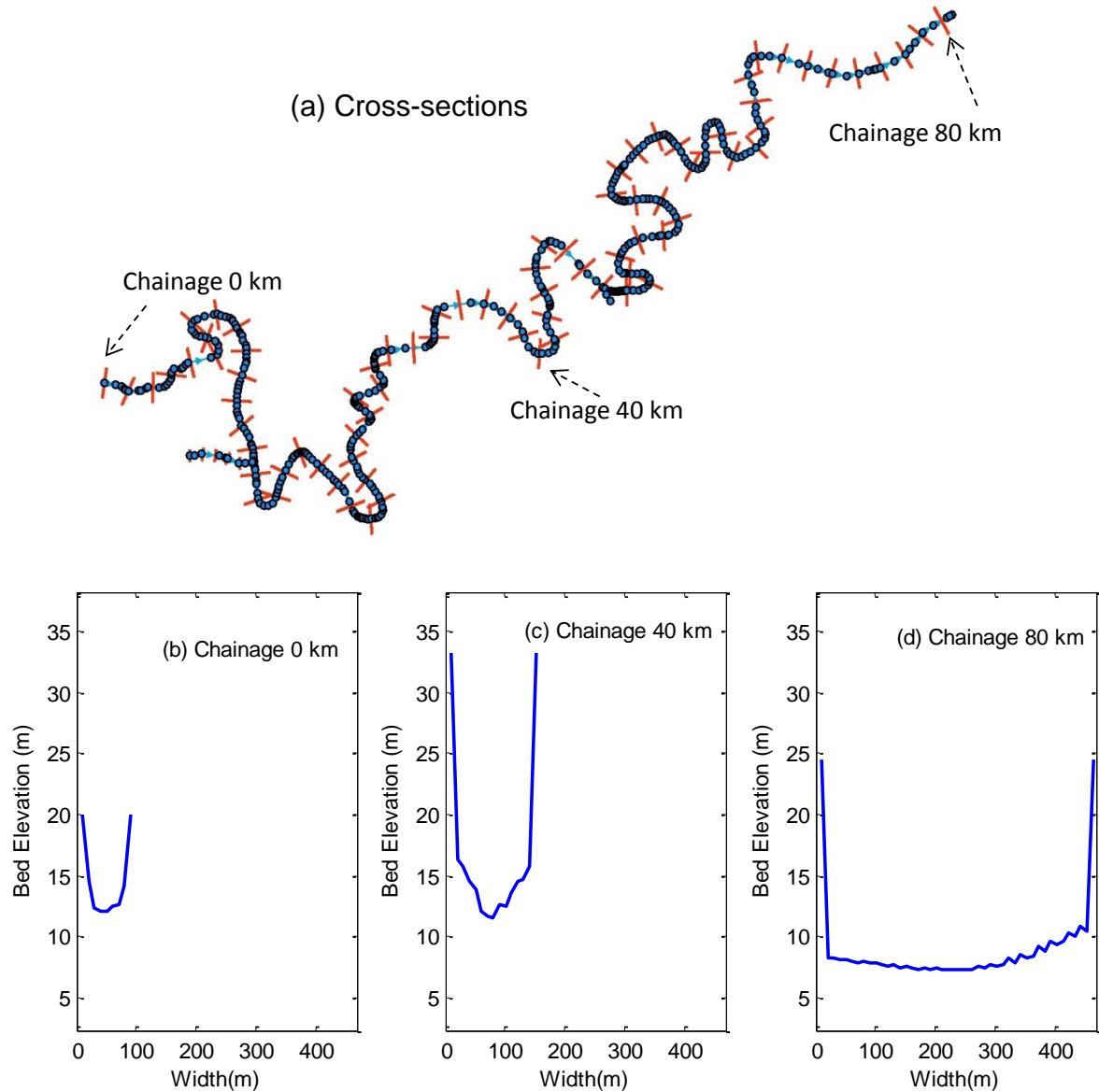
Figure 4.3-1 (a) The cross-sections along the BRE indicated by orange lines. Three typical cross-sections at (b) Chainage 0 km, (c) Chainage 40 km, and (d) Chainage 80 km, are displayed respectively. The elevations are in reference to the 0 m Australia Height Datum (AHD).

The hourly-measured river discharges and monthly-measured sediment concentration were used as the upstream open boundary conditions at the entrances of the BRE (Chainage 0 km),

the Bremer River, and Oxley Creek, respectively, as shown in Figure 4.2-1. The measured water levels at the river mouth (Chainage 80 km) and monthly-measured sediment concentration were applied as the downstream open boundary condition. The wind effects were not taken into consideration in this study, due to the lack of wind data along the estuary. The wind would enhance or restrain the estuary gravitational circulation and vertical mixing of sediment, in the water surface by wind force and within the water column by wind-driven turbulence (Zhang et al., 2009). Hence, without consideration of the wind effect in the simulation, the vertical distribution of salinity and turbidity might be under- / over- estimated. The available observed turbidity data were recorded in NTU; however, the MIKE 11 DHI model only works with the concentration of suspended sediment (C_s) (DHI Water and Environment, 2014a). In this case, the simple correlation proposed by Hossain et al. (2004), which described the relationship between the turbidity and SSC within the entire BRE and was defined in Eq. (3.3-2), was applied here. The salinity and temperature records at 16 EHMP sites along the estuary, and the estimated SSC based on the measured turbidity were added to the model as the initial simulation conditions. Additionally, a number of characteristic parameters including the critical shear stresses for erosion and deposition and sediment settling velocity, were set as 0.05 N/m², 0.03 N/m², and 6.5×10^{-4} m/s, respectively (Margvelashvili et al., 2003, Bell, 2010). These values were tested in previous studies (Margvelashvili et al., 2003, Bell, 2010), which proved that they were able to produce appropriate simulated turbidity results in the BRE.

To guarantee the stability of the numerical simulation that is described in Eq. (4.3-4), the spatial space and time step were determined to be 500 m and 15 seconds, respectively. The simulation period in this study was from 1 January, 2006 to 2008. The model first ran for a 1-year spin-up period to allow the model to reach a steady dynamic state and to ensure that this spin-up would not impact upon final model outputs.

$$\frac{V \Delta t}{\Delta x} \leq 1 \text{ to } 2 \qquad (4.3-4)$$

4.3.2.2 Model calibrations and verifications

In the hydrodynamic model, bed resistance is a vital parameter which largely determines the behaviour of the river flow and the development of other suspended materials (Lemckert et al., 2011). In this study, *Manning's n* was used to represent the bed resistance. The

Manning's n was uniformly adopted, with the assumption of constant roughness along the river in the model. The values of *Manning's n* ranging from 0.02 to 0.05 were found to be appropriate for open channels and all floodplains in the Brisbane Catchment, respectively (Brisbane City Council, 2003). Hence, the value of *Manning's n* from 0.01 to 0.06 with a step of 0.005 was individually tested in the simulation to evaluate the performance of the hydrodynamic model.

It was found that the model with the value of 0.03 for *Manning's n* produced the most comparable simulated results in this study, compared to other values for *Manning's n*. The value of 0.03 for *Manning's n* is close to the value of 0.025 which was used in Wolanski et al. (1997) to commonly represent sandy estuaries. Using the value of 0.03 for *Manning's n,* the simulated results were obtained. A comparison of simulated and measured daily-averaged water levels at Chainage 16 km is shown in Figure 4.3-2. In a normal condition, the mean water depth generally stayed at a level of 6 m, but it increased to approximately 8 m following the significant flood event in November, 2008. The normalised root mean square error (NRMSE) and RMSE between the simulated and measured water levels are 2.37% and 0.06 m, respectively. The simulated water levels generally matched the observed water levels with an R^2 of 0.97.
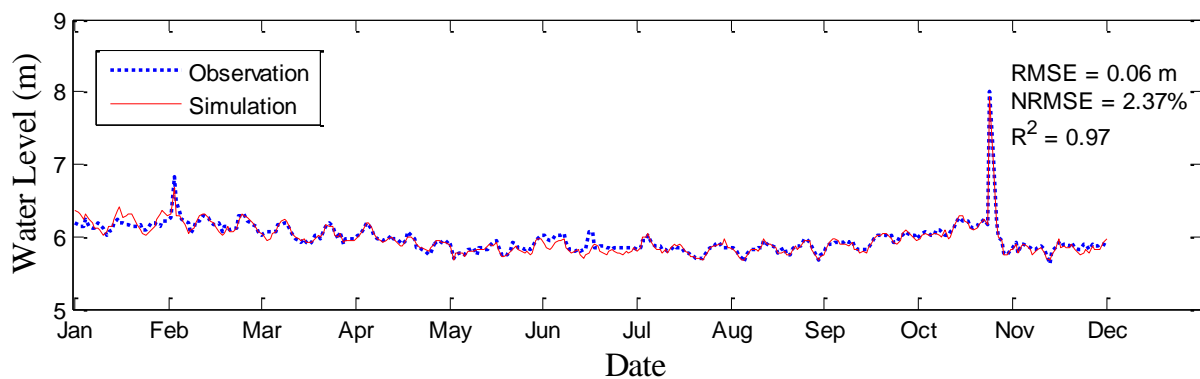
Figure 4.3-2 Comparison of the simulated and observed daily-averaged water levels in 2008.

Furthermore, within the advection-dispersion module, the dispersion coefficient (m^2/s) which largely influences the dispersive transport term due to concentration gradients, is defined as Eq. (3.2-1). In a previous study (Bell, 2010), the value of dispersion factor a_1, was estimated to range from 160 to 450 m in the BRE, associated with the non-dimensional, constant dispersion exponent b_1, which was set as 1. Therefore, the dispersion factor a_1, is in meters.

Based on Bell (2010)'s estimation, the value of dispersion factor a_1, ranging from 100 to 500 m with a step of 50 m, was tested.

Table 4.3-1 RMSE of salinity for varying dispersion factors in the BRE in 2007

RMSE (psu)	Run(#)					
	#1 $a_1 = 350$m	#2 $a_1 = 400$m	#3 $a_1 = 450$m	#4 $a_1 = 500$m	#5	
					RMSE (psu)	a_1 (m)
Chainage (km)						
0-10	0.32	0.19	0.23	0.33	0.16	400
10-20	0.78	1.75	0.93	1.71	0.71	350
20-60	2.67	2.59	2.82	2.88	2.35	400
60-80	1.91	2.04	1.31	0.97	0.95	500
0-80	2.01	2.37	1.93	2.12	1.62	-

The concentrations of salinity were used to calibrate and verify the dispersion coefficient in the BRE. For different values for dispersion factor (Run # 1 to 4), the calibrated results using the simulated salinity within the BRE from 2007 were listed in Table 4.3-1. It can be seen in Table 4.3-1 that the model with the constant dispersion factor, a_1, ranging from 350 to 500 m was able to produce comparable simulated outputs, which drove RMSE values to around 2 psu. Furthermore, in order to represent the dispersion condition more accurately, the estuary was separated into 4 sections, namely Chainage 0 to 10 km, Chainage 10 to 20 km, Chainage 20 to 60 km, and Chainage 60 to 80 km, corresponding to the varying salinity reduction rates within different river reach sections (Refer to Section 4.4.2.1 for the details regarding the salinity variation rates). The dispersion factors (Run #5 in Table 4.3-1) reduced in magnitude from 500 m at the river mouth to 350 m at Chainage 10 km, and were set back to 400 m in the vicinity of the tidal limit, resulting in the simulated results with an RMSE of approximately 1.78 psu. This set of values of the dispersion factor (Run # 5) was further verified using simulated salinity results from 2008, in terms of temperature and salinity. It

can be seen in Figure 4.3-3 that the NRMSE of the simulated temperature and salinity in the BRE are 6.02% and 4.88%, respectively, which indicates the high accuracy of the model.
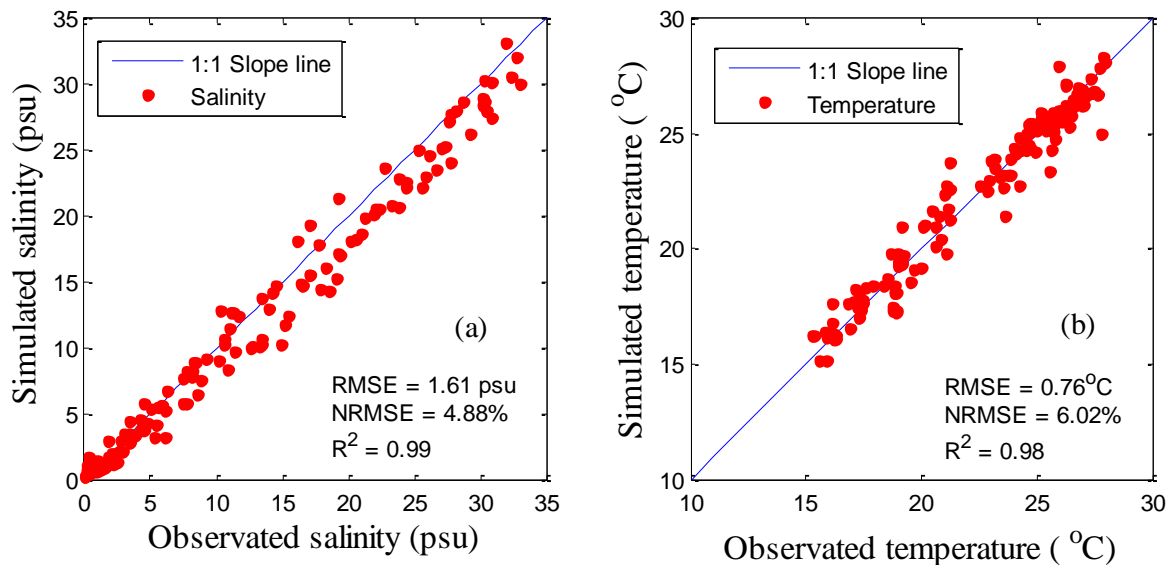
Figure 4.3-3 Comparison of the simulated and observed (a) temperature and (b) salinity within the entire BRE in 2008.

Moreover, the estimated SSC based on the field-measured turbidity was compared with the simulated result in Figure 4.3-4. With an R^2 of 0.9 and a NRMSE of 3.62%, the model produced a fairly comparable suspended sediment output, ranging from 0.9 to 650 mg/l. As shown in Figure 4.3-4, a fraction of the simulated results was underestimated, particularly at the moderate SSC level. This underestimation might have arisen in three different ways. Firstly, the relationship between turbidity and SSC in nature is complex and varying. It is therefore difficult if only using the simple correlation to reflect the real turbidity and SSC conditions within the entire estuary under different flow conditions. Secondly, as wind is one of main factors causing fine sediment resuspension (Hughes et al., 1998), the exclusion of wind effects in the simulation would weaken the resuspension of fine sediment. The difficulty in determining the values of characteristic parameters, including the critical shear stress for bed erosion and deposition and sediment settling velocity, is likely the third factor.

Overall, the model performance has been verified in terms of water levels, temperature, salinity and suspended sediment concentration. As evident in Figure 4.3-2 to Figure 4.3-4, the model is able to accurately reflect flow characteristics and sediment development in the Brisbane River estuary.
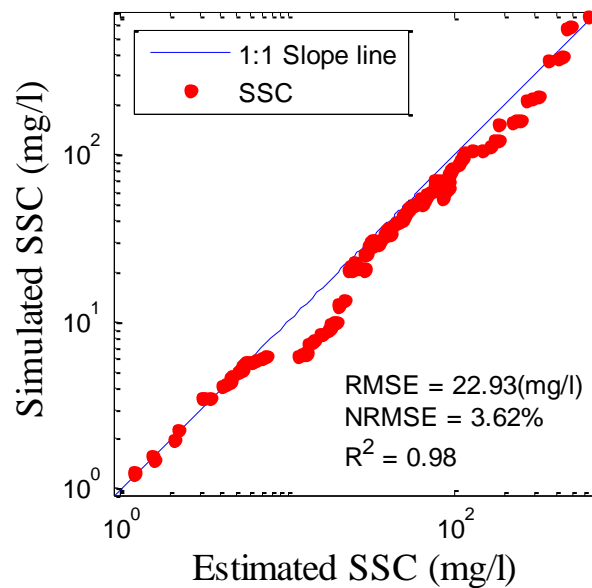
Figure 4.3-4 Comparison of the simulated and observed SSC in 2008.

4.3.3 Satellite remote sensing surface reflection

In addition to the usage of field observation data and model outputs, this study also used the MODIS Terra Surface Reflectance Daily L2G Global data to estimate the turbidity level within the estuary. These geometrically corrected data, with a spatial resolution of 250m at Bands 1-7, were downloaded from the EOSDIS, NASA. To exclude cloudy days, MODIS images were checked before surface water reflectance data were downloaded. Moreover, it was found that the water reflectance at Band 2 is significantly lower than the land radiance in the BRE, in the sense that the wavelengths at Band 2 clearly separate water bodies from land. For instance, Figure 4.3-5 shows on 16 November, 2006, the surface reflection conditions at Band 1 (with wavelengths from 620 to 670 nm), and Band 2 (with wavelengths between 841 and 876 nm). The Brisbane River estuary cannot be seen in Figure 4.3-5a; however, it is clearly distinguished from the land in Figure 4.3-5b. The surface reflectance at Band 2 at the sites which were marked in Figure 4.3-5b was therefore selected to estimate the turbidity distribution in the BRE. As can be seen in Figure 4.3-5c to e, the water reflectance at marked sites (at the narrowest channel within the river, approximately 150 m wide) was significantly different from the land reflectance, implying the data at selected sites are not impacted from the land.
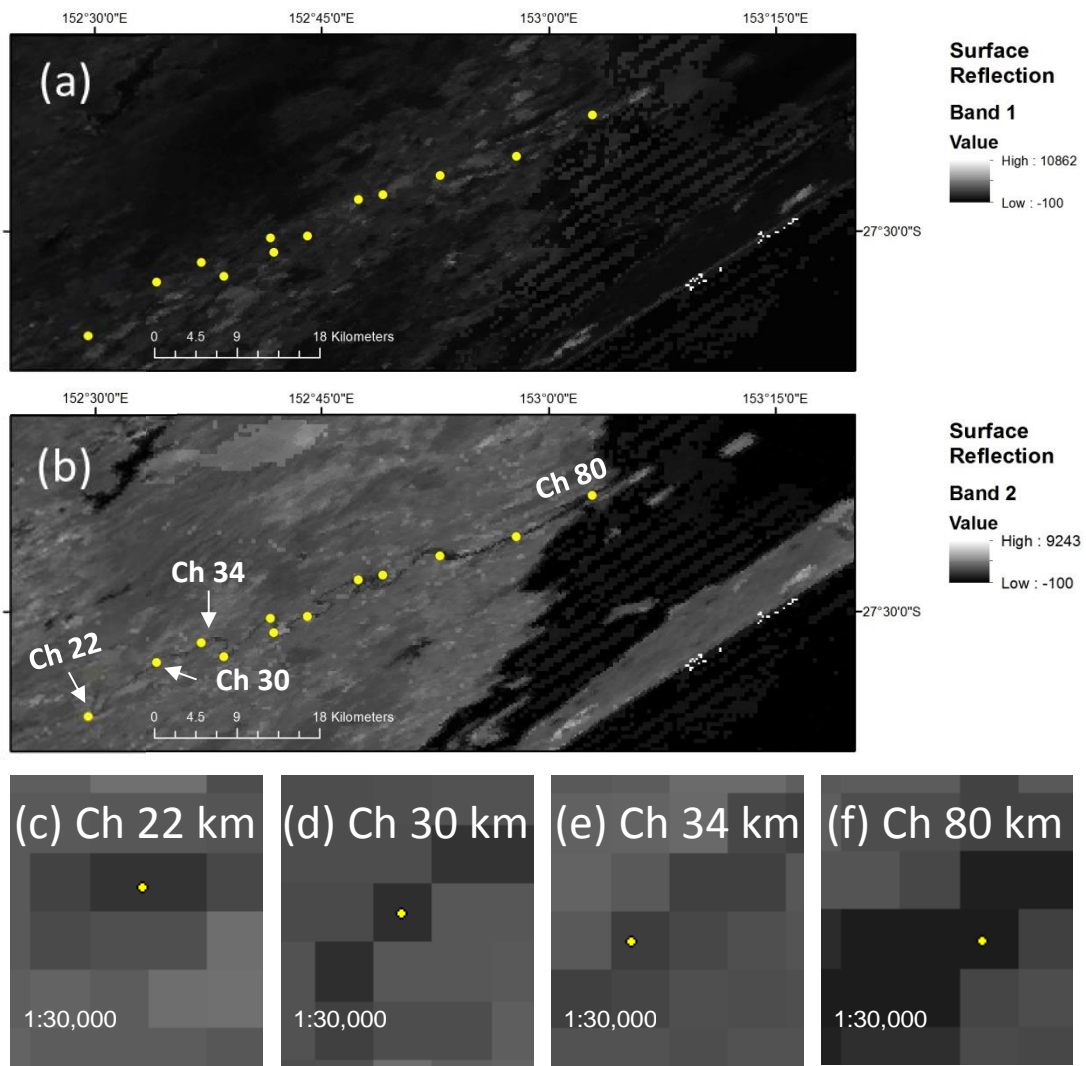
Figure 4.3-5 The surface reflection at (a) Band 1 and (b) Band 2 within the Brisbane Catchment. The yellow circles represent the EHMP observation sites. Three sites at the narrowest BRE and one site at the river mouth are selected and displayed in (c) to (f), showing the reflectance at Band 2 within the BRE clearly separating water bodies from land.

4.4 Results and discussion

4.4.1 Salinity and turbidity variations under tidal effects

The semidiurnal tide heights at the Brisbane River mouth range from about 0.5 to 2.1 m for neap tides and about 0.2 to 2.7 m for spring tides. Using a verified one dimensional numerical model, MIKE 11, the investigation into the tidal effects on the variations of salinity and turbidity (ST) within the BRE was conducted.

4.4.1.1 Longitudinal ST profiles during the tidal cycle

The depth-averaged longitudinal salinity and turbidity along the BRE were simulated. Figure 4.4-1c shows the depth-averaged longitudinal salinity profiles of the BRE during a spring tidal cycle, along with the velocity variation at the river mouth in Figure 4.4-1a, and comparison of the simulated and field measured salinity data in Figure 4.4-1b. with an R^2 of 0.99 and an RMSE of 0.67 psu. Note that the velocity is the result of the combined effects of the seaward river inflow and the tidal current; positive and negative velocities denote the flood tide and ebb tide directions, respectively. During the ebb tide period, the salinity in the mid and lower estuary decreased by 1.67 psu on average, while the magnitude of the velocity decreased between 10 a.m. and 1 p.m., as shown in Figure 4.4-1a and c. As a result, the salinity longitudinal profile at 1 p.m. was lower than it was at 10 a.m., as indicated in Figure 4.4-1c. During the flood tide period, the salinity level within the BRE progressively increased, with an average rate of 0.63 psu per hour from 1 p.m. to 3 p.m., and 0.69 psu per hour from 3 p.m. to 6 p.m. That is, the salt water intruded into the estuary at a higher rate after the magnitude of velocity reached its maximum. At the end of the flood tide, the freshwater-saltwater intersection (FSI) was pushed further upstream from approximately Chainage 39 km (at 1 p.m.) to Chainage 34 km (at 6 p.m.), indicating the position of FSI might be 5 km further upstream during the flood tide than during the ebb tide. Compared to the periodic variations in salinity which occurred in the mid and lower estuary, the longitudinal salinity distribution in the upper estuary was relatively steady during the tidal cycle.

As with the salinity profiles, the depth-averaged longitudinal turbidity profiles during the same period are shown in Figure 4.4-2c, which are associated with comparison of the field measured and simulated turbidity in Figure 4.4-2b with an R^2 of 0.98 and an RMSE of 1.58 NTU. Figure 4.4-2c indicates that the turbidity was at lower levels generally, without existence of the ETM. During the ebb-flood tide, there were no significant variations in the turbidity levels, which demonstrated that the amounts of sediment in the estuary were similar. The main visible difference is the longitudinal shift of turbidity profiles during the ebb-flood tide. It can be seen in Figure 4.4-2c that the turbidity profile at 1 p.m. had a similar shape to the profile at 10 a.m.; however, it shifted further downstream by approximately 5.6 km compared to the profile at 10 a.m. The turbidity profiles, such as the profiles at 3 p.m. and 6 p.m., then changed to shift back (upstream) while the estuary water flowed landwards. Although the tide has effects on fine cohesive sediment resuspension in an estuary (Rijn,

1993, Zhang et al., 2009), such impacts have not been discussed in this study due to the limitation of the one-dimensional model and available field measurement data.
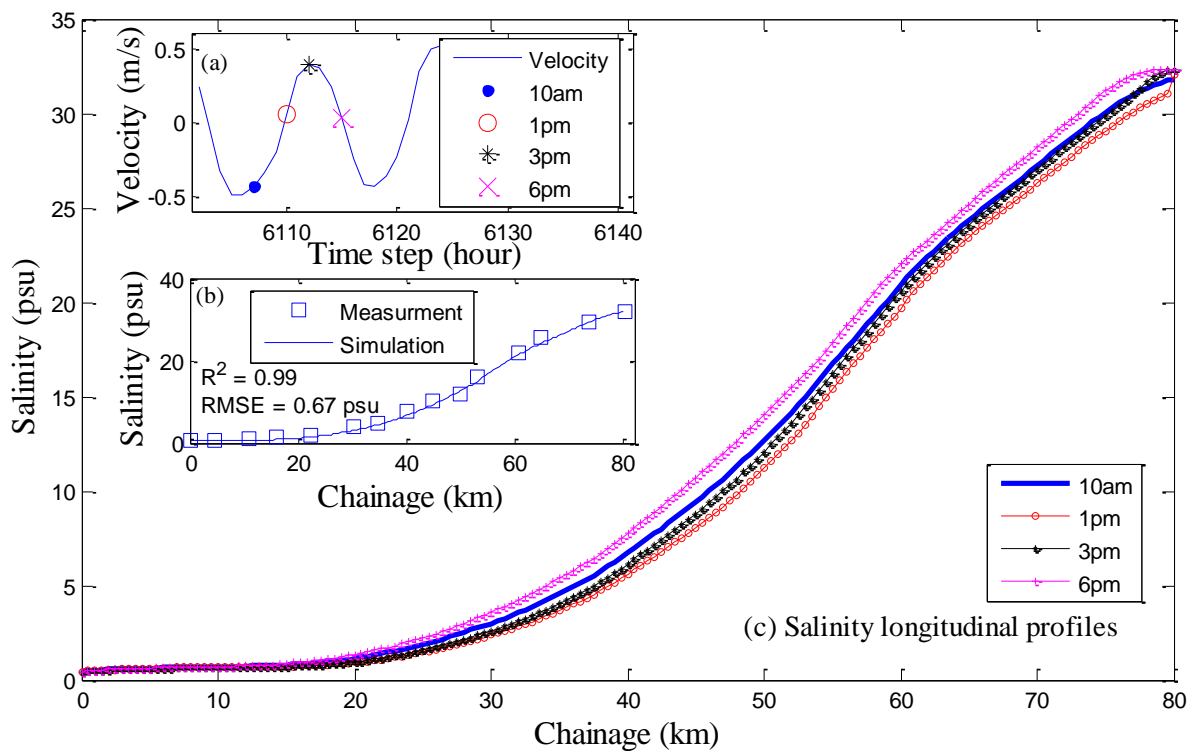
Figure 4.4-1 The velocity variations at 10am, 1pm, 3 p.m. and 6pm on 11 September, 2008. (b) Comparison of the field-measured salinity which was collected at 10am on 11 September, 2008 and simulated salinity. (c) The depth-averaged salinity longitudinal profiles at the corresponding time.

Generally, the longitudinal variation in ST during the neap tidal cycle was similar to its variance during the spring tide within the BRE, such as in the position of FSI which was 5 km further upstream during the neap flood tide than during the neap ebb tide. However, the simulated results indicated that the salinity varied by approximately 0.45 psu per hour during neap ebb-flood tide (see Table 4.4-1), compared to the variation rate of 0.61 psu per hour during spring ebb-flood tide. In addition to the salinity, the slight difference of turbidity variation during spring and neap tides was observed. Compared to the shift distance of 5.6 km during the spring tide cycle, the longitudinal turbidity profile moved by almost 3.4 km during the neap tide.
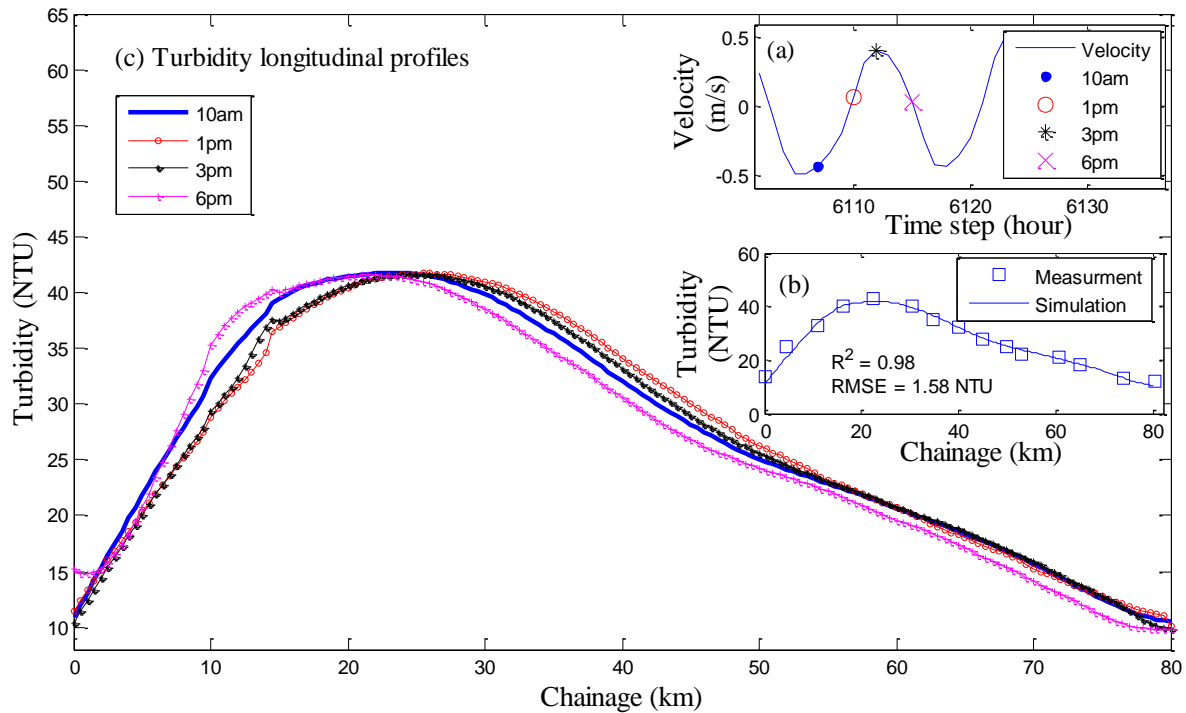
Figure 4.4-2 (a) The velocity variations at 10am, 1pm, 3 p.m. and 6pm on 11 September, 2008. (b) Comparison of the field measured turbidity which was collected at 10am on 11 September, 2008 and simulated turbidity. (c) The depth-averaged turbidity longitudinal profiles at the corresponding time.

Table 4.4-1 Longitudinal variation in ST during spring and neap tidal cycle

	Salinity		Turbidity
	FSI position (km)	Variation rate (psu/hour)	Longitudinal shift (km)
Spring tide	5	0.61	5.6
Neap tide	5	0.45	3.4

4.4.1.2 Salinity-velocity and turbidity-velocity patterns

The model output velocities, associated with the salinity and turbidity in the upper (e.g. Chainage 20 km), mid (e.g. Chainage 30 and 40 km), and lower (e.g. Chainage 70 km) reaches of the BRE were selected during tidal cycles to examine the variations in salinity and turbidity in response to the fluctuation of flow velocity.

It can be seen in Figure 4.4-3a. to d. that the salinity level was significantly sensitive to the flow velocity conditions, and had similar change patterns in the entire estuary. That is, the salinity reached its local highest value at slack water, which occurred before the direction of the river flow reversed (from positive to negative). The salinity then decreased during the ebb

tide and reached its local lowest value at slack water before the river flow changed from negative to positive. Although the same variation patterns in salinity were observed at all four sites, their fluctuation ranges were different. The largest variation range occurred at Chainage 40 and 70 km with ± 2.5 and ± 2.3 psu, respectively; the moderate range was observed at Chainage 30 km with ± 1.5 psu; and the smallest range was found at Chainage 20 km with ± 0.5 psu. Overall, the salinity fluctuated at the same pace as the tidal current variation; however, the ranges of resultant salinity fluctuation which occurred in the mid and lower reaches of the estuary were relatively larger than in the upper estuary.
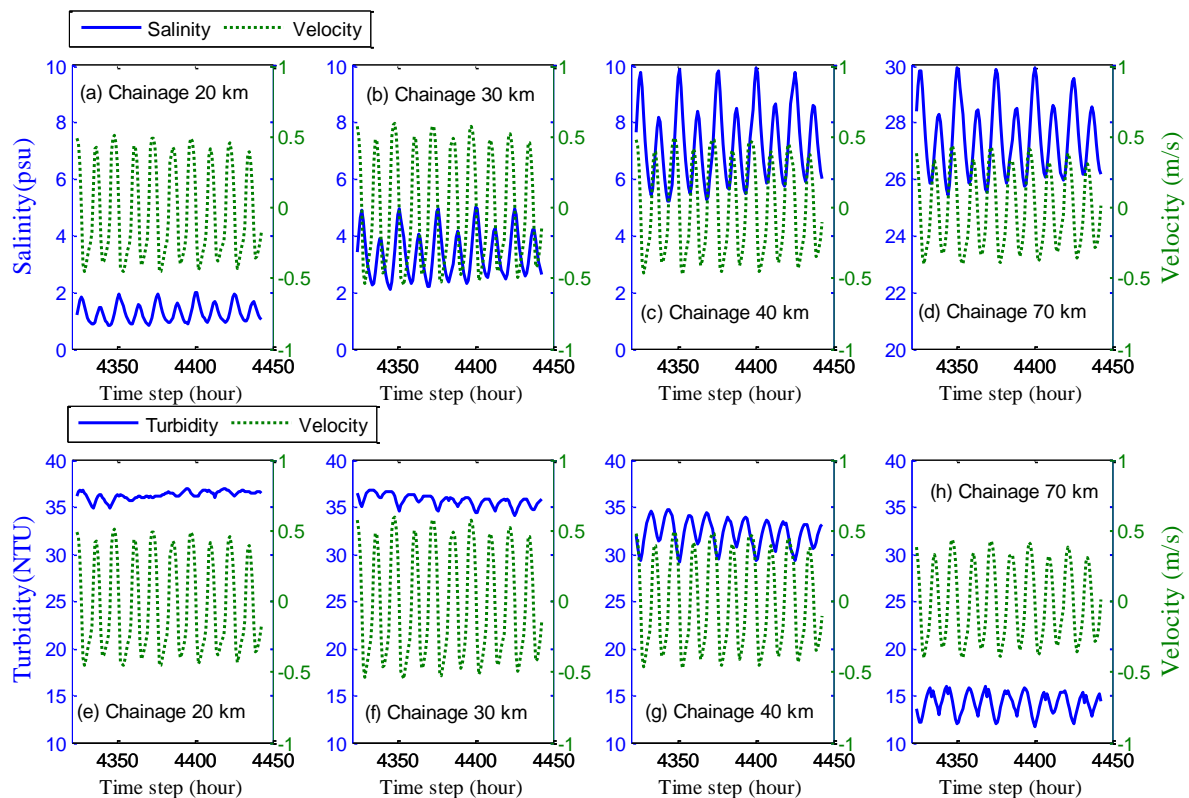
Figure 4.4-3 Simulated time series of velocity against salinity (see Figures (a) to (d)) and turbidity (see Figures (e) to (f)) at different sites, as indicated above. Positive and negative velocities denote the flood tide and ebb tide directions, respectively. The 4350th time step represents 6 a.m., 30 June, 2008.

Compared to the similar variations in the salinity in the entire BRE, the turbidity-velocity patterns varied at different sites. Figure 4.4-3e shows the turbidity and velocity variations at Chainage 20 km. The turbidity at this site maintained a high level with an average value of 35 NTU most of the time, instead of fluctuating during the tidal cycle. The most likely reason might be that the site was close to the tidal limit; that is to say, the tidal impacts upon the turbidity variation were relatively weaker. In contrast, the turbidity at Chainage 30 km relied

more upon the velocity conditions, as shown in Figure 4.4-3f. It was observed that the turbidity continuously decreased during the flood tide, and reached its lowest local value at slack water. Conversely, during the ebb tide, the turbidity level rose progressively until it reached its highest local value. At Chainage 30 km, the striking feature was that the highest turbidity was sustained for nearly 2 hours at slack water, which occurred before the direction of the river flow reversed from negative to positive, and the turbidity then changed to decrease through the remainder of the flood tide. The turbidity variation pattern at Chainage 40 km was the same as at Chainage 30 km, but it fluctuated within a wider range. The turbidity at Chainage 70 km experienced a similar fluctuation; however, it retained a much lower turbidity level. The significant low level in the lower estuary might be explained by three reasons under non-flood circumstances: i) the salt water intruding into the estuary at flood tide was relatively cleaner than the river water in the estuary (Eyre et al., 1998); ii) the particles carried by the freshwater might have already settled in the upper and mid estuary before arriving at the lower estuary; and iii) the tidal straining effect. Overall, the turbidity generally increased at ebb tide, or decreased at flood tide in the mid and lower estuary. The water column, therefore, tended to clear up while the tide was changing from flood to ebb. This finding is in accordance with the conclusions of Schacht and Lemckert (2003). In the upper estuary, the turbidity remained at a higher level with less impact from the tide. Conversely, the turbidity in the lower estuary was maintained at a lower level and was sensitive to the tidal conditions.

4.4.2 Seasonal variations of salinity and turbidity

To focus only on the seasonal variations in the BRE conditions, the rainfall-driven flood events (with an average flow rate higher than 100 m^3/s) which occurred over the last decade are excluded here.

4.4.2.1 Longitudinal and vertical distributions of salinity

Yu et al. (2013a) revealed that the salinity intrusion condition is a function of the upstream distance from the river mouth. In general, the surface salinity decreased continuously upstream from the river mouth in the BRE, as shown in Figure 4.4-4. The salinity was approximately 32 and 33 psu at the river mouth during the wet and dry seasons, respectively; the salinity reduced to around 0 psu at the tidal limit which was 86 km upstream from the river mouth during both seasons.

To examine the dilution of salinity intrusion within the BRE, the salinity dilution rate $S_p(x)$ (in percentage) along the estuary was calculated from the field observation data. In Eq.(4.4-1), the $S(x)$ (in psu) represents the value of salinity at the site x which is the chainage (in km) ranging from 0 to 80 km; hence, $S(80)$ denotes the value of salinity at the river mouth.

$$S_p(x) = \frac{|S(x) - S(0)|}{S(0)} \tag{4.4-1}$$

$$S(x) = \sum_{i=0}^{4} p_i x^i \tag{4.4-2}$$
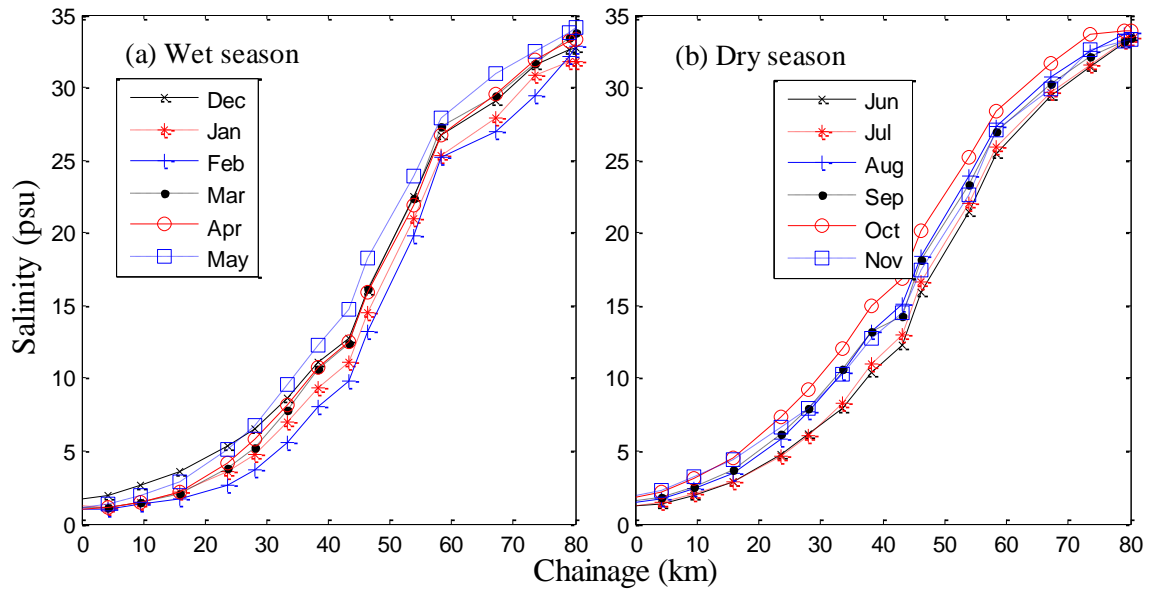
Figure 4.4-4 Monthly-averaged surface salinity distribution in the BRE during (a) wet and (b) dry seasons over a period of 10 years from 2002 to 2011.

Figure 4.4-5a and b show the changes in the dilution of salinity intrusion with upstream distance during the wet and dry seasons, and are associated with polynomial least square curves which fit the field measurement data. The function $S_p(x)$ is represented by the terms in Eq. (4.4-2), where the coefficients of p_i ($i = 0, 1, 2, 3, 4$) are specified as 97.3, -0.4, 0.03, -1.3 $\times 10^{-3}$ and 9.1 $\times 10^{-6}$ for the wet season, and 96.5, -0.3, 0.02, -8.7 $\times 10^{-4}$ and 6.8 $\times 10^{-6}$ for the dry season with an R^2 of 0.99, an RMSE of 3 psu, and a NRMSE of 10%. In Figure 4.4-5c, a comparison of salinity dilution rates from the river mouth (Chainage 80 km) up to the tidal limit (Chainage 0 km) is made between wet and dry seasons. During both seasons, there was a very slight reduction in salinity in Zone 1as well as in Zone 4, as indicated in Figure 4.4-4c.

However, in Zone 2, the salinity reduction rate rapidly increased by 20 %. The saltwater was continuously diluted in Zone 3 and it was almost 90 % diluted before it entered into Zone 4. The significant difference of salinity change rates during the two seasons, which was up to 5 %, occurred in the section of site 20 to 60 km. It can be seen in Figure 4.4-5c that the salinity decreased at a faster rate during the wet season than it did during the dry season. The rapid dilution rate was primarily attributed to higher river inflow during the wet season; however, this had little effect on salinity distribution within the lower estuary. The variation in salinity distribution within the lower estuary, particularly in Zone 1 as shown in Figure 4.4-5c, was therefore similar during the two seasons.
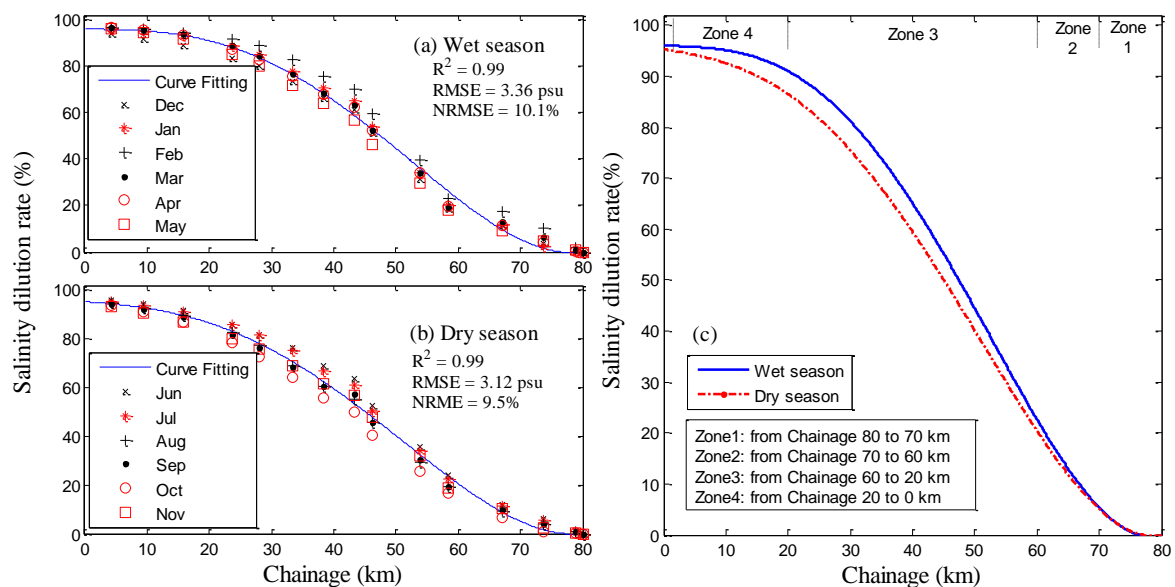
Figure 4.4-5 Salinity decreasing percentage along the Brisbane River estuary during (a) wet and (b) dry seasons. (c) Comparison of the salinity decrease in percentage during two seasons. The entire Brisbane River estuary has been separated into 4 zones as indicated above.

The BRE is typically a partially mixed, but tends to be partially stratified during periods of the ebb tides and can be stratified after large rainfall events (Wolanski, 2014). Based on this investigation of the salinity data, which all collected during the late stages of ebb tide, it was found that the lower BRE was stratified, particularly during the wet season – see the example of the salinity vertical distribution at Chainage 73 km as indicated in Figure 4.4-6a. In contrast, the distribution at Chainage 60 km in Figure 4.4-6b shows the mid and upper estuaries were vertically well-mixed during both seasons. Additionally, the salinity vertical

distribution within the entire estuary during the dry and wet seasons was depicted in Figure 4.4-6c to f. It can be seen that the front of the salinity intrusion, which is defined as the 30 psu isohaline, generally settled around 13 to 20 km upstream from the river mouth for both seasons. In contrast, the location of FSI in the estuary, in which the salinity isohaline is 5 psu, was considerably different in wet and dry seasons. Figure 4.4-6 indicates that the FSI was located near the 40 km site upstream from the river mouth during the wet season. Compared to the FSI in the wet season, the FSI was located around the 50 km site which was much closer to the tidal limit. The distinct difference of the FSI position clearly illustrates the influence of the volume of river inflow on the salinity structure in the estuary, particularly in the upper estuary.
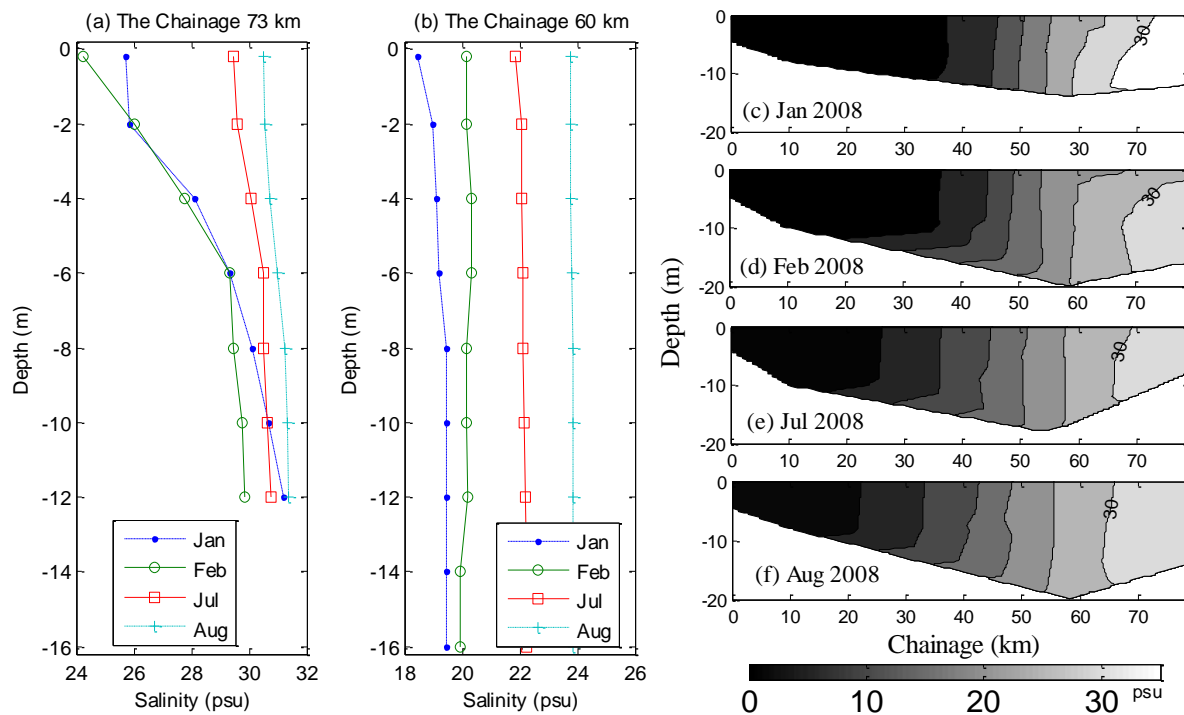
Figure 4.4-6 Vertical distributions of salinity in the BRE during the wet (e.g. January and February) and dry (e.g. July and August) seasons in 2008.

4.4.2.2 Longitudinal and vertical distributions of turbidity

Figure 4.4-7 shows the monthly-averaged turbidity distribution within the BRE over the last decade. Although the turbidity distribution along the BRE varied frequently and was more irregular than salinity variance, there were two striking characteristics as shown in Figure 4.4-7. The first feature was that the peak value of turbidity during the wet season was generally higher than during the dry season. The occurrence of higher peak turbidity during the wet season was mainly caused by three factors: i) the higher river inflow might have

brought a large amount of sediment from further upstream into the estuary; ii) the higher river inflow possibly eroded the solid river bank, generating fresh sediment that deposited and settled in the estuary; iii) the higher river inflow, combined with winds and tides, would have intensified the suspension of fine sediments. The second feature was the ETM always occurred in the upper and mid BRE (between 40 and 60 km upstream) during both seasons. The location of the ETM depended mainly on the influences of freshwater inflow and tidal straining (Uncles et al., 2006, Wang and Wang, 2010).
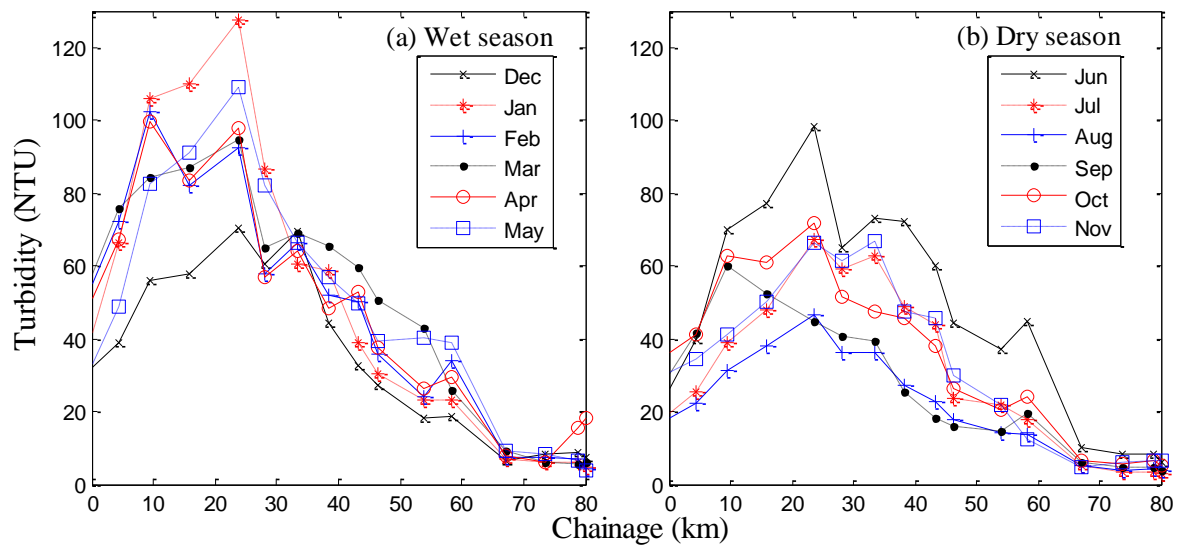
Figure 4.4-7 Monthly-averaged surface turbidity distribution in the BRE during (a) wet and (b) dry seasons over a period of 10 years from 2002 to 2011.

To adequately appreciate the turbidity distribution in the BRE under non-significant flood conditions, the frequency, site, and value of the peak turbidity for each month during a period of 10 years, were summarised in Figure 4.4-8. During the wet season, Figure 4.4-8a. illustrates that the peak turbidity usually occurred around 60 km upstream from the river mouth with occasional movements of about 10 km up or down-stream. In contrast, the peak turbidity often randomly occurred upstream between 25 km and 80 km and most often took place at around the 55 km site during the dry season, as shown in Figure 4.4-8b. In addition to the site in which the peak turbidity occurred, the values of peak turbidity were recorded in Figure 4.4-8c and d. The values which occurred most often for each month over the last decade, ranged from 50 to 120 NTU during the wet season, and were much larger than the often peak values ranging from 20 to 50 NTU during the dry season. Similar conditions were observed in the maximum peak values during the two seasons in Figure 4.4-8d. Compared to the maximum peak turbidity which was around 110 NTU during the dry season, the

maximum peak turbidity generally reached 200 NTU, with a largest value of 290 NTU, during the wet season.
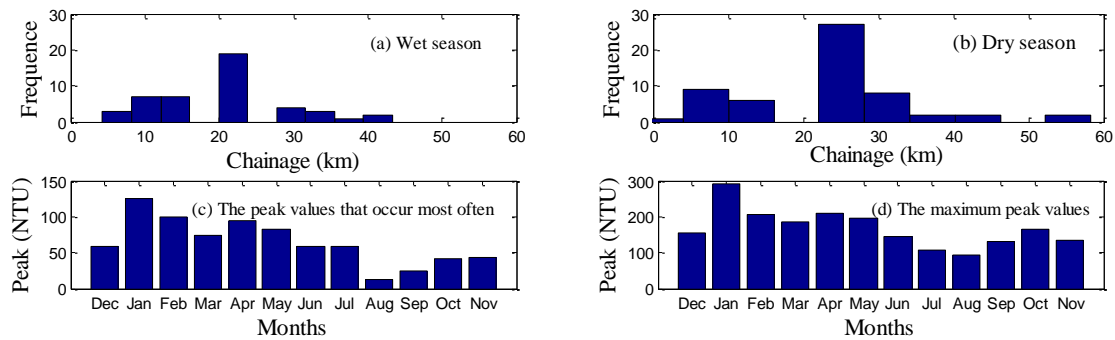
Figure 4.4-8 The occurrence of peak turbidity in the BRE for each month from 2002 to 2011 under non-significant flood conditions. (a) Wet season includes December, January, February, March, April, and May; (b) Dry season includes June, July, August, September, October, and November. (c) The peak values that occur most often and (d) the maximum peak values of the turbidity for each month from 2002 to 2011.

Furthermore, the vertical distributions of turbidity are depicted in Figure 4.4-9, taking the turbidity in January and February (the wet season), and July and August, 2008 (the dry season) as an example. Although the difference in magnitude of the turbidity was large during the two seasons, the vertical distribution patterns were much the same: the consistent turbidity distribution in the whole water column existed in the downstream estuary reach, at lower turbidity levels; the non-uniform distribution of the turbidity in the water column was observed from the mid reach up to the tidal limit of the estuary, at relatively higher turbidity levels due to high resuspension always occurring in this region. The occurrence of high resuspension was mainly attributed to tidal straining effect ($\frac{\partial u}{\partial z}\frac{\partial C}{\partial x}$) which was determined by the vertical gradients of current velocity and longitudinal gradients of suspended sediment concentration.
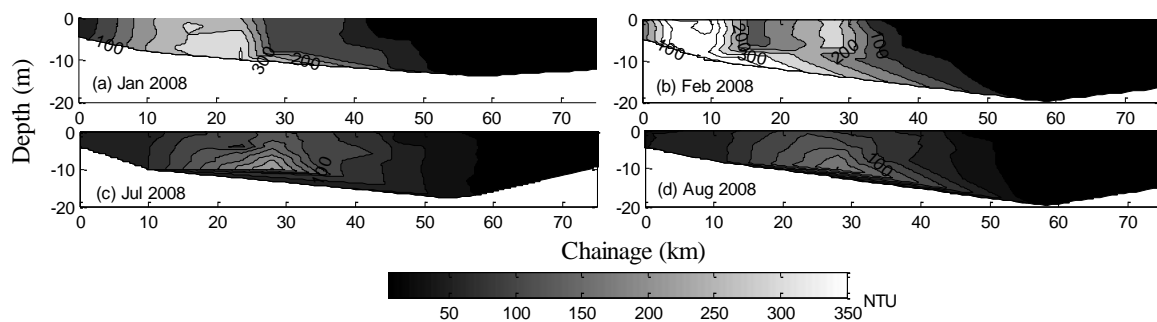
Figure 4.4-9 Vertical distributions of turbidity in the BRE during the wet (e.g. January and February) and dry (e.g. July and August) seasons in 2008.

4.4.2.3 Seasonal variations of the FSI and ETM

The FSI and ETM are the characteristic features of saltwater intrusion and the turbidity distribution within a river estuary. The locations of the FSI and the ETM in an estuary and the length of the ETM might be different during the two seasons. The depth-averaged salinity and turbidity longitudinal distributions for each month were calculated, and were further used to estimate the behaviours of the FSI and the ETM during the two seasons. In this study, the distance between the FSI (the salinity isohaline is 5 psu) and the tidal limit of the BRE is defined as x_s. Referring to the criteria applied in Bell (2010), the ETM zone in the BRE is defined as the area with turbidity values greater than 50 NTU. Hence, the distances between the tidal limit and character positions within the ETM including the head of the ETM (the landward boundary of the ETM), the site where the maximum turbidity occurred within the ETM, and the tail of the ETM (the seaward boundary of the ETM) are denoted as x_{t1}, x_{t2}, and x_{t3}, respectively. It implies that the (x_{t3} - x_{t1}) is equivalent to the length of the ETM, x_t.

Figure 4.4-10 shows the seasonal variations in the FSI and ETM within the BRE from 2002 to 2011. The FSI generally occurred at 30 to 40 km away from the tidal limit during the wet season. In contrast, the FSI was located further upstream during the dry season, which was usually 20 to 30 km away from the tidal limit. For the head of the ETM in the first group (in Figure 4.4-10a. and e.), x_{t1} the majority of data points were below the line in a slope of 1, implying that the heads of the ETM occurred further upstream than the corresponding FSI during both seasons. In the second group as shown in Figure 4.4-10b, the peak turbidity sites were always located around 20 km away from the tidal limit, which was closer than the corresponding FSI during the wet season. During the dry season, the data points in Figure 4.4-10f. mainly surrounded the line in a slope of 1. An R^2 of 0.52 between x_{t2} and x_s, indicates that the peak turbidity site within the ETM might be related to the corresponding FSI, particularly during the dry season. In Figure 4.4-10f, 44 % of x_{t2} surrounded the FSI (for the x_{t2} which was 5 km further downstream or upstream than the x_s), 38% of x_{t2} which was positioned further downstream ($x_{t2} > x_s+5$), and only 18% of x_{t2} which was located further upstream ($x_{t2} < x_s-5$). As can be seen in the third group (Figure 4.4-10c and g), the x_{t3} was significantly larger than the x_s, indicating the seaward boundary of the ETM was much closer to the estuary mouth than the FSI during the two seasons. Additionally, the lengths of the ETM, x_t, and the freshwater region, x_s, within the BRE were examined in the fourth group (Figure 4.4-10d and h). Compared to the stable length of the freshwater region within the estuary, the length of ETM varied widely from 10 to 60 km, particularly during the wet

season. Overall, the FSI were always located within the ETM region during both seasons. The site where the peak turbidity occurred in the ETM was very close to the corresponding FSI, particularly during the dry season. The results also demonstrate that a larger river inflow not only resulted in a longer ETM and caused the FSI to occur further downstream than those during the dry season. These findings are in agreement with Uncles et al. (2006) which found the seasonally longitudinal displacements both of the FSI and ETM.
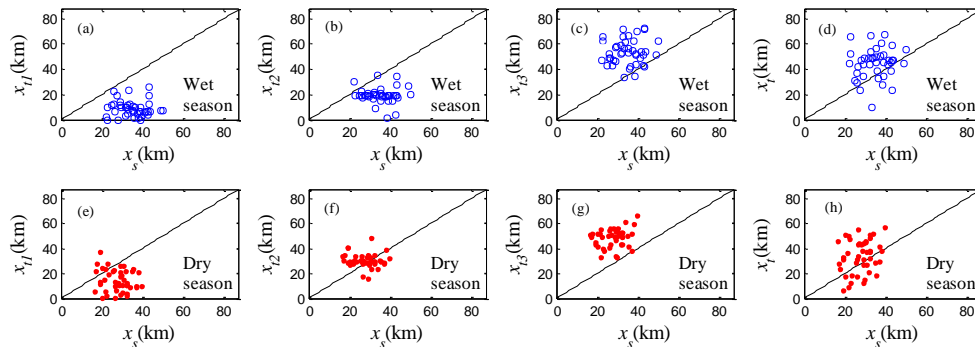
Figure 4.4-10 The seasonal variations of x_s, x_{t1}, x_{t2}, x_{t3}, and x_t within the BRE during 2002 to 2011. The straight line is in a slope of 1.

4.4.3   Turbidity condition under flood events

4.4.3.1 Estimation of turbidity from surface reflectance

To accurately and immediately estimate the surface turbidity level following flood events from surface reflectance, this study attempted to examine the natural connection between the surface reflectance collected by satellite at Band 2 and the field-observed surface turbidity level. The data from two different sources therefore should be collected on the same day at least. Due to the limitations of the available field-measured data and satellite remote sensing data, the data only on the certain days are applied, as indicated in Table 4.4-2.

Table 4.4-2 The available data from the following days are applied in the estimation

	2005	2006	2007	2008	2009	2010	2011
Non-flood (< 100 m^3/s)	13 Dec	8 Feb	10 Mar	11 Apr; 10 May	7 Jul	8 Aug	16 Nov
Flood (> 100 m^3/s)	-	10 Dec	-	-	9 Feb; 6 Jun; 6 Aug	-	24 Jan

The water reflectance at Band 2 is able to clearly separate the BRE from the land, compared to the reflectance at other bands, as shown in Figure 4.3-5. Based on the field measurement turbidity and satellite remote observed water reflectance, a linear regression was derived from

$$\ln(T_{ur}) = a_1 + a_2 W_r \qquad (4.4\text{-}3)$$

where T_{ur} represents the estuary's surface turbidity in NTU, a_i ($i = 1, 2$) denotes the coefficient, and w_r is the water reflectance at Band 2 in percentage. Given that turbidity values varied in a wide range within the BRE, the turbidity was therefore transformed by natural logarithm in the regression above.
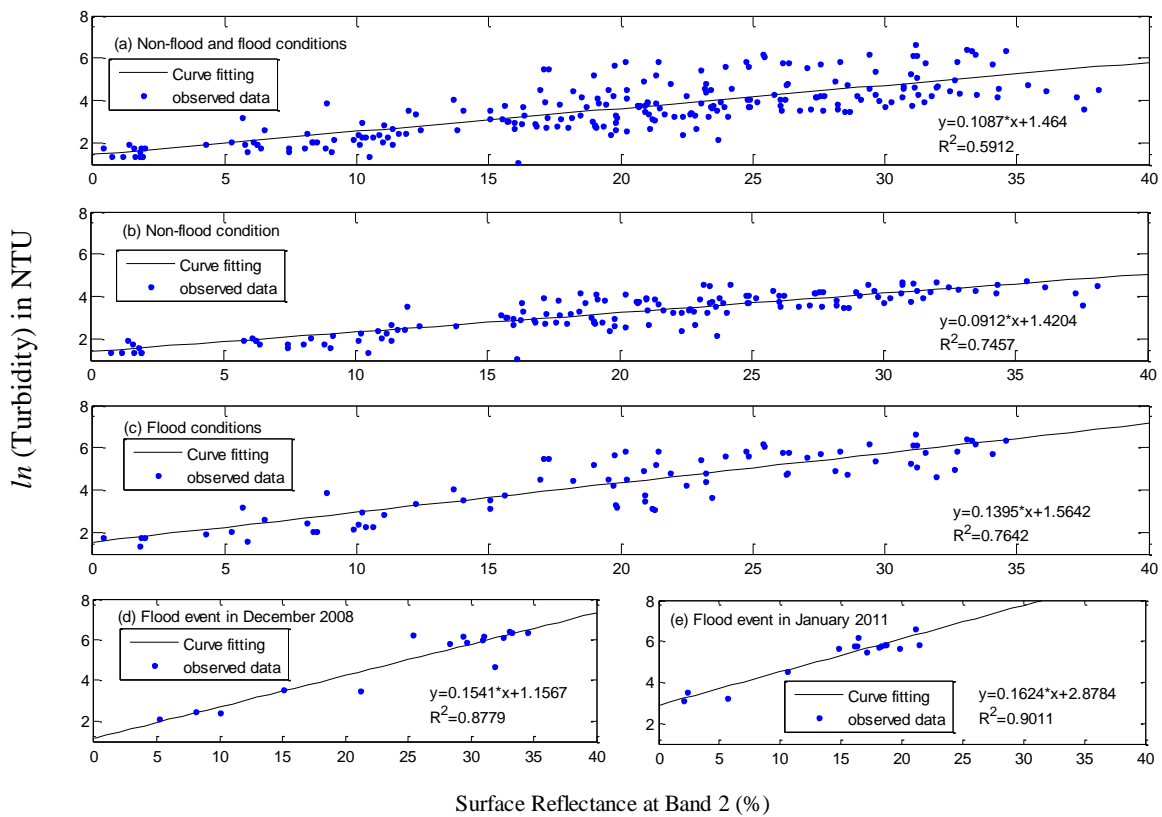
Figure 4.4-11 The field measured turbidity and satellite remote observed water reflectance at Band 2 in the BRE. (a) includes all data under both non-flood and flood conditions; (b) is plotted data only under non-flood conditions; and (c) shows the data only under flood conditions. (d) and (e) are the curve fitting for individual flood events.

Figure 4.4-11a shows all data points (n = 224) under both non-flood and flood conditions, with an R^2 of 0.59. This R^2 reveals the satellite remote water reflectance is able to reflect the variations in surface turbidity level at both low and high flow rates; that is, the water reflectance increased as the turbidity level rose. A higher R^2 was obtained if different

coefficients were applied in the regression, as shown in Figure 4.4-11b and c. The values of R^2 were 0.75 and 0.76 under non-flood and flood conditions, respectively. These R^2 values were in accordance with the findings in Wang and Lu (2010) which had an R^2 of 0.78 between the water reflectance and suspended sediment concentration in the Lower Yangtze River, China, using 35 water samples. If the flood events were considered individually, for example two flood events which occurred in December 2008 and January 2011 as shown in Figure 4.4-11d and e, there was more significant positive relationship with an R^2 reaching up to 0.9, implying the strong correlation between the turbidity and water reflectance. Although it is hard to determine the exact regression coefficients due to atmospheric impacts and other environmental influences, the regression conducted in this study clearly indicated that the water reflectance observed by satellite can be successfully applied to estimate turbidity level in the estuary under not only non-flood, but also significant flood conditions. The regression coefficients a_1 and a_2 which ranged from 0.1 to 1.6, and from 1 to 3, respectively, might provide a reasonable approximation of turbidity.

4.4.3.2 Turbidity variations after flood

Intense rainfall (193 mm on average) in late November 2008 across South East Queensland, caused local flash flooding (455 m³/s in average) occurring in the Bremer River within the Brisbane River catchment (Winant, 1983). As a consequence, the level of turbidity rose up to 3000 mg/l in the BRE, which was about 70 times higher than the typical level under non-flood conditions.

In simulating this event, Figure 4.4-12 shows the turbidity distribution on 10 December 2008. As can be seen in Figure 4.4-12a. and b., the simulation results generally match the EHMP observation (a NRMSE of 9.61%) and satellite estimation (a NRMSE of 13.34%), not only implying reasonable accuracy of simulation results, but also showing the reliability of the estimation of turbidity from satellite data. Furthermore, Figure 4.4-12d. demonstrates the depth-averaged longitudinal turbidity profiles during a spring tidal cycle. The level of turbidity was up to 650 NTU, which occurred in the mid estuary (around Chainage 45 km), while the ebb current reached its maximum at 9 a.m. as shown Figure 4.4-12c. As the ebb current decreased, the mean turbidity level decreased by 15.4% from 9 a.m. to 12 noon in the whole estuary, with the largest reduction occurring at around Chainage 45 km, revealing that the turbidity level in the ETM significantly dropped on the slack water periods during ebb-flood tides. This finding is in accordance with the Schacht and Lemckert (2003)'s observation in the BRE. After slack water periods, the turbidity level then gradually rose. In comparison

with the slighter variation in the turbidity distribution during tidal cycles under non-flood conditions, the tides significantly impacted the turbidity levels after floods. This might be attributed to two reasons: i) the larger river runoff bringing a large amount of sediment into the estuary, which is expected to increase the concentration of suspended sediment before settlement; and ii) the stronger current and tidal straining effect causing the significantly high resuspension after floods.
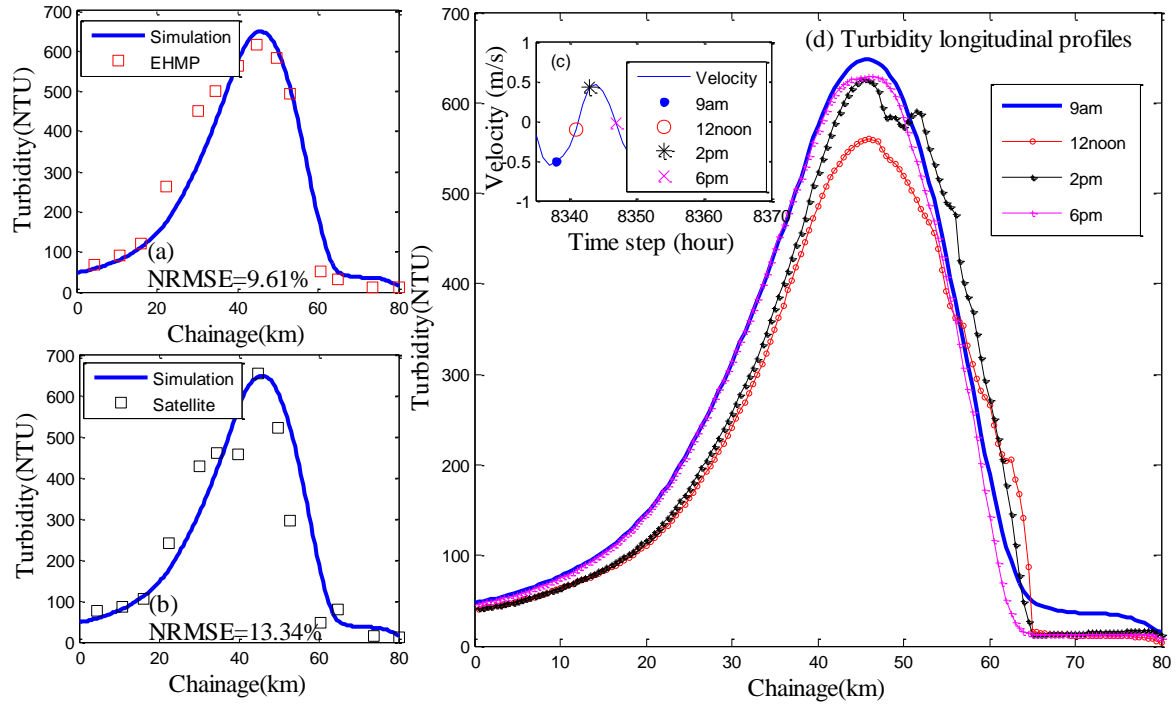
Figure 4.4-12 Turbidity distribution in the BRE during the flood in December 2008. The simulation results, which show the turbidity condition at 9a.m. on 10 December 2008, were compared with (a) the EHMP observation and (b) the satellite estimation of turbidity, respectively. (c) The velocities were at 9 a.m., 12 noon, 2 p.m., and 6 p.m. on 10 December, and (d) the depth-averaged turbidity longitudinal profiles varied at the corresponding time.

4.5   Conclusions

A comprehensive investigation, both in the short- and long-term, into the salinity and turbidity distributions in the Brisbane River estuary in Australia, was conducted in this study. The numerical results show that the FSI was pushed approximately 5 km further upstream during the flood than the ebb tide. In the upper estuary, the turbidity stayed at a higher level with less impact from the tide, while the turbidity in the lower estuary was maintained at a lower level and was sensitive to the tidal conditions. A large reduction in turbidity was found in the mid estuary, revealing the turbidity level in the ETM significantly dropped on the slack water periods after floods. Furthermore, a fourth-order polynomial equation was proposed with an R^2 of 0.99, describing the longitudinal variation in salinity dilution changes as the upstream distance changes in the BRE during wet and dry seasons. Two striking characteristics of turbidity distribution were found in the BRE: i) the peak turbidity always occurred in the upper and mid estuary during the two seasons; and ii) the peak value of turbidity during the wet season was generally higher than during the dry season. The observed results also demonstrated that a larger river inflow not only resulted in a longer ETM, but also caused the FSI to occur further downstream. Significantly, an approach of using water reflectance observed by satellite to estimate the turbidity level in the BRE was firstly proposed in this study. A linear equation was validated with an R^2 of 0.75. Although there are a number of factors which influenced the accuracy of the calculation, the results in this study clearly indicate the feasibility of using water reflectance to estimate turbidity levels in the BRE, not only under non-flood conditions, but also under severe flood conditions. Therefore, this approach allows the ecosystem conditions to be immediately and effectively evaluated, which is particularly helpful for ecosystem health assessment after severe flood events.

4.6   Acknowledgement

Chapter 5 An investigation of dispersion characteristics in shallow coastal waters

This chapter includes a co-authored peer- reviewed published paper.

The bibliographic details of article, including all authors, is:

> **Yu, Y**., Zhang, H., Spencer, D., Dunn, R.J.K., Lemckert, C.J., 2016. An investigation of dispersion characteristics in shallow coastal waters, Estuarine, Coastal and Shelf Science 180, 21-32.

The article has been reformatted to meet the thesis style guidelines.

My contribution to these published papers involved: literature review, model set-up, calibration and validation of the model, simulations, data processing, figures and tables, analysis of results, writing and editing.

Yingying Yu

Prof Hong Zhang (principal supervisor and co-author)

Prof Charles Lemckert (principal supervisor and co-author)

An investigation of dispersion characteristics in shallow coastal waters

Abstract

Hydrodynamic dispersion has a significant impact on the mass transport of sediments and contaminants within coastal waters. In this study apparent horizontal dispersion in a tidally-dominated shallow estuary was investigated using field observations and a numerical model. A cluster of four Lagrangian drifters was released in two shallow regions inside Moreton Bay, Australia: between two small islands and in an open water area. During a 16-hour tracking period, the drifters generally showed similar behaviour, initially moving with the dominant current and remaining together before spreading apart at the change of tide. Two dispersion regimes were identified, a slow dispersion during the earlier stage and a rapid dispersion during the latter stage of deployment. Such change in regime typically occurred during the succeeding ebb or flow tides, which may be attributable to residual eddies breaking down during reversal of tidal direction. In addition, a power function of the squared separation distance over the apparent dispersion coefficient produced an R^2 exceeding 0.7, indicating a significant relationship between them.

By applying a three- dimensional hydrodynamic model, the trajectories of artificial particles spreading in the bay were simulated, which allowed the calculation of dispersion coefficients throughout the entire bay. The study results demonstrate that the tidal effects on dispersion were dependent on the effect of tidal excursion and residual current. The tide was found to be the most dominant driver of dispersion in the bay when unobstructed by land; however, bathymetric and shoreline characteristics were also significant localised drivers of dispersion between the two islands as a result of island wake.

Keywords: Horizontal transport; drifter; numerical modelling; tide excursion

5.1 **Introduction**

Coastal areas are ecologically rich regions providing important habitats for a vast array of transient and resident species, in addition to playing a significant role in modifying the flow of matter and energy between terrestrial and open ocean environments. Furthermore, these areas offer important cultural and recreational benefits. However, many coastal environments have experienced growing urbanisation, often resulting in increased loads of pollutants entering the coastal zone, via sources such as river runoff or accidental releases associated with trade and infrastructure (e.g. accidental chemical or oil spill events). Such events may contribute to the degradation of ecosystem health.

Within coastal environments, mixing and dispersion play an important role in the distribution and fate of suspended biotic and abiotic substances. Particle dispersion within coastal areas, particularly in the shallow nearshore regions, is governed by local weather events, hydrodynamic flow dynamics and inter-related coastal processes (Zhang and Chan, 2003, Duarte and Boaventura, 2008, Xu and Xue, 2011). Therefore, understanding and predicting the characteristics of dispersion is fundamental for computational modelling efforts used to anticipate the fate of pollutants in the coastal environment for both preparedness and response causes.

Over the past decades a large number of *in-situ* investigations of particle dispersion behaviour have been performed using a variety of methodologies, with Eulerian and Lagrangian field-based observation methods representing the predominant approaches applied to estimate the magnitude of dispersion (Spencer et al., 2014). With recent significant developments in tracking technology, the Lagrangian method has been widely applied due to its greater flexibility and potential for increased sampling frequency (Spencer et al., 2014). Such estimates of dispersion obtained from Lagrangian drifter positioning contains the influence of shear current flow and horizontal turbulence (Tseng, 2002). Dispersion herein is referred to as the apparent dispersion including both shear dispersion and turbulent diffusion.

The relevant mechanisms governing dispersion and how physical drivers affect dispersion characteristics have been the focus of many previous studies. For example, Zimmerman (1976) revealed that particles would exhibit nearly random trajectories by considering the Lagrangian motions in tide-dominated estuaries. Geyer and Signell (1992) further pointed out that the effect of tidal currents on dispersion is subject to the length scales of the tidal excursion; as such, the tidal dispersion may significantly contribute to the entire flushing if

the tidal excursion is larger than the typical spacing of topographic features. The dispersion might only be localised without any influence on the overall flushing if the tidal excursion is smaller than the typical spacing. Besides the tidal current, it has been proposed that wind-driven currents are a dominant factor for particle dispersion in coastal areas (Zhang et al., 2009, Yu et al., 2013b). Xu and Xue (2011) found that the influence of wind blowing on the surface as well as turbulence mixing, would lead to shear dispersion. Additionally, Inoue and Siseman (2000) and Tseng (2002) reported that the coastal geomorphology partly affected the coastal current, which in turn was expected to affect the horizontal dispersion. Furthermore, in previous studies squared separation distance, D^2, which reflects the spread of a cluster of particles, has been typically applied to analyse dispersion characteristics (LaCasce and Bower, 2000, LaCasce and Ohlmann, 2003, Schroeder et al., 2011, Mantovanelli et al., 2012). In quantifying the horizontal dispersion, the dependence of D^2 on time (t) is generally classified with the following regimes: i) an exponential regime ($D^2 \sim \exp(t)$) within a smaller separation distance, approximately $1 \sim 50$ km; ii) a Richardson regime ($D^2 \sim t^2$) at the intermediate range; and iii) a diffusive regime ($D^2 \sim t$) at an asymptotic distance, where D^2 and time were taken to be numerically equal in these regimes (LaCasce and Bower, 2000, LaCasce and Ohlmann, 2003, Schroeder et al., 2011, Mantovanelli et al., 2012). Within Australian coastal waters, Mantovanelli et al. (2012) highlighted the effects of topography on dispersion behaviour in the Great Barrier Reef (GBR). The study revealed that the mean squared separation distance approached 625 km^2 in a low-density reef matrix of complex topography over a 12-day period, but only 3 km^2 inside a shelf lagoon over flat bathymetry. Although the higher dispersion along the reef matrix enhanced particle spreading, the presence of tidal circulations around islands acted as a trapping mechanism to retain particles within the reef matrix (Mantovanelli et al., 2012). Recently, Dunn et al. (2014) applied a dispersion model to simulate the fate of treated wastewater discharged under a different discharge scenario in Geographe Bay, Western Australia, demonstrating the usefulness of the numerical approach as a management tool when conducting environmental impact assessments.

Moreton Bay, Queensland (Australia), and its adjacent river estuaries represent a coastal area under threat due to increasing pressure from rapid population growth and urbanisation (Dennison and Abal, 1999) and is the setting for this study. In recent years an increasing number of severe flood events have occurred, resulting in large sediment transport in the bay and, consequently, harmful sediment plumes pose a threat to the bay. To date, dispersion

characteristics, which play an important role in determining the fate of such plumes within Moreton Bay, are still poorly understood.

This aim of this study was to investigate horizontal dispersion behaviour in Moreton Bay using Lagrangian drifters and to use these data to calibrate a three-dimensional hydrodynamic dispersion model. Carrying out this study over a semi-diurnal tidal cycle and estimating the dispersion coefficient of the cluster of drifters as a function of time was conducted to account for flow reversal and effects of residual eddy. Results from this study would provide valuable insight into dispersion characteristics inside Moreton Bay and the calibrated hydrodynamic model could be adjusted using particle size scaling for future studies (e.g. dispersion of harmful sediment plumes), further highlighting the importance of dispersion.

5.2 Methodology

5.2.1 Study area

Moreton Bay is a semi-enclosed subtropical embayment on the southeast coast of Queensland, Australia (Figure 5.2-1(a)), characterised by semi-diurnal tides, with a range of 1-2 m and M_2 as the dominant tidal constituent (Dennison and Abal, 1999). Three major entrances provide oceanic exchange through tidal flushing of the bay with the majority of exchange occurring through the ≈15.5 km wide North Passage (Gibbes et al., 2014). In comparison, exchange through the narrower South Passage (≈3.7 km wide) and Jumpinpin Bar (≈0.8 km wide), located between Moreton and North Stradbroke Islands, North and South Stradbroke Islands, respectively, are relatively restricted. (Dennison and Abal, 1999).

Moreton Bay is characterised by two distinct seasonal rainfall patterns that are typified by short-lived episodic high freshwater inflows leading to runoff events and occasional flooding during the wet season and very little to no runoff events during the dry season (Chanson et al., 2014, Gibbes et al., 2014). Such seasonal variations in runoff events can result in rapid shifts between (i) freshwater inflow dominated and (ii) wind, wave and tidally dominated hydrological modes (Gibbes et al., 2014).

The largest river emptying into the bay, the Brisbane River estuary (BRE) runs through the city of Brisbane before flowing into (west side) Moreton Bay, and has a mean annual discharge of approximately 1.65×10^8 m^3 (Queensland Department of Natural Resources Mines and Water, 2006). Driven by moderate flood events (mean flow rate of 487 m^3/s) the

BRE plume has been shown to extend up to 5.5 km east of the river mouth (Yu et al., 2011), whilst during large flood events (e.g. January 2011; peak discharge 5100–17000 m^3/s) the sediment plume has been revealed to influence roughly 500 km^2 of the bay, persisting for approximately 20 days (Yu et al., 2013b). A summary of physical and hydrological characteristics of Moreton Bay is presented in Gibbes et al. (2014).
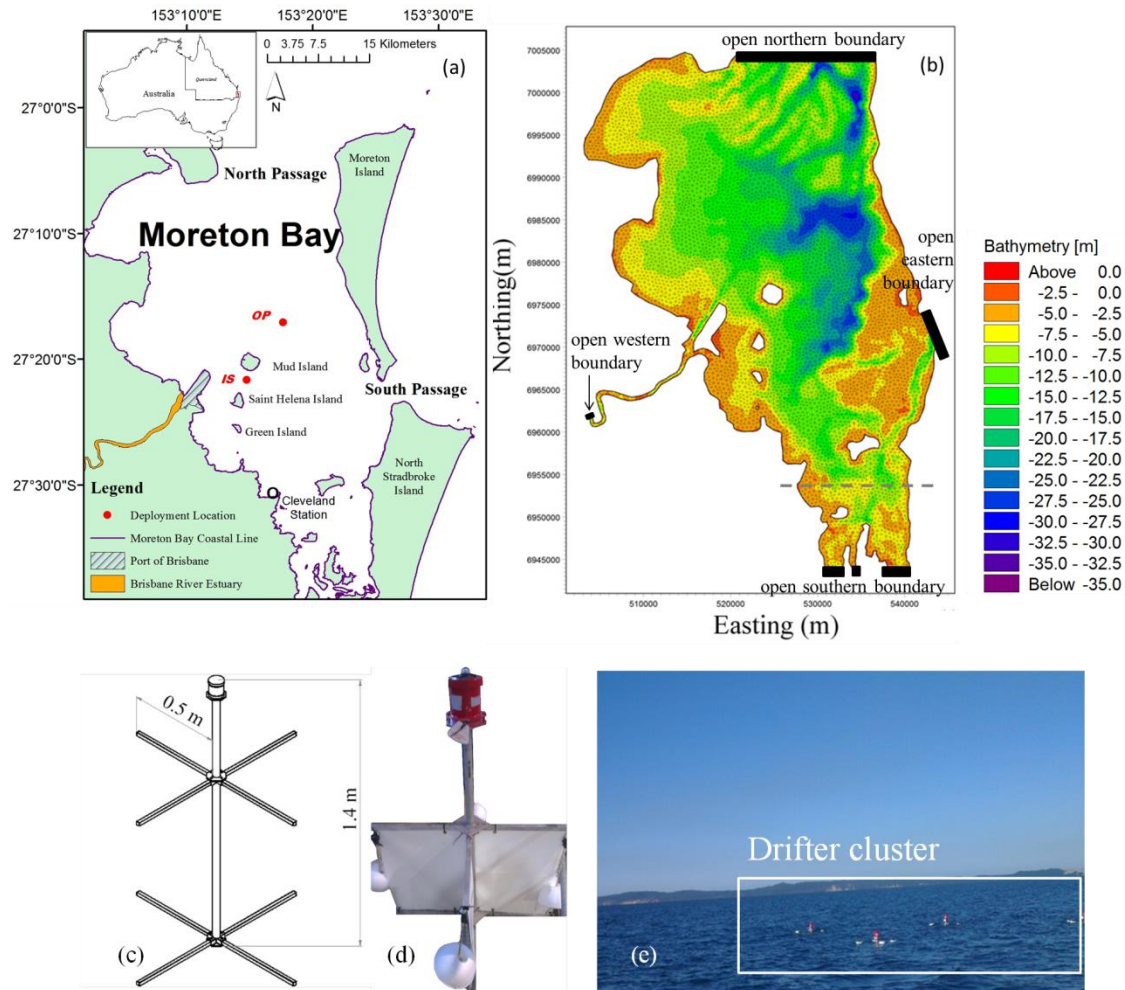
Figure 5.2-1 (a) Map of Moreton Bay and the Brisbane River estuary. The red icons (IS and OP) indicate the two chosen locations for the drifter deployments, (b) the mesh structure of Moreton Bay used in the numerical model, consisting of 13918 elements with resolution ranging from 90 to 500 m, (c) design frame of the Self-Locating Datum Marker Buoy Drifter (SLDMB) used in this study, (d) actual SLDMB utilised during the study, and (e) drifter cluster post-deployment in Moreton Bay.

5.2.2 Drifter measurement

To assist in developing an understanding of the horizontal dispersion within the bay, multiple drifters were assembled (1 m (L) $\times$ 1 m (W) $\times$ 1.4 m (H) fitted with GPS) following a standard drifter design as outlined in Poulain (1999). Similar designs have been used in many ocean and coastal water studies, including an identical design used within Moreton Bay (see Spencer et al. 2014; Figure 5.2-1c and d).

Each drifter had four drag-producing vanes held by eight arms, with a housed transmitting GPS (SPOT2^{TM}), allowing each drifter to be tracked near real-time within a position fixing error of approximately 5 m (Spencer et al., 2014).

As part of this study, two investigations (SLDMB cluster deployments) were conducted in Moreton Bay at sites IS and OP as marked in Figure 5.2-1a. A cluster of SLDMB drifters was deployed in the vicinity of Mud Island (IS) on 23 July 2013 and at the open water site (OP) on 21 August 2013. The deployment information is summarised in Table 5.2-1.

Table 5.2-1. Summary of deployment information

	Deployment details						Investigation duration (h)
Trip	Site (see Fig. 1(a))	Start time	Date	Location (Deg.)	Approx. water depth (m)	No. of drifters	
Trip #1	IS	15:36	23-Jul-13	153.24^o E, 27.36^o S	10	4	Approx. 16
Trip #2	OP	16:05	21-Aug-13	153.29^o E, 27.28^o S	20		

Each cluster comprised four SLDMBs which were released within seconds of each other, satisfying the minimum requirement for the number of drifters proposed by Okubo and Ebbesmeyer (1976). Their positions were logged at 10-minute intervals. The position data was then applied to estimate the horizontal apparent dispersion coefficient as follows:

$$K(t) = \frac{1}{4}\frac{d}{dt}D^2(t) \tag{5.2-1}$$

where

$$D^2(t) = \sigma_x \sigma_y \tag{5.2-2}$$

$$\sigma_x^2(t) = \frac{1}{N-1}\sum_{i=1}^{N}\left[x_i(t) - \bar{x}(t)\right]^2 \tag{5.2-3}$$

$$\sigma_y{}^2(t) = \frac{1}{N-1} \sum_{i=1}^{N} \left[y_i(t) - \bar{y}(t) \right]^2 \tag{5.2-4}$$

$$\bar{x}(t) = \frac{1}{N} \sum_{i=1}^{N} x_i(t), \text{ and } \bar{y}(t) = \frac{1}{N} \sum_{i=1}^{N} y_i(t) \tag{5.2-5}$$

in which K represents the apparent dispersion coefficient with respect to time t; the (i, j) refers to each distinct particle pair in the cluster; D^2 is the squared separation distance calculated by using the sample standard deviation $\sigma_x{}^2$ and $\sigma_y{}^2$ about the geometrically-averaged centroid ($\bar{x}$, $\bar{y}$) of the cluster; x and y correspond to the Easting and Northing drifter coordinates in Universal Transverse Mercator (UTM) projection at each instant of time (LaCasce, 2008, Brown et al., 2009). The dispersion coefficient is proportional to the rate of dispersion for the cluster.

5.2.3 Model descriptions

A 3D hydrodynamic and transport model, MIKE3 DHI, with a particle tracking module was applied to assist with the analysis of the dispersion behaviour. This model was calibrated based on the field deployment data and was then used to numerically simulate and analyse the apparent dispersion coefficients in the entire bay.

5.2.3.1 Hydrodynamic and transport model

Numerical simulations were conducted with unstructured triangular meshes, a free surface, and 3D incompressible Reynolds-averaged Navier-Stokes equations and the transport conservation equation:

$$\frac{\partial C}{\partial t} + \frac{\partial}{\partial x}(uC) + \frac{\partial}{\partial y}(vC) + \frac{\partial}{\partial z}(wC) = \frac{\partial}{\partial x}\left(D_h \frac{\partial C}{\partial x}\right) + \frac{\partial}{\partial y}\left(D_h \frac{\partial C}{\partial y}\right) + \frac{\partial}{\partial z}\left(D_v \frac{\partial C}{\partial z}\right) + S_c \tag{5.2-6}$$

where: C represents the concentration of the scalar quantity. D_h and D_v denote the horizontal and vertical turbulent dispersion coefficients, respectively. S_c is a constant source/sink term, (Rodi, 1984, DHI Water and Environment, 2014b).

As shown in Figure 5.2-1 (b), the computational domain covered the major part of Moreton Bay, as well as the BRE, extending approximately 30 km from the river mouth. Based on the raw bathymetry data provided by the Griffith Centre for Coastal Management on behalf of Gold Coast City Council, the horizontal domain was presented as a network of flexible

unstructured triangular grids, consisting of 13918 elements. A fine (<100 m) grid resolution was used in the vicinity of the river mouth and near coastal region, while a relatively coarser grid resolution (ranging from 100 to 500 m) was applied for the far-field. The accurate performance of such a domain configuration for Moreton Bay has been proved by Yu et al. (2012), Yu et al. (2013b).

The four open boundaries are illustrated in Figure 5.2-1 (b). The BRE open western boundary is denoted by the circle icon (Figure 5.2-1a). Hourly river discharge data derived from field observations by the Department of Environment and Resource Management, Queensland (Australia), were used at the west boundary for the boundary condition. Tidal elevations at 10 minute intervals provided by Maritime Safety Queensland (Australia), served as open boundary conditions at the northern, eastern and southern boundaries. One-minute interval wind data sourced from the Australian Bureau of Meteorology at deployment site IS (153.24 °E, 27.26 °S; Figure 5.2-1a) was used as model input across the model domain.

5.2.3.2 Particle tracking module

The particle tracking module was applied for simulating particle tracks and following trajectories in the water environment. The basic idea behind the tracking module is to transport particles according to a drift regime and turbulent dispersions by employing a random walk term (DHI Water and Environment, 2014b). The technique describing dispersion of particles follows the Langevin equation defined as:

$$dX_t = m_d(t, X_t)dt + n_d(t, X_t)\xi_t dt \tag{5.2-7}$$

where: m_d is a drift term, n_d is a dispersion term, and ξ is a random number with values between 0 and 1 (DHI Water and Environment, 2014b).

The combined effects of current and wind cause the drift of the particles, as described the drifter term in Eq. (5.2-8). The wind indirectly affects particle spreading as a consequence of its influence on the currents, U_{shear}. The surface stress is determined by the wind speed over the water (Eq. (5.2-9)), where: C_D is the drag coefficient; ρ is the water density and W_{10} represents the 10 m wind speed (m/s). The empirical formulae Eq. (5.2-10) proposed by Wu (1994) was used for parameterisation of the drag coefficient to account for wind stress on water surface, where the empirical factors $c_a = 1.255 \times 10^{-3}$ and $c_b = 2.425 \times 10^{-3}$. The wind also directly affects particles spreading when they are exposed to wind in the water surface,

expressed as U_{slip} (DHI Water and Environment, 2014b). Approximately 0.3 m of the upper portion of the SLDMB was exposed above the water line. The velocities induced by wind slip were derived from Eq. (5.2-11) and (5.2-12), where W_d is defined as wind direction (in degrees) respectively; θ_w represents the wind drift angle which is calculated by Eq. (5.2-13). Niller and Paduan (1995) confirmed that the wind slip experienced by a drifter increases as a function of wind speed and shear across the drifter itself, and proposed that the slip is inversely proportional to the drag area. The wind factor W_w, therefore acted here as a calibration factor for wind drags on the surface float. Based on the calibrated model results, the W_w of 0.034 was applied in this study, which was close to the value of 0.031 suggested by Al-Rabeh (1994).

$$m_d(t, X_t) = U_{current}(X_t, t) + U_{shear}(t) + U_{slip}(t) \tag{5.2-8}$$

$$\tau_W = C_D\, \rho\, W_{10}^2 \tag{5.2-9}$$

$$c_{fe} = \begin{cases} c_a & W_{10} < 7 \\ c_a + \dfrac{c_b - c_a}{18} \times (W_{10} - 7) & 7 \leq W_{10} \leq 25 \\ c_b & W_{10} > 25 \end{cases} \tag{5.2-10}$$

$$U_{slip} = W_w \times W_s \times \sin(W_d - \pi + \theta_w) \tag{5.2-11}$$

$$V_{slip} = W_w \times W_s \times \cos(W_d - \pi + \theta_w) \tag{5.2-12}$$

$$\theta_w = 28.6° \times \exp\left(\frac{-2.63 \times 10^{-4} \, |W_s|^3}{g} \right) \tag{5.2-13}$$

$$D_h = \frac{V_h}{\sigma_T} \text{ and } D_v = \frac{V_v}{\sigma_T} \tag{5.2-14}$$

The horizontal turbulent dispersion coefficients, D_h and D_v, can be calculated as the eddy viscosity multiplied by a scaling factor Eq. (5.2-14) (DHI Water and Environment, 2014b). The horizontal eddy viscosity, V_h, is specified by using the Smagorinsky formulation which expresses sub-grid scale transports by an effective eddy viscosity related to a characteristic length scale (Smagoringsky, 1963); and the vertical eddy viscosity V_v is derived from a standard k-ε model, whilst the scaling factor can be estimated by $1/\sigma_T$, where: σ_T is the Prandtl number. The empirical value for the Prandtl number was assigned 0.9, which corresponds to a scaling factor of 1.1 (Rodi, 1984).

5.2.3.3 Model calibration

The hydrodynamic model was calibrated using field observed data in Yu et al. (2012), Yu et al. (2013b). To ensure the accuracy of the high-resolution hydrodynamic and dispersion models, the model configuration was carefully considered, including additional parameters which were further calibrated in terms of drifter trajectories in open water.

The southern boundary in the previous study was set at the 6955000 m northing, as indicated by the dotted line in Figure 5.2-1 (b), to avoid the extremely complex topography of the southern bay. Considering that the drifter transport is sensitive to flow conditions, the computational model domain for this study was extended southward to 6944500 m northing, and the predicted tidal elevation from the DHI model was utilised as the boundary condition. With the application of a higher resolution approximately 100 m grid in the complex water areas such as the river mouth and around islands, the NRMSE (Normalised Root Mean Square Error) between simulated and observed drifter trajectories consequently decreased from 18 % to 15 %.

The mean resolution of bathymetry applied in Yu et al. (2013b) was approximately 500×500 m. However, experimental measured data shows that the drifters moved approximately 50-100 m in the longitudinal direction (*x*-axis) and 100 - 300 m in the latitudinal direction (*y*-axis), every 10 minutes. Taking into account the need for monitoring the drifters' movement and maintaining the efficiency and stability of the model, bathymetry resolutions ranging from 500 m to 50 m were calibrated. Sensitivity analysis comparing the measured data and simulated drifter trajectories generated NRMSE of approximately 15 %, 12%, 11%, 10% and 10% for the model, with mean bathymetry resolutions of 500, 200, 150, 100 and 75 m, respectively. The decreasing NRMSE illustrated that the accuracy of the simulated outcomes was progressively improved by refining the mesh resolution with the 100 m and 75 m scaled resolutions producing the same NRMSE. As such, the mean resolution of 100 m was therefore applied in this study (Figure 5.2-1 (b)).

Figure 5.2-2 Model calibration and verification. (a1) to (a4) model calibrated results in terms of four individual drifters trajectories for the second trip (21-Aug-13), respectively, (b) deviation of simulated water level at the Brisbane Bar (153.17° E, 27.37° S), (c1) to (c4) model calibrated results in terms of four individual drifters trajectories, in the first trip (21-
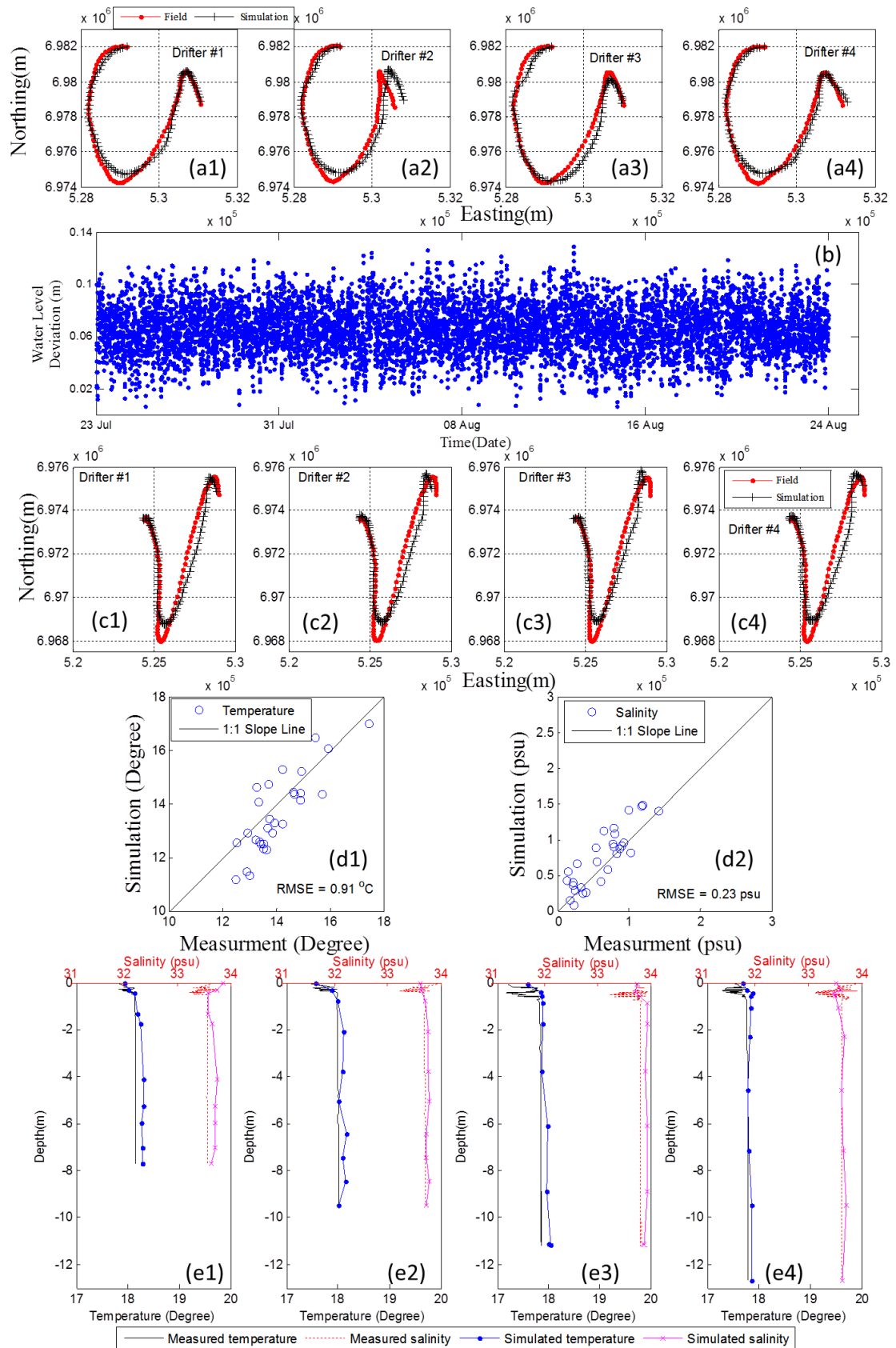
Jul-13), respectively, (d1) and (d2) comparison of the simulated and measured water surface temperature and salinity; (e) comparison of the simulated and measured vertical temperature and salinity profiles at following positions: (e1) location (153.25^o E, 27.36^o S), at 6 p.m., 23–Jul-13, (e2) location (153.25^o E, 27.41^o S) at 10 p.m., 23–Jul-13, (e3) location (153.27^o E, 27.38^o S), at 2 a.m., 24-Jul-13, and (e4) location (153.29^o E, 27.34^o S) at 6 a.m., 24-Jul-13.

Bed drag coefficients of approximately 2.96×10^{-3} and 1.42×10^{-3} for the centre of Moreton Bay (approximately 15 m deep) and North Passage, respectively, are proposed by You (2005). Similarly, Lemckert et al. (2011) estimated the bed drag coefficient in Moreton Bay ranges from 6×10^{-4} to 2.2×10^{-3}. Hence, a reasonable range of bed drag coefficients from 5×10^{-4} to 2.5×10^{-3}, constantly distributed over the entire bay region, was utilised during model calibration. Sensitivity analysis identified a uniform bed drag coefficient of 2.15×10^{-3} generated the best agreement with the field measurement data (NRMSE 8.2 %).

With consideration that the SLDBMs were exposed to wind influences on the water surface, the weight factor of wind W_w which was applied in Eq. (5.2-11) and (5.2-12) was calibrated by varying W_w from 0.02 to 0.05 with increments of 0.001.

The wind direction during Trip 2 (21-Aug-13) changed from north-easterly to west-south-westerly after approximately six hours, and wind speed reached a peak of 8 m/s at the eighth hour. Generally, as the weight factor of wind increased, the drifter was further driven towards the west in the first six hours, then towards the east for the rest of the period. The wind weight factor of 0.034, as a function of wind-induced flow velocities, produced relatively comparable results, as shown in Figure 5.2-2 (a1) to (a4). The squared separation distance was up to 0.5×10^4 m^2 after 16-hour spreading. The NRMSE of drifter trajectories in longitudinal and lateral directions was 2.15% and 7.39%, respectively.

The model generally produced accurate results for water level, drifter trajectories, surface water temperature and salinity, and vertical temperature and salinity profiles. A comparison of measured water levels at the Brisbane Bar which were obtained from Maritime Safety Queensland, and simulated water levels at the corresponding position is displayed in Figure 5.2-2 (b). The comparison demonstrated that the simulated water level was slightly higher at high tide than the observed level, resulting in the RMSE (Root Mean Square Error) of 0.07 m. Moreover, the field measurements of drifter trajectories during the first trip were compared with the simulated paths of the four drifters. Figure 5.2-2 (c) illustrates the similarity in the trends of the simulated and measured drifter paths. The squared separation distance

approached 6×10^4 m^2 after 16-hour spreading. The NRMSE of drifter trajectories in longitudinal and lateral directions was 1.26% and 7.45%, respectively. A significant difference of approximately 1000 m between the simulated and observed trajectories was found at the turning points, as shown in Figure 5.2-2 (c). The difference may be attributed to the simplification of the complex bathymetry at the southern-most region of the southern section of Moreton Bay. A number of small islands and sandbanks exist in this region, which proved challenging to accurately simulate flows over such complex topography without high resolution topography data, which was not available at the time of the study. Therefore, end part of the southern bay was removed and the open southern boundary was set before those islands. As a result, the simulated tidal elevation and water flows were correspondingly affected, causing the difference of trajectories at the change of tide.

Figure 5.2-2 (d) indicates that the model results typically provided a good agreement with the measured datasets. The RMSE of the simulated surface water temperature and salinity during the first trip were 0.9^{o}C and 0.23 psu. Further, the vertical distributions of temperature and salinity at different locations were examined. Figure 5.2-2 (e) illustrates the water column during the first trip was completely mixed and the simulated results agreed well with the field observation data, with RMSEs of 0.8^{o}C and 0.21 psu.

5.3 Results and discussion

5.3.1 Observed drifter routines and dispersion

The SPOT2 GPS units returned accurate displacement datasets, recording each drifter position every 10 min throughout the field study. No high frequency related noise (unrealistic position fixing) was observed in the raw dataset. Accordingly, no data points were removed during quality assurance/quality control procedures. The quality of the raw data was assessed using multiple linear regressions by analysing combinations of drifter pairs and how they moved from each GPS position relative to one another. Each test returned a coefficient of determination (R^2) value greater than 0.99 and, consequently, no data filtering of the raw GPS data was carried out.

As shown in Figure 5.3-1 and Figure 5.3-2, dispersion behaviour was described using measured drifter trajectories during semidiurnal tidal cycles at the two deployment locations in Moreton Bay (IS and OP; see Figure 5.2-1(a)). The drifter trajectories are illustrated along with the cluster centroid's velocity and squared separation distance.

5.3.1.1 Between islands

The cluster of drifters was deployed south of Mud Island (IS) at low tide. As shown in Figure 5.3-1 (a) and (b), the drifters headed in a south-east direction at first, as they were deployed just before peak low tide. Then the drifters took the south route during the flood tide. The drifters changed direction and headed roughly north-northeast during the ebb tide. Figure 5.3-1 (c) illustrates that the along-shore speed (magnitude of *v* component) of the cluster centroid was much larger than that of the across-shore, ranging from 0 to 0.5 m/s. In this first trip of the study, the cluster of drifters travelled mainly alongshore, for approximately 5.2 and 6.5 km during flood and ebb tides, respectively, compared with 4.6 km in the across-shore direction.

Figure 5.3-1 (d) illustrates the time evolution of the cluster squared separation distance. The squared separation distance varied minimally and generally remained small, with a maximum area of 1000 m^2 during the first 12 hours, but significantly increased to 2000 m^2 after 16 hours. Although the squared separation distance remained small in the first 12 hours, two peaks occurred immediately after slack tide, between the 5th and 6th hour and between the 10th and 11th hour, respectively. During these two time periods of slack tide, the cluster of drifters experienced its largest speed of 0.5 m/s, as shown in Figure 5.3-1 (c), and the drifters rapid spread which produced the peaks of separation distance.
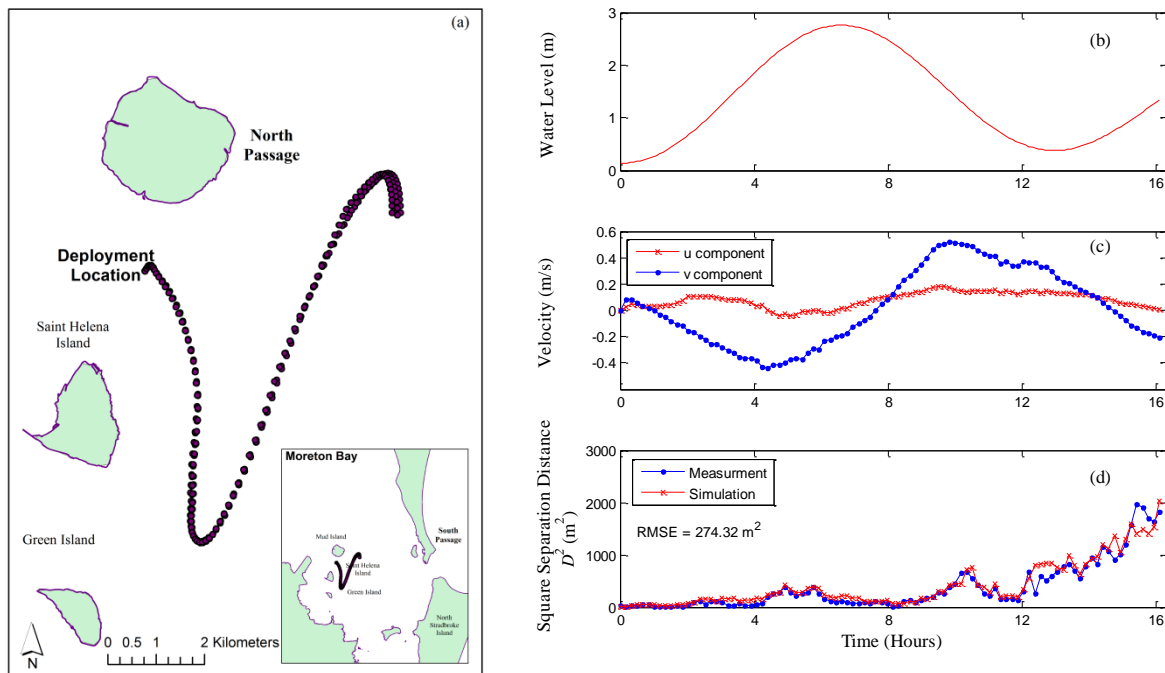
Figure 5.3-1 Trip 1: (a) Observed trajectories with (b) tidal condition, (c) centroid velocity of the cluster of drifters, and (d) squared separation distance during the period of 16 hours commencing 23-Jul-13.

5.3.1.2 Open water location

The drifters, which were deployed at an open water location, OP, just after low tide, headed southwest in an anti-clockwise direction within a 16-hours spreading period Figure 5.3-2 (a) and (b). The cluster centroid velocity exhibited variation trends very similar to those of the first trip, the alongshore velocity having semi-diurnal variations, while the across-shore velocity remained stable, as shown in Figure 5.3-2 (c). Generally, during the second trip the cluster of drifters also travelled predominantly alongshore, with distances of approximately 8 km and 6.3 km during flood and ebb tides, respectively, compared with 2.1 km for the across-shore direction.
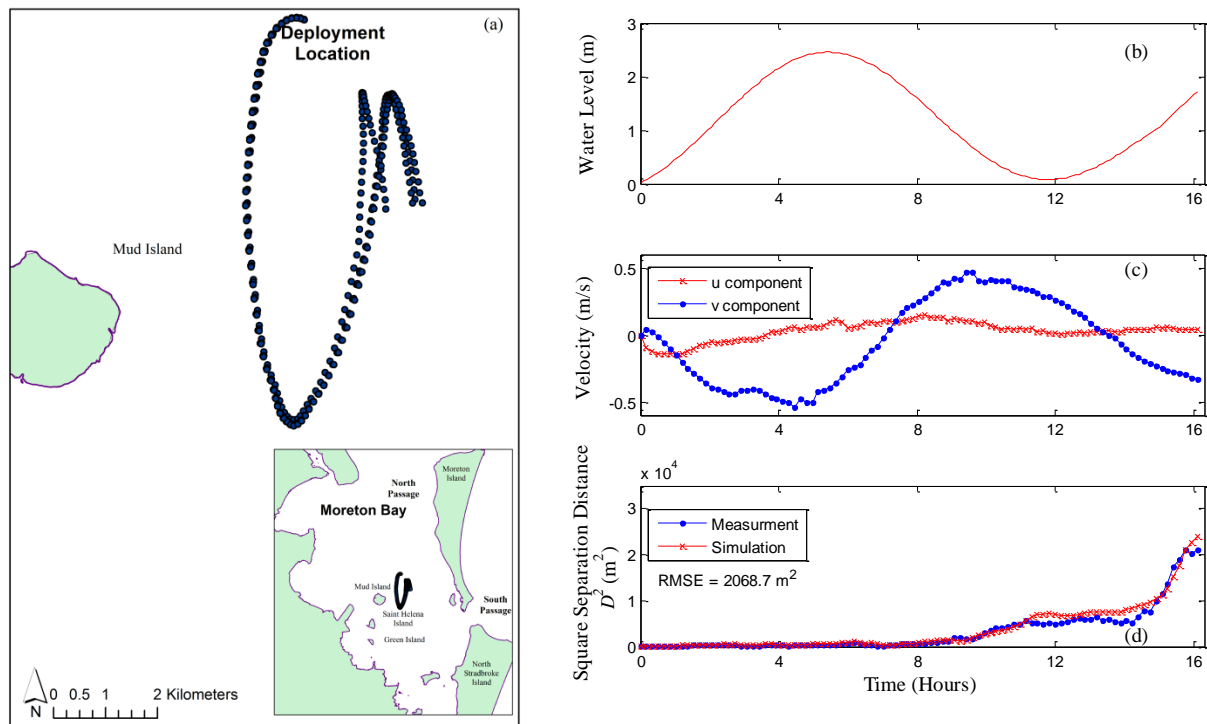
Figure 5.3-2 Trip 2: (a) Observed trajectories with (b) tidal condition, (c) centroid velocity of the cluster of drifters, and (d) squared separation distance during the period of 16 hours commencing 21-Aug-13.

In the earlier stages of the second trip, the drifters at the open location experienced little dispersion, which was similar to their performance during the first trip. The drifters began to spread out during the second tide slack, approximately at the 8th hour. Thereafter, the drifter dispersion consisted of three stages as shown in Figure 5.3-2 (d). After the second slack tide period, between the 8.5th and 11th hour, the squared separation distance of drifters rapidly increased from 1000 to 5000 m^2, with an average rate of 0.45 m^2/s. Following low tide,

between the 11th and the 15th hour, the increase of squared separation distance was relative slow, from 5000 to 1.1×10^4 m^2, with an average rate of 0.34 m^2/s. The separation distance however significantly increased after the third tide slack, with an average rate of 2.8 m^2/s.

5.3.1.3 Dispersion regime and apparent dispersion coefficient

The drifters, which were released both between the islands (IS) and at the open location (OP), generally showed similar behaviour characteristics. The drifters initially moved with the dominant current and remained together, but spread apart after the change in the tide. The squared separation distance correspondingly remained small at the beginning of cluster deployment, and then significantly increased after the 2nd tide slack. Two regimes are identified. Firstly, a slow dispersion regime was identified in the earlier stage followed by a rapid dispersion regime during the later deployment stage. The change of regime generally occurred during the succeeding ebb or flow tide, which may be attributable to residual eddies breaking down from the flow during reversal of the tidal currents.

Further interpretation of the visual data required the analysis of apparent dispersion coefficient, which was calculated using Eq. (5.2-1). The apparent dispersion coefficient, *K*, represents the rate of dispersion, indicating the changing rate of squared separation distance of the drifters. As shown in Figure 5.3-3 (a), the first two peaks of the apparent dispersion coefficient occurred during two periods of slack tides in the earlier stage, the $4^{th} - 6^{th}$ hour and the $10^{th} -12^{th}$ hour, approached approximately 0.2 and 0.4 m^2/s, respectively. The dispersion slowly increased with low values of coefficient after high tide, between the 6th and 10th hour. In the latter stage, the coefficient then significantly increased to 0.7 m^2/s with fluctuations. The variations in the apparent dispersion coefficient not only reveal the two dispersion regimes but also indicate that the relative rapid dispersion is expected to occur at slack tide. The similar behaviour of dispersion coefficient was also demonstrated during the second trip, as shown in Figure 5.3-3 (b). Although the peak coefficient was not shown during the 1st slack tide due to the relative larger range of dispersion coefficient in this trip, the peak of dispersion coefficient was examined immediately following the 2nd slack tide, around the 10th hour. In the latter stage, the apparent dispersion coefficient significantly increased and produced a largest coefficient of 6 m^2/s at the 3rd slack tide. Another distinctive feature is the dispersion slowly increased with small apparent dispersion coefficient during high tide, which was similar to the dispersion coefficient observed for the trip 1. Overall, the cluster of drifters experienced rapid dispersion following the slack tide after drifter deployment, but relative slow dispersion during high tide, and then significant rapid spread at

following slack tide again until reaching their largest values of apparent dispersion coefficient in the later stage.
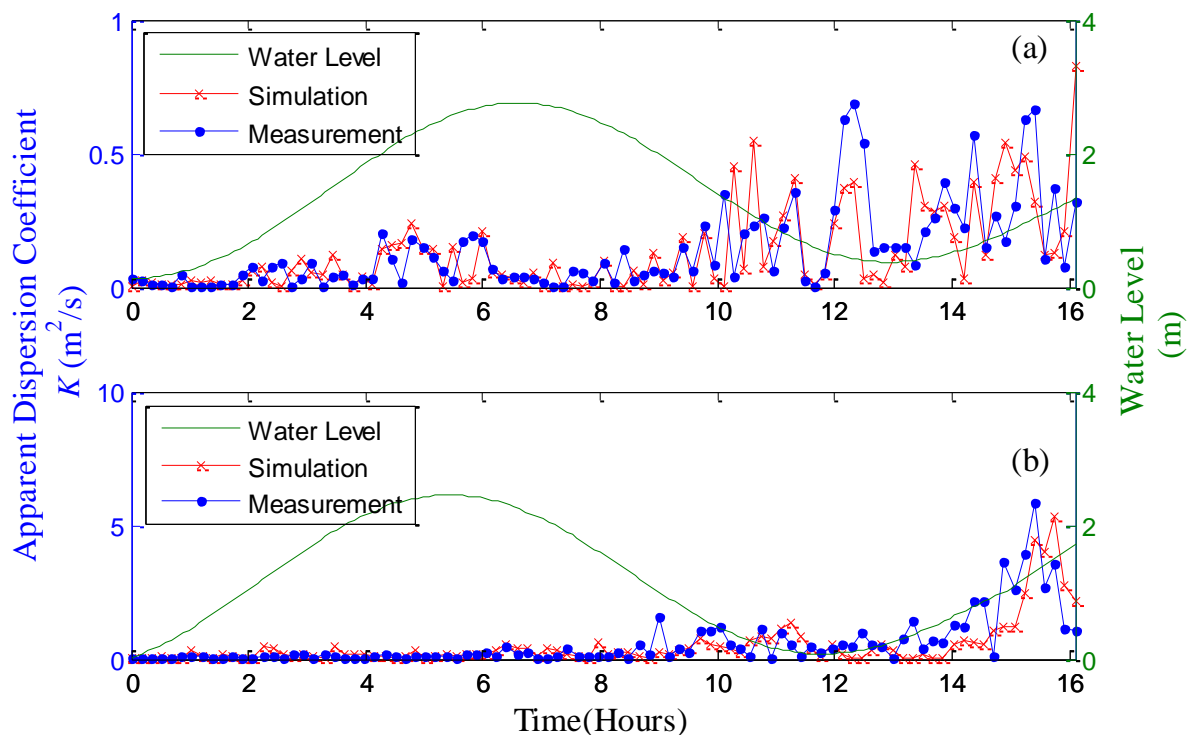
Figure 5.3-3 The calculated dispersion coefficients based on the measured and simulated results (a) between the islands (IS deployment location) and (b) within open waters (OP deployment location) in Moreton Bay.

The relationship between squared separation distances of the cluster and their variation rate which is the apparent dispersion coefficients are shown in Figure 5.3-3 (a) and (b) for the first and second trips, respectively. A power regression was derived from:

$$\ln(D^2) = a \times K^b \tag{5.3-1}$$

where a and b denote the regression coefficients. Given that the squared separation distance varied over a wide range during the two trips, the squared separation distance was therefore transformed by natural logarithm in the regression above. It can be seen in Figure 5.3-4 that the separation distance increased as the apparent dispersion coefficient increased, at a higher rate when the dispersion coefficient was small but at a more stable rate when the dispersion coefficient was large. During the 16-hour period, the squared separation distance (D^2) was up to 2.2 $\times$ 104 m^2, which was defined as a small separation distance in the previous studies (LaCasce and Bower, 2000, LaCasce and Ohlmann, 2003, Schroeder et al., 2011,

110

Mantovanelli et al., 2012). The curve therefore reveals a significant relationship between the squared separation distance and the apparent dispersion coefficients at a small separation distance, with the R^2 of approximately 0.7 in both trips.
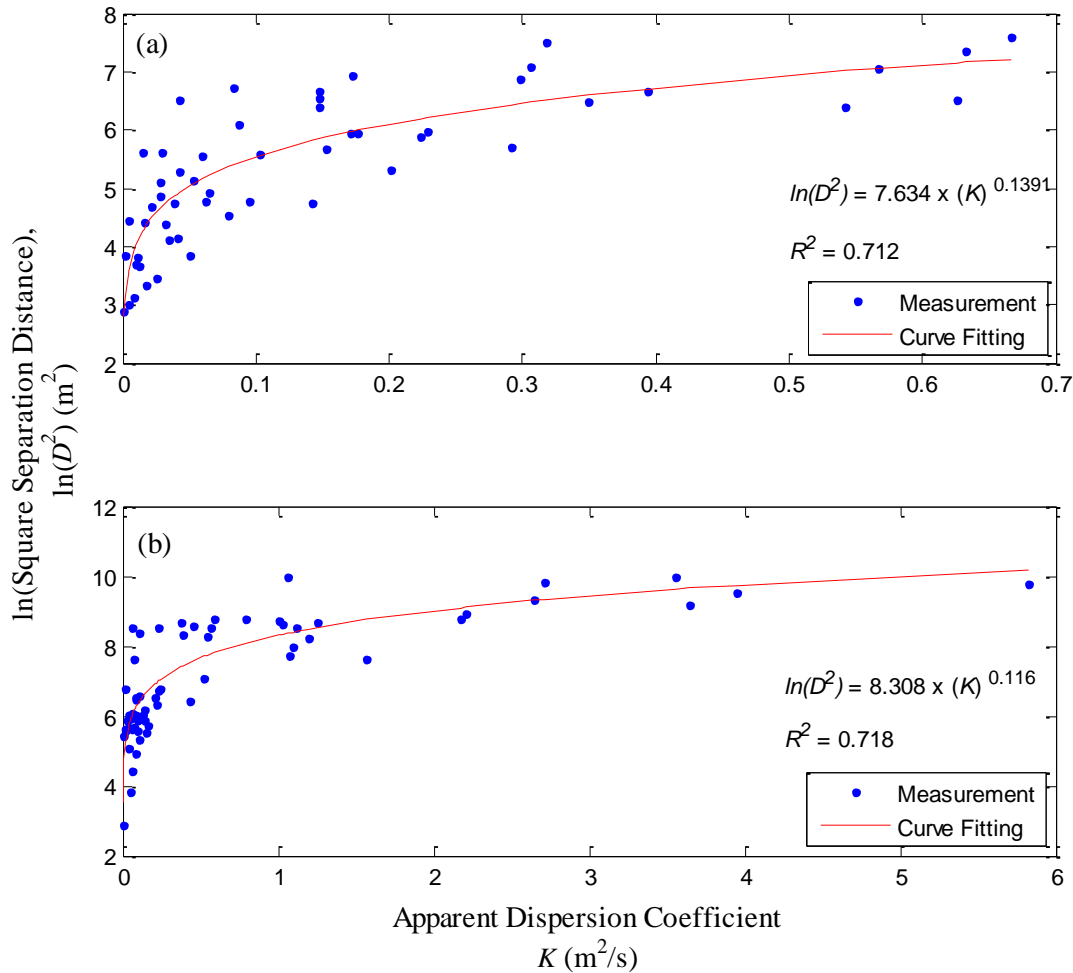
Figure 5.3-4 The squared separation distances, $D^2(t)$ and curve fitting for (a) the first trip and (b) the second trip.

5.3.2   Simulated horizontal dispersion in the bay

To examine horizontal dispersion behaviour at the different locations, all simulations were run for 12 hours (about one tidal cycle). It should be noted that the model had already been run for a one-month spin-up period before conducting this simulation, to allow the model to reach a dynamic steady state and to ensure that the model spin-up would not impact the final model results. During the simulation, artificial particles were released at low tide at select locations. If particles arrived at any solid boundary during the simulation, it would not be allowed to cross. The path would be projected onto the land border line and the particle would be reflected back into the domain (DHI Water and Environment, 2014b). During the

dry season from 2000 to 2011 , the Brisbane river discharge was as low, approximately 3.2 m^3/s (Yu et al., 2014b), with tidal currents representing the dominant hydrological driving force within the bay. During this corresponding period the wind condition was stable with wind speeds fluctuating at 5 to 6 m/s and generally blowing from a westerly direction.
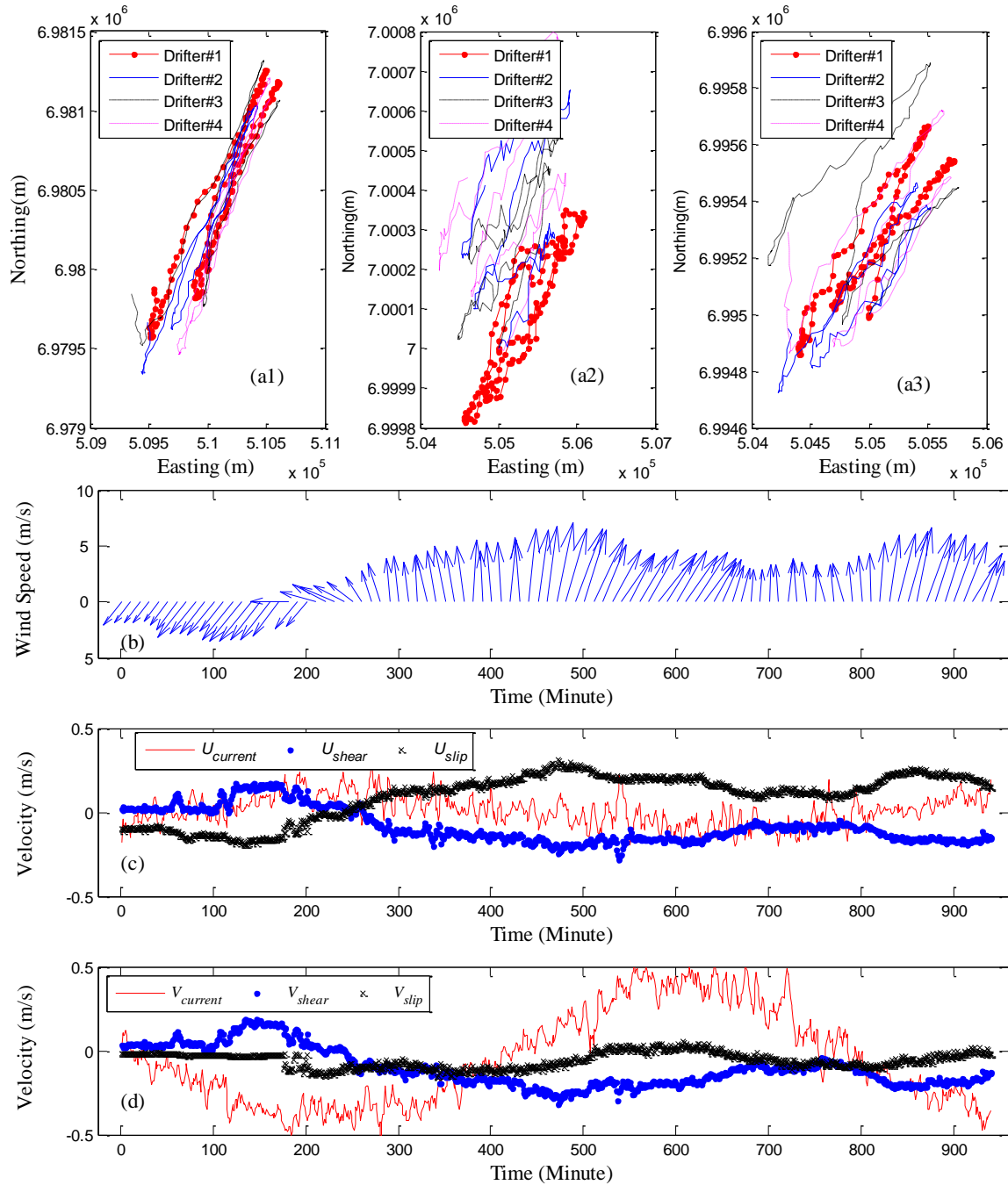
Figure 5.3-5 (a) Simulated trajectories of particles in the vicinity of the land boundary in Moreton Bay, (b) wind condition during Trip 2. The length and direction of arrows represent wind speed and direction, respectively, (c) $U_{current}$, is simulated velocity of the drifter without considering wind condition; U_{slip} calculated using Eq. (5.2-7); and $\underline{U_{shear}}$ calculated as the simulated velocity of the drifter, accounting for wind condition, minus $U_{current}$, minus U_{slip}, and (d) same definitions as (c) for V component.

112

Figure 5.3-5 (a) shows the simulated trajectories of particles at three positions nearby the northwest coastline in the vicinity of the river mouth where the water depth was approximately 6 m. The chaotic nature of the trajectories demonstrate the complexity of the Lagrangian geometric structure of the flow field (Niller and Paduan, 1995).

5.3.2.1 Wind effects on dispersion

To evaluate the wind effects on dispersion, the trajectories of the drifter spread in the open water (OP) area were simulated with and without consideration of the wind. As defined in Eq. (5.2-8), velocities of drifters under real wind conditions consist of three components: U_{slip}, U_{shear}, and $U_{current}$, which is velocity of the drifter under nil wind conditions, as shown in Figure 5.3-5 (b) to (d).

During the 16-hour experiment in open water, the wind blew predominantly from south to north, with an average speed of 5 m/s. As shown in Figure 5.3-5 (c), U_{slip} is the largest component compared with $U_{current}$ and U_{shear}, demonstrating that the wind slip effects significantly contributed to the drifter's cross-shore movement. However, Figure 5.3-5 (d) illustrates that alongshore movement was mainly driven by the tidal current with a velocity of up to 0.5 m/s, so wind effects were less significant.

5.3.2.2 Tidal residual current and excursion

The tidal residual circulation was estimated from one tidal cycle in Moreton Bay, as defined in Eq. (5.3-2). The current vectors presented in Figure 5.3-6 (a) illustrate that the tidal residual current in the vicinity of North Passage was significantly large, exceeding 0.5 m/s; demonstrating the large (majority share) of the oceanic exchange occurring at North Passage. In comparison, the residual current at South Passage was comparatively smaller— approximately 0.2 m/s, indicating that the water exchange was more restricted in this region. The tidal residual currents obtained from the simulation were within the same range, 0.17 to 0.61 m/s which was observed in Moreton Bay by Pattiaratchi and Harris (2003). Besides North Passage and South Passage, a large residual current was also found at r5-r8 and c5-c6 bounding transects in Figure 5.3-6 (a). Taking into account the water depth distribution, the appearance of a large residual current in this area could be attributed to the existence of a considerable depth gradient due to the steep slope of the seabed. Within the rest of the bay the residual current was very small. Furthermore, it was identified that some distinct eddies formed in the northern part of the bay, with an eddy diameter of about 1.5 km. Additionally,

relatively smaller eddies generated in the vicinity of Mud Island and the South Passage as well, with a diameter of approximately 0.5 km.

$$U_r = \frac{\int_0^T U_{current}(x,y,t)dt}{T} \text{ and } V_r = \frac{\int_0^T V_{current}(x,y,t)dt}{T}$$ (5.3-2)
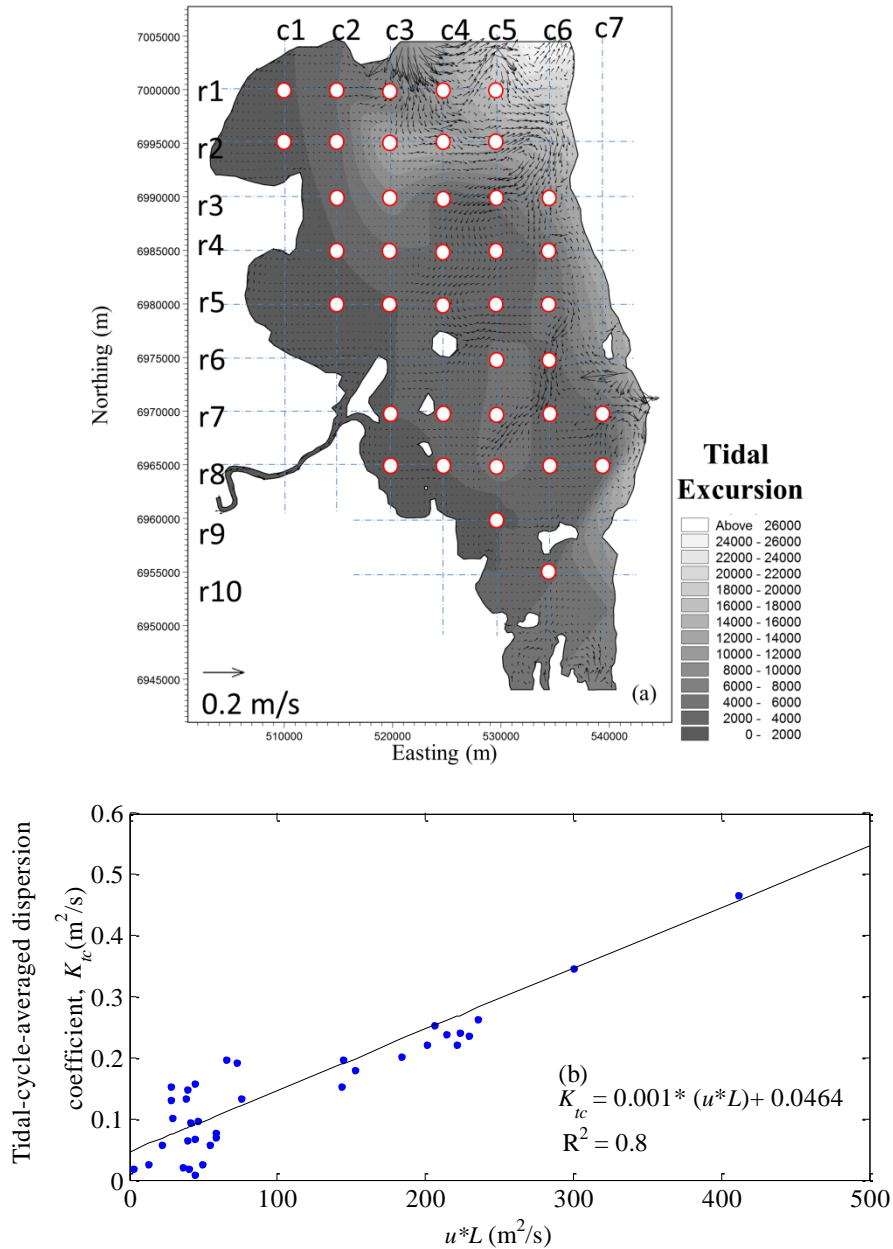
Figure 5.3-6 (a) Simulated depth-average tidal residual current vectors and tidal excursion contour for select locations within the bay, (b) plot of simulated tide-cycle-averaged dispersion coefficient (K_{tc}) vs prediction based on the product of the residual current (u^*) and tidal excursion (L).

Tidal excursion was calculated as the sum of displacement of particles within one tidal cycle. The gradient in tidal excursion in the entire bay was from the longest displacement in the northern region of the bay and along the eastern shoreline (about 20 km) to the shortest displacement in the west nearshore area (about 1.5 km). The largest tidal excursion occurred in the north of the bay, with a displacement of 26 km. As the tidal excursion gradually decreased from east to west, as shown in Figure 5.3-6 (b), the tidal excursions dropped to 1.5 km in the western region of the bay. The shortest tidal excursion refers to the greatest residence time which indicates a parcel of water in the western part of the bay would remain at a certain location for a relatively long period of time.

5.3.2.3 Apparent dispersion coefficient

The tide-cycle-averaged apparent dispersion coefficient, K_{tc}, was defined as the mean dispersion coefficient over a tidal cycle at select locations. Results are presented in Table 5.3-1. It should be noted that the artificial model particles released at r1c3, r1c4, and r1c5 (see Figure 5.3-6a) had moved out of the study area within one tidal cycle, and so dispersions at these locations were not taken into account. Table 2 indicates that the tide-cycle-averaged apparent dispersion coefficient was generally less than 0.5 m^2/s in the entire bay. The overall variation trends of coefficients were quite similar to the distribution of the tidal excursion, being smaller nearshore and gradually increasing from west to east, as indicated by the mean coefficient on each longitudinal transect. The coefficient in the eastern region of the bay was approximately two times greater than those in the western region of the bay. The largest coefficient occurred at transect c5 which was located in the center of the bay, with a value of 0.2 m^2/s. In addition to the transect c5, the same large coefficient was found at transect c7, which was close to the South Passage. Similarly, the dispersion in the vicinity of the North Passage would be comparably large, although it could not be estimated here due to the limited study area.

Table 5.3-1 Dispersion coefficient (m^2/s) at the selected bay locations

	c1	c2	c3	c4	c5	c6	c7
r1	0.02	0.06					
r2	0.01	0.06	0.24	0.35	0.47		
r3		0.13	0.07	0.20	0.20	0.22	
r4		0.02	0.02	0.15	0.20	0.24	
r5		0.09	0.07	0.10	0.25	0.13	
r6					0.19	0.18	
r7			0.10	0.15	0.24	0.22	0.26
r8			0.16	0.03	0.02	0.08	0.15
r9					0.06		
r10						0.13	
mean	0.015	0.072	0.110	0.163	0.204	0.171	0.205

In a tidal-dominated bay the influence of tide currents was proposed as a principal factor for particle dispersion at length scales of the tidal excursion (Geyer and Signell, 1992). Ridderinkhof and Zimmerman (1992) revealed that the dispersion coefficient may be equivalent to the product of eddy velocity and length scale with a constant factor. Therefore, in this study the tide-cycle-averaged dispersion (K_{tc}) was estimated using the product of the speed of residual currents (u^*) and tidal excursion (L), following Xu and Xue (2011). As shown in Figure 5.3-6 (b) that the linear curve fitting $K_{tc} = 10^{-3} \times (u^* \times L) + 0.0464$ produced a comparable outcome, with an R^2 of 0.8. The dispersion consequently increased as the product of the tidal excursion and residual current increased, although the underestimation/ overestimation of dispersion coefficient occurred at an early stage. In Figure 5.3-6 (b), the linear estimation of dispersion was more accurate when the product of tidal excursion and residual current was larger than 100 m^2/s. Overall, the dispersion coefficient can be estimated using tidal excursion and residual current in the tidal-dominated bay, which is $K_{tc} = c^* \times (u^* \times L) + d^*$, where coefficients c^* and d^* vary in different coastal regions.

5.4   Conclusions

Based on field measurements and numerical simulations, this study provides novel insights into the dispersion of particles within in a shallow coastal bay environment. Firstly, two dispersion regimes were identified, a slow dispersion in the earlier stage and a rapid dispersion in the latter stage. The change of regime generally occurred during the succeeding ebb tides, which may be attributable to residual eddies breaking down during reversal of tidal direction. Furthermore, it was identified that the relative slow spreading occurred during high tide with small apparent dispersion coefficients, in comparison to the rapid spreading immediately following slack tide with larger dispersion coefficient. In addition, a power function of the squared separation distance over the apparent dispersion coefficient produced an R^2 exceeding 0.7, indicating a significant relationship. The apparent dispersion was further quantified with the tidal residual current and tidal excursion length, based on simulated results. The apparent dispersion coefficient within one tidal cycle was found to be a linear function of the product of the tidal excursion and residual current which was mostly attributed to eddies during slack tide periods. By taking careful consideration of these dispersion characteristics, the apparent dispersion coefficient can be estimated in similar tidally-dominated coastal regions for future related research.

5.5   Acknowledgements

Chapter 6 Sediment transport in a tidal estuary following severe flood events

Statement of contribution to co-authored published paper

This chapter includes a co-authored peer- reviewed published paper.

The bibliographic details of article, including all authors, is:

> **Yu, Y.**, Zhang, H., Lemckert, C.J. Sediment transport in a tidal estuary following severe flood events (submitted to *Environmental Fluid Mechanics* in December 2016)

The article has been reformatted to meet the thesis style guidelines.

My contribution to these published papers involved: literature review, model set-up, calibration and validation of the model, simulations, data processing, figures and tables, analysis of results, writing and editing.

Yingying Yu

Prof Hong Zhang (principal supervisor and co-author)

Prof Charles Lemckert (principal supervisor and co-author)

Sediment transport in a tidal estuary following severe flood events

Abstract

Severe floods usually result in harmful sediment and pollutant dispersion in shallow coastal regions. This study therefore presents a three-dimensional hydrodynamic and transport model investigation into the sediment transport behaviour following severe flooding which occurred in the Brisbane River catchment in Australia. It was found that the flood-driven sediment plume formed in the adjacent bay and spread along the coastline in the northern bay. Based on the analysis of variations of sediment horizontal flux, four distinct characteristics of sediment transport were identified, responding to the combined effects of flooding runoff and tidal currents. Firstly, within the estuary, the sediment was driven by the flood discharge and primarily transported in the seaward direction. Secondly, at the river mouth, the transport pattern of sediment was similar to what it was in the first region, however, the horizontal flux was significantly smaller by 50%. Thirdly, a short distance from the river mouth, variations occurred not only in magnitude but also in transport pattern. The sediment horizontal flux was about one order of magnitude lower than it was in the estuary and the direction of sediment movement fluctuated with tides switching between landwards and seawards. Lastly, within the coastal bay, the sediment transport was mainly driven by tides, resulting in the changing direction of sediment movement. Its horizontal flux further decreased by one order of magnitude, compared to the flux in the third region. In addition, due to the large flood discharge, the amount of sediment loading generally increased over each individual tidal cycle. It was estimated that approximately 1.01×10^6 tonnes was discharged from the Brisbane River estuary into the bay during the flood event in January 2011.

Keywords: Sediment plume, numerical modelling, the Brisbane River estuary, Moreton Bay, Queensland floods 2010-2011.

6.1 **Introduction**

Estuaries deliver water and pollutants from surrounding urban activities into their adjacent coastal regions causing ecosystem degradation. Severe storm runoff associated with contamination has therefore been recognised as one of the major sources of coastal pollution in the short term. Due to climate change worldwide, it is expected that extreme flooding events would increase both in occurrence and severity (Babister and Retallick, 2011). A flood-driven sediment plume would carry a large volume of sediment which may contain a variety of pollutants and spread them through coastal areas, causing further deterioration of the coastal system.

A number of studies have been conducted to investigate flood-driven sediment plumes in recent years (Geyer et al., 2000, Shi and Wang, 2009, Yu et al., 2013b). Yu et al. (2013b) revealed that the amount of runoff was the principle factor leading to sediment plume generation and development, and that wind played another important role in plume movement. Geyer et al. (2000) investigated the variation of the sediment plume from the Eel River, United States, during the floods of 1997 and 1998. The peak discharge persisted for three days, ranging from 4000 to 12000 m^3/s, and was accompanied by strong winds from the southern quadrant. The sediment plume travelled 7 km offshore with northward velocities of 0.5-1 m/s. An investigation after the Mississippi River experienced its highest runoff with a discharge of 30674 m^3/s, reported that the size of the plume area reached up to 5984 m^2, which was twice as large as the six-year mean value. As the sediment plume spread into coastal regions, the mean concentration of the suspended matter increased from the six-year mean value of 20 mg/l to more than 30 mg/l, predicting a long-term harmful impact on the coastal ecosystem (Shi and Wang, 2009).

Various visible and near infrared bands were proposed as water turbidity level indicators to observer the plume in previous studies (Yates et al., 1993, Tang et al., 2003, Wang and Lu, 2010). For instance, Shi and Wang (2009) used the satellite images to observe the flood-driven Mississippi River sediment plume development. Wang et al. (2009) retrieved water reflectance at Band 4 (with a wavelength range of 770 to 860 nm) from The Enhanced Thematic Mapper Plus (ETM+) images to estimate the suspended sediment concentration in the large, turbid Yangtze River. A similar investigation was conducted by Wang and Lu (2010), which retrieved water reflectance at Band 2 (with wavelength range of 841 to 876 nm) from the Moderate Resolution Imaging Spectroadiometer (MODIS) aboard NASA'S Terra

satellite to estimate the suspended sediment concentration in the Lower Yangtze River. It can be seen in previous studies (Wang et al., 2009, Wang and Lu, 2010) that the band selection for turbidity estimation generally depends on the wavelengths of bands and other geographically correlated factors, such as the particle properties.

Cheng et al. (2013) identified three stages of development of a flood-driven plume. Flood river runoff dominated the first stage, estuarine circulation drove the plume at the second stage, and then sediment settling was predominant in the third stage. Cheng et al. (2013) also found that most of the floodwater was trapped in the estuarine turbidity maximum (ETM) area, and a small amount of very fine sediment was transported seaward into the mid-bay, due to the tidal asymmetries.

In Australia, the input of marine sediment from Moreton Bay (about 456000 tonnes) was the major source of suspended sediment that ran into the Brisbane River estuary during an average flow year (Eyre et al., 1998). However in January 2011, the State of Queensland experienced the largest flood event since 1974. As a result, the channel banks of the Brisbane River were severely eroded and an estimated 1040000 tonnes of sediment was subsequently delivered into Moreton Bay (Department of Environment and Resource Management, 2011). Yu et al. (2013b) estimated that the sediment plume travelled in a northward direction and formed a 500 km^2 plume region in the bay following the event. Several studies have been carried out on the issue of the Brisbane River flood-driven sediment plume. Dennison (2011) identified the location of the sediment plume using remote satellite images. Yu et al. (2013b) reported that the sediment plume flowed along-shore for a distance of about 30 km and cross-shore for a maximum width of 14 km. It was also found that the plume typically reached the sea bottom in the shallow bay area. The behaviour characteristics of sediment transport, such as sediment plume evolution and sediment deposition and erosion following the severe flood event, is still unknown, even if the sediment plume was identified in the previous mentioned studies. Therefore, the sediment transport during this extreme flood event was investigated in the present study by using a three dimensional numerical model, focusing on the investigation of sediment plume evolution and sediment transport behaviour in a shallow coastal region during peak flood discharges.

6.2   **Methodology**

6.2.1   **Study area**

The semi-closed Moreton Bay is located in sub-tropical Southeast Queensland, Australia. The bay extends from 153.1^o E to 153.3^o E and from 27.05^o S to 27.5^o S, and covers an area of 1523 km^2, with a water depth ranging from 2 to 27 m, as shown in Figure 6.2-1 a and b (Dennison and Abal, 1999). The Brisbane River, which passes through the city of Brisbane, empties into the west of the bay with a mean annual flow runoff of 1.65×10^8 m^3, and contributes approximately 1.78×10^5 tonnes of sediment during an average flow year (Eyre et al., 1998, Queensland Department of Natural Resources Mines and Water, 2006). The ETM zone usually occurs in the upstream reach of the Brisbane River estuary, ranging from 100 to 160 NTU, during the wet season under non-significant flood conditions (Yu et al., 2013c).
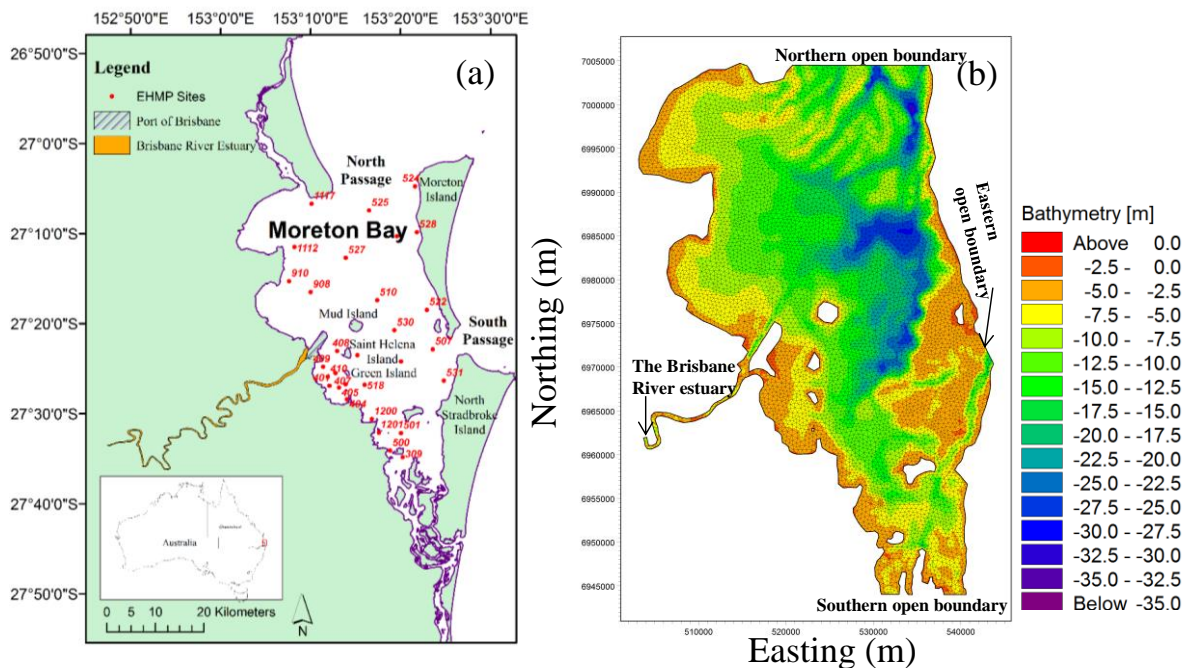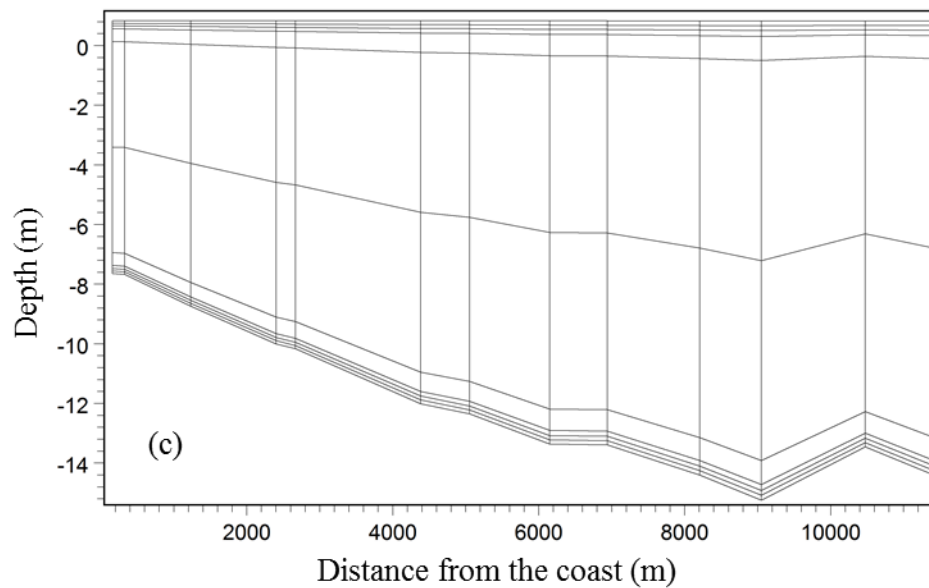
Figure 6.2-1 (a) Map of study site (source: Geoscience Australia). All observation sites of EHMP are indicated using red points. (b)The modelled mesh structures of Moreton Bay. Different colours represent different water depths (source: Marine Safety Queensland, Australia). (c) The vertical distribution of water column in this study.

The eastern Australian coast experienced an extremely wet period from late November 2010 to January 2011. The highest peak rainfall took place from 10 to 12 January and the majority of the Brisbane River catchment received in excess of 286 mm of precipitation in three days (National Climate Centre Bureau of Meteorology, 2011). Following this heavy rainfall, the most devastating floods occurred during the second week of January 2011, with an estimated peak discharge of over 11500 m^3/s at the Savages Crossing of the Brisbane River (Babister and Retallick, 2011). As enormous volumes of flood water flowed down the river, the turbidity distribution significantly changed to a gradually increasing pattern from upstream to downstream (approaching approximately 2000 NTU) within the estuary (Yu et al., 2015). A large sediment plume was observed as the flood water passed through the river mouth and settled in the bay. Both the river and bay displayed elevated turbidity levels.

6.2.2 Field measurement and satellite MODIS images

The Ecosystem Health Monitoring Program (EHMP) Queensland conducted water sampling to monitor the water salinity, temperature and turbidity in the river and bay before and after the flood event. Currently, there are 16 monitoring sites along the estuary from the river mouth up to the tidal limit, and 30 monitoring sites throughout the bay which are marked in Figure 6.2-1a. In addition to the field measurement data, satellite MODIS images, which are

124

taken on a daily basis with a spatial resolution of 250 m, were applied to identify the plume in the bay. After excluding cloudy day images, Figure 6.2-2 exhibits the visible sediment plume in Moreton Bay on certain days of the flood event. A small sediment plume was observed in the vicinity of the river mouth on 22 December 2010 (Figure 6.2-2a), which spread into the northern bay. It then produced a more visible sediment plume on 30 December (Figure 6.2-2b). In consequence of the high flood discharge in early January 2011, a larger plume, which developed in the northern bay (Figure 6.2-2c-e), flowed into the adjacent ocean at the North Passage. As the flow runoff decreased, the plume gradually diluted. It can be seen in Figure 6.2-2f that the sediment plume was no longer visible on 1 February.
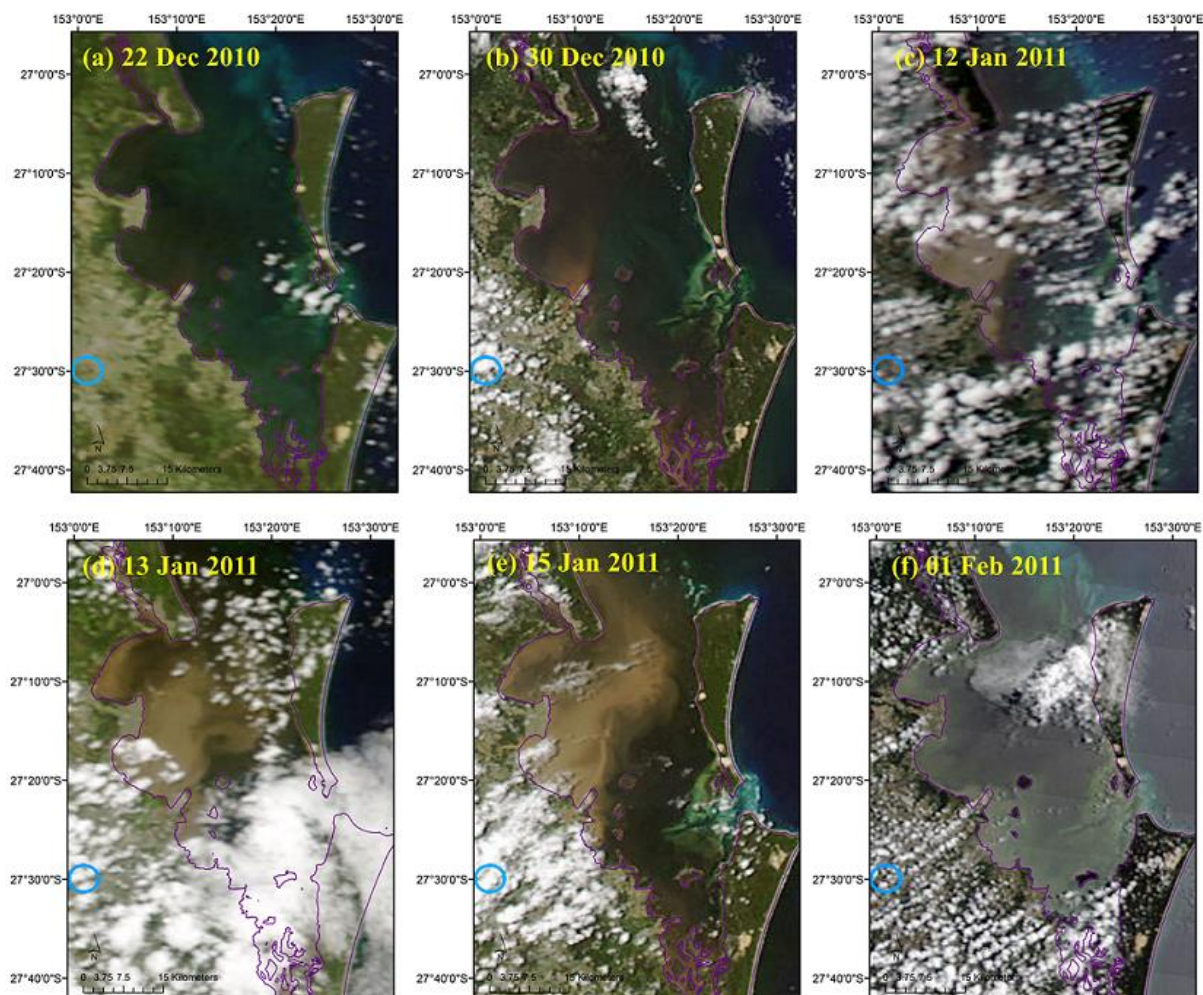
Figure 6.2-2 Satellite MODIS images of the Brisbane River and Moreton Bay on the different dates: (a) 22 Dec 2010, (b) 30 Dec 2010, (c) 12 Jan 2011, (d) 13 Jan 2011, (e) 15 Jan 2011, and (f) 1 Feb 2011. The blue circle indicates the position of the Brisbane City. The purple line represents the coastal line of Moreton Bay. The water looked brown as the flood-driven sediment plume developed and moved within the bay during this flood event.

6.2.3 Sediment rating curve and estimation

The Department of Environment and Resource Management (DERM) Queensland regularly records the volume of water (Q) and turbidity levels (T_{ur}) at their stream monitoring sites in the Brisbane River catchment. Due to the scarcity of data on suspended sediment concentrations (SSC) during the flood event, sediment concentration of the river runoff was estimated.

The available measurements of the daily river discharge and estimation of the daily SSC from 2001 to 2014 were applied to develop a sediment rating curve following Eq (6.2-1), in which a_2 is the rating coefficient and b_2 is the rating exponent. It was found that the best rating curve was obtained with a R^2 of 0.73, based on the factor a_2 of 14.87 and b_2 exponent of 0.36 which was close to the value of 0.4 suggested by Ciesiolka et al. (1995). The sediment rating curve was therefore applied to estimate the suspended sediment concentration of the river estuary during the January 2011 flood event.

$$C = a_2 \times Q^{b_2} \tag{6.2-1}$$

$$C = \max\left(0, \frac{T_{ur}\text{-}9.85}{1.25}\right) \tag{6.2-2}$$

The water turbidity, T_{ur}, at certain locations (as marked in Figure 6.2-1a) was monthly measured and recorded in NTU by the EHMP. The simplified correlation in Eq. (6.2-2) was applied to estimate the SSC, C, which was proposed by Hossain et al. (2004) to describe the relationship between sediment concentration (mg/L) and water turbidity levels (NTU) in the Brisbane River estuary.

6.2.4 Model set-up and results validation

To conduct an investigation into sediment transport in Moreton Bay during the January 2011 flood event, MIKE3 DHI, a three dimensional hydrodynamic model coupled with a mud transport module was used. This model was calibrated in our previous studies (Yu et al., 2013b, Yu et al., 2014a).

The domain of Moreton Bay is presented as a network of three - dimensional elements. In the horizontal domain, the model geometry consists of a mesh with 13,918 elements, with spatial resolutions ranging from 250 to 1,000 m, as shown in Figure 6.2-1b. In the vertical domain,

the variable sigma co-ordinates formulated by Song and Haidvogel (1994) were applied, with 10 vertical layers in each water column. This permitted the resolutions at the surface, mid-depth and bottom to be about 0.5, 1-2 and 0.5 m, respectively. To guarantee the stability of the numerical simulation, the time step was determined to be 30 seconds to ensure that the Courant Friedrichs and Lewy (*CFL*) number was less than 1 (DHI Water and Environment, 2014b).

The tidal elevations at 10 minute intervals predicted by MIKE DHI served as open boundary condition at the northern, eastern and southern sides. The sea surface temperature and salinity data recorded at the EHMP sites were applied as the initial conditions in the simulation. Daily wind data collected at the site (153.13^{o} E, 27.39^{o} S) by the Australian Bureau of Meteorology was used as model input, and was constant throughout the entire study area.

Brown et al. (2011) collected water samples in the BRE on 13 and 14 January and found that the median particle size d_{50} was about 25 μm. The mud transport module was therefore included in the simulation. The dispersion parameter setting in this module was the same as the setting used by Yu et al. (2015). The critical shear stresses of deposition and erosion were set as 0.03 N/m^{2} and 0.05 N/m^{2} respectively (Margvelashvili et al., 2003, Bell, 2010, Yu et al., 2014b).
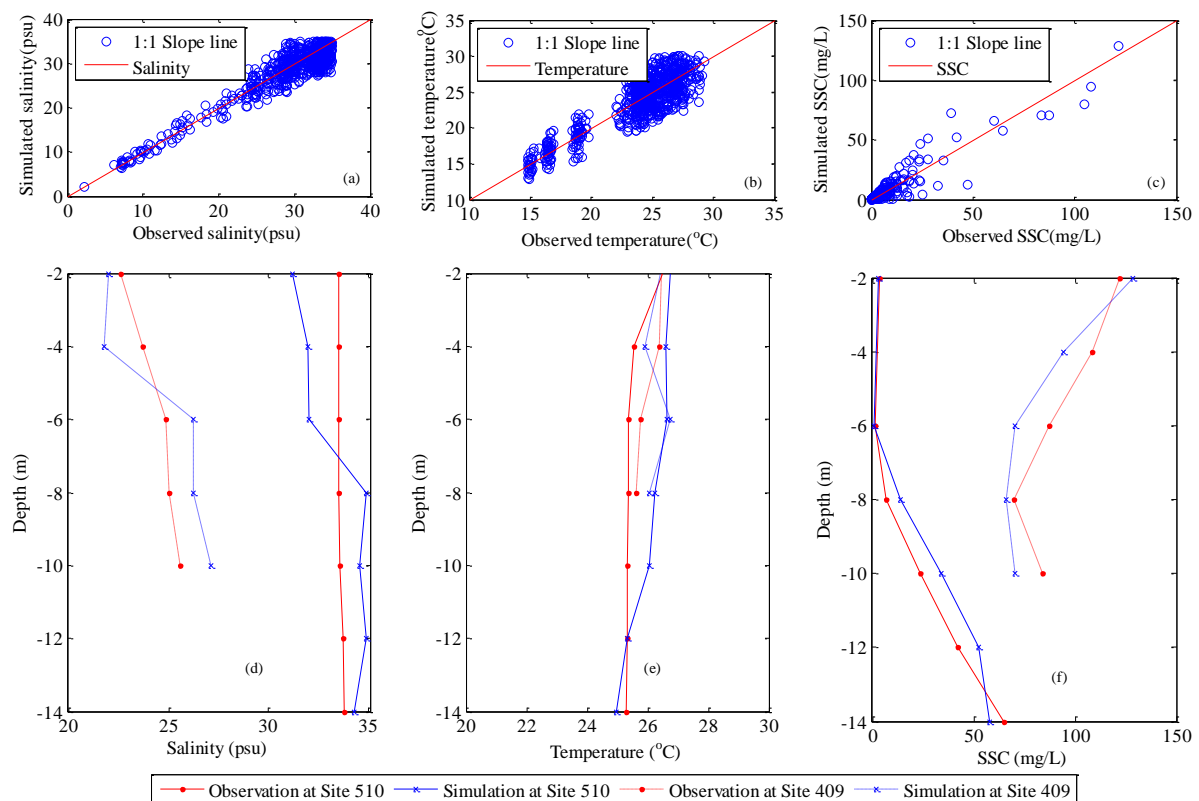
Figure 6.2-3 Validation of the simulated results. The comparison of the simulated and

observed (a) salinity, (b) temperature and (c) SSC at different sites in Moreton Bay during the period from December 2010 to January 2011. The comparison of the vertical profiles of simulated and observed (d) salinity, (e) temperature and (f) SSC at Site 409 (close to the coast) and Site 510 (at open water), respectively.

The simulation ran from November 2010 to February 2011, based on the model configuration described above. The simulated results were validated in terms of temperature, salinity and suspended sediment concentration. The efficiency of the simulation is shown in Figure 6.2-3, and the statistical error is estimated in Table 6.2-1. These parameters, mean absolute error (MAE) and scatter index (SI), are defined in the following Eq. (6.2-3) - (6.2-5), where η_{obs} and η_{sim} represent the observation and simulation data, respectively, and n is the number of data record.

$$\text{MAE} = \frac{\sum |\eta_{obs} - \eta_{sim}|}{n} \qquad (6.2\text{-}3)$$

$$\text{SI} = \sqrt{\frac{\sum (\eta_{obs} - \eta_{sim})^2 / n}{\bar{\eta}_{obs}}} \qquad (6.2\text{-}4)$$

$$\bar{\eta}_{obs} = \frac{\sum \eta_{obs}}{n} \qquad (6.2\text{-}5)$$

Table 6.2-1 Mean absolute error (MAE) and scatter index (SI) of the simulated salinity, temperature and SSC.

	MAE	SI
Salinity	1.77 psu	0.32
Temperature	1.54 $^{\circ}$C	0.28
SSC	2.48 mg/L	0.48

Site 510 is at open water and Site 409 is close to the coast as shown in Figure 6.2-1a. The measured data of salinity, temperature and SSC were applied to validate the model. As can be seen in Figure 6.2-3a and Table 6.2-1, the model well simulated the salinity in near-field where the salinity was lower than 20 psu, but under - predicted in far-field where the salinity was higher than 30 psu. The deviation of salinity in far-field is mainly due to the lack of salinity data at open boundaries, however comparable simulated salinity results in near-field indicates the model reproduced the river flood-driven plume spreading in the vicinity of the

river mouth. The scatter diagram (Figure 6.2-3b) depicts the temperature comparison between observation and simulation during one-month period, with a scatter index of 0.28. The deviation was similar at different temperature levels. Figure 6.2-3c shows the sediment concentration comparison, with a relatively larger scatter index of 0.48. This might be attributed to having to estimate the relationship between the sediment concentration and water turbidity, as well as the sediment rating curve based on the river discharge. In addition, the vertical profiles of salinity, temperature, and SSC are shown in Figure 6.2-3d-f, respectively. The simulated vertical profiles generally matched the observed profiles, both at Site 510 (at open water) and Site 409 (close to the coast). Overall, the numerical model used in the study gave fairly reasonable predictions regarding the salinity, temperature, and SSC in horizontal and vertical distributions.

6.3   Results and discussion

6.3.1   The evolution of the flood-driven sediment plume

6.3.1.1 The horizontal evolution of the plume

The flood-driven sediment plume discharging from the Brisbane River estuary was investigated. Figure 6.3-1 shows the horizontal evolution of the sediment plume before, during and after the flood peak discharge in January 2011.

As shown in Figure 6.3-1a to b, the sediment plume was first formed in the vicinity of the river mouth after the high rainfall occurred in the Brisbane River catchment from November 2010. The sediment plume mainly spread towards the east and along the northern coast, due to the combined effects of the Coriolis force and large river runoff, with the SSC ranging from the 0.08 to 0.32 kg/m^3. The high SSC was observed around the Brisbane Bar at the river mouth, as shown in Figure 6.3-1c. As the Brisbane River estuary remained at a low level of SSC during this period, the high level of SSC was attributed to the sediment resuspension in the vertical direction, which would be discussed later.

The sediment plume significantly spread in the bay during the flood peak discharge, as shown in Figure 6.3-1d to f. Following the large flood runoff, the plume water not only continuously travelled in the northern bay and passed through the North Passage but also extended eastward (in the seaward direction) forming a visible bulge plume at the entrance of the bay, and covering an area of approximately 360 km^2 (Figure 6.3-1d). The higher level of SSC

occurred at the river mouth (Figure 6.3-1e), and was similar to the distribution of SSC in Figure 6.3-1c. The largest discharge occurred in the Brisbane River catchment on 12 January 2011, producing a high concentration of flood runoff entering the bay. As a result, the level of SSC was up to 1.12 kg/m^3 in the estuary and in the plume bulge at the river mouth. The sediment plume was growing and further dispersed within the bay as shown in Figure 6.3-1f.

After the flood peak discharge, the sediment plume started to be settled and be diluted. On the one hand, the SSC of river runoff decreased significantly, and therefore the sediment plume in the vicinity of the river mouth was diluted by the river runoff with the lower level of SSC; on the other hand, the clear oceanic water entering from the North Passage and East Passage mixed with the plume water. Therefore, it can be seen in Figure 6.3-1 that the region of plume bulge with higher SSC became smaller (Figure 6.3-1 g), and the concentration dropped further (Figure 6.3-1 h). The level of SSC and the size of the plume also decreased as shown in Figure 6.3-1 i and j. Overall, the simulated horizontal evolution of the sediment- plume is consistent with the finding of salinity dispersion in Yu et al. (2013b) and Yu et al. (2016).

In addition, the outermost boundary of the simulated plume was outlined that overlapped with the satellite image in Figure 6.3-1 k, to show the comparison of the plume between the simulation and remote observation. The major part of the simulated sediment plume was the same as observed by Satellite. The minor difference was that a small section of the sediment plume was pushed further to North Passage rather than spread in the central bay as indicated by the simulation result. Taking account of the dependence of the plume movement on the tidal current in the central bay, the discrepancy was probably attributed to the use of the predicted data of tidal elevation at open boundaries, due to a lack of field measurement record.
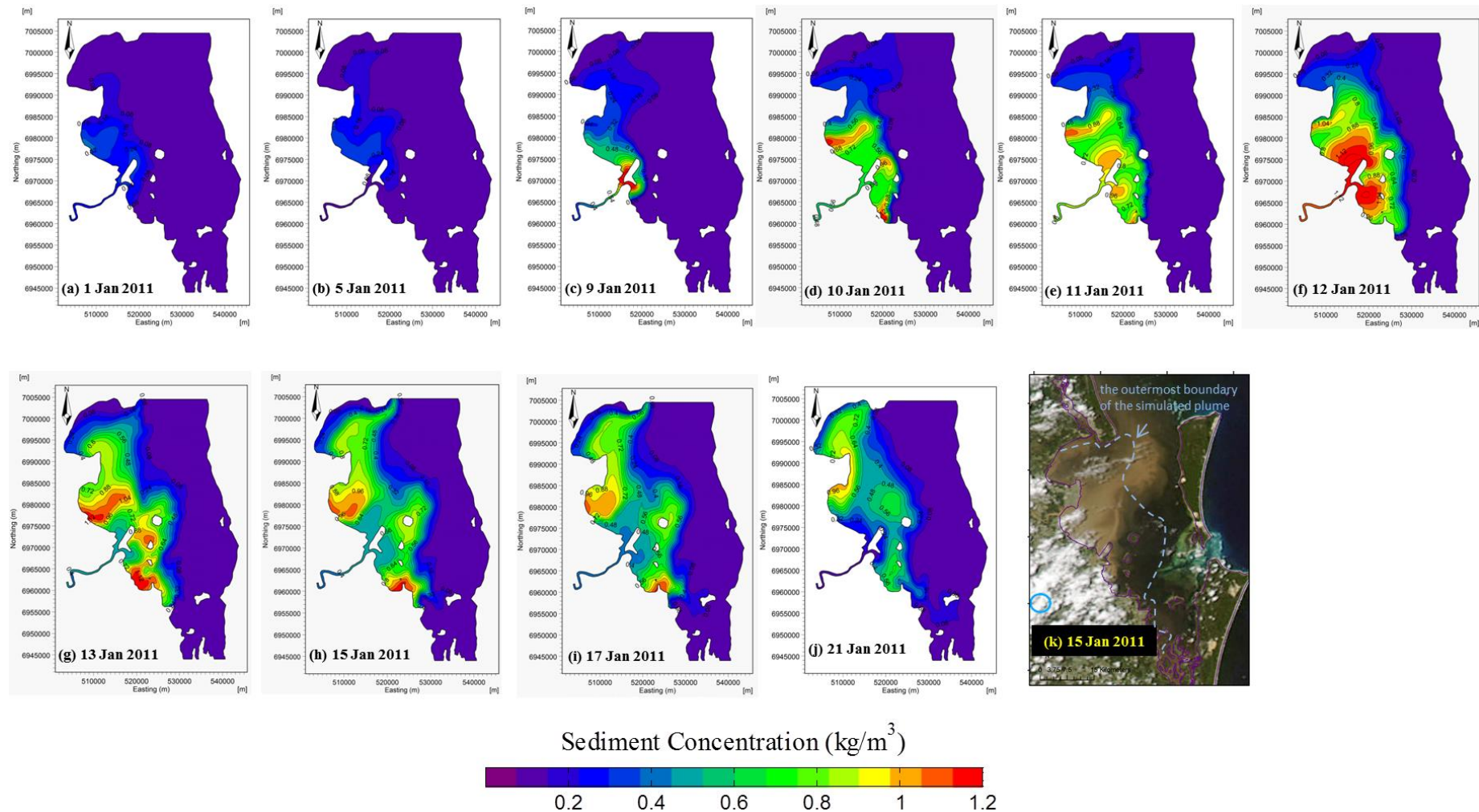
Figure 6.3-1 The simulated horizontal evolution of flood-driven sediment plume during the severe flood event in Moreton Bay, including the sediment plume (a)-(c) before, (d)-(g) during, and (h)-(j) after the flood peak discharge. (k) Satellite MODIS images of the Brisbane River. The outermost boundary of the simulated sediment plume is marked. The colour contours represent the SSC (kg/m^3).

6.3.1.2 The vertical evolution of the plume

The sediment resuspension usually took place in the vicinity of the river mouth during the plume development, resulting in higher concentration distribution. To illustrate the sediment resuspension process, Figure 6.3-2 exhibits the vertical distributions of the sediment plume (from Figure 6.3-2 a to c), the vector of flow velocity (from Figure 6.3-2 d to f) on 9 January. In the vertical direction, the variable sigma co-ordinates formulated by Song and Haidvogel (1994) were applied to ensure a high resolution at both the surface and the bottom layer. The whole water column was divided into 10 layers, as shown in Figure 6.2-1 c. Therefore, the Layer 1, 5, and 10 represent near-bottom, intermediate, and water surface, respectively. In addition, seven points along the river estuary were selected and the vertical transections were taken.

As shown in Figure 6.3-2a, the high concentration (in red) occurred only in the near-bottom layer (Layer 1) within the middle Brisbane River estuary. Because the sediment concentration in the bottom layer remained at a relatively low level at the estuarine entrance, the high concentration of the sediment was considered to be the result of erosion from the active bed layer in areas where the bed shear stress was larger than the critical stress. It was observed that the bed erosion first occurred at three places, as circled in Figure 6.3-2d. The appearance of high concentration here resulted from the occurrence of river bed erosion and sediment resuspension which was essentially due to the large shear stress and turbulence. Figure 6.3-2b shows that after 45 minutes of resuspension from the bottom layer, the concentration in the intermediate layer (Layer 5) increased to approximately 1.2 kg/m^3. The particles in the bottom layer were not only lifted, but also pushed outward by the river runoff, as shown in Figure 6.3-2e. The water column was then well mixed after another 45 minutes, as depicted in Figure 6.3-2c and f, and the concentration in the surface layer (Layer 10) was around 1.2 kg/m^3. Before the incidence of flood peak discharge, the anticipated dominant process of sediment transport was that the particles would be lifted from the near-bottom layer due to the large shear stress and turbulence, and then the whole water column would be well mixed in a short time.
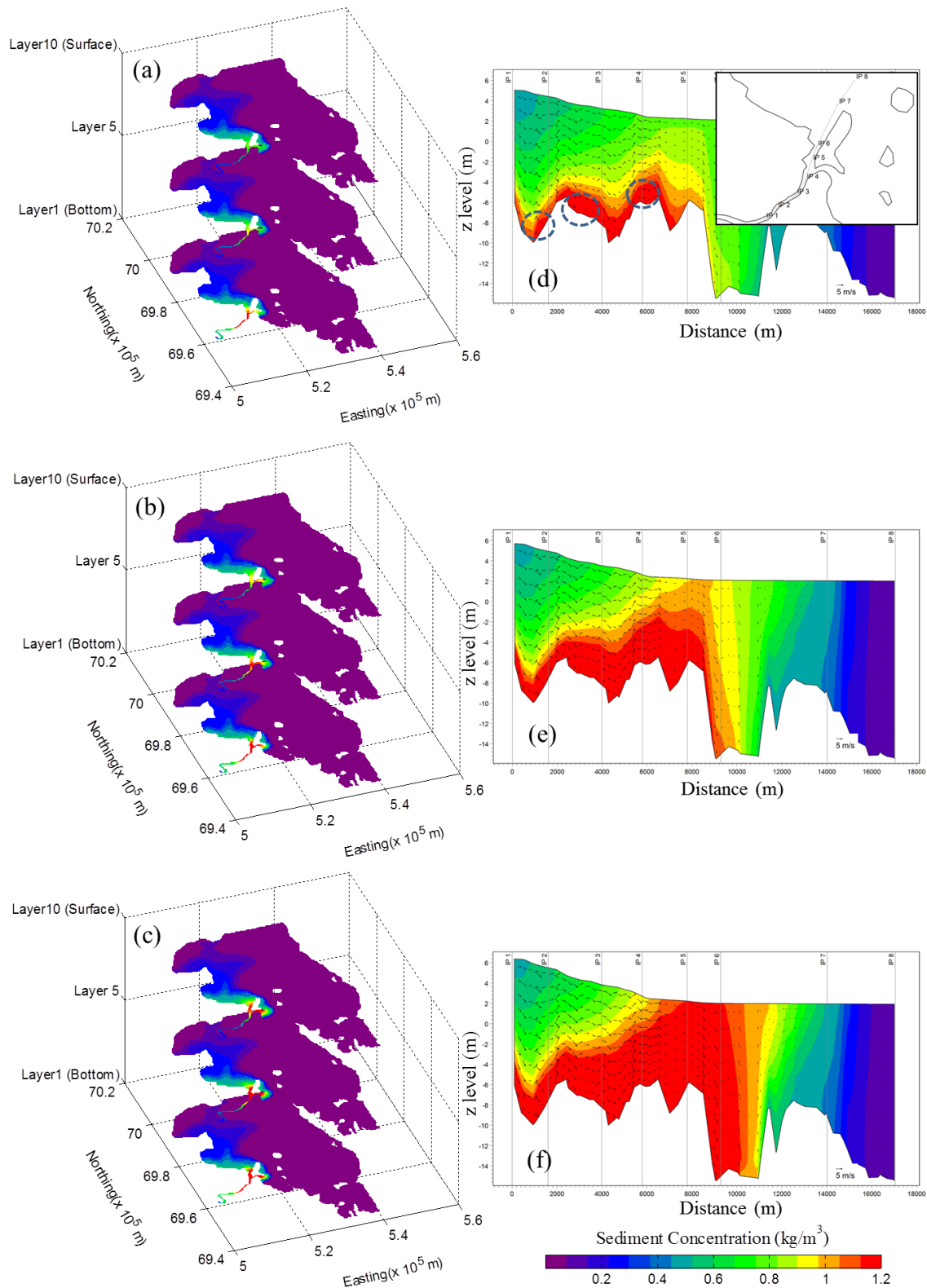
Figure 6.3-2 The simulated vertical evolution of flood-driven sediment plume on 9 January. The distribution of sediment concentration on Layer 1 (bottom), Layer 5 (intermediate), and Layer 10 (Surface) are at 45-minute interval in (a) to (c), respectively. The corresponding vertical transections represent the contour of sediment concentration and the vector of flow velocity as shown in (d) to (f).

During the flood peak discharge, the large amount of sediment was easily transported downstream, and sediment resuspension was no longer the dominant process in the water column. Figure 6.3-3a shows that the water had been well mixed in the shallow upstream estuary (IP1-IP5) on 12 January, and the high concentration runoff was pushed to the river mouth (IP5-IP7). The flood water was discharged into the bay at a high rate, while another
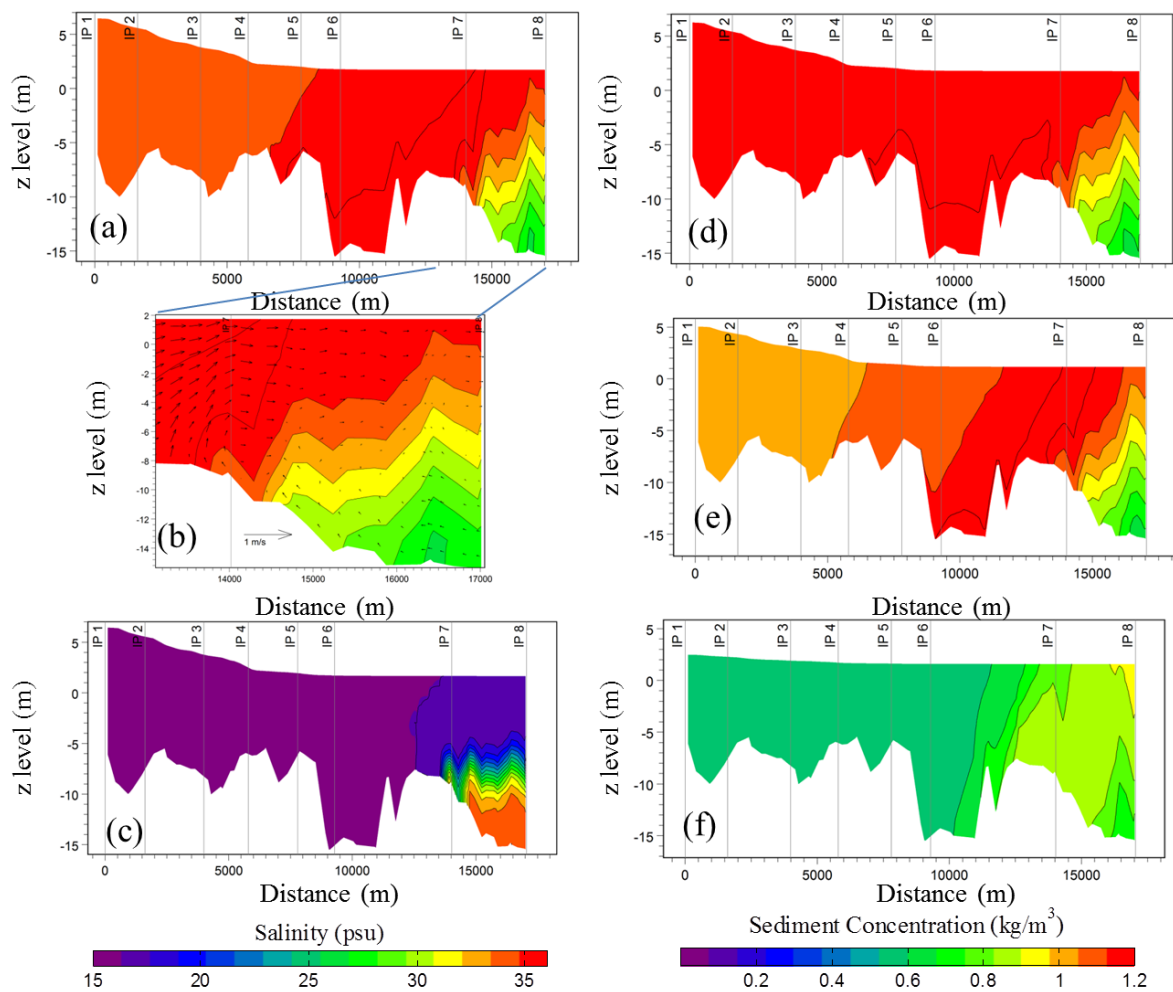
Figure 6.3-3 The simulated vertical evolution of flood-driven sediment plume during the flood peak discharge on 12 January. (a) Vertical distribution of sediment concentration at 7 a.m., with (b) the current vector within the region between IP7 and IP8 and (c) the salinity distribution at the same time. (d) – (f) The variation of the vertical distribution of sediment concentration at 8.45 a.m., 1.45 p.m. on 12 January, and 12 noon on 13 January, respectively.

stream of water flowed into the river estuary in the near-bottom layer between IP7 and IP8, as shown in Figure 6.3-3b. This stream of water was believed to be the saline water via the bay, as its salinity was around 32 psu (Figure 6.3-3c). It is therefore evident that saline waters at relatively low SSC from the bay, flowed into the estuary in the near-bottom layer, while the flood water at high SSC level rushed into the bay via the surface layer, resulting in significant

134

stratification of concentrations in the vicinity of the river mouth. As the flood runoff continuously discharged from the upstream area, the region (IP1 - IP7) was filled by water with high SSC as shown in Figure 6.3-3d. However, the stratification at the river mouth still remained the same. The long lasting presence of the stratification at the river mouth reveals that the horizontal movement of sediment plume was predominant under high flood river discharge, and sediment settling was minor. After the peak flood discharge, the concentration level of sediment fell back within the region between IP1 and IP4 (Figure 6.3-3e). As a result, the water was progressively diluted, within the region where the highest concentration occurred (IP4 – IP7), as shown in Figure 6.3-3f.

6.3.2 Suspended sediment transport during peak discharges

It was found that the tidal limit s is approximately 80 km upstream from the Brisbane River mouth (Ecosystem Health Monitoring Program, 2007). The flow conditions in the BRE were significantly affected by the tidal currents under normal weather conditions, particularly during the dry season (Yu et al., 2014b). It can be seen in Figure 4.4-3 that the velocity of river flow regularly oscillated between positive and negative values not only at Chainage 70 km (downstream), but also at Chainage 20 km (upstream). The horizontal fluxes of salinity and suspended sediment concentration would accordingly oscillate between positive and negative values. However, during severe flood events, the variations of fluxes within the BRE are different.

Suspended sediment flux in the vicinity of the river mouth during the flood peak discharge was investigated following Eq. (6.3-1)

$$F_{u,v,w}(t) = C(t)U_{u,v,w}(t) \qquad (6.3\text{-}1)$$

where F is suspended sediment flux, U donates instantaneous flow velocity, and C is suspended sediment concentration. Both F and U are separated into $u,$ $v,$ and w components. The suspended sediment flux in the surface layer, near-bottom layer and as well as the depth-averaged flux along the BRE estuary were calculated.

Figure 6.3-4 exhibits variations of suspended sediment flux at three locations, IP1 (downstream estuary, close to the river mouth), IP4 (at the river mouth) and IP8 (off the river mouth), during the largest peak discharge of this flood event. The water level, horizontal sediment flux in the u- (longitudinal) and v- (latitudinal) components, and vertical sediment

flux in the *w-* component at IP1, are presented in Figure 6.3-4 (a1) – (a4), which are the same layouts for IP4 (b1 – b4) and IP8 (c1 – c4), respectively.
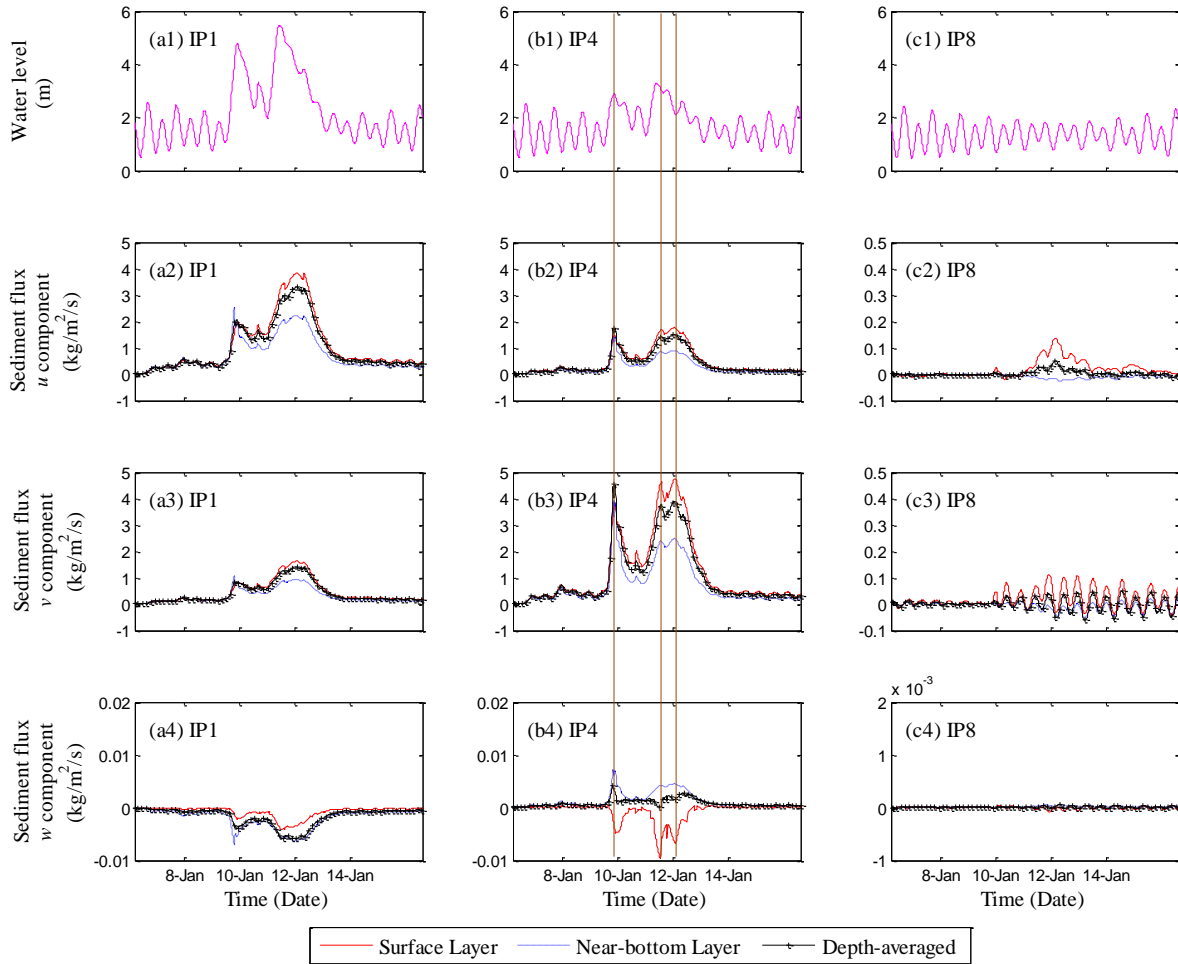
Figure 6.3-4 Water level and sediment flux in *u, v,* and *w* components in the surface layer, near-bottom layer and depth-averaged at locations (a1-a4) IP1, (b1-b4) IP4 and (c1-c4) IP8 during peak flood discharge, respectively.

The water level at IP1 responded to the rainfall by rising rapidly, with two remarkable peaks between 9 and 12 January (Figure 6.3-4 (a1)), and then falling slowly within hours of the rain ceasing. The *u-* component of suspended sediment flux at IP1 correspondingly increased between 10 and 12 January, reaching up to 4 kg/m^2/s. The variations of sediment flux in the surface and near-bottom layers were consistent with the depth-averaged flux as shown in Figure 6.3-4 (a2), implying that the suspended sediment in the entire water column had the same behaviour. Compared to the significant changes in *u-* component flux during peak discharges, suspended sediment flux in the *v-* and *w-* components varied slightly. The value

of flux in the v- component was up to 2 kg/m^2/s as shown in Figure 6.3-4 (a3), which was approximately 50% less than it was in the u- component. The w- component flux level was two orders of magnitude lower than it was in the v- component, indicating that the horizontal component was more predominant. As shown in Figure 6.3-4 (a4), the negative suspended sediment flux in the w- component demonstrates that the suspended sediment was moving downwards in the water column, with the effect of flux increasing from the surface layer to the near-bottom layer during the peak flood discharge. Overall, at IP1 which is within the downstream estuary, the horizontal suspended sediment flux was more predominant compared to the small amount of flux in the vertical direction. It was also found that the sediment transport behaviour was consistent throughout the whole water column at IP1.

The fluctuation of the water level at IP4 was less affected by flood water runoff compared to IP1. Two small peaks of the water level were observed between 9 and 12 January in Figure 6.3-4 (b1). It was evident that the suspended sediment flux in the u- component was significantly smaller than the v- component as shown in Figure 6.3-4 (b2) and (b3), which was completely the opposite to the conditions at IP4. The reason was that the change in the direction of the river course resulted in the change of predominant flow from the u- component to the v- component. The w- component flux level was still two orders of magnitude lower than the u- component in Figure 6.3-4 (b4). However, it was found that the w- component of near-bottom flux was positive, which indicated the occurrence of sediment resuspension in the near-bottom layer at IP4 during the period.

It was indicated by straight lines in Figure 6.3-4 that three peaks of sediment flux were observed. To further investigate the behaviour of sediment transport, the flow velocity and the SSC at IP4 were examined separately, as shown in Figure 6.3-5, focusing on these three peaks. They were i) the first peak of suspended sediment flux occurred immediately after the first peak of water level at high tide; ii) the second and third peaks of sediment flux occurred at low tide, following the occurrence of the second peak of water level. The first peak of sediment flux was attributed to the sediment resuspension in the water column at IP4, which was shown in Figure 6.3-2 and discussed in the previous section. Therefore, it can be seen in Figure 6.3-5 (b) that the peak of surface sediment flux resulted from the combination of large velocity (approximately 5 m/s in the v- component) and low level of SSC (approximately 1 kg/m^3). Conversely, the peak of sediment flux in the near-bottom layer was caused by the combination of small velocity (approximately 2 m/s in the v- component) and high level of SSC (up to 2 kg/m^3), as shown in Figure 6.3-5 (c). When the resuspension receded, the level

of SSC dropped rapidly which in turn decreased the value of suspended sediment flux. Following the highest flood peak discharge, the river water carried a large amount of sediment travelling downstream, leading to increasing levels of SSC both in the surface and near-bottom layers. The progressively increasing SSC and large velocity of flood runoff resulted in the second and third peaks of the suspended sediment flux, particularly in the surface layer of the water column, approaching 5 kg/m^2/s, as shown in Figure 6.3-4 (b3).
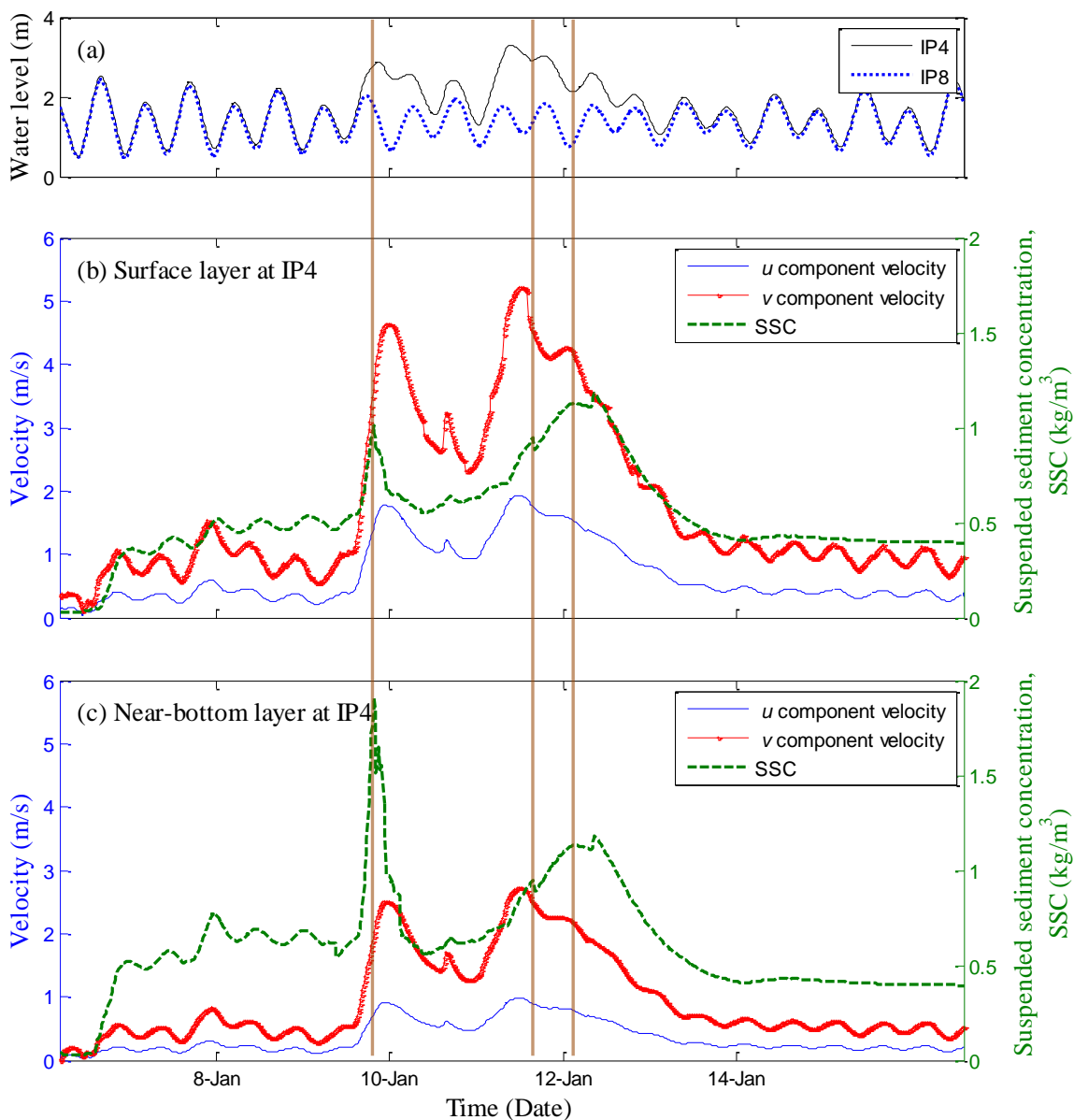
Figure 6.3-5 Variations of flow velocity and the SSC in the surface and near-bottom layers at IP4 during the peak flood discharges.

Compared to the suspended sediment flux at IP1 and IP4, the flux variations at IP8 were about one order of magnitude smaller in all three components. Panel c in Figure 6.3-5 exhibits the water level variation without spikes, slight peaks of flux in the u- component, regular fluctuation in the v- component, and negligible variance in the w- component. In general, the sediment flux off the river mouth was mainly driven by tidal currents. The large flood runoff might cause a sudden peak in the u- component of the sediment flux; however, the tidal effects on the v- component of flux were more evident.

In addition to the three components of flux discussed above, the sediment horizontal flux was calculated following from Eq. (6.3-2) to (6.3-4),

$$\left| Fh_{avg}(t) \right| = \sqrt{F_{u-avg}(t)^2 + F_{v-avg}(t)^2} \tag{6.3-2}$$

with

$$F_{u-avg} = \int_{z_1}^{z_2} F_u(t)dz \quad \text{and} \quad F_{v-avg} = \int_{z_1}^{z_2} F_v(t)dz \tag{6.3-3}$$

$$\theta_F(t) = \tan^{-1}\left(\frac{F_{u-avg}(t)}{F_{v-avg}(t)} \right), \text{ with } -180° \leq \theta_F \leq 180° \tag{6.3-4}$$

where Fh_{avg} is depth-averaged horizontal flux, F_{u-avg} and F_{v-avg} are depth-averaged sediment flux in u- and v- components, respectively, θ_F is the angle between Fh_{avg} and the true north. The positive sign of horizontal flux denotes seaward direction transport, and vice versa, landward direction transport. Considering the river channel is about $52°$ east of the true north, the horizontal flux is positive if θ_F is between -38^0 and 142^0, otherwise the flux is negative.

Figure 6.3-6 shows the variations of the horizontal flux at all selected locations during this flood event. The large flood discharge resulted in a net seaward horizontal flux of sediment in the region between IP1 and IP6 during the event, then dropping back towards zero following the second peak discharge, as shown in Figure 6.3-6 (a) and (b). For the two locations IP7 and IP8 which were off the river mouth, apart from the effects of the flood discharge, the horizontal flux variation was also highly dependent on the tidal conditions. Figure 6.3-6 (c) and (d) depict that the horizontal flux typically fluctuated as tidal currents, resulting in the sediment transport in the seaward direction during the flood tide, and turned landward direction during the ebb tide. The two flood peaks discharge caused the high value of horizontal flux on the day at IP7 and IP8, however, the peak values dropped rapidly. It was found that the section of downstream estuary and river mouth area could be generally separated into four regions, according to the variations of their horizontal fluxes. They are i)

Region One, bounded by IP1 and IP4 in the estuary; ii) Region Two, between IP4 and IP6 at the river mouth; iii) Region Three, between IP6 and IP7 which is a short distance from the river mouth; iv) Region Four, between IP7 and IP8 in the bay. In Region One, it was estimated that the horizontal flux continually increased by 0.9%, 12.3%, and 14.6%, respectively, between each investigated point (IP) along the downstream estuary. However, the horizontal flux then changed to decline in Region Two, which decreased by approximately 15.4% from IP4 to IP5. The largest reduction in the horizontal flux occurred in Region Three, with the value significantly dropping by 48.3% from IP6 to IP7, compared to the 5.6% decrease in Region Four.
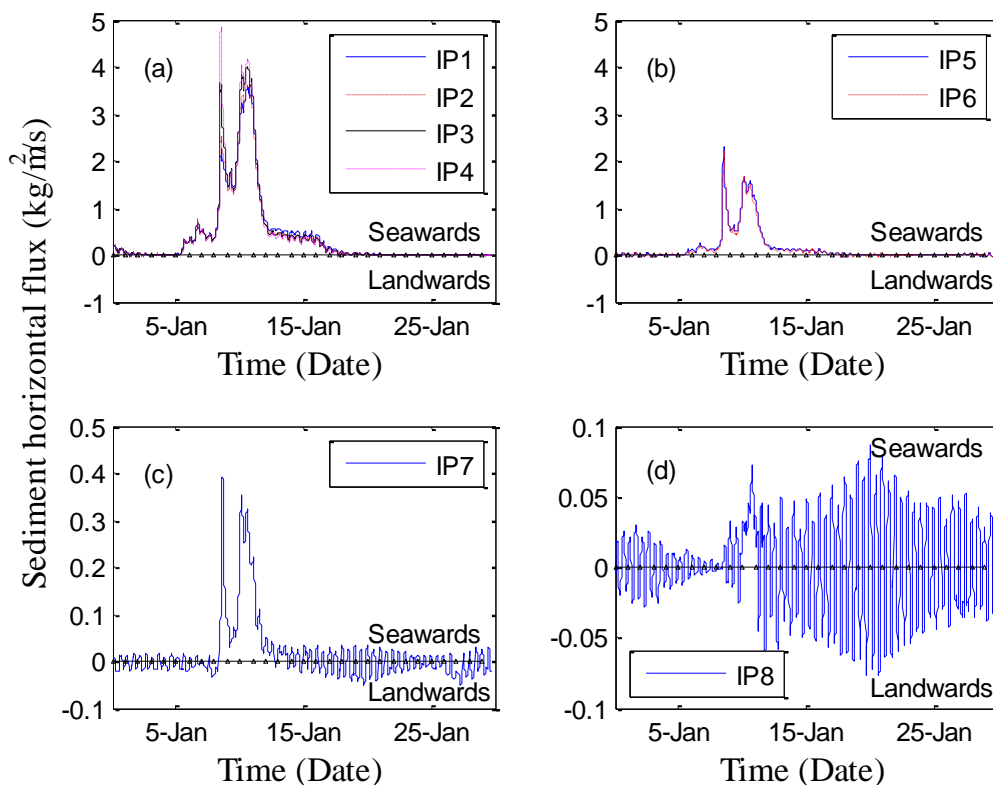
Figure 6.3-6 Horizontal flux at all selected locations, from IP1 to IP8, during the whole period of flood event in January 2011. Seawards and landwards indicate the direction of towards the sea (eastern) and inland (western), respectively, in this study.

The different variations of flux within these regions indicate the distinct behaviour of sediment transport during the flood, corresponding to the combined effects of the flood discharge and tidal conditions. Within the first region, the sediment transport was mainly driven by the flood discharge. The sediment was therefore carried in the seaward direction, with the horizontal flux increasing along the estuary. Within the second region, the sediment

140

transport was similar to what it was in the first region. However, the magnitude of horizontal flux decreased, as water exchange took place at the river mouth which in turn reduced both the flow velocity and sediment concentration. Within the third region, the tidal effect was more and more evident on the sediment transport, resulting in the fluctuation in the direction of sediment movement and significant decrease of magnitude of the sediment horizontal flux. Within the fourth region, tidal effects became the major factor driving sediment transport, whereas the flood peak discharge could only cause significant variation in the short term.

6.3.3 Sediment loading during the flood event

6.3.3.1 Cumulative sediment loading at the river mouth

The cumulative sediment loading, Q_{cum} was estimated as Eq. (6.3-5) during a certain period of time,

$$Q_{cum} = \int_{t_1}^{t_2} Fh_{avg}(t)A(t)dt \tag{6.3-5}$$

where Fh_{avg} is the depth averaged horizontal sediment flux and A denotes the area of cross-sections. The negative sign of Q_{cum} represents sediment transport in the landwards direction. The cumulative sediment loadings at IP4 were calculated during each individual flood tide, ebb tide and tidal cycle, as shown in Figure 6.3-7, respectively. A tidal cycle is defined as high tide – low tide – high tide hereafter.

It can be seen in Figure 6.3-7 (a) that the sediment was transported in the seaward direction during ebb tides. Approximately 500 tonnes of sediment were discharged into the coastal bay over an individual ebb tide at the beginning of January. During flood tides in early January, the amount of the cumulative sediment loading usually increased in the first hour and then changed to decrease. As shown in Figure 6.3-7 (b), for instance, the amount of cumulative sediment loading increased up to 31 tonnes, but it then decreased to -332 tonnes at the end of spring flood tide. The increase-then-decrease pattern of the cumulative sediment loading indicates that the sediment was initially transported in the seaward direction, which was mainly driven by the flood runoff. With the rising water level, the sediment was then pushed back from the bay to the river estuary, which was primarily driven by the flood tidal current. The negative Q_{cum} demonstrates the occurrence of net sediment transport in the landward direction over each individual flood tide at the beginning of January. However, the net sediment loading over the individual ebb tide was typically one order of magnitude higher

than it was over the individual flood tide, resulting in all positive values of Q_{cum} which indicated the sediment transport being directed seawards over the individual tidal cycle.
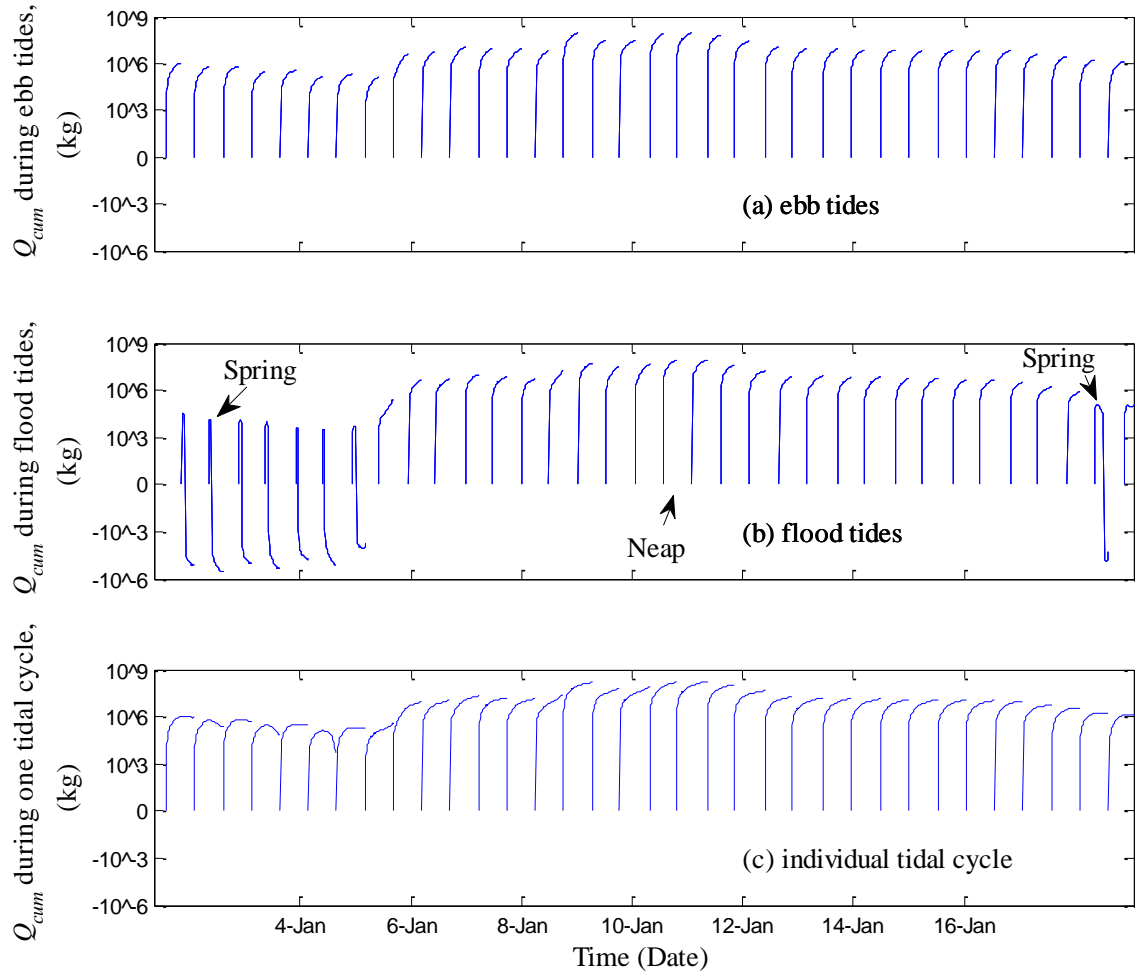
Figure 6.3-7 Cumulative sediment transport at IP4 over each individual (a) flood tide, (b) ebb tide, and (c) tidal cycle, between two spring tides in January 2011.

As the flood discharge gradually increased from 6 January, the behaviour of sediment transport at IP4 was more dependent on flood conditions than tidal currents. As shown in Figure 6.3-7, the values of Q_{cum} were all positive from 6 January, implying that the sediment was continually discharged in the seaward direction over both ebb and flood tides. During the period of flood peak discharge, the amount of sediment loading was approximately 9.5×10^4 and 8.5×10^4 tonnes over neap ebb and flood tides, respectively, resulting in a total amount of 1.8×10^5 tonnes over one tidal cycle. As the flood discharge gradually decreased, the increase-then decrease pattern of the cumulative sediment loading was observed again during the spring flood tide at the end of January, as marked in Figure 6.3-7 (b). The appearance of

the increase-then-decrease pattern of sediment loading indicates the significant effects of tidal current on the sediment transport. Figure 6.3-8 shows the cumulative sediment loading during the flood event in January 2011. The amount of sediment loading significantly increased during the flood peak discharge, which contributed to about 95% of sediment loading in the event. It was estimated that approximately 1.01×10^6 tonnes of sediment loading was discharged from the BRE into the bay during the flood event. This value was similar to the Olley and Croke (2011)'s evaluation which estimated the sediment loading to be 1.04×10^6 tonnes, with a discrepancy of 2.9 %.
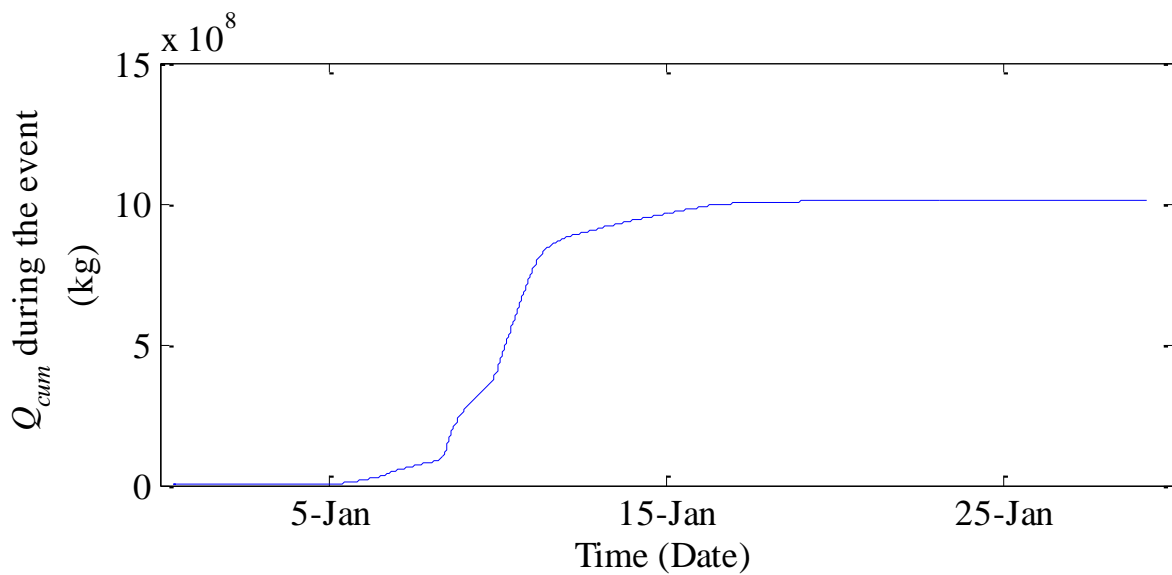
Figure 6.3-8 Cumulative sediment loading at IP4 during the flood event.

6.3.3.2 Estimation of sediment erosion

Based on the estimation method of the cumulative sediment loading above, the difference of the cumulative sediment loading ΔQ_{cum} between IP1 and IP4 was calculated, where negative denotes the sediment deposition and positive represents the sediment erosion from the river bed and channel.

Table 6.3-1 shows the cumulative sediment loading over different tidal cycles at IP1 and IP4. Over the 5th tidal cycle (before flood peak), about 157 and 240 tonnes of sediment was transported seawards through IP1 and IP4, respectively, implying that approximately 83 tonnes of sediment were being eroded from the river channel between IP1 and IP4. Over the 21st tidal cycle (during the flood peak discharge), the cumulative sediment loading was all

positive, implying that the net sediment transport being seawards both over ebb and flood tides was due to the strong effects of flood runoff. The large flood discharge also led to approximately 6.1×10^4 tonnes of sediment erosion within the region between IP1 and IP4. After the rainfall ceased, the sediment loading gradually decreased. For example, there was 1.6×10^3 tonnes of sediment being transported in the seaward direction over the 36th tidal cycle, with only 546 tonnes of sediment caused from erosion.

In addition, the tidal asymmetries in sediment transport were observed at IP4 over the 54th tidal cycle, with magnitude of Q_{cum} over the flood tide which was larger than it being ebb tide. It was estimated that approximately 95 tonnes of sediment were moved seawards during the ebb tide, compared to 183 tonnes of sediment being transported in the landward direction during the flood tide. There was about 89 tonnes of sediment left at IP4 after the whole tidal cycle, substantially due to the tidal asymmetries.

The estimation of sediment erosion was conducted above. The analysis of the difference of the cumulative sediment loading shows that significant erosion took place during the flood event, which contributed to a large amount of sediment being transported into the bay. Sediment deposition rarely occurred during the event. The tidal asymmetries in sediment transport were also identified. Without the influence of flood runoff, the sediment was typically transported in the landward direction, from the bay to the estuary. The estimation method of sediment erosion based on the cumulative sediment loading, however, was limited. The sediment erosion / deposition status in a certain region cannot be determined if the directions of net sediment transport are different at boundaries. Over the 54th tidal cycle, for an instance, the sediment was transported in the seaward direction at IP1, with the cumulative loading of 27 tonnes, whereas the net sediment transport was directed landwards at IP4. The ΔQ_{cum} therefore cannot be applied to explain the variation of sediment loading.

Table 6.3-1 The cumulative sediment loading over individual ebb, flood and the whole tidal cycle at IP1 and IP4. The ΔQ_{cum} is the difference of the cumulative sediment loading between IP1 and IP4. All units are in tonnes.

Tidal Cycle	IP1			IP4			ΔQ_{cum}
	Ebb	Flood	Cycle	Ebb	Flood	Cycle	
#5 (spring tide)	208	-51	157	573	-333	240	83
#21 (peak discharge)	62569	56233	118803	95210	84810	180020	61217
#36 (spring tide)	970	143	1113	1677	-19	1659	546
#54	53	-26	27	95	-183	-89	-

6.4   **Conclusions**

This study simulated and analysed the hydrodynamic and transport behaviour of the flood-driven sediment plume in the Brisbane River estuary and Moreton Bay. The numerical simulation results showed that the sediment plume widely spread in the bay following the flood peak discharge. The flood runoff was the main factor to drive the plume generation and development in the horizontal direction. In the vertical direction, the significant sediment resuspension in the water column was usually found at the river mouth. Before the incidence of flood peak discharge, the anticipated dominant process of sediment transport was that the particles would be lifted from the near-bottom layer due to the large shear stress and turbulence, and then the entire water column would be well mixed in a short time. Due to the extremely large flood discharge, the estuary was filled by flood water with high SSC, during the flood tide, saline water flowed into the estuary via the near-bottom layer, while the flood water at high SSC level rushed into the bay via the surface layer, resulting in significant stratification of concentrations at the river mouth.

It was also found that the characteristics of sediment transport were determined by the combined effects of flood runoff and tidal currents. Four distinct characteristics of sediment transport were identified, based on the analysis of variations of sediment horizontal flux. Firstly, within the estuary, the sediment was driven by the flood discharge and primarily transported in the seaward direction, leading to an increase of the sediment horizontal flux (up to 5 kg/m^2/s) along the estuary. Secondly, at the river mouth, the transport pattern of

sediment was similar to what it was in the first region, however, the horizontal flux was significantly smaller by 50%. Thirdly, a short distance from the river mouth, the difference occurred not only in magnitude but also in transport pattern. The sediment horizontal flux was about one order of magnitude lower than it was in the estuary, and the direction of sediment movement fluctuated with tides switching between landwards and seawards. Lastly, within the coastal bay, the sediment transport was mainly driven by tides. Its horizontal flux further decreased by about one order of magnitude, compared to the flux in the third region.

The analysis on sediment loading during the individual ebb tide, flood tide and the whole tidal cycle was conducted. Due to the large flood discharge, the amount of sediment loading generally increased over each individual tidal cycle. The increase-then-decrease pattern of sediment loading was observed only over spring flood tides before and after peak discharge, indicating the significant effects of tidal current on the sediment transport. It was estimated that approximately 1.01×10^6 tonnes of sediment loading was discharged from the BRE into the bay during the flood event in January 2011.

6.5 Acknowledgement

Chapter 7 Conclusions and Future Research Plan

The main objectives of this research were i) to investigate the characteristics of salinity and turbidity distribution along the estuary during tidal cycle and dry and wet seasons; ii) to estimate and implement dispersion module in model; and iii) to study the hydrodynamic and sediments transport following severe flood events. These objectives have been achieved, and the accomplishment is discussed below.

Chapter 2 presented the literature review regarding the main characteristics of turbidity, hydrodynamic and sediment transport. It was found that a majority of the previous studies only focused on the investigation of behaviour of sediment transport under non-flood conditions. The motivation for this research is therefore not only driven by the lack of comprehensive knowledge of salinity and turbidity distribution of the BRE in the short- (under tides) and long- term (during the wet and dry seasons), but also by the increasing demand for the understanding of sediment transport behaviour following severe flood events. Based on the review of numerical model comparison, MIKE3 DHI shows outstanding capacity of modelling cohesive sediment in high resolutions. Hence, this research applies this numerical model to investigate the hydrodynamic and sediment transport in the BRE and Moreton Bay following severe flooding.

In Chapter 3, three preliminary studies on numerical model and turbidity conditions in the BRE have been conducted. In the first section of this chapter, the effects of mesh resolution of bathymetry on the numerical modelling were investigated. This study proposed an efficient and high-performance bathymetry, and so has significant implications for the model set-up. In the rest of the sections of this chapter, the tidal influences on the turbidity maximum were examined. Under non-significant flood conditions, the tidal currents impact turbidity distribution at different degrees at different sites. For the middle reach, the turbidity difference between at the flood and ebb tides, reached a maximum of approximately 60 NTU during one tidal cycle. The significant difference might be caused by the larger amount of fine sediment accumulated in this section of the estuary which was available for suspension. Under moderate flood conditions (an average flow rate < 3000 m^3/s), a high-low-high pattern of turbidity distribution was found in the estuary. After the experience of severe flood, however, the turbidity level generally increased from upstream to downstream within the estuary. The gradually increasing turbidity distribution had remained for several days and then changed to a relatively even condition.

Based on the validated model and preliminary results presented in Chapter 3, comprehensive investigations (both in the short- and long-term) into the salinity and turbidity distributions in the BRE were conducted in Chapter 4. A fourth-order polynomial equation was proposed with an R^2 of 0.99, describing the longitudinal variation in salinity dilution changes as the upstream distance changes in the BRE during wet and dry seasons. Two striking characteristics of turbidity distribution were found in the BRE: i) the peak turbidity always occurred in the upper and mid estuary during the two seasons; and ii) the peak value of turbidity during the wet season was generally higher than during the dry season. The observed results also demonstrated that a larger river inflow not only resulted in a longer ETM, but also caused the FSI to occur further downstream. Significantly, an approach of using water reflectance observed by satellite to estimate the turbidity level in the BRE was firstly proposed in this study, which provided a practical solution for estimating surface turbidity levels not only under normal weather conditions, but also during flood events.

In Chapter 5, as one of the most important factors influencing sediment transport in coastal regions, hydrodynamic dispersion was examined experimentally and numerically. A cluster of four Lagrangian drifters were released into two shallow coastal regions and the movement of drifters were recorded. Two dispersion regimes were identified, a slow dispersion in the earlier stage and a rapid dispersion in the latter stage. The change of regime generally occurred during the succeeding ebb tides, which may be attributable to residual eddies breaking down during reversal of tidal direction. Furthermore, it was identified that the relative slow spreading occurred during high tide with small apparent dispersion coefficients, in comparison to the rapid spreading immediately following slack tide with larger dispersion coefficient.

Chapter 6 focuses on the investigation of sediment spread and suspension in the BRE and Moreton Bay during severe flood events. The flood-driven plume evolution was simulated, sediment flux was estimated, and effects of flooding discharge and tides on sediment transport were examined. It was found that the sediment plume widely spread in the bay following the flood peak discharge. The flood runoff was the main factor to drive the plume generation and development in the horizontal direction. In the vertical direction, the significant sediment resuspension in the water column was usually found at the river mouth. Before the incidence of flood peak discharge, the anticipated dominant process of sediment transport was that the particles would be lifted from the near-bottom layer due to the large shear stress and turbulence, and then the entire water column would be well mixed in a short

time. Four distinct characteristics of sediment transport were identified, based on the analysis of variations of sediment horizontal flux. Firstly, within the estuary, the sediment was driven by the flood discharge and primarily transported in the seaward direction, leading to an increase of the sediment horizontal flux along the estuary. Secondly, at the river mouth, the transport pattern of sediment was similar to what it was in the first region, however, the horizontal flux was significantly smaller by 50%. Thirdly, a short distance from the river mouth, the difference occurred not only in magnitude but also in transport pattern. The sediment horizontal flux was about one order of magnitude lower than it was in the estuary, and the direction of sediment movement fluctuated with tides switching between landwards and seawards. Lastly, within the coastal bay, the sediment transport was mainly driven by tides. Its horizontal flux further decreased by about one order of magnitude, compared to the flux in the third region.

Despite these informative and beneficent results, this research also has certain aspects which could be amended and improved.

The performances of turbulence closure have not been fully evaluated in this study. The sediment resuspension is highly dependent on the turbulence conditions. Therefore, the evaluation of turbulence closure would be helpful to improve the accuracy of numerical simulation. In addition, the lack of consideration of wave-current interaction would also affect the sediment erosion and deposition.

Furthermore, sediment transport behaviour is sensitive to sediment parameters, such as settling velocity and critical shear stress. A sensitivity-analysis test would thus be a key for precise determination of the parameters, to improve the accuracy of simulated results.

References

Al-Rabeh, A. H. 1994. Estimating surface oil spill transport due to wind in the Arabian Gulf. *Ocean Engineering*, **21,** 461-465.

American Public Health Association 1998. APHA. 1998. *Standard Methods for the examination of Water and Wastewater,* **20**.

Amoudry, L. & Souza, A. J. 2011. Impact of sediment-induced stratification and turbulence clousres on sediment transport and morphological modelling. *Continental Sehlf Research,* **31,** 912-928.

Ariathurai, R. & Krone, R. B. 1976. Finite element model for cohesive sediment transport. *Journal of the Hydraulics Division,* **102, 3,** 323-338.

Ataie-Ashtiani, B., Volker, R. E. & Lockington, D. 1999. Tidal effects on sea water intrusion in unconfined aquifers. *Journal of Hydrology,* **216, 1-2,** 17-31.

Babister, M. & Retallick, M. 2011. Flood frequency analysis. *Brisbane River 2011 flood event.* WMA Water.

Bainbridge, Z. T., Wolanski, E., Alvarez-Romero, J. G., Lewis, S. E. & Brodie, J. E. 2012. Fine sediment and anutrient dynamics related to particle size and floc formation in a Burdekin River flood plume, Australia. *Marine Pollution Bulletin,* **65,** 4-9.

Bell, P. 2010. Finite element water quality modelling of WWTP discharges and resuspended sediments in the Brisbane River Estuary and Moreton Bay. *Proceeding 19th NSW Coastal Coference.* Batemans Bay, NSW, Australia.

Blumberg, A. F. & Mellor, G. L. 1987. A Description of a three-dimensional coastal ocean circulation model. *In:* HEAPS, N. S. (ed.) *Three Dimensional Coastal Ocean Models.* Washington, DC.: American Geophysical Union.

Brisbane City Council 2003. Natural Channel Design Guidelines. Brisbane City Council, Queenslanda, Australia.

Brown, J., MacMahan, J., Reniers, A. & Thornton, E. 2009. Surf zone diffusivity on a rip-channeled beach. *Journal Geophysical Research,* **Vol 114, No. C11,** C11015.

Brown, R., Chanson, H., McIntosh, D. & Madhani, J. 2011. Turbulent velocity and suspended sediment concentration measurements in an urban environment of the Brisbane River flood plain at Gardens Point on 12-13 January 2011. *Hydraulic Model Reports.* The University of Queensland, St Lucia QLD.

Cambell, P. G. 2009. *Measuring turbulence in the bottom boundary layer of moreton Bay, Queensland, Australia.* Bachelor, Griffith University.

Celik, I. B. 1999. Introdcutory Turbulence Modelling. Mechanical and Aerospace Engineering Department: West Virginia University.

Chanson, H., Gibbes, B. & Brown, R. 2014. *Turbulent mixing and sediment processes in peri-urban estuaries in south-east Queensland (Australia),* Spring Science Business Media Dordecht.

Cheng, P., Li, M. & Li, Y. 2013. Generation of an estuarien sediment plume by a tropical storm. *Journal of Geophysical Research,* **118, 2,** 856-868.

Ciesiolka, C. A., Coughlan, K. J., Rose, C. W., Escalante, M. C., Hashim, G. M., Paningbatan, E. P. & Somebatpanit, S. 1995. Methodology for a multi-country study of soil erosion management. *Soil Technol,* **8,** 179-192.

Dennison, W. C. & Abal, E. G. 1999. *Moreton Bay study: a scientific basis for the Healthy Waterways Campaign,* Brisbane, Queensland, Australia, South East Queensland Regional Water Quality Management Strategy.

Dennison, W. C., Udy, J., Schneider, P. & Moore, K. 2011. South East Queensland Floods 2011: Overview of the flood. *South East Queensland Floods 2011.* HealthyWaterways.

Department of Environment and Resource Management 2011. Queensland Coastal Plan.

DHI Water and Environment 2011. User guide of MIKE3: Estuarine and coastal hydraulics and oceanography, Hydrodynamic module. *Scientific documentation.*

DHI Water and Environment 2013. *MIKE 21 & MIKE 3 FlOW MODEL FM*, DHI.

DHI Water and Environment 2014a. MIKE11, a modelling system for rivers and channels, Reference Manual. 17-19.

DHI Water and Environment 2014b. *MIKE 21 & MIKE 3 FlOW MODEL FM*, DHI.

Dix, J. K., Lambkin, D. O. & Cazenave, P. W. 2008. Development of a regional sediment mobility model for submerged archaeological sites. *English Heritage ALSF project,* **5224**.

Done, T. 1982. Patterns in the distribution of coral communities across the central Great Barrier Reef. *Coral Reefs,* **1,** 95-107.

Duarte, A. A. L. S. & Boaventura, R. A. R. Dispersion modelling in rivers for water sources protection, based on tracer experiments. Case studies. 2nd International Conference on Water Management, Water Pollution, Air Pollution, Indoor Climate, 2008 Corfu, Greece. 205-210.

Dunn, R. J. K., Zigic, S. & Shiell, G. R. 2014. Modelling the dispersion of treated wastewater in a shallow coastal wind-driven environment, Geographe Bay, Western Australia: implications for environmental management. *Environmental Monitoring and Assessment*, 6107-6125.

Dyer, K. R. 1986. *Coastal and estuarine sediment dynamics,* Great Britain, A Wiley-Interscience Publication.

Dyer, K. R. 1989. Sediment processes in estuarines: future research requirements. *Journal of Geophysical Research,* **93, 14,** 327-339.

ECOMSED 2002. A primer for ECOMSED. *Version 1.3 Users Mannual.*

Ecosystem Health Monitoring Program 2007. *Ecosystem Health Monitoring Program 2005-06 Annual Technical Report,* Brisbane, South East Queensland Healthy Waterways Partnership.

Eisma, D. 1986. Flocculation and de-flocculation of suspended matter in estuaries. *Netherlands Journal of Sea Research,* **20, 2.3,** 183-199.

Engedahl, H. Hindcast simulations of ocean currents in the Norwegian coastal waters Part 1: Model set uo and sensitivity tests. *In:* SPAULDING, M. & CHENG, R. T., eds. Estuarine and coastal modelling, 1995 San Diego, California. American Society of Civil Engineers, 379-390.

Eyre, B., Hossain, S. & McKee, L. 1998. A suspended sediment budget for the modified subtropical Brisbane River estuary, Australia. *Estuarine, Coastal and Shelf Science,* **47,** 513-522.

Fugate, D. C. & Friedrichs, C. T. 2002. Detrmining concentration and fall velocity of estuarine particle poplulations using ADV, OBS and LISST. *Continental Sehlf Research,* **22,** 1867-1886.

Furnas, M. 2003. Catchments and corals: terrestrial runoff to the Great Barrier Reef. Townsville, Queensland, Australia: Australia Institue of Marine Science.

Geyer, W. R. & Signell, R. P. 1992. A reassessment of the role of tidal dispersion in estuaries and bays. *Estuaries,* **15, 2,** 97-108.

References

Geyer, W. R., Hill, P., Milligan, T. & Traykovski, P. 2000. The structure of the Eel River plume during floods. *Continental Shelf Research,* **20,** 2067-2093.

Gibbes, B., Grinham, A., Neil, D. T., Olds, A., Maxwell, P., Connolly, R., Weber, T., Udy, N. & Udy, J. 2014. *Moreton Bay and its estuaries: a sub-tropical system under pressure from rapid population growth,* Estuaries of the world, Spring Science Business Media Dordecht.

Gorman, G. J., Piggott, M. D., Pain, C. C., Olivieira, C. R. E., Umpleby, A. P. & Goddard, A. J. H. 2006. Optimisation based bathymetry approximation throuh constrained unstructured mesh adaptivity. *Ocean Modelling,* **23,** 436-452.

Grant, W. & Madsen, O. S. 1979. Combined waver and current interaction with a rough bottom. *Journal of Geophysical Research,* **84, C4,** 1797-1808.

Hayes, M. O. 1975. Morphology of sand accumulations in estuaries. *Estuarine Research, Geology and Engineering***, 2,** 3-22.

Henley, W. F., Patterson, M. A., Neves, R. J. & Lemly, A. D. 2000. Effects of Sedimentation and Turbidity on Lotic Food Webs: A Concise Review for Natural Resource Managers. *Reviews in Fisheries Science,* **8, 2,** 125-139.

Hill, P. S., Syvitski, J. P. & Cowan, E. A. 1998. In situ observations of floc settling velocites in Glacier Bay, Alaska. *Marine Geology,* **145,** 85-94.

Hollywood, S., Lemckert, C. J., Howes, T. & Nuiman, L. Suspended sediment dynaymics in a highly modified microtidal estuary. *In:* EDGE, B. L., ed. Proceedings Australian Coast and Ports Conference, 26-28 September 2001 Gold Coast, Queensland, Australia. 517-522.

Hossain, S., Eyre, B. D. & McKee, L. J. 2004. Impacts of dredging on dry season suspended sediment concentration in the Brisbane River estuary, Queensland, Australia. *Estuarine, Coastal and Shelf Science,* **61,** 539-545.

Howes, T., Lemckert, C. J. & Moss, A. 2002. Long term monitoring of estuarine water quality: Brisbane River Turbidity. *Journal of Australian Water Association,* **Water September,** 37-39.

Hu, C. H., Ji, Z. W. & Wang, T. 1998. Dynamics characteristics of sea currents and sediment dispersion in the Yellow River Estuary. *International Journal of Sediment Research,* **13, 2,** 20-30.

Hughes, M. G., Harris, P. T. & Hubble, T. C. T. 1998. Dynamics of the turbidity maximum zone in a micro-tidal estuary: Hawkesbury River, Australia. *Sedimentology***, 45,** 397-410.

Hunt, S., Lemckert, C. J. & Schacht, C. 2006. Location of turbidity maxima within a microtidal estuary and some limitations of laser In situ particle sizing. *Journal of Coastal Research,* **SI 39,** 520-525.

Hwant, K. N. & Mehta, A. J. 1989. Fine sediment erodibility in Lake OKEECHOBEE. *Report UFL/COEL.* Coastal and Oceanographic engineering Department: University of Florida.

Inoue, M. & Siseman, W. J. 2000. Transport, mixing and stirring processes in a Louisiana estuary: A model study. *Estuarine Coastal and Shelf Science,* **50,** 449-466.

Jiang, W. S., Pohlmann, T., Sudermann, J. & Feng, S. Z. 2000. A modeling study of SPM ransport in the Bohai Sea. *Journal of Marine Research,* **24, 3-4,** 175-200.

Jiang, W. S., Pohlmann, T., Sun, J. & Starke, A. 2004. SPM transport in the Bohai Sea: field experiments and numerical modelling. *Journal of Marine System,* **44, 3-4,** 175-188.

Jimenez, J. A. & Madsen, O. S. 2003. A simple formula to estimate settling velocity of natural sediments. *Journal of Waterway, Port, Coastal and Ocean Engineering, ASCE,* **130, 4,** 220-221.

Kirby, R. & Parker, W. R. 1980. Fine sediment studies relevant to dredging practice and control. *Second International symposium on dredging technology.* Texas Univeristy, USA.

Kirby, R. & Parker, W. R. 1983. Distribution and behaviour of fine sediment in Severn Estuary and Ineer Bristol Channel. *Canadian Journal of Fisheries and Quatic Sciences,* **40, 1**.

Kranck, K. 1980. Experiments on the significance of flocculation in the settling of fine-grained sediment in sitll water. . *Canadian Journal of Earth Science,* **17,** 1517-1526.

Krone, R. B. 1962. *Flume studies on the transport of sediment in estuarine shoaling process.* University of Berkeley, California, USA.

LaCasce, J. H. & Bower, A. 2000. Relative dispersion in the subsurface North Atlantic. *Journal of Marine Research,* **58,** 863-894.

LaCasce, J. H. & Ohlmann, C. 2003. Relative dispersion at the surface of the Gulf of Mexico. *Journal of Marine Research,* **61,** 285-312.

LaCasce, J. H. 2008. Statistcs from Lagrangian observations. *Prog. Oceanogr,* **Vol 77,** 1-29.

Lambeck, A. & Woolfe, K. J. 2000. Composition and textural variability along the 10 m isobath, Great Barrier Reef: evidence for pervasive northward sediment transport. *Australia Journal of Earth Sciences,* **47,** 327-335.

Lambrechts, J., Humphrey, C., McKinna, L., Gourge, O., Fabricius, K., Mehta, A. J., Levis, S. & Wolanski, E. 2010. The importance of wave-indcued bed fluidisation in the fine sediment budget of Cleveland Bay, Great Barrier Reef. *Estuarine, Coastal and Shelf Science,* **89,** 154-162.

Lee, J. & Valle-Levinson, A. 2012. Influence of bathymetry on hydrography and circulation at the region between an estuary mouth and the adjacent continental shelf. *Continental Sehlf Research,* **Vol 41,** 77-91.

Legrand, S., Deleersnijder, E., Hanert, E., Legat, V. & Wolanski, E. 2006. High-resolution, unstructred meshes fro hydrodynamic models of the Great Barrier Reef, Australia. *Estuarine, Coastal and Shelf Science,* **68,** 36-46.

Lemckert, C. J., Cambell, P. G. & Jenkins, G. A. 2011. Turbulence in the bottom boundary layer of Moreton Bay, Queensland, Australia. *Journal Coastal Research***, No. 64,** 1091-1094.

Lentz, S. J. & Limeburner, R. 1995. The Amazon River plume during AMASSEDS: spatial characteristics and salinity variability. *Journal of Geophysical Research, Oceans,* **100, C2,** 2355-2375.

Li, G. S., Tang, Z., Yue, S., Zhuang, K. & Wei, H. 2001. Sedimentation in the shear front off the Yellow River mouth. *Continental Sehlf Research,* **21,** 607-625.

Li, M. & Amos, C. L. 2001. SEDTRANS96: the upgraded and better calibrated sediment transport model for continental shelves. *Computers and Geosciences,* **27, 6,** 941-970.

Liang, B. C., Li, H. J. & D.Y., L. 2007. Numerical study of three-dimensional suspended sediment transport in waves and currents. *Ocean Engineering,* **34, 11-12,** 1569-1583.

Liu, J., Li, A. & Chen, M. 2010. Environmental evolution and impact of the Yellow River sediments on deposition in the Bohai Sea during the last deglaciation. *Journal of Asian Earth Sciences,* **38,** 26-33.

Loftus, M. E. & Seliger, H. H. A comparative study of primary production and standing crops of phytoplankton in a protion of the upper Chesapeake Bay subsequent to tropical storm Agnes, in the effects of tropical storm Agnes on the Chesapeake estuarine system. *In:* RUZEEKI, E. P., ed. CRC publication, 1976 Baltimore and London. The Johns Hopkins University, 509-521.

Lu, J., Qiao, F. L., Wang, X. H., Wang, Y. G., Teng, Y. & Xia, C. S. 2011. A numerical study of transport dynamics and seasonal variability of the Yellow River sediment in the Bohai and Yellow seas. *Estuarine, Coastal and Shelf Science,* **96,** 39-51.

Lumborg, U. & Pejrup, M. 2005. Modelling of cohesive sediment transport in a tidal lagoon-An annual budget. *Marine Geology,* **318, 1-4,** 1-16.

Mantovanelli, A., Heron, M. L., Heron, S. F. & Steinberg, C. R. 2012. Relative dispersion of surface driftersr in a barrier reef region. *Journal of Geophysical Research,* **Vol 117, No. C11,** C11016.

Margvelashvili, N., Robson, B., Sakov, P., Webster, I. T., Parslow, J., Herzfeld, M. & Andrewartha, J. 2003. Numerical modelling of hydrodynamics, sediment tranpsort and biogeochemistry in the Fitzroy Estuary. CSIRO Marine Research: CRC for Coastal Zone Estuary & Waterway Management.

Martin, P. J., Peggion, G. & Yip, K. J. 1998. A comparison of several coastal ocean models. *Defense Technical Information Center OAI-PMH Repository (United States)* [Online].

Massei, N., Wang, H. Q., Dupont, J. P., Rodet, J. & Laignel, B. 2003. Assessment of direct transfer and resuspension of particles during turbid floods at a karstic spring. *Journal of Hydrology,* **275, 1-2,** 109-121.

McCave, I. N. 1979. *Suspended Sediment*, Cambridge University Press.

Mehta, A. J. 1986. *Characterization of cohesive sediment transport processes in estuarines,* Berlin, Springer-Verlag.

Mehta, A. J., Hayter, E., Parker, W. R., Krone, R. B. & Teeter, A. M. 1989. Cohesive sediment transport part I: Process Description. *Journal of Hydraulic Engineering* **115, 8,** 1076-1093.

Mellor, G. L. 1982. Development of a trubulence closure model for geophyscial fluid problems. *Reviews of Geophysics and Space Physics,* **20, 4,** 851.

Mu, J. & Zhang, X. 2007. Real-time flood forecasting method with 1-D unsteady flow model. *Journal of Hydrodynamics,* **19, 2,** 150-154.

National Climate Centre 2011. Frequent heavy rain events in late 2010/early 2011 lead to widespread flooding across eastern Asutralia. Special climate statement 24. Bureau of Meteorology.

National Climate Centre Bureau of Meteorology 2011. Frequent heavy rain events in late 2010/early 2011 lead to widespread flooding across eastern Australia. *Special Climate Statement 24.* Australia's National Meteorological Service.

Neil, D. T., Orpin, A. R., Ridd, P. V. & Yu, B. 2002. Sediment yield and impacts from river catchments to the Great Barrier Reef lagoon. *Marine Freshwater Research,* **53,** 733-752.

Neumann, L. E. 2004. *Modelling of flocculation and settling of suspended sediments using population balances.* PhD, University of Queensland.

Nezlin, N. P., Digiacomo, P. M., Diehl, D. W., Jones, B. H., Johnson, S. C., Mengel, M. J., Reifel, K. M., Warrick, J. A. & Wang, M. 2008. Stormwater plume detection by MODIS imagery in the southern California coastal ocean. *Estuarine, Coastal and Shelf Science,* **80,** 41-152.

Nielsen, P. 1992. Coastal bottom boundary layers and sediment transport. *In:* LIU, P. L.-F. (ed.) *Advanced series on ocean engineering.* Cornell University, USA: World Scientific Publishing Co. Pte. Ltd.

Niller, P. P. & Paduan, J. D. 1995. Wind-driven motions in the Northeast Pacific as measured by Lagranigan drifters. *American Meteorological Society,* **25,** 2819-2830.

O'Brien, K., Tuazon, D., Grinham, A. & Callahan, D. 2012. Impact of mud deposited by 2011 flood on marine and estuarine habitats in Moreton Bay. Healthy Waterways, Brisbane Australia.

Okubo, A. & Ebbesmeyer, C. C. 1976. Determination of vorticity, divergence and deformation rates from analysis of drogue observations. *Deep-Sea Research,* **23,** 349-352.

Olley, J. & Croke, J. 2011. Sources of sediment delivered to Moreton Bay and the Brisbane River floodplain during the January 2011 floods. The Department of Natural Resources and Mines, Queensland Government, Australia.

Page, L. V. & Shaw, L. C. 1973. Floods of June 1972 in the Harrisburg area, Pennsylvania. *U.S. Geological Survey, Hydrologic Investigation Atlas,* **530**.

Parchure, T. & Mehta, A. J. 1985. Erosion of soft cohesive sediment deposits. *Journal of Hydraulic Engineering,* **111, 10,** 1308-1326.

Parker, W. R. On the characterisation of cohesive sediment for transport modelling. *In:* BURT, N., PARKER, R. & WATTS, J., eds. 4th Nearshore and estuarine cohesive sediment transport conference, 1994 Wallingfor, England, UK. British Library Cataloguing in Publication Data.

Partheniades, E. 1965. Erosion and deposition of cohesive soils. *Journal of the Hydraulics Division,* **91,** 105-139.

Pattiaratchi, C. B. & Harris, P. T. 2003. Hydrodynamic and sand-transport controls on en echelon sandbank formation: an example from Moreton Bay, eastern Australia. *Marine and Freshwater Research* **53, 7,** 1101-1113.

Peck, A. J. & Hatton, T. 2003. Salinity and the discharge of salts from catchments in Australia. *Journal of Hydrology,* **272, 1-4,** 191-202.

Postma, H. 1967. Sediment transport and sedimentation in the estuarine environment. *In:* IN: ESTUARIES, E. B. G. H. L. A. A. (ed.) *American Assoc. for the Advancement of Science.*

Poulain, P. M. 1999. Drifter observations of surface circulation in the Adriatic Sea between December 1994 and March 1996. *Journal of Marine Systems,* **Vol 20, No. 1,** 231-253.

Qiao, F. L., Yuan, Y. L., Yang, Y. Z., Zheng, Q. A., Xia, C. S. & Ma, J. 2004. Wave-induced mixing in the upper ocean: distribution and application to a global ocean circulation model. *Geopysical Research Letters,* **31, 11**.

Qiao, S., Shi, X., Zhu, A., Liu, Y., Bi, N., Fnag, X. & Yang, G. 2010. Distribution and transport of suspended sediments off the Yellow River (Huanghe) mouth and the nearby Bohai Sea. *Estuarine, Coastal and Shelf Science,* **86,** 337-344.

Queensland Department of Natural Resources Mines and Water 2006. *Moreton draft water resource plan overview report and draft plan : incorporating the catchments of : Brisbane River, Pine River, Caboolture River, Cabbage Tree Creek, Pumicestone Creeks / prepared by Water Planning Group and Water Services (South East Region), Department of Natural Resources, Mines and Water.,* Brisbane.

Rhodes, M. 1998. *Introductionn to particle technology,* John Wiley & Sons Ltd, England, British Library Cataloguing in Publication Data.

Richardson, J. F. & Zaki, W. N. 1954. Sedimentation and fluidisation, Part I. *Transactions of the Institution of Chemical Engineers,* **32, 1,** 35-53.

Ridderinkhof, H. & Zimmerman, J. T. F. 1992. Chaotic stirring in a tidal system. *Science*, **No. 258,** 1107-1111.

Rijn, L. C. V. 1993. *Principles of sediment transport in rivers, estuaries and coastal seas,* Netherlands, Aqua Publications.

Rodi, W. 1984. Turbulence models and their applications in hydraulics. *International Association for the History of Religions (IAHR).* Delft, the Netherlands.

Rouse, H. 1937. Modern conceptions of the mechanics of turbulence. *Transactions American Society of Civil Engineers,* **102,** 463-505.

References

Sabet, B. S. & Barani, G. A. 2011. Design of small GPS driftres for current measurements in the coastal zone. *Ocean & Coastal Management,* **Vol 54, No. 2,** 158-163.

Sanford, L. P. & Halka, J. P. 1993. Assessing the paradgim of mutually esclusive erosion and deposition of mud, with examples from upper Chesapeake Bay. *Marine Geology,* **114,** 37-57.

Schacht, C. & Lemckert, C. J. Quantifying the estuarine surface-sediment dynamics in the Brisbane River. Coasts and Ports Australiasian Conference, 9-12 September 2003 Auckland, New Zealand. 131.

Schacht, C. 2005. *The Quantification of estuarine suspended sediment dynamics: a drogue's perspective.* PhD, Griffith University.

Schroeder, K., Haza, A. C., Griffa, A., Ozgokmen, T. M., Poulain, P. M., Gerin, R., Peggion, G. & Rixen, M. 2011. Relative dispersion in the Liguo-Proventcal basin: From submesoscale to mesoscale. *Deep-Sea Research,* **58,** 209-228.

Schubel, J. R. Effects of Agnes on the suspended sediment of the Chesapeake Bay and contiguous shelf waters. *In:* DAVIS, J. & LAIRD, B., eds. The Effects of Tropical Storm Agnes on the Chesapeake Bay Estuarine System, 1977 Baltimore and London. The Johns Hopkins University Press.

Shetye, S. R. & Murty, C. S. 1987. Seasonal variation of the salinity in the Zuari estuary, Goa, India. *Earth Planet Science,* **96, 3,** 249-257.

Shi, C., Dian, Z. & You, L. 2002. Changes in sediment yield of the Yellow River basin of China during the Holocene. *Geomorphology,* **46,** 267-283.

Shi, M. C., Zhao, J. P. & Sun, Y. Y. 1985. The analyses of hydrographical characteristic in estuary of Huanghe River. *Journal of Shangdong College of Oceanology,* **15, 2,** 81-95.

Shi, W. & Wang, M. 2009. Satellite observation of flood-driven Mississippi River plume in the spring of 2008. *Geophysical Research Letters,* **36**.

Shrestha, P. A. & Orlob, G. T. 1996. Multiphase distribution of cohesive sediments and heavy metals in estuarine systems. *Journal of Environmental Engineering,* **122,** 730-740.

Signell, R. P. & Geyer, W. R. 1990. Numerical simulation of tidal dispersion around a coastal headland. *Coastal and Estuarine Studies***, No. 38,** 210-222.

Smagoringsky, J. 1963. General circulation experiments with the primitive equation. I. The basic experiment. *Monthly Weather Review,* **91,** 99-164.

Song, Y. & Haidvogel, D. 1994. A semi-implicit ocean circulation model using a generalized topography-following coordinate system. *Journal of Computational Physics,* **115,** 228-244.

Spencer, D., Lemckert, C. J., Yu, Y., Gustafson, J., S.Y., L. & Zhang, H. 2014. Quantifying dispersion in an estuary: A lagrangian drifter approach. *Journal Coastal Research***, Special Issue 66,** 48-53.

Stern, M. E. 1998. Seperation of a density current from the bottom of a continental shelf. *Journal of Physical Oceanography,* **Vol 28,** 2040-2049.

Sumer, B. M. & Oguz, B. 1978. Particle motions near the bottom in turbulent flow in an open channel. *Journal of Fluid Mechanism,* **86,** 109-127.

Tang, D. L., Kester, D. R., Wang, Z. D., Lian, J. S. & Kawamura, H. 2003. AVHRR satellite remote sensing and shipboard measurements of the thermal plume from the Daya Bay, nuclear power station, China. *Remote Sensing of Environment,* **84,** 506-515.

Teeter, A. M. 1986. *Vertical transport in fine-grained suspension and newly-deposited sediment,* New York, Springer-Verlag.

Tseng, R. S. 2002. On the dispersion and diffusion near estuaries and around islands. *Estuarine, Coastal and Shelf Science,* **54,** 89-100.

Umlauf, L. & Burchard, H. 2003. A generic lenght-scale equation for geophyscial turbulence models. *Journal of Marine Research,* **61, 2,** 235.

Uncles, R. J. & Stephens, J. A. 1996. Salt Intrusion in the Tweed Estuary. *Estuarine, Coastal and Shelf Science,* **43,** 271-293.

Uncles, R. J., Stephens, J. A. & Smith, R. E. 2002. The dependence of estuarine turbidity on tidal intrusion length, tidal range and residence time. *Continental Sehlf Research***, 22,** 1835-1856.

Uncles, R. J., Stephens, J. A. & Harris, C. 2006. Runoff and tidal influences on the estuarine turbidity maximum of a hihgly turbid system: The upper Humber and Ouse Estuary, UK. *Marine Geology,* **235, 1-4,** 213-228.

Van Leussen, W. 1988. *Aggregation of particles, settling velocity of mud flocs: A Review,* Springer-Verlag, Netherlands.

Van Rijin, L. C. 1984. Sediment tranposrt, Part II: Suspended load transport. *Journal of Hydraulic Engineering,* **110, 22,** 1613-1641.

Wang, H. J., Yang, Z. S. & Bi, N. 2006a. 3-D simulation of the suspended sediment transport in the Yellow River mouth I: shear front off the Yellow River mouth. *Journal of Sediment Research,* **2,** 1-9.

Wang, H. J., Yang, Z. S., Satio, Y., Liu, J. P. & Sun, X. X. 2006b. Interannual and seasonal variation of the Huanghe (Yellow River) water discharge over the past 50 years: connections to impacts from ENSO events and dams. *Global and Planetary Change,* **50, 3-4,** 212-225.

Wang, J. J., Lu, X. X., Liew, S. C. & Zhou, Y. 2009. Retrieval of suspended sediment concentrations in large turbid rivers using Landsat ETM+: an example from the Yantze River, China. *Earth Surface Processes and Landforms,* **34,** 1082-1092.

Wang, J. J. & Lu, X. X. 2010. Estimation of suspended sediment concentrations using Terra MODIS: An example from the lower Yangtze River, China. *Science of the Total Environment,* **408,** 1131-1138.

Wang, X. H. & Wang, H. J. 2010. Tidal strainig effect on the suspended sediment transport in the Huanghe (Yellow River) Estuary, China. *Ocean Dynamics,* **60,** 1273-1283.

Warner, J. C., Sherwood, C., Signell, R. P., Harris, C. K. & Arango, H. 2008. Development of a three-dimensional, regional , coupled, wave,current and sediment transport model. *Computers and Geosciences,* **34,** 1284-1306.

Werner, A. D. & Lockington, D. 2006. Tidal impacts on riparian salinities near estuaries. *Journal of Hydrology,* **328, 3-4,** 511-522.

Wilcox, D. C. 1988. Reassessment of the scale-determining equation for advanced turbulence models. *The American Institue of Aeronautics and Astronautics Journal,* **26, 11,** 1299-1310.

Winant, C. D. 1983. Longshore coherence of currents on the southern California shelf during the summer. *Journal of Physical Oceanography***, 13,** 54-64.

Winterwerp, J. C. 2002. On the flocculation and settling velocity of estuarine mud. *Continental Sehlf Research,* **22,** 1339-1360.

Winterwerp, J. C. & Van Kesteren, W. G. M. 2004. Introduction to the physics of cohesive sediment in the marine environment. *Developments in Sedimentology,* **56**.

Wolanski, E., King, B. & Galloway, D. 1997. Salinity intrusionin the Fly River estuary, Papua New Guinea. *Journal Coastal Research,* **13, 4,** 983-994.

Wolanski, E., Fabricius, K., Cooper, T. & Humphrey, C. 2008. Wet season fine sediment dynamics on the inner shelf of the Great Barrier Reef. *Estuarine, Coastal and Shelf Science,* **77,** 755-762.

Wolanski, E. 2014. *Estuaries of Australia in 2050 and beyond,* Dordrecht, Germany, Springer.

Wu, J. 1994. The sea surface is aerodynamically rough even under light winds. *Boundary-Layer Meteorology,* **69, 1-2,** 149-158.

Xu, D. & Xue, H. 2011. A numerical study of horizontal dispersion in a macro tidal basin. *Ocean Dynamics,* **Vol 61, No. 5,** 623-637.

Yang, Z. S., Ji, Y. J., Bi, N., Lei, K. & Wang, H. J. 2011. Sediment transport off the Huanghe (Yellow River) delta and in the adjacent Bohai Sea in winter and seasonal comparison. *Estuarine, Coastal and Shelf Science,* **91,** 173-181.

Yates, M. G., Jones, A. R., McGrorty, S. & Goss-Custard, J. D. 1993. The use of satellite imagery to determine the distribution of intertidal surface sediments of the Wash, England. *Estuarine, Coastal and Shelf Science,* **1993, 36,** 333-344.

You, Z.-J. & Yin, B.-S. 2007. Fine sediment resuspension dynamics in Moreton Bay. *China Ocean Engineering,* **32, 2,** 267-280.

Yu, Y., Zhang, H. & Lemckert, C. J. 2011. The response of the river plume to the flooding in Moreton Bay, Australia. **Special Issue No. 64,** 1214-1218.

Yu, Y., Zhang, H. & Lemckert, C. J. Effects of mesh resolution for hydrodynamic and transport modelling in coastal area. *In:* GU, Y. & SAHA, S. C., eds. Proceedings of the 4th International Conference on Computational Methods, 2012 Crowne Plaza, Gold Coast, Australia. 21-27.

Yu, Y., Zhang, H. & Lemckert, C. J. 2013a. Seasonal variations of the salinity and turbidity in the Brisbane River estuary, Queensland, Australia. *Journal of Coastal Research,* **Special Issue No. 65**.

Yu, Y., Zhang, H. & Lemckert, C. J. 2013b. Numerical analysis on the Brisbane River plume in Moreton Bay due to Queensland floods 2010-2011. *Environmental Fluid Mechanics,* **Vol 14, No. 1,** 1-24.

Yu, Y., Zhang, H. & Lemckert, C. J. The tidal influence on the turbidity maximum in a tide-dominated estuary: The Brisbane River estuary, Australia. *In:* WANG, Z., LEE, J. H.-W., GAO, J. & CAO, S., eds. Proceedings of the 35th IAHR World Congress, 2013c Chengdu, China. 7998-8007.

Yu, Y., Spencer, D., Zhang, H. & Lemckert, C. J. 2014a. Numerical and experimental study of dispersion in a shallow coastal area. *11th Pacific Asia Offshore Mechanics Symposium.* Shanghai, China.

Yu, Y., Zhang, H. & Lemckert, C. J. 2014b. Salinity and turbidity distributions in the Brisbane River estuary, Australia. *Journal of Hydrology,* **519, PartD,** 3338-3352.

Yu, Y., Zhang, H. & Lemckert, C. J. 2015. Turbidity distribution in the Brisbane River estuary during the 2010-2011 Queensland floods. *the 36th International Association for Hydro-Environment Engineering and Research (IAHR) World Congresses.* The Hague, the Netherlands.

Yu, Y., Zhang, H., Spencer, D., Dunn, R. J. K. & Lemckert, C. J. 2016. An investigation of dispersion characteristics in shallow coastal waters. *Estuarine, Coastal and Shelf Science,* **180,** 21-32.

Zann, L. 1995. Our Sea, Our Future. *Major findings of the state of the Marine environment report for Australia.* Department of Environment, Sport and Territories, Canberra, Australia.

Zhang, H. & Chan, E. S. 2003. Modeling of the turbulence in the water column under breaking wind waves. *Journal of Oceanography,* **59, 3,** 331-341.

Zhang, H., Madsen, O. S., Sannasiraj, S. A. & Chan, E. S. 2004. Hydrodynamic model with wave-current interaction applied in coastal regions. *Estuarine, Coastal and Shelf Science,* **61,** 317-324.

Zhang, H., Sannasiraj, S. A. & Chan, E. S. 2009. Wind wave effects on hydrodynamic modelling of ocean circulation in the South China Sea. *The Open Civil Enginerring Journal,* **Vol 3,** 48-61.

Ziegler, C. K. & Nesbitt, B. 1994. Fine-grained sediment transport in Pawtuxet River, Rhode Island. *Journal of Hydraulic Engineering,* **120,** 561-576.

Zimmerman, J. T. F. 1976. Mixing and flushing of tidal embayments in the western Dutch Wadden Sea, Part II: Analysis of mixing processes. *Netherlands Journal of Sea Research***, 10,** 601-630.

Appendices

This section presents two other publications which provided supplementary information and helped understand the results of this PhD research.

Appendix A

Yu, Y., Zhang, H. and Lemckert, C., 2013. Seasonal variations of the salinity and turbidity in the Brisbane River estuary, Queensland, Australia. In: Conley, D.C., Masselink, G., Russell, P.E. and O'Hare, T.J. (eds.), Proceedings 12th International Coastal Symposium (Plymouth, England), Journal of Coastal Research, Special Issue No. 65, pp. 1253-1258, ISSN 0749-0208.

Appendix B

Yu, Y., Spencer, D., Zhang, H. & Lemckert, C. J. Numerical and experimental study of dispersion in a shallow coastal area. The 11th Pacific Asia Offshore Mechanics Symposium, October 12-16, 2014 2014 Shanghai, China. (1 USB)

Appendix A

Seasonal variations of the salinity and turbidity in the Brisbane River estuary, Queensland, Australia

Abstract

The Brisbane River estuary, Queensland, Australia, is a vital ecological region and of importance for people who live nearby. The estuarine health status has been influenced by both marine and riverine conditions. The estuary experiences high turbidity and salinity throughout most of the year, however, little is known about the actual turbidity and salinity structures within it. This study examined ten-years of field data to investigate the seasonal variations in salinity and turbidity. The results revealed that the salinity at the Brisbane River mouth was estimated to be 31.7 and 32.8 ppt during wet and dry seasons, respectively. The surface longitudinal salinity then decreased along the estuary, with the highest decreasing rates of 0.7 and 0.6 ppt/km occurring within the mid-estuary. The average salinity flux was 8.19×104 and 8.25×104 ppt m^3/s during the wet and dry seasons, respectively. The slight discrepancy of salinity fluxes between two seasons may be attributed to the lack of consideration of the other freshwater inflows to the estuary. The actual salinity flux through the estuary will therefore fall within the two estimated flux values. It was also found that the length of the turbidity maximum was approximately 35 km during wet season, which was three times as long as it is during the dry seasons. The values indicate the perceived, and actual, health of the estuary changes with season and location and thus care must be taken when interpreting ad-hoc measurements.

Keywords: Salinity intrusion, Salinity flux, Turbidity maximum

A.1. Introduction

An estuary forms an interaction region between coastal river and ocean environments. The health condition of an estuary is therefore subject to both marine impacts, namely tides and waves, and riverine influences, such as the influx of freshwater and sediment. Generally, an estuary brings marine conditions into a coastal river as far as the tidal limit, which raises a number of issues, such as the salinity intrusion and the existence of a possible turbidity maximum zone. The presence and movement of saltwater intrusion and the turbidity maximum not only affect the physical environment, but also lead to contamination of drinking water sources. Excess amounts of suspended particles can even contribute to environmental damage (Ecosystem Health Monitoring Program, 2007).

In recent years, a large number of studies have examined the characteristics of salinity intrusion and turbidity maximum variations in estuaries. Engedahl (1995) reported the salinity distribution in the Zuari estuary in India during one tidal cycle once every month from 1977 to 1978. Based upon analysis of the data, (Rijn, 1993) found that the Zuari estuary was partially stratified during wet seasons but vertically mixed during dry seasons. They also demonstrated two processes controlling the transport of salt: i) runoff induced advective transport out of the estuary and ii) tidally induced diffusive transport into the estuary during dry seasons. (Hill et al., 1998) measured the turbidity at spring and neap tides during a one year period throughout the length of the upper Humber and Ouse Estuary, UK. Their data consistently exhibited a strong estuarine turbidity maximum (ETM) in the lower estuary during high-runoff winter but in the upper estuary during low-runoff summer. Studies (Kranck, 1980, Jimenez and Madsen, 2003) on suspended sediment dynamics within the Brisbane River estuary (BRE) indicated that the ETM extended from about 20 to 60 km upstream from the mouth, with the peak turbidity levels occurring at around 45 km. Additionally, (Richardson and Zaki, 1954) measured the salinity and turbidity at a single site in the BRE over a period of thirteen-months. A significant feature of their study was that the magnitude of turbidity measurements was strongly influenced by the sediment carried into the estuary from runoff. Although some previous studies confirmed the existence of the ETM within the BRE, no study regarding the seasonal variations of the salinity intrusion and ETM has been undertaken thus far.

The motivation for this study was therefore driven by the need to enhance the state of knowledge of the changes in salinity and turbidity distributions within the BRE, during wet and dry seasons, so that future river management strategies can be appropriately planned.

A.2. Methods

A.2.1 Study Site

The Brisbane River is located in south-east Queensland, Australia and has a catchment of 13560 km^2 (Eyre et al., 1998). It is distinctly brown in colour, especially after rain. It has low biological diversity, with a limited number of organisms that can survive the high turbidity, highly variable discharge and salinity (Dennison and Abal, 1999). The Brisbane River estuary is a micro-tidal estuary, with a tidal section of approximate 80 km in length (Ecosystem Health Monitoring Program, 2007), and salt water intruding about 60 km upstream from the mouth for most of the year (Richardson and Zaki, 1954). The maximum depth along the estuary varies from approximate 15 m at the mouth to about 4m at the tidal limit (Eyre et al., 1998). This micro-tidal estuary has a maximum spring tidal range of 2.6 m, with various dams along the estuary limiting estuary inflows to 1-2 m^3/sec during most of the year (Richardson and Zaki, 1954).

A.2.2 Salinity, Turbidity and Discharge Data

The Queensland Government Ecosystem Healthy Monitoring Program (EHMP) has implemented consistent water sampling and monitoring at monthly intervals along the BRE. There are currently 16 monitoring sites located along the axis of the estuary from the river mouth of the estuary to the tidal limit, as marked in Figure A. 1, with all measurements made on the ebbing tide. Profile measurements (at depth intervals of 2 m) of temperature, conductivity (from which salinity is derived) and turbidity (in NTU) were conducted at each site from 2002 to 2011 (Ecosystem Health Monitoring Program, 2007). Turbidity was observed with a YSI 6920 turbidity sensor consisting of an LED, near infrared light with the wavelengths ranging from 830 to 890nm. A YSI 6920 temperature sensor which comprises a thermistor of sintered metallic oxide was used to measure the water temperature. Salinity was measured indirectly with a YSI6920 conductivity sensor. The output from the sonde's conductivity and observed temperature were applied to calculate the salinity (American Public Health Association, 1998, Ecosystem Health Monitoring Program, 2007).

The Department of Environment and Heritage Protection, Queensland, Australia, regularly measures the volume of water at their stream monitoring sites. One site, named as the

164

Brisbane River at Savages Crossing, has the closest proximity to the tidal limit of the BRE. The river inflow throughout the Savages Crossing site is used in this paper as an indicator of the seasonal variability of freshwater BRE inflow. To focus on the seasonal variation of the BRE condition, the rainfall-driven flood events (with the average flow greater than 100 m^3/s) are excluded here.
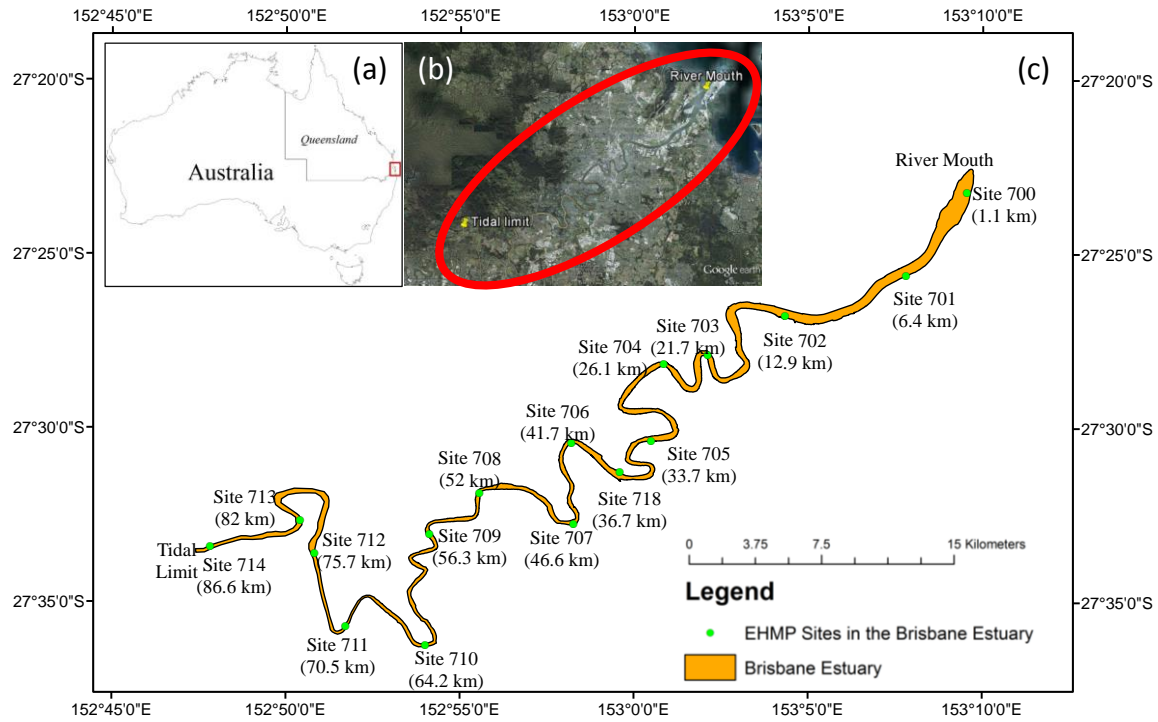

Figure A. 1. The Brisbane River estuary (BRE), Queensland, Australia. The green dots and their numbers indicate observation sites with their ID along the BRE. The AMTD (km) from the river mouth are marked for each site. (Data Source: (a) and (c) from Geoscience Australia; (b) from Google Map).

A.3. Results

A.3.1 Longitudinal and Vertical Distribution of Salinity and Turbidity

The discharge was different from dry seasons (with an average flow of 5.8 m^3/s) during June-November to wet seasons (7.8 m^3/s) during December-May. Figure 2 presents the distribution of surface salinity along the BRE, together with the curves which are polynomial least square fits to the observation data. These curves describe salinity (S) in ppt as a continuous function of x, the upstream distance (in metres) from the Brisbane River mouth. Correspondingly, the function $S(x)$ is defined as Eq. (4.4-3), in which coefficients of p_i (i = 1, 2, 3, 4, 5) are specified as -2.48×10^{-18}, 5.39×10^{-13}, -3.48×10^{-8}, 2.02×10^{-4} and 32.8 for dry seasons and -3.37×10^{-18}, 6.95×10^{-13}, -4.22×10^{-8}, 2.77×10^{-4} and 31.7 for wet seasons, respectively.
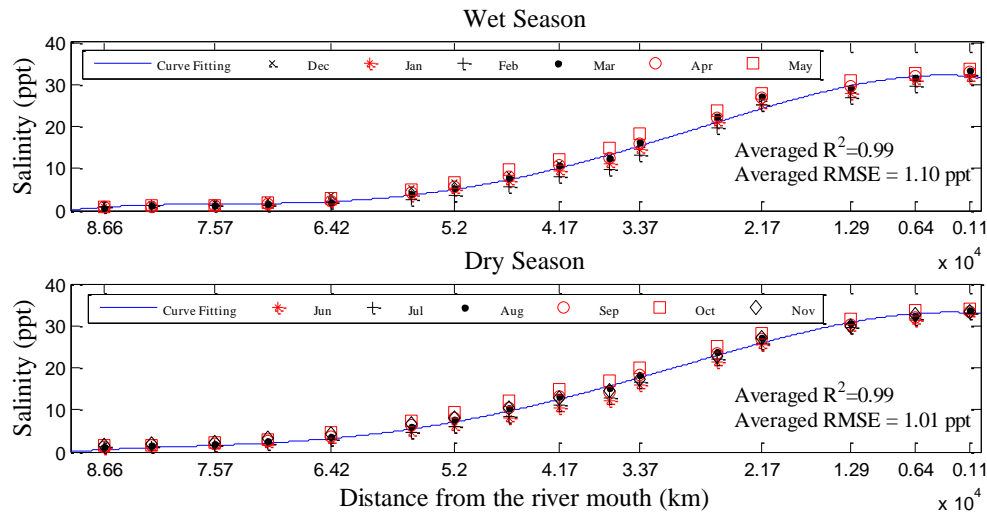
165

Figure A. 2 Monthly-averaged salinity distribution in the BRE. The horizontal axes indicate the distance from the river mouth. The observed values are denoted by a variety of markers. The solid lines represent polynomial fit $S(x)$ to the observed salinity along the estuary.

It is estimated that the salinity was 32.8 and 31.7 ppt at the Brisbane river mouth during dry and wet seasons, respectively, which are in accordance with the findings in (Yu et al., 2011). In addition, it was also found that the surface salinity decreases continuously upstream from the river mouth. The rates of salinity decrease were approximately 0.3 and 0.4 ppt/km up to 20 km upstream; 0.6 and 0.7 ppt/km along the mid-estuary; and 0.4 and 0.3 ppt/km from 60 km upstream to the tidal limit during dry and wet seasons, respectively. This indicates the salinity at the river mouth was lower and decreased faster along the estuary during the wet season compared to the dry season.

The observed data demonstrates the BRE is vertically mixed during ebb-tide for both seasons. As shown in Figure A. 3 the front of salinity intrusion (defined as the 30 ppt isohaline) extended around 12 km upstream from the river mouth during both seasons. However, the location of freshwater-saline interaction zone (FSI), where the salinity isohaline is 5 ppt, significantly differed between the two seasons. As seen in Figure A. 3, the FSI was located at 41 and 64 km from the river mouth during wet and dry seasons, respectively, demonstrating the effects of the large discharge during the wet season.

As shown in Figure A. 4 the turbidity along the BRE had a greater variation in character than the salinity pattern, with the location and magnitude of the turbidity maximum varying significantly between seasons. Figure A. 4 clearly shows that the ETM zone, which is defined as the region with values greater than 50 NTU (Bell, 2010), extended throughout the mid-estuary. The length of ETM was approximately 35 km during wet seasons, which was three

times as long as it is during dry seasons. The peak turbidity levels occurred at 70 and 55 km upstream from the river mouth during dry and wet seasons, respectively. There might be two reasons to explain how the higher flow rates in wet seasons result in the larger turbidity: i) the larger discharge most likely eroded the soil from the river banks providing fresh sediment that deposited in the estuary; and ii) a greater level of resuspension of fine-grained sediments occurred, with wind, tides and higher discharge intensifying currents and subsequently resuspension (Zhang and Chan, 2003, Zhang et al., 2004).

Figure A. 5 shows the vertical turbidity distribution in January and September, 2008. Although the difference in magnitude of the turbidity maximum was large, the vertical distribution patterns were similar during the two seasons. This indicates that the vertical structure of turbidity was stable and did not significantly change with the magnitude of discharge.
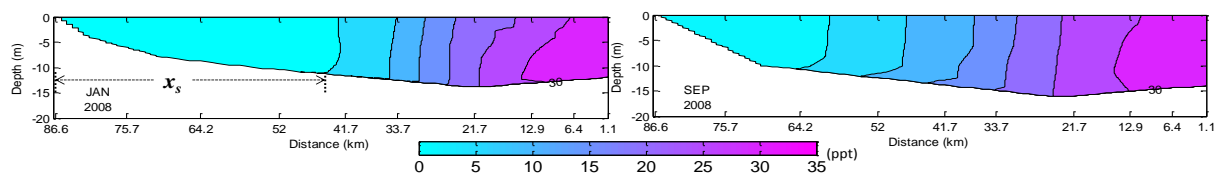

Figure A. 3 Vertical distributions of salinity in January (wet) and September (dry), 2008.
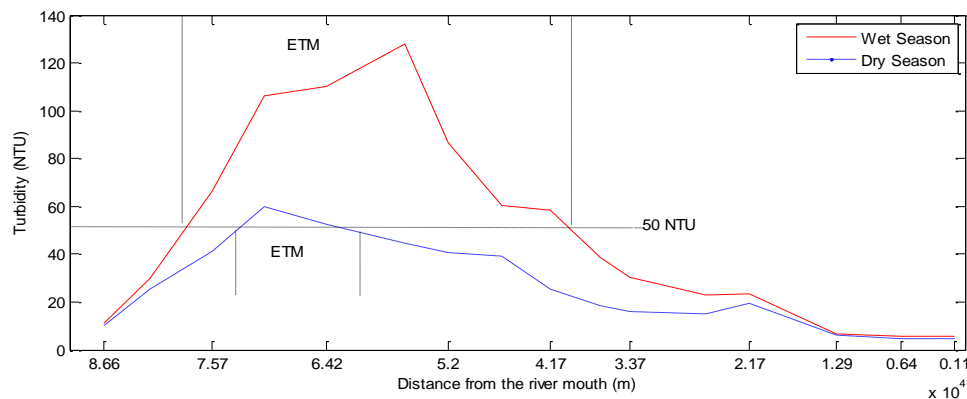

Figure A. 4 Monthly-averaged turbidity distribution in the BRE over the last 10 years, i.e. 2002-2011.
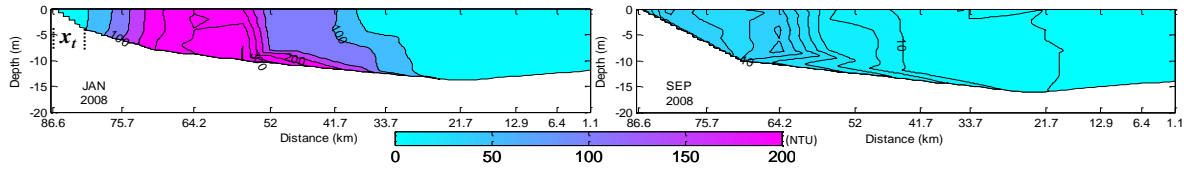
Figure A. 5 Vertical distributions of turbidity in January (wet) and September (dry), 2008

A.3.2 Seasonal Variations of the FSI and ETM

A spatially defined FSI is characteristic of the saltwater intrusion and the ETM is a feature of the suspended particulate matter distributions within the estuary. The distance between the FSI and the tidal limit is denoted as x_s, and the distance between the head of the ETM and the tidal limit is represented as x_t. Two quantities were determined from the longitudinal and vertical distributions of salinity and turbidity as functions of distance from the tidal limit, as shown in Figure A. 3 and Figure A. 5. These two variables are affected by the tidal conditions and thus vary frequently within a narrow range over the tidal cycle. Note that the evaluations of these variables in this study are based on the field data which were all measured on the ebbing tide. Therefore, their variations corresponding to tidal conditions are not considered here.
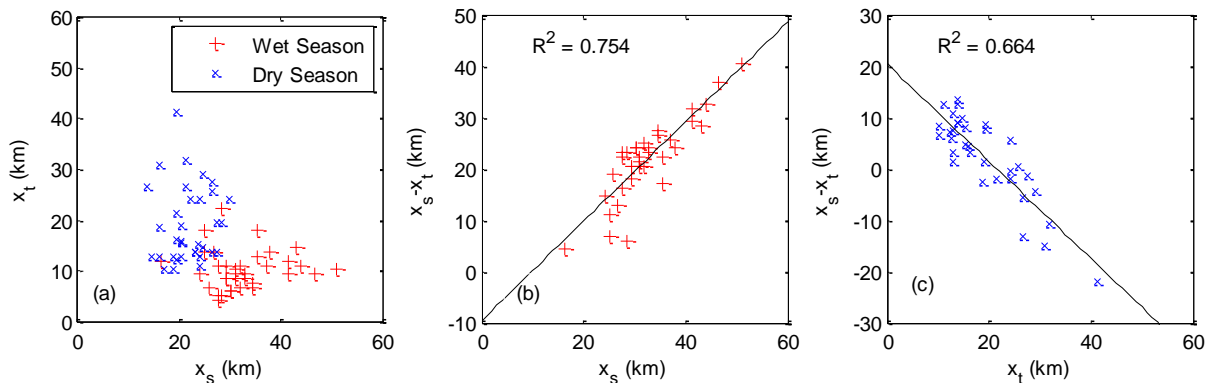

Figure A. 6 Seasonal variation of x_s and x_t within the BRE during 2002 to 2011. The $(x_s - x_t)$ represents the separation distance of the ETM head and FSI.

Figure A. 6 (a) shows the seasonal variations of estimated x_s and x_t within the BRE. The occurrence of the larger x_s (around 30 km) together with the smaller x_t (approximate 10 km) during wet seasons indicates the FSI was close to the river mouth but the head of the ETM was near to the tidal limit. During the dry season the FSI retreated but the ETM head moved toward the river mouth with the x_s and x_t being about 20 km and 23 km from the tidal limit, respectively. It was further found that the separation distance of the FSI and ETM head ($x_s - x_t$), is a function of the distance of the FSI from the tidal limit, x_s, during the wet season, as

shown in Figure A. 6 (b). Positive values of the separation distance indicate the ETM front was on the left side of the FSI, implying that the head of the ETM occurred within the estuary where the salinity was less than 5 ppt. Therefore, all points in Figure A. 6 (b) indicate the ETM head was located in fresh or very low salinity waters during wet seasons. With the onset of dry seasons, the ETM head might appear down-estuary of the FSI in some months, as shown by negative separation distances in Figure A. 6 (c). Additionally, due to the slight changes in x_s, the separation distance mainly depends on the distance of the ETM head from the tidal limit, x_t, during the dry season.

A.3.3 River Discharge Influences on the Salt Budget

Based upon the polynomial curve fitting functions inFigure A. 2, the total salt transported within the estuary over every month, F_s, is given by Eq.(A. 1)

$$F_s = \int_0^{86600} S(x)F_q(x)dx \qquad (A. 1)$$

where $F_q(x)$ represents the river discharge flux. The lower limit of the integral is the river mouth and the upper is the tidal limit.

As the vertical salinity is relatively uniform throughout the estuary as shown in Figure A. 3, the contribution of the gravitational circulation to the salinity transport is ignored here. Hence, the salinity flux of the estuary, F_s, is mainly determined by the discharge-induced salinity advection from the upper-stream boundary (the salt is running out of the estuary), and tidally-induced salinity diffusion from the lower-stream boundary (the salt is running into the estuary).

Figure A. 7 shows the monthly-averaged salinity flux and flow discharge over a period of 2002-2011. The salinity flux continually decreased during the wet season, implying that the decreasing amount of saltwater intruded into the estuary. Conversely, the salinity flux significantly increased during the dry season, indicating that the increasing amount of saltwater was intruded. The average salinity flux was 8.19×10^4 and 8.25×10^4 ppt m^3/s during the wet and dry seasons, respectively. The salt loss during the wet season were progressively recovered in the follwing months, due to the smaller flow discharge during the dry season compared to the wet season.

The slight discrepancy of salinity fluxes between two seasons may be attributed to the lack of consideration of the freshwater inflows from the Bremer River and Oxley Creek, which were the main two tributaries that joined into the BRE. Thus, the salinity flux during the wet season was underestimated; on the contrary, it was overestimated during the dry season. The actual salinity flux through the BRE would fall within the two estimated flux values; that is the actural salinity flux within the Brisbane River estuary was greater than 8.19×10^4 ppt but less than 8.25×10^4 ppt.
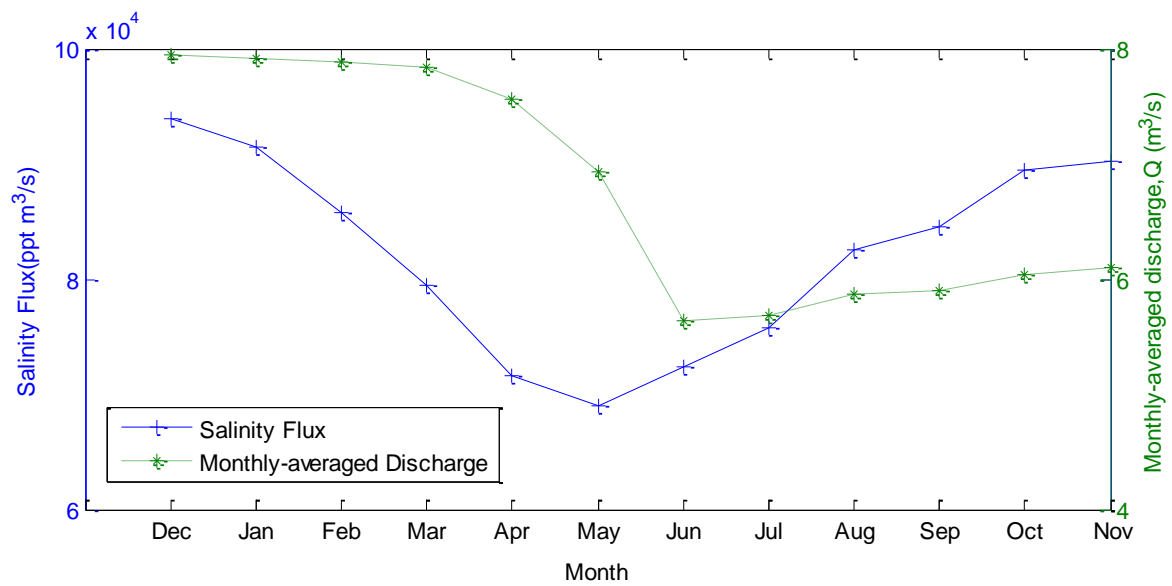

Figure A. 7 Monthly-averaged Salinity flux (ppt m^3/s) and monthly-mean river discharge (m^3/s) over a period of 2002-2011.

A.4. Conclusions

This study examined the seasonal variations of salinity and turbidity distribution within the Brisbane River estuary. The results revealed that the salinity at the Brisbane River mouth was estimated to be 31.7 and 32.8 ppt during wet and dry seasons, respectively. The rates of salinity decrease were approximately 0.3 and 0.4 ppt/km up to 20 km upstream; 0.6 and 0.7 ppt/km along the mid-estuary; and 0.4 and 0.3 ppt/km from 60 km upstream to the tidal limit during dry and wet seasons, respectively. This indicates the salinity at the river mouth was lower and decreased faster along the estuary during the wet season compared to the dry season.

During the wet season, the length of the turbidity maximum was approximately 35 km, which was three times as long as in the dry seasons. Although the distribution of surface salinity and

turbidity varied significantly between wet and dry seasons, the vertical distribution patterns tended to be similar: salinity fairly well mixed but turbidity significantly stratified. It also found that the front of the ETM was located in fresh or very low salinity waters, particularly during the wet season.

The average salinity flux was 8.19×10^4 and 8.25×10^4 ppt m^3/s during the wet and dry seasons, respectively. The slight discrepancy of salinity fluxes between the two seasons may be attributed to the lack of consideration of the freshwater inflows from the Bremer River and Oxley Creek, which were the main two tributaries that joined into the BRE. Thus, the salinity flux during the wet season was underestimated; on the contrary, it was overestimated during the dry season. The actual salinity flux through the BRE will therefore fall within the two estimated flux values.

The values attained throughout the study can be used to evaluate changes and patterns when evaluating the health status of the Brisbane River estuary, as well as being utilised for numerical modelling purposes as a basis for further studies. However, due to a lack of field data over a tidal cycle, it is difficult to determine the variations in salinity and turbidity distributions corresponding with tidal changes. This therefore will be investigated in further studies.

A.5. Acknowledgement

A.6. References

American Public Health Association 1998. APHA. 1998. *Standard Methods for the examination of Water and Wastewater,* **20**.

Dennison, W. C. & Abal, E. G. 1999. *Moreton Bay study: a scientific basis for the Healthy Waterways Campaign,* Brisbane, Queensland, Australia, South East Queensland Regional Water Quality Management Strategy.

Ecosystem Health Monitoring Program 2007. *Ecosystem Health Monitoring Program 2005-06 Annual Technical Report,* Brisbane, South East Queensland Healthy Waterways Partnership.

Engedahl, H. Hindcast simulations of ocean currents in the Norwegian coastal waters Part 1: Model set uo and sensitivity tests. *In:* SPAULDING, M. & CHENG, R. T., eds. Estuarine and coastal modelling, 1995 San Diego, California. American Society of Civil Engineers, 379-390.

Eyre, B., Hossain, S. & McKee, L. 1998. A suspended sediment budget for the modified subtropical Brisbane River estuary, Australia. *Estuarine, Coastal and Shelf Science,* **47,** 513-522.

Hill, P. S., Syvitski, J. P. & Cowan, E. A. 1998. In situ observations of floc settling velocites in Glacier Bay, Alaska. *Marine Geology,* **145,** 85-94.

Jimenez, J. A. & Madsen, O. S. 2003. A simple formula to estimate settling velocity of natural sediments. *Journal of Waterway, Port, Coastal and Ocean Engineering, ASCE,* **130, 4,** 220-221.

Kranck, K. 1980. Experiments on the significance of flocculation in the settling of fine-grained sediment in sitll water. . *Canadian Journal of Earth Science,* **17,** 1517-1526.

Richardson, J. F. & Zaki, W. N. 1954. Sedimentation and fluidisation, Part I. *Transactions of the Institution of Chemical Engineers,* **32, 1,** 35-53.

Rijn, L. C. V. 1993. *Principles of sediment transport in rivers, estuaries and coastal seas,* Netherlands, Aqua Publications.

Yu, Y., Zhang, H. & Lemckert, C. J. 2011. The response of the river plume to the flooding in Moreton Bay, Australia. **Special Issue No. 64,** 1214-1218.

Zhang, H. & Chan, E. S. 2003. Modeling of the turbulence in the water column under breaking wind waves. *Journal of Oceanography,* **59, 3,** 331-341.

Zhang, H., Madsen, O. S., Sannasiraj, S. A. & Chan, E. S. 2004. Hydrodynamic model with wave-current interaction applied in coastal regions. *Estuarine, Coastal and Shelf Science,* **61,** 317-324.

Appendix B

Numerical and experimental study of dispersion in a shallow coastal area

Abstract

Horizontal dispersion plays an important role in coastal water sediment and pollutant transport and therefore it must be well assessed and understood for the successful development of any numerical modelling scheme. The performance of a dispersion model was assessed, using experimental Lagrangian drifter data. The method applied in the drifter tracking experiments was introduced, and the numerical modelled results were compared with the *in situ* data. It appears that the simulated results were sensitive to the bathymetry resolution and wind conditions. In addition, the in-situ drifter trajectories were compared with the numerical modelling results in Moreton Bay, Australia. Good correlation with an R^2 of 0.73 between drifter data and modelled results was achieved indicating that the same set of model evaluations can be used to compute the particles spreading in further dispersion research.

B.1. Introduction

Coastal areas are generally ecologically rich regions and a popular place for human recreational activities. Spatially, the region encompasses the interaction zone between the coastal river and ocean. With an increasing amount of river borne sediment, and a greater variety of pollutions entering the coastal zone, in particular the likelihood of accidental oil spills, there could be a significant degradation of ecosystem health. Local weather, flow conditions and coastal processes all impact on the horizontal dispersion of particles and pollutants within the coastal waters (Zhang et al., 2009, Lemckert et al., 2011, Yu et al., 2013b). Therefore, understanding the characteristics of horizontal dispersion is fundamental for predicting the fate of pollutants in the coastal environment.

Over the past decades, a large number of in-situ investigations on horizontal dispersion have been carried out using a variety of methodologies. The Eulerian and Lagrangian field based measurement methods are the two main approaches that have been applied to estimate the magnitude of dispersion. With the recent significant development in tracking technology, the Lagrangian method has been widely applied due to its greater flexibility and possibility of a much higher sampling frequency. In addition, Sabet and Barani (2011) revealed that the data attained from the Lagrangian dispersion gives further insight into the flow dynamics, which the Eulerian data does not. Mantovanelli et al. (2012), for example, applied the Lagrangian method, by satellite-tracking surface drifters, to examine the particle dispersion and the diffusivity dynamics at the Great Barrier Reef, Australia.

As computational technology develops, an increasing amount of dispersion research has been conducted using numerical models. The configurations of numerical models, including the bathymetry mapping boundary conditions set-up and the adjustments of parameterization, have been the most important aspects that determine the performance of coastal modelling (Yu et al., 2012, Yu et al., 2013a). The application of a fully calibrated and verified model provides a powerful tool for research investigations with high temporal and spatial resolutions as it allows for a large range of environmental conditions to be explored. (Ridderinkhof and Zimmerman, 1992) simulated a large number of non-dissolving buoyant particles over five tidal cycles in the Wadden Sea. The study revealed that the tidal dispersion mechanism produced rapid water exchange along the channel and could be representative of many shallow tidal seas. Similarly, (Xu and Xue, 2011) modeled 250 particles over 12 hours

in a macro tidal basin in Cobscook Bay, USA, and found that the fundamental mechanism for particle dispersion was the chaotic advection arising from long tidal excursions.

The purpose of the present study is to investigate the capacity of a hydrodynamic dispersion model and estimate its performance comparing modelled and measured data. The measure data was derived from a series of drifter tracking experiments in Moreton Bay, Australia. The calibrated and verified model, which is being derived for Moreton Bay resulting from this study, can now be applied in further studies to investigate the effects of the tidal current variations, multiple wind condition and altering topography on the dispersive behavior in coastal waters. Therefore, it could be used as an operational tool to improve management practices for efficient protection of the coastal ecosystem.

B.2. Methodology

B.2.1 Study Area

Moreton Bay is located in sub-tropical southeast Queensland, Australia, as shown in Figure B. 1. It extends from 153.1^0 E to 153.5^0 E and from 27.05^0 S to 27.5^0 S, and covers an approximate area of 1523 km^2, with an average water depth of 6.8 m (Dennison and Abal, 1999). Moreton Bay is a largely confined body of ocean water which is adjacent to the urban region of Brisbane in the south west. It receives a mean annual river water of approximately 1.65×10^8 m^3, which is discharged through the Brisbane River catchment (Queensland Department of Natural Resources Mines and Water, 2006). Additionally, two large sewage plants are located at Oxley Creek, 32 km upstream from the Brisbane River mouth and Luggage Point at the river mouth. Consequently, significant volumes of sewage are discharged into the Brisbane River estuary can contribute to nutrient enrichment in Moreton Bay. A number of barrier islands on the western side of the bay restrict water exchange between the bay and ocean. As shown in Figure B. 1, there are three openings between the bay and the ocean - being north, east and south. The North Passage, with a width of 15.5 km, accounts for most of the water exchange between the Pacific Ocean and Moreton Bay (Dennison and Abal, 1999). The oceanic exchange for the South Passage, located between two large islands is more restricted. Extensive islands at the south lead to the least oceanic exchange in comparison with the other two openings (Queensland Department of Natural Resources Mines and Water, 2006).
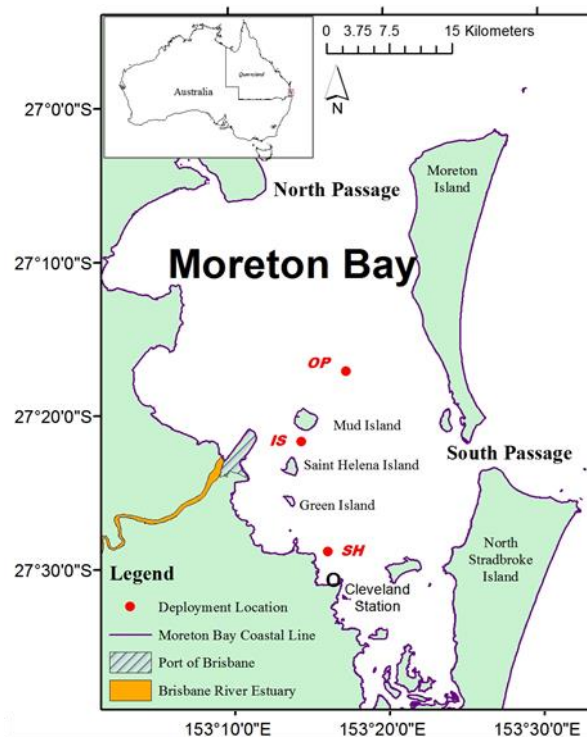
Figure B. 1 Map of Moreton Bay and the Brisbane River estuary. The red dots indicate the three chosen locations for drifters' deployments.

B.2.2 Drifter Measurement

To assist in developing an understanding of the horizontal dispersion in the Moreton Bay region a set of drifters were designed and deployed. The Lagrangian Self-locating Datum Marker Buoys (SLDMB) drifters were designed following Poulain (1999) as this follows the standard drifters used in many ocean and coastal water studies. The drifters were built with a strong aluminium frame, as shown in Figure B. 2 (a) and (b), consisting of four drag-producing vanes which worked together as a large effective drogue for stability. A SPOT 2 Satellite GPS Messenger unit was located within a PVC container bolted to the top of frame. The activated 'Track Progress' feature of the GPS allowed the position of the SLDMBs to be tracked in near real-time throughout the duration of the deployment, with a position fixing error of approximately 5 m (Spencer et al., 2014). The entire SLDMB drifter (Figure B. 2 (b)) had dimensions 1 (L) x 1 (W) x 1.4 (H) m and weighed approximately 10 kg.

Three experiments were conducted using the SLDMB drifters at three different sites (IS, SH and OP) in Moreton Bay, as marked in Figure B. 1. Four SLDMB drifters, which is the minimum required number to calculate the dispersion coefficient (REF), were deployed as a small cluster, initially spaced approximately 1 m apart. The drifter were deployed for up to 16 hours in the vicinity of Mud Island (IS) on 23 July; at the location close to a shore (SH) on 6

August; and in an open water area (OP) on 21 August 2013. Their positions were logged at 10-minute intervals. The position data was then used to estimate the dispersion coefficient, following the formula proposed by Signell and Geyer (1990).
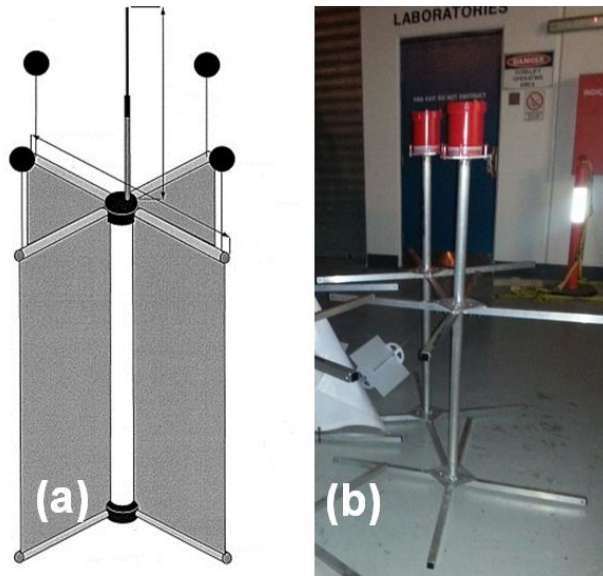

Figure B. 2 Example of a surface drifter design (a) (Poulain, 1999) and the frame (b) of the Self-Locating Datum Marker Buoy used in this study.

B.2.3 Numerical Model Configuration

The numerical model, DHI MIKE3 FM, was applied to simulate the dispersion in Moreton Bay. The MIKE 3 FM which is based on the numerical solution of the 3D incompressible Reynolds average Navier-Stokes Equations, with the assumption of Boussinesq and of hydrostatic pressure, is a three-dimensional hydrodynamic model associated with the Particle Tracking module formulated using sigma coordinates (DHI Water and Environment, 2013).

The bathymetry was represented by a network of flexible triangular cells. The higher resolution unstructured mesh allows the model to attain more accurate results than lower resolution schemes (Lee and Valle-Levinson, 2012). However, the time integration of the shallow water equations is performed using a semi-implicit scheme, that is, the horizontal terms are treated explicitly and the vertical terms implicitly (DHI Water and Environment, 2013). It implies that the Courant-Friedrich-Levy (CFL) condition has to be satisfied (CFL<1), in order to completely secure the stability of the numerical scheme in practice (DHI Water and Environment, 2013). Considering the stability restrictions of the model and the investigation of mesh resolution effects in a previous study (Yu et al., 2012), the bathymetry was presented as follows: the spatial resolution in the Brisbane River estuary (BRE) and

shallow coastal area was about 100 m; while the resolution became larger towards the far-field (deep areas), ranging from 100 to 1500 m. It therefore produced 4500 elements covering the entire Moreton Bay. The time step was set as 10 seconds to satisfy the critical CFL. In the vertical direction, the variable sigma co-ordinate, with 10 layers for the water column, permitted high resolutions (0.5 m) near the surface and bottom. The co-ordinate also maintained a reasonable resolution (2-3 m) at mid-depth.
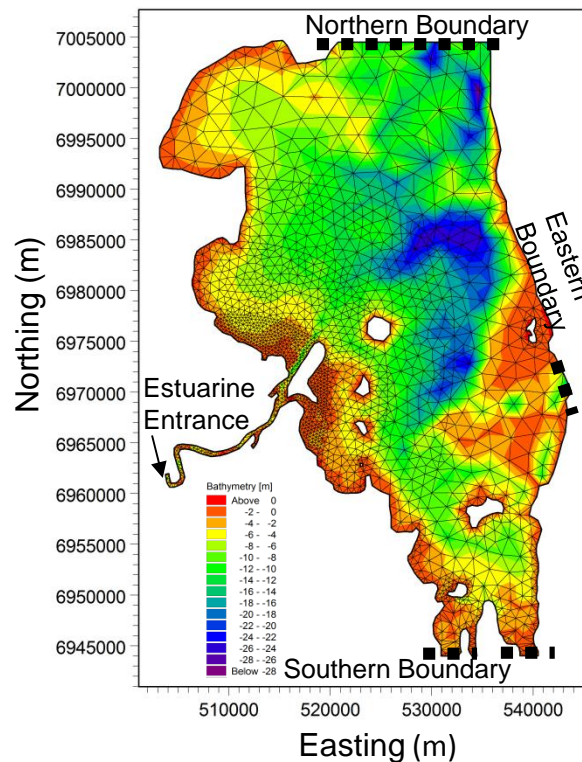

Figure B. 3 The bathymetry of Moreton Bay was represents by a network of flexible meshes.

There are four open boundaries surrounding Moreton Bay, as illustrated in Figure B. 3. The open western boundary denotes the entrance of the estuary. Hourly river discharge at this site derived from field observations by the Department of Environment and Heritage Protection, Queensland, was applied as the western boundary condition. The northern and eastern boundaries represent the North and South Passages of the Bay, respectively. The tidal elevations at these two open boundaries were predicted by the Marine Safety Queensland with a time interval of 10 minutes. Considering the complexity of the topography in the southern bay (a number of islands exist in the narrow channel), different set-ups was evaluated to determine the best condition to use. The open boundary was set at the bottom of southern bay, as marked in Figure B. 3, which consists of three segments separated by two

islands along the boundary. The tide at the southern open boundary condition was from the Global Tide Model DHI developed by DTU Space (http://www.space.dtu.dk/) using 12 major tidal harmonic constituents with a horizontal resolution of 0.125^0. Additionally, the surface wind forcing was accounted for using the 1 minute datasets from the inner reciprocal marker station provided by the Australian Bureau of Meteorology (BOM).

B.3. Result and Discussion

B.3.1 Sensitivity Tests

The results for different configurations of the numerical model are presented in Figure B. 4. In the first configuration (corresponding to Figure B. 4 (a)), the model was running with a relatively higher resolution ranging from 100 to 1500 m as described in the previous section, while the coarser resolution ranging from 500 to 5000 m was applied in the second model configuration (corresponding to Figure B. 4 (b)). In the third model configuration (corresponding to Figure B. 4 (c)), the finer resolution was applied (the same as the first configuration); the wind force, however, was not taken into account in the simulation of dispersion.
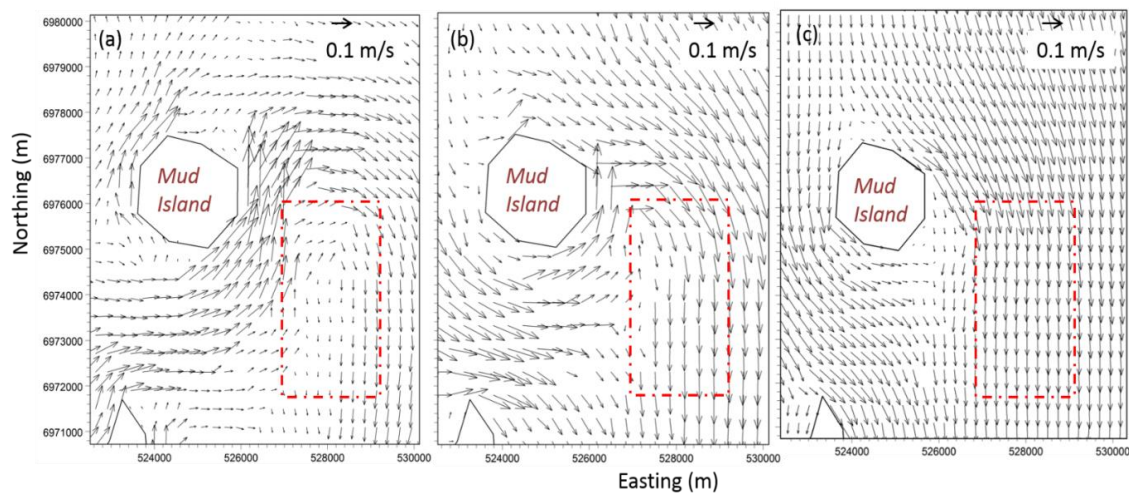

Figure B. 4 The depth-averaged current simulated near the Mud Island for 23 July2013. The model was running under real wind condition with (a) finer resolution and (b) coarse resolution, respectively. The model with finer resolution was running without any wind forcing in (c). Red dash-dotted frame indicates the significant differences of simulated current from these three different configuration models.

Figure B. 5 shows the comparison of surface elevations at the Brisbane Bar (153.17^0 E, 27.37^0 S) between the tidal gauge data and model results with coarser resolution and finer resolutions for July 2013. It can therefore be seen that the modelled elevations were well

matched with the measured tidal data, both in phase and amplitude. However, the tidal peaks were slightly underestimated, possibly because of the complex topography around the bar. The root-mean-square error (RMSE) was 8.73% and 7.22% for the corresponding model configurations with coarser and finer resolutions, respectively. As such, the decreasing RMSE illustrated that the quality of simulation results might be improved by using higher resolution. It has to be noted that the further reductions in element size produced very similar results to those with the first model configuration, with a RMSE of 7.21%, however the model running time increased by 50%.
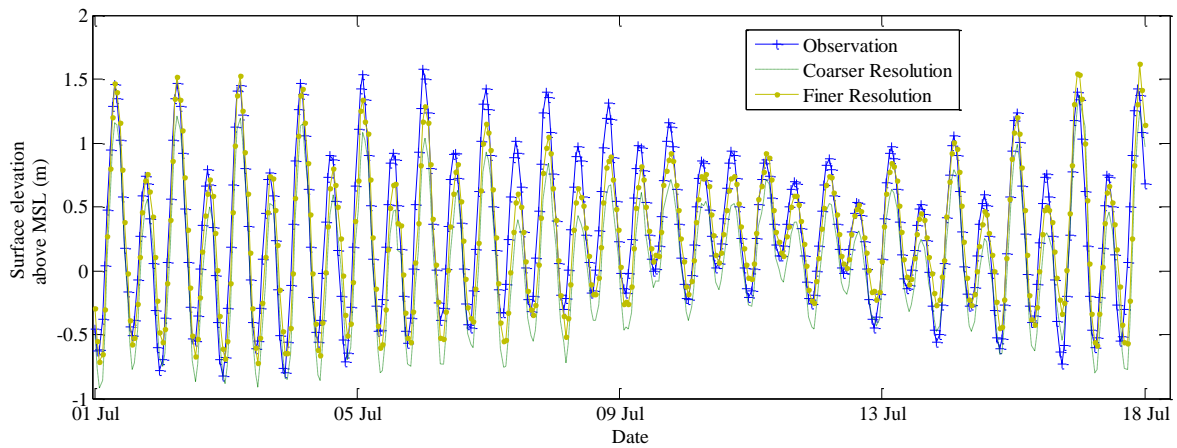

Figure B. 5 Comparison of surface elevations between the tidal gauge data and model results with coarser resolution and finer resolution for July 2013.

Furthermore, it was found that the first model configuration that has a higher resolution of complex topography and coastline, produces better non-linear flow behaviour. Figure B. 4 (a) clearly shows the current circulation in the vicinity of Mud Island, but the circulation was very weak and less evident in Figure B. 4 (b). In contrast, the appearance of the current circulation in Figure B. 4 (a) implies the simulated results are sensitive to the mesh configuration of the model, which agreed with the findings of Stern (1998) and Yu et al. (2012).

Figure B. 4 (c) shows the modelled depth-averaged current distribution in the vicinity of Mud Island without the consideration of the wind force. The Bay was fully driven by the tidal force and the model exhibited a strong north-southward current during the flood tide. The current circulation disappeared near the island. The differences between the simulated dynamics with (Figure B. 4 (a)) and without wind (Figure B. 4 (c)) reveal the importance of the wind effects in the coastal simulation.

B.3.2 Comparison of Measured and Simulated Trajectories of Drifters

The drifters were tracked for 16 hours and the trajectory of the drifters is shown in Figure B. 6 (a). Corresponding to the variation in the tidal elevation in Figure B. 6 (b), the drifters mainly moved in a southerly direction during the ebb tide. During the second half of flood tide, the drifters turned around and headed towards the northern part of the bay. The drifter travelled approximately 5 km when the elevation increased from low to high tide and 7.5 km when the elevation decreased from high to low tide. The effective displacement of the drifters was about 4.5 km during one tidal cycle. Besides the tidal current effects, wind forcing also impacted the drifter movement. The wind on this occasion was a south-westerly with a mean speed of 28 km/h, as shown in Figure B. 6 (c). Therefore, the drifter not only moved along a westerly direction (latitudinal), but also tended to head roughly in an easterly direction (longitudinal).
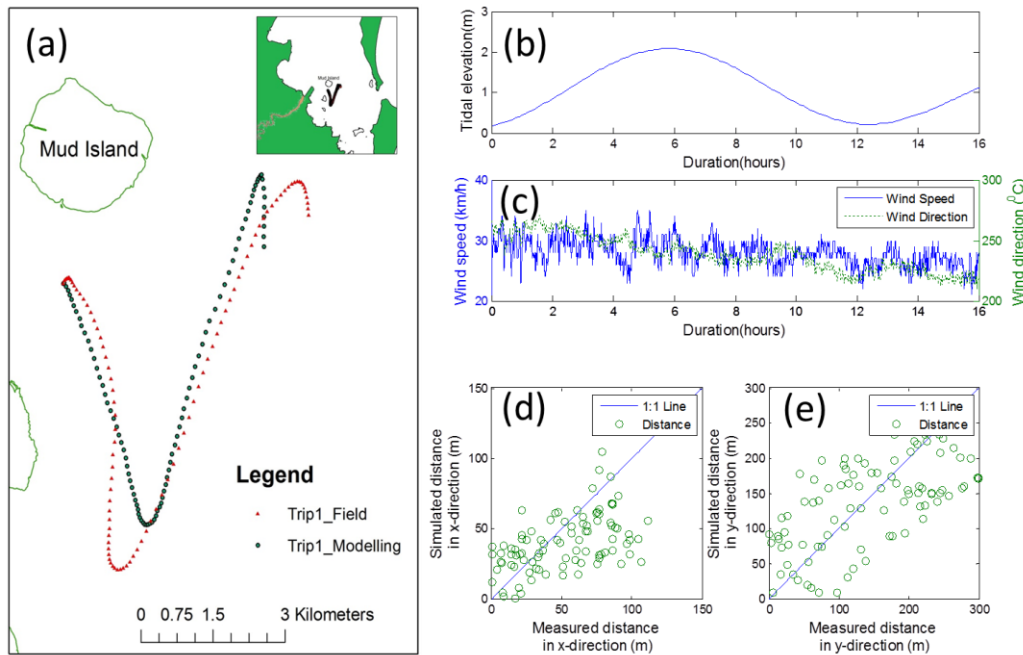

Figure B. 6 (a) The trajectory of the drifter in the first field trip, corresponding to (b) the change of the tidal elevation. (c) The wind condition over this duration. The comparison of the travelling distances between the measured and simulated drifter at each recorded time step (approximately 10 minutes) in (d) *x*- and (e) *y*- directions, respectively.

The simulated results exhibit very similar drifter trajectories to the drifter measurements. The comparison of the distances between the measured and simulated drifter trajectories at each recorded time step (approximately 10 minutes) in *x*- (longitudinal) and *y*- (latitudinal) directions are shown in Figure B. 6 (d) and (e), respectively. It can be seen that the model produced comparative accurate travelling distance of the drifter in *x*- direction with a mean

error of 23 m and a maximum error of 80 m. In contrast, the difference of travelling distance in y- direction was relatively larger, with a mean error of 60 m and a maximum error of 134 m. The root-mean-square error (RMSE) was approximately 70 m between the simulated and measured results, with a correlation of 0.73. It has been noted that the error in the location of the drogues and the large size of the bin of drifters might affect the accuracy of field measured data. Moreover, the finest resolution of bathymetry with a cell size of approximately 100 m was less than the calculated mean error of travelling distance, implying that the simulated results might be slightly impacted. However, overall, the satisfactory agreement between model results and field measured data validates the relative parameters, such as the horizontal dispersion coefficient and wind friction coefficients, adopted for Moreton Bay model calibration.

B.3.3 The Horizontal Dispersion in Moreton Bay

The cluster of four surface drifters was released during a period of approximately 16 hours and the position data recorded from these drifters was used to describe the dispersion behaviour of the water body, as defined in from Eq. (5.2-1) to (5.2-5).

Figure B. 7 shows the simulated and measured dispersion coefficient k, during the 16-hour deployment. The simulated results generally agreed with the measured data, with a RMSE of 0.1 m^2/s and an R^2 of 0.77. During the entire duration, the dispersion coefficient was less than 1 m^2/s. In particular, the dispersion coefficient was smaller than 0.1 m^2/s before around the 10th hour, as shown in Figure B. 7. After the 10th hour, the dispersion coefficient was significantly larger than the previous stage, although it also experienced some fluctuation. At approximately the 13th hour, the coefficient approached its peak value of 0.5~ 0.6 m^2/s. The variation of the dispersion coefficient in Figure B. 7 implies that the dispersion coefficients is roughly proportional to the rate of time change of dispersion for the cluster, which is consistent with the findings in LaCasce (2008) and Brown et al. (2009).
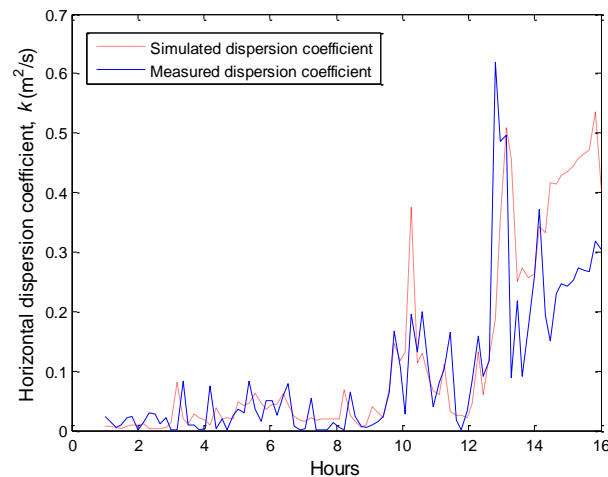
Figure B. 7 The simulated and measured horizontal dispersion coefficient k (m^2/s)

B.4. Conclusions

A three-dimensional hydrodynamic model coupled with the dispersion module was validated. The modelled outcomes which were associated with the field measurement dispersion results were used to investigate the dispersion behavior in Moreton Bay. By comparing simulated results from different model configurations, it appears that the results were sensitive to the bathymetry resolution and wind conditions. In addition, the in-situ drifter trajectories were compared with the numerical modelling results in Moreton Bay, Australia. The model results show a reasonable agreement with experimental data, with a correlation of 0.73 and a RMSE of 70 m, indicating the adequate ability of the model which could be applied in future studies. Further investigations could involve analyzing the tide and wind effects on the local horizontal dispersion behavior in Moreton Bay by applying the proposed model configuration.

B.5. Acknowledgements

B.6. References

Brown, J., MacMahan, J., Reniers, A., Thornton, E., (2009). "Surf zone diffusivity on a rip-channeled beach", *Journal Geophysical Research*, Vol 114, No. C11, pp C11015.

Dennison, W.C., Abal, E.G., (1999). *Moreton Bay study: a scientific basis for the Healthy Waterways Campaign*, South East Queensland Regional Water Quality Management Strategy, pp 245-278

DHI Water and Environment, (2013). *MIKE 21 & MIKE 3 FlOW MODEL FM*, Hydrodynamic and transport module scientifc documentation, DHI, pp 20-35

LaCasce, J.H., (2008). "Statistcs from Lagrangian observations", *Prog. Oceanogr*, Vol 77, pp 1-29.

Lee, J., Valle-Levinson, A., (2012). "Influence of bathymetry on hydrography and circulation at the region between an estuary mouth and the adjacent continental shelf", *Continental Sehlf Research*, Vol 41, pp 77-91.

Lemckert, C.J., Cambell, P.G., Jenkins, G.A., (2011). "Turbulence in the bottom boundary layer of Moreton Bay, Queensland, Australia", *Journal Coastal Research*, No. 64, pp 1091-1094.

Mantovanelli, A., Heron, M.L., Heron, S.F., Steinberg, C.R., (2012). "Relative dispersion of surface driftersr in a barrier reef region", *Journal of Geophysical Research*, Vol 117, No. C11, pp C11016.

Poulain, P.M., (1999). "Drifter observations of surface circulation in the Adriatic Sea between December 1994 and March 1996", *Journal of Marine Systems*, Vol 20, No. 1, pp 231-253.

Queensland Department of Natural Resources Mines and Water, (2006). *Moreton draft water resource plan overview report and draft plan : incorporating the catchments of : Brisbane River, Pine River, Caboolture River, Cabbage Tree Creek, Pumicestone Creeks / prepared by Water Planning Group and Water Services (South East Region), Department of Natural Resources, Mines and Water.*, pp 28-50

Ridderinkhof, H., Zimmerman, J.T.F., (1992). "Chaotic stirring in a tidal system", *Science*, No. 258, pp 1107-1111.

Sabet, B.S., Barani, G.A., (2011). "Design of small GPS driftres for current measurements in the coastal zone", *Ocean & Coastal Management*, Vol 54, No. 2, pp 158-163.

Signell, R.P., Geyer, W.R., (1990). "Numerical simulation of tidal dispersion around a coastal headland", *Coastal and Estuarine Studies*, No. 38, pp 210-222.

Spencer, D., Lemckert, C.J., Yu, Y., Gustafson, J., S.Y., L., Zhang, H., (2014). "Quantifying dispersion in an estuary: A lagrangian drifter approach", *Journal Coastal Research*, Special Issue 66, pp 48-53.

Stern, M.E., (1998). "Seperation of a density current from the bottom of a continental shelf", *Journal of Physical Oceanography*, Vol 28, pp 2040-2049.

Xu, D., Xue, H., (2011). "A numerical study of horizontal dispersion in a macro tidal basin", *Ocean Dynamics*, Vol 61, No. 5, pp 623-637.

Yu, Y., Zhang, H., Lemckert, C.J., (2012). "Effects of mesh resolution for hydrodynamic and transport modelling in coastal area", *Proceedings of the 4th International Conference on Computational Methods*, Crowne Plaza, Gold Coast, Australia, pp 21-27.

Yu, Y., Zhang, H., Lemckert, C.J., (2013a). "Numerical analysis on the Brisbane River plume in Moreton Bay due to Queensland floods 2010-2011", *Environmental Fluid Mechanics*, Vol 14, No. 1, pp 1-24.

Yu, Y., Zhang, H., Lemckert, C.J., (2013b). "The tidal influence on the turbidity maximum in a tide-dominated estuary: The Brisbane River estuary, Australia", *Proceedings of the 35th IAHR World Congress*, Chengdu, China, pp 7998-8007.

Zhang, H., Sannasiraj, S.A., Chan, E.S., (2009). "Wind wave effects on hydrodynamic modelling of ocean circulation in the South China Sea", *The Open Civil Enginerring Journal*, Vol 3, pp 48-61.